Titre: Title:	Characterization of the slug flow formation in vertical-to-horizontal channels with obstructions
Auteur: Author:	Ebru Nihan Onder
Date:	2004
Type:	Mémoire ou thèse / Dissertation or Thesis
Référence: Citation:	Onder, E. N. (2004). Characterization of the slug flow formation in vertical-to-horizontal channels with obstructions [Thèse de doctorat, École Polytechnique de Montréal]. PolyPublie. https://publications.polymtl.ca/7450/

URL de PolyPublie: PolyPublie URL:	https://publications.polymtl.ca/7450/
Directeurs de recherche: Advisors:	Alberto Teyssedou
Programme: Program:	Non spécifié

UNIVERSITÉ DE MONTRÉAL

CHARACTERIZATION OF THE SLUG FLOW FORMATION
IN VERTICAL-TO-HORIZONTAL CHANNELS
WITH OBSTRUCTIONS

EBRU NIHAN ONDER
DÉPARTEMENT DE GÉNIE PHYSIQUE
ÉCOLE POLYTECHNIQUE DE MONTRÉAL

THÈSE PRÉSENTÉE EN VUE DE L'OBTENTION
DU DIPLÔME DE PHILOSOPHIÆ DOCTOR
(GÉNIE NUCLÉAIRE)
Mai 2004

Your file Votre référence
ISBN: 0-612-98182-7
Our file Notre référence
ISBN: 0-612-98182-7

UNIVERSITÉ DE MONTRÉAL

ÉCOLE POLYTECHNIQUE

Cette thèse intitulée:

CHARACTERIZATION OF THE SLUG FLOW FORMATION
IN VERTICAL-TO-HORIZONTAL CHANNELS
WITH OBSTRUCTIONS

présentée par: ONDER Ebru Nihan

en vue de l'obtention du diplôme de: Philosophiæ Doctor
a été dûment acceptée par le jury d'examen constitué de:

M. CHAOUKI Jamal, Ph.D., président

M. TEYSSEDOU Alberto, Ph.D., membre et directeur de recherche

M. DOERFFER Stefan, Ph.D., examinateur externe

M. TAPUCU Altan, D.Sc.A., membre

To the memories of *Beria Barbars* and *Halil Ünal*,

To *my mother*,

& To *Danushka*.

ACKNOWLEDGEMENTS

I would like to thank my thesis director Dr. A. Teyssedou for his guidance, support and encouragement during the course of this project. I would also like to express my special thanks to Dr. A. Tapucu for his continued interest in this research project.

I also wish to thank Mr. J.C. Juneau for his help in constructing the test facility and Mrs. Catherine Caffiaux for her rapid verification of French in the "Condensé en français" and "Résumé".

I would also like to thank all the members of my jury for taking the time to read my thesis.

Last but not least, I would like to thank my parents, my sister and my friends for their encouragements during the time that I was carrying out this study.

RÉSUMÉ

Au cours de cette thèse, nous présenterons les résultats des travaux effectués dans le but d'étudier la formation de l'écoulement par bouchons de liquide pour un écoulement à contre-courant en conduite verticale–horizontale. L'instabilité d'écoulement est un mécanisme proposé pour obtenir la formation de l'écoulement par bouchons de liquide dans un écoulement à co-courant. Toutefois, à la connaissance de l'auteur, aucun travail n'a été effectué pour étudier la formation de l'écoulement par bouchons de liquide dans une conduite ayant une branche verticale connectée à une branche horizontale à contre-courant avec obstructions. De très rares études existent sur ce type d'écoulement ayant pourtant une importance capitale dans le domaine de l'analyse de sûreté des réacteurs nucléaires de puissance.

Pour réaliser ces travaux, nous avons utilisé une section d'essais de 63.5 mm de diamètre intérieur fabriqué avec des tubes de plexiglass transparents. Cette section est composée d'une branche verticale de 2022 mm de longueur reliée à une branche horizontale de 3327 mm de longueur par un coude en PVC de 90°. Deux brides, dans lesquelles une obstruction peut être installée sont situées dans la branche horizontale à 1110 mm et à 2217 mm du coude.

Les expériences ont été effectuées pour étudier la fréquence de formation des bouchons, la vitesse de propagation des bouchons de liquide et le taux de vide moyen. Nous avons également effectué des expériences pour la caractérisation de la propagation des vagues. Elles ont permis d'obtenir les conditions initiales requises par le modèle proposé pour prédire la formation de l'écoulement par bouchons de liquide. Dans ce modèle, l'amplitude initiale des vagues est utilisée pour partir les calculs. Donc, le but de ces expériences est d'obtenir l'amplitude des vagues.

La comparaison des résultats expérimentaux au point d'engorgement avec ceux correspondant au début de la formation de l'écoulement par bouchons, nous a montré que les deux résultats sont presque identiques. C'est–à–dire que l'engorgement est simultanement accompagné par la formation de l'écoulement par bouchons dans la section horizontale. Nous avons également trouvé que pour un débit de liquide donné, la présence d'un orifice réduit de façon significative le débit du gaz correspondant au point d'engorgement et au début de la formation de l'écoulement par bouchons. De plus, nous avons constaté que cette réduction est inversement proportionnelle au rapport β de l'orifice.

Pour tous les cas étudiés, la fréquence de la formation de bouchons diminue en augmentant la vitesse superficielle du gaz. Nous avons constaté que, pour un débit de gaz et un rapport β donnés, la fréquence de formation des bouchons est plus élevée quand l'orifice est installé près du coude. De plus, cette fréquence augmente en diminuant le rapport β.

Nous avons observé que le taux de vide pour l'écoulement par bouchons de liquide atteint une valeur asymptotique de 80% lorsque la vitesse superficielle du gaz est supérieure à 0.5 m/s. De plus, nous avons trouvé que cette valeur asymptotique semble être indépendante de la taille de l'orifice et de sa position par rapport au coude. Pour les expériences effectuées sans orifice, nous avons constaté qu'il y a une dispersion importante dans les données. Dans ce cas, la valeur asymptotique est legèrement plus élevée que celle observée lors des expériences effectuées avec orifice. La dispersion de données est probablement due à la formation de deux types de bouchons de liquide; dans le premier type, de longs bouchons de liquide se génèrent près du deuxième coude, et dans le deuxième type, les bouchons courts de liquide se forment près du premier coude. Nous avons également trouvé plus de gaz emprisonné par les bouchons longs de liquide, ce qui explique le haut taux de vide mesuré lors des expériences effectuées sans orifice.

Nous avons observé que la vitesse de propagation des bouchons de liquide ne dépend ni de la taille ni de l'emplacement de l'orifice par rapport au coude. Nous avons trouvé que le débit de liquide n'a pas d'influence sur la vitesse de propa-

gation des bouchons de liquide. Nous avons également constaté que la vitesse de propagation diminue linéairement en augmentant la vitesse superficielle du gaz.

Nous avons également développé un modèle basé sur la théorie de Boussinesq pour la formation de l'écoulement par bouchons. En se basant sur ce modèle, nous avons calculé la fréquence de formation des bouchons et la vitesse de propagation des bouchons de liquide. Pour la fréquence de formation des bouchons de liquide, nous avons trouvé que les prédictions du modèle sont légèrement supérieures aux données expérimentales. Comme nous avons supposé que les bouchons de liquide se forment sans délai; c'est-à-dire qu'il n'y a pas de délai entre le temps où un bouchon de liquide est formé et le temps où la vague précurseure se génère dans la branche horizontale. Ce délai qui devrait être ajouté au calcul de période peut expliquer les valeurs élevées obtenues.

Pour le calcul de la vitesse de propagation des bouchons de liquide, nous avons constaté que les prédictions du modèle sont légèrement supérieures aux données expérimentales. Etant donné que nous n'avons pas pu calculer l'écoulement qui entre dans le volume de contrôle où se forme le bouchon, nous avons trouvé que le manque de ce terme peut expliquer la différence obtenue entre les prédictions et les données.

ABSTRACT

This thesis presents the results of the work carried out to study the formation of slugs under conditions of vertical-to-horizontal counter-current flow with obstructions. A flow instability is the mechanism proposed for the formation of slugs in a co-current flow. However, to the best of author's knowledge no work has been carried out for the formation of slugs in a vertical-to-horizontal counter-current flow with obstructions. Despite the existence of a few studies on counter-current vertical-to-horizontal slug flow with obstructions, it is in particular of great importance in the area of nuclear reactor safety analysis of a CANDU reactor.

A test section manufactured of 63.5 mm inner diameter (ID) plexiglass was used for this work. The test section consists of 2022 mm long vertical and 3327 mm long horizontal legs connected by a 90° PVC elbow. The horizontal leg contains flanges in which an orifice may be installed. These flanges are located at the distance of 1110 mm and 2217 mm from the elbow.

The experiments were carried out to study the frequency of the formation of slugs, the slug propagation velocity and the averaged void fraction of slugs. We also carried out experiments for the characterisation of the propagation of waves. This allowed us to obtain the initial conditions required by the present model in order to predict the formation of slugs. In this model, the initial profile of waves was used to start calculations. Therefore, the aim of these experiments was to obtain the initial profile of these waves.

The comparison of the experimental data collected at the onset of flooding with that collected at the onset of slugging shows that the restults are very close to each other. This reflects the fact that flooding is simultaneously accompanied by the formation of slugs in the horizontal leg. We found that, for a given liquid flow

rate, the gas flow rate, necessary to form the slugs as well as to provoke flooding, decreases as the severity of the obstruction increases.

We also found that, for all the cases studied, the slug frequency decreases with increasing superficial gas velocity. It is also observed that for a given superficial gas velocity and orifice β ratio, the slug frequency is much higher if the orifice is located closer to the elbow. Furthermore, the predominant slug frequency increases with decreasing orifice β ratios.

We observed that, for superficial gas velocities higher than 0.5 m/s, an almost unique asymptotic value of the average void fraction is reached. This asymptotic value is close to 80% and seems to be independent of the size of the orifice and its position with respect to the elbow. For the case without an orifice, a huge scattering in the data is observed. However, the asymptotic value of the average void fraction seems to be slightly higher than that observed for the experiments carried out with an orifice. The scattering in the data is due to the fact that two different types of slugs are formed when there is no orifice installed in the pipe: very long slugs are generated closer to the second elbow and very fast and shorter ones are formed quite close to the first elbow. The fact that longer slugs trap more gas can also be used to explain the higher average void fraction observed for the case without an orifice.

In general, it is observed that the slug propagation velocity does not depend on both the orifice size and the position. It is also observed that the liquid flow rate does not affect the slug propagation velocity. Furthermore, the slug propagation velocity decreases almost linearly with increase of the superficial gas velocity.

Taking into account the Boussinesq system of equations, a model for the formation of slugs has been developed. Based on this model, slug frequencies and slug propagation velocities have been calculated. We found that the predicted frequencies are slightly higher than the experimental data. Since we assumed that the slugs are formed without any delay, i.e., there is no time delay between the formation of a slug and the precursor wave necessary to form the next slug, this assumption

results in a lower period. As the frequency is inversely proportional to the period, it explains higher frequency values predicted by the model.

Calculations for the slug propagation velocity have been carried out by using the mass conservation equation. The averaged horizontal velocity obtained from the model has been used in these calculations. We found that the model predictions are slightly higher than the experimental data. As we were not capable of predicting the flow that enters into the control volume, we were not able to substract the corresponding term in the slug propagation velocity equation. This results in higher predicted values of slug propagation velocity.

We found that the model slightly overpredicts the experimental data. However, in general, the agreement between the predictions and the experimental data is good.

CONDENSÉ EN FRANÇAIS

1 Introduction (Chapitre 1)

Dans les réacteurs CANDU, suite à certaines pertes de caloporteur hypothétiques, l'eau de refroidissement qui vient des collecteurs d'entrées et de sorties est acheminée aux canaux de combustible par les tuyaux d'alimentation. Ceux-ci comportent des sections verticales et horizontales; dans certains tuyaux d'alimentation, des orifices et/ou des venturis sont installés pour fin de contrôle ou mesure de débit. La vapeur produite dans les tuyaux d'alimentation et/ou dans les canaux de combustible peut s'écouler dans la direction opposée à celle de l'eau de refroidissement créant ainsi un écoulement diphasique à contre-courant. Dans de telles conditions, le débit de l'eau de refroidissement qui se rend aux canaux de combustible peut être limité par le phénomène d'engorgement. À la suite d'engorgement, l'écoulement à contre-courant de la vapeur et de l'eau peut créer la formation d'écoulement par bouchons de liquide (Slug Flow).

Il est clair que dans le cas évèntuel d'une Perte de Caloporteur (PERCA), la prédiction du comportement du système de refroidissement d'urgence est essentielle. De plus, la connaissance de l'écoulement par bouchons de liquide dans des géomètries semblables à celles du système d'alimentation d'eau dans un réacteur CANDU est alors importante pour l'analyse de sûreté.

Ainsi, le but de ce travail est d'étudier l'écoulement par bouchons de liquide dans des systèmes géométriquement similaires à celui du système de refroidissement d'urgence d'un réacteur CANDU, et de développer un modèle qui peut prédire la formation de l'écoulement par bouchons ainsi que le comportement.

2 Revue bibliographique (Chapitre 2)

Un grand nombre de travaux expérimentaux et analytiques ont été effectués dans le passé pour étudier l'écoulement par bouchons à co-courant. Cependant, il y a peu des travaux dévoués à étudier des écoulements diphasiques à contre-courant.

Expériences en écoulement par bouchons co-courant dans des conduites horizontales

Vermulen et Ryan (1971) ont effectué des expériences dans une conduite ayant un diamètre intérieur de 3.75 *cm*. Pour des débits du gaz faibles, ils ont observé que la perte de pression augmente legèrement en augmentant le débit du gaz. Toutefois, une augmentation de débit du gaz au délà d'une certaine valeur, entraîne l'augmentation abrupte de la perte de pression. Les auteurs ont observé des fluctuations de pression presque constantes quand le débit du gaz est faible. Pour un débit de gaz élevé, les fluctuations de pression augmentent; un accoissement du débit de liquide provoque une augmentation des fluctuations de pression et elles atteignent leur maximum. Après ce maximum, toute augmentation de débit du liquide est suivie par une baisse des fluctuations. Vermulen et Ryan (1971) ont trouvé que les bouchons de liquide sont longs, i.e., environ de 30 *cm* à 45 *cm* et que leur fréquence est faible. Les auteurs ont également observé que les bouchons de liquide se propagent à basse vitesse. Cependant, une augmentation du débit de liquide augmente la fréquence des bouchons de liquide. Contrairement à ce qui avait été observé pour le débit de liquide, une augmentation du débit de gaz cause la diminution de la fréquence des bouchons de liquide jusqu'au point où la fréquence devient presque constante.

Jepson et Taylor (1993) ont effectué des expériences dans une conduite horizontale ayant un diamètre intérieur de 30 *cm*. Ils ont comparé leur données avec celles d'autres chercheurs. Les auteurs ont trouvé que la fréquence des bouchons de liquide diminue en augmentant le diamètre de la conduite, ainsi qu'en diminuant la vitesse superficielle du liquide. Pour de grandes vitesses superficielles du gaz, ils ont observé une limite de 76 % du taux de vide moyen pour le film de liquide dans

la partie posterieur du bouchon, ainsi qu'une limite de 62% du taux de vide moyen dans le corps du bouchon. Pour tous les cas étudiés, une augmentation de diamètre de la conduite provoque une diminution de toutes ces limites. Le rapport entre la vitesse de propagation de bouchons et la vitesse du mélange, v_t/v_m, diminue continuellement de 2.0 à 1.25 en augmentant la vitesse superficielle du gaz. D'autre part, ils ont observé aussi que la longeur de bouchons de liquide augmente avec le diamètre de la conduite. La perte de pression augmente avec l'accroissement des vitesses superficielles du gaz et du liquide jusqu'au point où les bouchons de liquide deviennent très écumants. À ce point-là, la perte de pression commence à diminuer. Les auteurs ont également observé que la perte de pression diminue en augmentant le diamètre de la conduite.

Modèles et corrélations pour les écoulements par bouchons en écoulement co-courant dans des conduites horizontales

Dukler et Hubbard (1975) ont proposé un modèle pour prédire la vitesse de propagation de bouchons, en supposant que le liquide est entraîné par le front des bouchons; ainsi le liquide s'accélère jusqu'à atteindre la vitesse du bouchon de liquide pour ensuite se placer à l'arrière de celui-ci. Bien que ce modèle fournisse un bon apprentissage des mécanismes, trops de paramètres sont requis par le modèle afin d'effectuer un calcul.

Taitel et Dukler (1977) ont développé un modèle basé sur des vagues instables formées sur la surface du liquide stratifié. Ces vagues augmentent leur amplitude et bloquent le passage de l'air. Cependant, les auteurs ont trouvé que la théorie ne serait pas capable de prédire la fréquence de formation de bouchons si l'écoulement à l'entrée du liquide (où les bouchons de liquide se forment) n'est pas stratifié.

Kordyban (1969) a effectué des expériences sur les écoulements diphasiques dans une conduite rectangulaire. Il a également développé un modèle pour prédire la transition de l'écoulement stratifié vers l'écoulement par bouchons. Ce modèle est basé sur l'instabilité de Kelvin-Helmholtz. Il a utilisé ses données expérimentales pour valider le modèle. En 1985, Kordyban a montré que la formation de

l'écoulement par bouchons est dûe à l'instabilité locale au sommet des vagues, plutôt qu'à l'instabilité globale de la vague. Toutefois, Kordyban (1985) a conclu que le dernier modèle (1985) est valide pour des fluides ayant une basse tension de surface; si ce n'est pas le cas, l'auteur a proposé l'utilisation de son premier modéle (1969) basé sur l'instabilité de Kelvin-Helmholtz.

Crowley *et al.* (1992) ont développé un modèle basé sur la théorie d'une vague unidimensionnelle pour prédire la vitesse de propagation. Les auteurs ont également comparé les prédictions du modèle à celles de Taitelet Dukler (1976). Pour de basses densités de la phase liquide et vitesses faibles du gaz, ce modéle donne de meilleures prédictions que celles obtenues par d'autres chercheurs (Taitel et Dukler, 1976). Crowley *et al.* (1992) ont également étudié le développement, la décroissance ainsi que l'interaction des vagues par l'utilisation de la méthode de caractéristiques.

Expériences en écoulement par bouchons contre-courant dans des conduites horizontales

Wallis et Dobson (1973) ont effectué des expériences pour étudier les écoulements countre-courant et co-courant. Les auteurs ont également étudié la formation de l'écoulement par bouchons dans le cas où l'eau était stationnaire. Ils ont observé que le début de la formation de l'écoulement par bouchons est atteint, soit en augmentant les débits du gaz ou du liquide dans le cas où l'eau s'écoule, soit en changeant la pente du canal dans le cas où l'eau est stationnaire.

Chun *et al.* (1995) ont effectué des expériences pour déterminer la hauteur des vagues et pour étudier la transition de l'écoulement par vagues ondulatoires vers l'écoulement par bouchons. Les auteurs ont observé une augmentation legère de la hauteur non-dimensionnelle de la vague, quand le débit du liquide est augmenté.

Modèles et corrélations pour l'ecoulement par bouchons contre-courant dans des conduites horizontales

Johnston (1985) a effectué des expériences en utilisant le kérosène et le chlorure

de zinc à pression atmosphérique comme fluides de travail. En modifiant le critère d'instabilité de Taitel et Dukler (1976), Johnston (1985) a proposé un autre critère d'instabilité. L'auteur a constaté qu'une transition de l'écoulement stratifié à l'écoulement par bouchons peut être prédite en utilisant son critère d'instabilité. La différence entre les données expérimentalles et leurs prédictions obtenues avec ce critère, était inférieure à ± 17 %. Pour des inclinaisons legères de la conduite, Johnston a observé que le critère d'instabilité est influencé par les forces visqueuses, les conditions d'entrée et la gravité. Cependant, pour des inclinaisons raides de la conduite, la stabilité de l'écoulement est affectée essentiellement par la gravité.

Chun *et al.* (1995) ont développé un critère de transition entre l'écoulement stratifié et l'écoulement par bouchons en calculant l'énergie totale sur le sommet de la vague. Les auteurs ont montré que la différence entre les prédictions en utilisant ce critère et les données experimentales est à l'intérieur de $\pm$ 8%.

3 Montage Expérimental (Chapitre 3)

La section d'essais est composée d'une branche verticale de $2022\,mm$ de longueur reliée à une branche horizontale de $3327\,mm$ de longueur par un coude en PVC de 90°. Une bride dans laquelle une obstruction peut être installée est située dans la branche horizontale à $1110\,mm$ et à $2217\,mm$ du coude respectivement. L'eau et l'air à pression atmosphérique sont utilisés comme fluides de travail. La section d'essais est fabriquée de plexiglass transparent pour permettre la visualisation de l'écoulement. Son diamètre intérieur est de $63.5\,mm$. Les parties principales de la section d'essais sont : *le réservoir supérieur* qui sert de système de séparation et de collecte de l'eau entraînée par l'air, *le système d'injection d'eau* qui consiste en un tube de $63.5\,mm$ de diamètre intérieur ayant 800 trous de $1\,mm$ percés dans sa paroi et des brides qui permettent sa fixation aux sections d'essais, *le réservoir inférieur* qui inclut le système d'entrée d'air ainsi que le système de décharge d'eau. Un système y est installé pour contrôler le niveau de l'eau dans le réservoir inférieur. Le système de contrôle du niveau est capable de maintenir le niveau de l'eau constant dans le réservoir pour une grande gamme de débits d'eau. *Les orifices* qui ont été fabriqués à partir des plaques d'acier inoxydable de 1.5 mm

sans chanfrein ont des rapports $\beta \left(= \frac{d_{orifice}}{d_{conduite}}\right)$ de 0.83, 0.77, 0.72 et 0.66.

Instrumentation

Le montage expérimental est instrumenté pour mesurer les débits de liquide et de gaz, leurs températures, ainsi que la pression absolue du système. Le débit de liquide est mesuré en utilisant des débitmètres à turbine de type "Flow Technology". Ces débitmètres peuvent couvrir la plage allant de 0.054 à 4.54 m^3/h avec une précision supérieure à ± 1 % de la pleine échelle. Le débit de gaz est mesuré en utilisant un groupe de cinq rotamètres "Brook" qui couvrent la plage allant de 0.085 à 132.5 m^3/h à une pression de 2 bar. La précision des rotamètres est de ± 2 % de la pleine échelle. La température du gaz est mesurée à l'aide d'un thermocouple de type K installé près de l'entrée d'air dans le réservoir inférieur. La température du liquide est également mesurée et contrôlée à une température de $20 \pm 0.5\ ^\circ C$. La pression absolue dans le réservoir inférieur est mesurée à l'aide d'un capteur de pression "Sensotec". La plage de pression absolue couverte est de 1 à 1.14 bar avec une précision de ± 0.25 % de la pleine échelle. Le système de mesure du taux de vide, également utilisé pour la détection de l'écoulement par bouchons de liquide comprend trois capteurs capacitifs mobiles (Teyssedou et Tye, 1999). Les sorties des modules de capteur sont connectés à un système d'acquisition des données.

4 Conditions et procédures expérimentales (Chapitre 4)

Deux types d'expériences ont été effectuées; les expériences pour l'écoulement par bouchons de liquide et les expériences pour la propagation des vagues qui mènent à la formation de l'écoulement par bouchons de liquide.

Procédures expérimentales: Commencement de l'engorgement et de l'écoulement par bouchons de liquide

Pour une taille et une position d'orifice données, le débit du liquide injecté à l'entrée de la section d'essai est fixé. Le débit du gaz est augmenté jusqu'au point où la formation de l'écoulement par bouchons de liquide peut être observée. Cette

procédure expérimentale est répétée pour tous les débits de liquide et tous les orifices étudiés.

Expériences pour la propagation des vagues

Les expériences effectuées pour la caractérisation de la propagation des vagues ont permis d'obtenir les conditions initiales requises par le modèle proposé pour prédire la formation de l'écoulement par bouchons de liquide. Dans ce modèle, l'amplitude initiale des vagues est utilisée pour partir les calculs. Donc, le but de ces expériences est d'obtenir l'amplitude des vagues.

Les expériences ont été effectuées dans la même section d'essais qui avait été utilisée pour ceux de l'écoulement par bouchons de liquide. Après avoir filmé les expériences avec une caméra numérique opérant à 30 champs/s, une technique de détection des bonds a été utilisée pour obtenir l'amplitude des vagues. Une quantité de colorant bleu a été ajoutée afin d'augmenter le contraste optique des images collectées.

Conditions Expérimentales

Les expériences de la propagation des vagues ont été effectuées sans utilisation d'orifice. Une réflexion de l'orifice a été simulée en utilisant un coefficient de réflexion. Ce coefficient a été déterminé comme une fonction simple des débits partiels à la décharge que des débits d'eau refoulés.

Procédures Expérimentales

Après avoir fixé le débit de liquide à l'entrée de la section d'essais, le débit du gaz a été augmenté jusqu'au point où les vagues commencent à apparaître sur la surface du liquide. Cette procédure a été répétée pour les débits de liquides suivants : 0.8 m^3/h, 1.1 m^3/h, 1.5 m^3/h, 1.8 m^3/h. Chaque cas a été filmé par la camera numérique à raison de 30 champs/s pendant 4 *min.* pour chaque cas. Une série d'images (champs) a été extraite de chaque filmation en utilisant le logiciel *Adobe Premiere* (version 6.0). L'amplitude des vagues a été obtenue en détectant les bonds dans les images en utilisant une macro de MATLAB et un programme

ecrit en MATLAB.

5. Résultats expérimentaux (Chapitre 5)

Il est important de noter que pour tous les cas étudiés (avec et sans orifice), avant d'arriver au début de la formation de l'écoulement par bouchons; au point d'engorgement, une colonne oscillante est formée dans la branche verticale de la section d'essais. Cette colonne provoque la formation des vagues dans la branche horizontale. Quand un orifice est installé dans la branche horizontale, les vagues se propagent jusqu'à l'orifice et en fonction de la dimension et l'emplacement de l'orifice ainsi que le débit d'eau. Quand les vagues frappent l'orifice, une réflexion partielle de ces vagues se produit. Il faut noter que pour les expériences effectuées sans orifice, la réflexion a lieu au deuxième coude. Finallement, en amont de l'orifice, la vague incidente et la vague réflechie interfèrent. Lorsque l'amplitude de cette interférence devient similaire au diamètre interne de la conduite, il y a un blocage de l'écoulement causant la formation d'un bouchon.

Nous avons également observé que les vagues peuvent être dispersées au cours de leur propagation. Cette observation nous a permis d'utiliser les équations de type de Boussinesq ou Korteweg–de Vries pour dévélopper notre modèle.

Le point d'engorgement et le début de la formation de l'écoulement par bouchons

Après avoir comparé les résultats expérimentaux pour le point d'engorgement avec ceux du début de la formation de l'écoulement par bouchons, nous avons constaté qu'ils sont presque identiques. C'est–à–dire que l'engorgement est simultanement accompagné par la formation de l'écoulement par bouchons dans la section horizontale. Nous avons également trouvé que pour un débit de liquide donné, la présence d'un orifice réduit de façon significative le débit du gaz correspondant au point d'engorgement et au début de la formation de l'écoulement par bouchons. De plus, nous avons constaté que cette réduction est inversement proportionnelle au rapport β de l'orifice.

Fréquence des bouchons de liquide

Pour tous les cas étudiés, la fréquence de la formation de bouchons diminue en augmentant la vitesse superficielle du gaz. Nous avons constaté que, pour un débit de gaz et un rapport β donnés, la fréquence de formation des bouchons est plus élevée quand l'orifice est installé près du coude. De plus, cette fréquence augmente en diminuant le rapport β.

Taux de vide moyen pour l'écoulement par bouchons

Nous avons observé que le taux de vide pour l'écoulement par bouchons de liquide atteint une valeur asymptotique de 80% lorsque la vitesse superficielle du gaz est supérieure à 0.5 m/s. De plus, nous avons trouvé que cette valeur asymptotique semble être indépendante de la taille de l'orifice et de sa position par rapport au coude. Pour les expériences effectuées sans orifice, nous avons constaté qu'il y a une dispersion importante dans les données. Dans ce cas, la valeur asymptotique est legèrement plus élevée que celle observée lors des expériences effectuées avec orifice. La dispersion de données est probablement dûe à la formation de deux types de bouchons de liquide; dans le premier type, de longs bouchons de liquide se génèrent près du deuxième coude, et dans le deuxième type, les bouchons courts de liquide se forment près du premier coude. Nous avons également trouvé plus de gaz emprisonné par les bouchons longs de liquide, ce qui explique le haut taux de vide mesuré lors des expériences effectuées sans orifice.

Vitesse de propagation des bouchons de liquide

Nous avons observé que la vitesse de propagation des bouchons de liquide ne dépend ni de la taille ni de l'emplacement de l'orifice par rapport au coude. Nous avons trouvé que le débit de liquide n'a pas d'influence sur la vitesse de propagation des bouchons de liquide. Nous avons également constaté que la vitesse de propagation diminue linéairement en augmentant la vitesse superficielle du gaz.

Propagation des vagues en surface libre

Les expériences effectuées pour la caractérisation de la propagation des vagues ont

été effectuées afin d'obtenir le profile initial des vagues incidentes. Ce profile est requis comme condition initiale par le modéle. Pour un débit de liquide donné, le débit de gaz a été augmenté jusqu'au point d'engorgement en faisant attention de ne pas arriver à l'engorgement. Cette condition des débits, i.e., le débit du gaz et le débit du liquide, a été gardée constante pendant la prise des films. Après avoir filmé chaque expérience, les images ont été transférées à l'ordinateur. Une macro de MATLAB pour déterminer les bonds des images et un programme écrit en MATLAB ont été utilisés pour déterminer l'amplitude des vagues. Après avoir comparé les résultats de quelques méthodes utilisées pour détecter les bonds dans une image, i.e., Prewitt, Roberts, Laplacian, Canny, Zero-Crossing et Sobel, nous avons trouvé que la méthode de Sobel donne le meilleur résultat. Donc, nous avons opté pour cette méthode avec un seuil (threshold) de 0.04 pour effectuer le traitement numérique des images.

6. Les modèles théoriques

Suivant nos observations reliées au comportement des vagues, nous avons trouvé qu'il est nécessaire d'utiliser une théorie d'ondes solitaires qui s'appuie sur la dispersion de vagues pour décrire le phénomène observé. Nous avons opté pour le système des équations de Boussinesq. Le système des équations de Boussinesq est donné par:

$$\frac{\partial \eta}{\partial t} + \frac{\partial}{\partial x}\left[(1+\eta)\, u\right] = 0, \tag{1}$$

et

$$\frac{\partial u}{\partial t} + u\frac{\partial u}{\partial x} + \frac{\partial \eta}{\partial x} = \frac{1}{3}\frac{\partial^3 u}{\partial x^2 \partial t}, \tag{2}$$

où η est l'amplitude de la vague et u est la vitesse moyenne de propagation dans la direction x.

7. Modèle pour la formation de l'écoulement par bouchons

Nous avons discrétisé les équations 1 et 2 en utilisant le schéma de Péregrine (1966). La solution numérique a été effectuée en utilisant $\Delta x = 0.5$ et $\Delta t = 0.004$

(noter que ces variables sont non-dimensionnelles). L'algorithme consiste dans le calcul d'une valeur estimative de η à partir de la solution de l'équation 1. Par la suite, on utilise cette valeur estimée pour calculer la vitesse de propagation avec l'équation 2. Cette vitesse est utilisée de façon récursive pour obtenir une valeur corrigée de η à partir de l'équation 1. Cette procédure est répetée dans le temps et dans l'espace. Les conditions initiales nécessaires pour partir l'algorithme de calcul sont obtenues à partir des champs (des images) de vagues filmées lors des expériences.

Nous avons calculé la fréquence de formation des bouchons en supposant que la fréquence est inversement proportionnelle à la période. Cette période représente la somme des intervales suivants: T_i qui est le temps nécessaire pour que la vague incidente se propage jusqu'à l'orifice, T_r qui est le temps nécessaire pour que la vague incidente soit reflechie par l'orifice, T_{ir} qui est le temps nécessaire pour que la vague incidente et la vague reflechie produissent une interférence.

Nous avons trouvé que les prédictions du modèle sont legèrement supérieures aux données expérimentales. Comme nous avons supposé que les bouchons de liquide se forment sans délai; c'est–à–dire qu'il n'y a pas de délai entre le temps où un bouchon de liquide est formé et le temps où la vague précurseure se génère dans la branche horizontale. Ce délai qui devrait être ajouté au calcul de période peut expliquer les valeurs élevées obtenues.

Nous avons calculé la vitesse de propagation des bouchons de liquide en se basant sur la conservation de la masse. Nous avons contaté que les prédictions du modèle sont legèrement supérieures aux données expérimentales. Il faut mentionner que nous n'avons pas pu prédire l'écoulement qui entre dans le volume de contrôle. Nous avons trouvé que ce terme peut expliquer la différence obtenue entre les prédictions et les données.

8. Conclusion et recommandation (Chapitre 8)

Au cours de cette thèse, nous avons présenté les résultats des travaux effectués dans le but d'étudier la formation de bouchons dans un écoulement contre-courant

horizontal.

Il est important de noter que pour tous les cas étudiés (avec et sans orifice), avant d'arriver au début de la formation de l'écoulement par bouchons; au point d'engorgement, une colonne oscillante est formée dans la branche verticale de la section d'essais. Cette colonne provoque la formation des vagues dans la branche horizontale. Quand un orifice est installé dans la branche horizontale, les vagues se propagent jusqu'à l'orifice et en fonction de la dimension et l'emplacement de l'orifice ainsi que le débit d'eau. Quand les vagues frappent l'orifice, une réflexion partielle de ces vagues se produit. Il faut noter que pour les expériences effectuées sans orifice, la réflexion a lieu au deuxième coude. Finallement, en amont de l'orifice, la vague incidente et la vague réflechie interfèrent. Lorsque l'amplitude de cette interférence devient similaire au diamètre interne de la conduite, il y a un blocage de l'écoulement causant la formation d'un bouchon. Nous avons également observé que les vagues peuvent être dispersées au cours de leur propagation. Cette observation nous a permis d'utiliser les équations de type de Boussinesq ou Korteweg de Vries pour dévélopper notre modèle.

Après avoir comparé les résultats expérimentaux pour le point d'engorgement avec ceux du début de la formation de l'écoulement par bouchons, nous avons constaté qu'ils sont presque identiques. C'est–à–dire que l'engorgement est simultanement accompagné par la formation de l'écoulement par bouchons dans la section horizontale. Nous avons également trouvé que pour un débit de liquide donné, la présence d'un orifice réduit de façon significative le débit du gaz correspondant au point d'engorgement et au début de la formation de l'écoulement par bouchons. De plus, nous avons constaté que cette réduction est inversement proportionnelle au rapport β de l'orifice.

Pour tous les cas étudiés, la fréquence de la formation de bouchons diminue en augmentant la vitesse superficielle du gaz. Nous avons constaté que, pour un débit de gaz et un rapport β donnés, la fréquence de formation des bouchons est plus élevée quand l'orifice est installé près du coude. De plus, cette fréquence augmente en diminuant le rapport β.

Nous avons observé que le taux de vide pour l'écoulement par bouchons de liquide atteint une valeur asymptotique de 80% lorsque la vitesse superficielle du gaz est supérieure à 0.5 m/s. De plus, nous avons trouvé que cette valeur asymptotique semble être indépendante de la taille de l'orifice et de sa position par rapport au coude. Pour les expériences effectuées sans orifice, nous avons constaté qu'il y a une dispersion importante dans les données. Dans ce cas, la valeur asymptotique est legèrement plus élevée que celle observée lors des expériences effectuées avec orifice. La dispersion de données est probablement dûe à la formation de deux types de bouchons de liquide; dans le premier type, de longs bouchons de liquide se génèrent près du deuxième coude, et dans le deuxième type, les bouchons courts de liquide se forment près du premier coude. Nous avons également trouvé plus de gaz emprisonné par les bouchons longs de liquide, ce qui explique le haut taux de vide mesuré lors des expériences effectuées sans orifice.

Nous avons observé que la vitesse de propagation des bouchons de liquide ne dépend ni de la taille ni de l'emplacement de l'orifice par rapport au coude. Nous avons trouvé que le débit de liquide n'a pas d'influence sur la vitesse de propagation des bouchons de liquide. Nous avons également constaté que la vitesse de propagation diminue linéairement en augmentant la vitesse superficielle du gaz.

Nous avons également développé un modèle basé sur la théorie de Boussinesq pour la formation de l'écoulement par bouchons. En se basant sur ce modèle, nous avons calculé la fréquence de formation des bouchons et la vitesse de propagation des bouchons de liquide. Pour la fréquence de formation des bouchons de liquide, nous avons trouvé que les prédictions du modèle sont legèrement supérieures aux données expérimentales. Comme nous avons supposé que les bouchons de liquide se forment sans délai; c'est-à-dire qu'il n'y a pas de délai entre le temps où un bouchon de liquide est formé et le temps où la vague précurseure se génère dans la branche horizontale. Ce délai qui devrait être ajouté au calcul de période peut expliquer les valeurs élevées obtenues.

Pour le calcul de la vitesse de propagation des bouchons de liquide, nous avons constaté que les prédictions du modèle sont legèrement supérieures aux données

expérimentales. Etant donné que nous n'avons pas pu calculer l'écoulement qui entre dans le volume de contrôle où se forme le bouchon, nous avons trouvé que le manque de ce terme peut expliquer la différence obtenue entre les prédictions et les données.

TABLE OF CONTENTS

LIST OF FIGURES

LIST OF TABLES

LIST OF APPENDICES

LIST OF ABBREVIATIONS

CANDU	Canadian Deterium Uranium reactor
CCF	Counter-Current Flow
CCFL	Counter-Current Flooding Limit
DAS	Data Acquisition Syytem
ECC	Emergency core Cooling
KdV	Korteweg-de Vries
LOCA	Loss Of Coolant Accident
PERCA	Perte de Colloporteur

LIST OF SYMBOLS

a	Parameter defined in Equation 2.26
A_o	Constant wave amplitude
A	Cross sectional area (m^2)
$\bar{A}$	Dimensionless cross sectional area
c_o	Velocity (m/s)
C	Constant, Equations 2.8 and 2.10
$C(k)$	Group velocity (m/s)
C_d	Drag coefficient
$C_{p,cr}$	Geometric factor defined in Equation 2.52
C_s	Interfacial shape coefficient given in Equation 2.33
D	Diameter of the tube (m)
D_d	Droplet diameter (m)
ΔE_k	Net kinetic energy increase over the wave crest ($Joules$)
f	Frequency (Hz)
f_i	Interfacial friction factor
f_w	Wall friction factor
F_d	Drag force (N)
F_σ	Retaining force of the surface tension (N)
j	Superficial velocity (m/s)
j^*	Dimensionless Superficial velocity
$F(x,y)$	Image field
g	Gravitational acceleration (m/s^2)
$G(x,y)$	Edge gradient
h	Height (m)
$\bar{h}$	Dimensionless height
h_o	Unperturbed liquid height (m)
H	Channel depth (m)
$H(x,y)$	Impulse response arrays
K	Parameter defined in Equation 2.24

K_c	constant given in Equation 2.42
L	Length (m)
Lp	Length parameter defined in Equation 2.22
m	Constant, Equations 2.8 and 2.10
$\dot{m}$	Mass flow rate (kg/s)
$P_\circ$	Constant pressure (Pa)
P_D	Probability of correct edge detection defined in Equation 4.3a
P_F	Probability of false edge detection defined in Equation 4.3b
P_w	Wetted perimeter (m)
Q	Flow rate (m^3/h)
t_r	Edge detection threshold
T	Period (s)
T_s	Surface tension
$\mathbf{u}$	Velocity vector (m/s)
u	Velocity component in x direction (m/s)
v	Velocity component in y direction (m/s)
w	Velocity component in z direction (m/s)
W_t	Workdone by the shear stress on the front surface of the wave crest $(Joules)$

Greek Letters

α	Void fraction
β	Orifice ratio $(= D_{orifice}/D_{tube})$
δ	Film thickness (m)
δ	Shallowness parameter
δ^*	Dimensionless film thickness
ε	Amplitude parameter
η	Wave amplitude
γ	Reflection coefficient defined in Equation 4.2
κ	Wave number (m^{-1})
λ	Wave length (m)

μ	Viscosity (Ns/m^2)
ν	Kinematic viscosity (m^2/s)
ω	Angular frequency $(2\pi/s)$
ϕ	Velocity potential
ρ	Density (kg/m^3)
σ	Surface tension (N/m)
σ_n	Noise standart deviation
τ	Shear stress (N/m^2)
θ	Phase
φ	Wave function
ϑ	Inclination angle from the horizontal (Degree)

Dimensionless Groups

Bo	Bond number
Fr	Froude number
F	Modified Froude number given in Equation 2.47
Kr	Kutateladze number
Re	Reynolds' number
We	Weber number

Subscripts and Superscripts

f	Fluid
g	Gas
l	Liquid
w	Water
$\prime$	Dimensional variable

CHAPTER 1

INTRODUCTION

1.1 SIGNIFICANCE OF THE PROBLEM

In the event of a postulated Loss of Coolant Accident (LOCA) in a CANDU reactor, the emergency coolant water is injected into the headers and flows through the feeder pipes into the pressure tubes in the core. The coolant flow, through the feeder pipes, may be hindered by rising vapour stream which is generated as the hot fuel and feeder pipes are quenched by the coolant and vaporization takes place at the quench front. If the vaporization rate is sufficiently high and the differential pressure driving the flow to the fuel channels is low, counter-current flooding limit may be reached in various parts of the feeder pipe. These pipes typically contain vertical, horizontal and inclined sections, as well as, elbows of varying angles. In some feeders, orifices and/or venturi type flow obstructions are installed for flow adjustments and measurements; these components may affect substantially the flooding limit. The occurrence of flooding conditions can impede the penetration of the emergency coolant into the reactor core and may deteriorate the cooling conditions of the fuel and fuel channels. Under flooding flow conditions, where steam produced in the feeders and/or in the fuel channels flows in the direction opposite to the emergency cooling water, the counter-current flow of steam and water can give rise to the formation of a slug flow. For safety reasons, slug flow is an undesirable flow pattern because long lumps of liquid moving at high speed are transported backwards the steam which reduces substantially the amount of coolant that can reach the core.

1.2 OBJECTIVES OF THE WORK

During the channel refilling stage of a LOCA, where the emergency coolant flow is introduced to the channels through the headers and feeders, it is important to

predict flow characteristics in order to determine whether or not the fuel elements will overheat. For such a postulated accident, slug flow is one of the possible flow regimes. Thus, the objective of this research is to study all aspects of slug flow as they apply to systems having a geometry similar to that seen in the header feeder system of a CANDU nuclear reactor. These aspects include an experimental study of slug flow parameters, such as: slug frequency, slug propagation velocity as well as average void fraction of slugs. Another objective is to study the effect of orifice type obstructions on the counter-current slug flow, as venturi type flow obstructions can be installed in some feeders. To investigate this, four different dimensions of orifice were used. Also, the location of these orifices were changed to see if the slug flow characteristics would be affected.

The knowledge of the slug flow, in a geometry similar to the header-feeder system in a CANDU reactor, is important in the safety analysis and the safety analysis of a system depends on realistic and accurate mathematical models. Therefore, it is also the aim of this study to develop a phenomenological model to explain the formation of slugs, as well as to predict the slug propagation velocity and the slug frequency in order to compare with the data obtained from the experimental study that has been carried out for this research. Thus, a model is proposed here to study the formation of slugs. In this model, a concept of interaction of high amplitude waves travelling in the opposite directions is used. Indeed, observing many patterns of slug formation in our test section during the slug flow experiments, we concluded that the main mechanism responsible for the formation of slugs seems to be the interaction (a kind of head-on collision) between incident and reflected waves.

It must be pointed out that the work presented in this thesis constitutes a natural continuation to the counter-current flow research carried out by other students (Bédard 1997, and Tye 1998) at the Institute of Nuclear Engineering.

1.3 OUTLINE OF THE THESIS

An overall view of the experimental and theoretical studies on counter-current flow

and slug flow in different geometries, with and without blockages, is presented in Chapter 2. The experimental facility is discussed in Chapter 3. In Chapter 4, the conditions and procedures for both slug flow and wave propagation experiments are described. The experimental results of slug flow and wave propagation are presented in Chapter 5. The wave theory is introduced in Chapter 6. The model, as well as the comparison of the model predictions with the experimental data, are discussed in Chapter 7. Finally, Chapter 8 gives conclusions and recommendations for future works.

CHAPTER 2

LITERATURE REVIEW

The Counter-Current Flow (CCF) and the flooding phenomena, known also as the Counter-Current Flooding Limit (CCFL), have been studied for several decades. However, the data in the open literature show huge scattering. Furthermore, the proposed models for predicting CCFL are not able to completly reproduce the experimental observations. Some authors identified CCFL with liquid bridging, surface wave instabilities, inception of droplet entrainment, etc. None of these phenomena necessarily leads to a net upward liquid flow. The liquid that is entrained above the liquid inlet may subsequently flow downward. In general, three main criteria have been used by different authors for the characterization of the CCFLs (Tien *et al.*, 1979): a) point of inception of liquid entrainment; b) inception of liquid film up flow and c) zero liquid penetration. It is important to mention that, for a given liquid flow rate, these events can occur at significantly different gas flow rates. The standard definition of the CCFL, and the one used in this work, is (Bankoff and Lee, 1986): "for a given downward liquid flow the maximum upward gas flow rate which full liquid delivery out the bottom of the tube is maintained, corresponds to the counter–current flooding limit." Thus, the CCFL is just a limit for the gas flow rate beyond which only partial liquid delivery out of the lower plenum will occur. This point corresponds to the maximum gas flow rate for which full liquid delivery still exists.

In the case of a vertical flow, the liquid film flows down smoothly along the tube wall for small upward gas flow rates in the core region (Fig. 2.1a). As the gas flow rate is gradually increased, a point is reached (Fig 2.1b) at which large surface waves are formed; this results in a chaotic flow pattern with some of the liquid being entrained as droplets by the upward gas flow. Since droplet entrainement provokes an unbalance between the inlet and outlet liquid flow rates, this condition

can be used to identify the onset of flooding. As the gas velocity is increased beyond the flooding point, both the climbing and falling liquid film flows occur simultaneously; this results in a considerable liquid delivery flow rate reduction (Fig. 2.1c). Finally, as the gas velocity is further increased, all the liquid will be carried upward, i.e., complete liquid film flow reversal (Fig. 2.1d). This condition corresponds to the zero penetration point. Starting from this condition, as the gas velocity is decreased, the liquid film starts to flow downward (Fig 2.1e). A further decrease in gas flow rate results in the climbing and falling liquid film flow (Fig. 2.1f). A fully counter-current flow can be reestablished by decreasing the gas flow rate much below that of the flooding point (Fig. 2.1g).

In this chapter, vertical and horizontal CCFL experiments, as well as some of the existing models used to predict flooding conditions, are discussed. The experimental part will be presented accordingly to the flow parameters that different authors have used to represent the CCFL phenomenon. These parameters include the pressure drop, the mean film thickness and the flooding curves, that is the flow mapping based on the superficial gas and liquid velocities. In some cases, other parameters that affect the flooding, such as, the presence of flow obstructions, the tube diameter, the tube length, the liquid viscosity, have also been studied.

In this chapter, the experimental and theoretical studies on co-current and counter-current slugging phenomena will be also discussed.

2.1 VERTICAL CCF EXPERIMENTS

The first two parts of this section discuss the experiments carried out to measure the pressure drop and the mean film thickness in vertical tubes. Besides these experiments, other experiments also have been conducted to study the parameters that affect CCF in vertical channels. These experiments will be discussed in Section 2.1.3. The effect of an obstruction on flooding in vertical channels will be presented in Section 2.1.4.

2.1.1 PRESSURE DROP IN VERTICAL CCF

Bharathan *et al.*(1979) measured the pressure gradient with three pressure taps. Two of them installed in the test section and the third one in the lower plenum. They presented their experimental results qualitatively as shown in Figure 2.2. The axis of the figure are presented in terms of the dimensionless superficial velocities, dimensionless pressure gradient and the liquid fraction. The dimensionless superficial velocity of the k_{th} phase is defined as:

$$j_k^* = \frac{\rho_k^{1/2} j_k}{\left[\left(\rho_l - \rho_g\right) gD\right]^{1/2}}, \tag{2.1}$$

where subscript k can be g or l that represents the gas and liquid phases, respectively. The dimensionless pressure gradient is given by:

$$\left(\frac{dp}{dz}\right)^* = \frac{dp/dz}{g\left(\rho_l - \rho_g\right)}. \tag{2.2}$$

The authors reported that as the gas velocity is increased up to the flooding point where a sharp increase in the liquid fraction and the pressure gradient is observed, large amplitude waves start appearing on the liquid film surface. This explains the increase in the liquid fraction and the pressure gradient.

Hawley and Wallis (1982) measured the pressure drop under counter-current flow conditions across a 1.83 m long and 51 mm inside diameter ID test section. They presented the dimensionless pressure drop which is defined as:

$$\Delta P^* = \frac{\Delta P}{\left[gD\left(\rho_l - \rho_g\right)\right]}, \tag{2.3}$$

as a function of the dimensionless superficial gas velocity and compared the various characteristic stages in the pressure gradient variation with the observed stages of the film flow. At low gas flow rates, (stage a, Figure 2.3) a smooth falling film is observed in the tube with a correspondingly small pressure gradient. As

the gas flow rate was increased, a region of increased pressure drop was observed where the gas pulled the water, exiting the tube, into a neck, or contraction, as shown in Figure 2.3 (stage b). At yet higher gas flow rates, (stage c, Figure 2.3) the air entering the test section rips droplets from the water exiting the tube. The entrained droplets are seen to occur only in the lower 10–30 *cm* of the test section. The impact of the droplets on the liquid film causes waves to form; variations are also observed in the film thickness. In the upper portion of the tube, the film remains smooth. At this stage, a slight pressure rise from that of stage b is observed. Stage c, however, is unstable and the rough film region grows successively larger (stage d, Figure 2.3) until it covers the entire length of the tube, as shown in Figure 2.3 (stage e). In the transition from stage c to stage e, a sharp increase in the pressure drop across the tube was observed. Hawley and Wallis (1982) considered stage e to correspond to the onset of flooding. Due to the nature of the liquid inlet used by these reseachers, which was by overflow at the top of the tube, the onset of flooding limited the inlet liquid flow and a decrease in the pressure drop was thus observed (stages f and g, Figure 2.3). It can, again, be seen from these results that the flooding point corresponds to the point where a sharp increase in the pressure drop occurs.

Zabaras (1985), Zabaras and Dukler (1988) carried out experiments to measure the pressure gradient and the film thickness in a pipe of 1.57 *m* long and 50.8 *mm* ID. As working fluids, the authors used air and a solution of NaOH into which potassium ferrocyanide and ferricyanide were dissolved. They collected the data for four liquid flow rates: 0.0126, 0.0315, 0.0635 and 0.126 *kg/s*. They installed a measuring station on which two film thickness probes and a differential pressure transducer were mounted. The authors measured the pressure gradient over a distance of 89 *mm* with a reluctance differential pressure transducer. The film thickness probes consist of two parallel wires, and the technique that the authors used was the variation of the conductivity between the two wires. The two wires are lacquer-insulated, over one-half of their length, so that the system would respond to film changes on only one side of the pipe. The authors placed the probes 53 *mm* apart from each other. They observed a minimum in the pressure gradient

for increasing gas flow rates beyond the flooding point. The pressure gradient increases with increasing the liquid flow rates.

Meyer and Giot (1987) conducted experiements not only in a 3 m long pipe of 110 mm ID but also in an annular pipe, by placing a tube with an outer diameter of 50 mm in the former one. They observed different flooding mechanisms for each geometry. In the single pipe, they observed that big roll waves, with small ripples at the top, appear on the liquid film. At first, the distance between the successive roll waves decreases to remain constant afterwards. Further increases of the air flow rate do not cause any increase in the amplitude of the waves; droplets are detached from the crests of the waves and their redeposition occurs below and above the water injection point. The water collected at the wall of the upper part of the tube flows toward the water injector until this water flow rate starts to reverse. Then, the water flow at the lower end of the tube disappears. For still higher air flow rates, the tube section, located below the water injection, dries out. In the annular pipe, the roll waves and ripples are located at two sections where the film flow appears to be highly agitated. The first section is near the air inlet, covering a range of 30 cm, and the other section is located below the water injection point, covering a range of 15 cm. For a highly increased power of the centrifugal fan for which they used to obtain the air flow rate, the authors observed an increase in the length of the lower agitated zone. Further increase in the power of the fan does not increase significantly the air flow but results in a rapid dry-out of the tube. They explained this observation by using the shape of the characteristic curve of the fan linked to the evolution of the flow resistance of the tube. They presented the pressure drops in the single pipe by the use of non-dimensional parameters defined in Equations 2.1 and 2.2. They stated that the same observations had been done for the annular pipe. The authors distinguished 4 regions; in the region of $0 \leq j_g^* \leq 0.3$, the pressure drop is small, and in the region of $0.3 \leq j_g^* \leq 0.4 - 0.45$, the pressure drop increases very rapidly at the beginning of the air-liquid interaction, and in the region of $0.4 - 0.45 \leq j_g^* \leq 0.65$, the pressure drop increases less rapidly and reaches a maximum value at the point where the downward flow vanishes and finally in the region of $j_g^* > 0.65$, the

pressure drop decreases sharply during the dry-out of the tube.

Based on their experiments, Lacy and Dukler (1994) reported that the liquid film undergoes a transition from counter-current to co-current flow inside the liquid injection. The authors conducted the experiments in a 6.37 *m* long and 50.8 *mm* ID tube by using an aqueous NaCl solution and air as working fluids. A 114 *mm* long, porous plastic tube was mounted between two acrylic tubes with the porous tube's outer surface surrounded by a liquid filled reservoir. The porous tube was then mounted to 50.8 *mm* ID. They measured the film thickness across the liquid injection by the use of 8 liquid film thickness probes. The authors also measured the pressure drop across the liquid injection system over a distance of 152 *mm* by the use of a reluctance differential pressure transducer. They compared the pressure drop results with those of Dukler *et al.*(1984) who measured the average pressure drop above the location of the liquid injection over a distance of 1.78 *m*. The authors concluded that the comparison of the experimental results of Lacy and Dukler (1994), with those of Dukler *et al.* (1984), showed that the pressure drop inside the injection zone is about 50% larger than that above this region, under similar conditions.

Tye (1998) measured the pressure drop under counter-current flow conditions in a 63.5 *mm* ID vertical test section by the use of reluctance pressure transducer one side of which was open to the atmosphere. He observed that the pressure decreases in the upward direction and the total pressure difference increases with increasing the gas flow rate.

Vijayan *et al.*(2002) conducted air-water counter-current flow experiments to study the pressure drop and liquid film thickness in tubes of 25, 67, and 99 *mm* ID under pre-flooding and post-flooding conditions. The authors used water or mercury filled manometers to measure the pressure drop and a two-pin type of conductance probe to measure the variation of the liquid film thickness. They observed a churn-like flow of the liquid before flooding starts taking place, in the cases of 67 and 99 *mm* ID tubes, and a sudden increase in the pressure drop at the onset of flooding in all the cases. Since the authors changed the liquid flow rate, due to the diameter

of the tube, requiring different gas flow rate to provoke flooding, the pressure gradients cannot be comparable for the three tube diameters. Neverthless, in the case of 25 mm ID tube, for a given liquid flow rate (0.0278 *kg/s*), the corresponding gas flow rate which provoked flooding was approximately 0.0007 *kg/s* and the pressure gradient was 0.5 *Pa/m* and, in the case of 99 *mm* ID, for a given liquid flow rate (0.444 *kg/s*), the corresponding gas flow rate which provoked flooding was approximately 0.05 *kg/s* and the pressure gradient was 2.5 *Pa/m*.

2.1.2 MEAN FILM THICKNESS IN VERTICAL CCF

Hewitt and Wallis (1963) conducted air-water experiments in a 3.125 *cm* ID tube. The water was injected and extracted through a porous section of the tube wall. The authors measured the liquid film thickness by using conductance probes located at the top and the bottom of the tube. They reported that, at zero gas flow rate, the liquid film is smooth at the top but that the waves increase in amplitude down the tube. As the gas flow rate increases, the roughness of the waves grows and, just below the flooding point, very sharp peaked waves appear. A relatively small increase in the gas flow rate provokes a flooding condition characterized by a sudden growth in the liquid film thickness, at the top of the tube, accompanied by violent flow oscillations.

Dukler *et al.* (1984) carried out experiments to measure the liquid film thickness above and below the liquid injector. They observed that the liquid film thickness below the liquid injection point was constant, with increasing gas flow, until the flooding point is reached. At the flooding point, depending on the liquid flow rate, they observed two different flow behaviours. At low liquid flow rates, there is a step increase in the liquid film thickness whereas, at high liquid flow rates, the liquid film thickness decreases with increasing the gas flow rate. Above the liquid injection point, the liquid film thickness increases, with increasing the gas flow rate, and reaches a maximum value at the flooding point. After this point, the thickness of the liquid film starts decreasing with increasing the gas flow rate.

Zabaras and Dukler (1988) measured the liquid film thickness, as discussed in

section 2.1.1. The authors observed that the liquid film thickness decreases with increasing the gas flow rate, but increases, with increasing the liqud flow rate. The authors conducted experiments for the same working fluids and the same liquid flow rates for two different locations of the measurement stations. The probe station was installed 0.15 m below the liquid injection point and, subsequently it was placed 1.7 m below the liquid injection point. The authors observed that the liquid film thicknesses, measured at the first location, is slightly lower than those measured at the second location. However, they reported the same flow behaviour for both locations. They also argued that flooding is not necessarily the condition at which a very drastic increase in the liquid film thickness takes place; the film thickness may increase monotonicly as a function of gas flow rate and, after this point, the film thickness decreases with increasing the gas flow rate. They also observed that flooding conditions occur simultaneously with the liquid film reversal observed at the liquid injector.

Vijayan *et al.* (2002) measured the mean liquid film thickness. As explained in section 2.1.1, they observed a sudden increase in the mean liquid film thickness at the flooding point, followed by a gradual decrease under post-flooding conditions. They also found that the increase in the mean liquid film thickness at the flooding point is much more pronounced in a 25 mm diameter than in a 67 mm diameter tube. They explained this observation by the formation of large amplitude liquid waves near the outlet of the test section.

2.1.3 OTHER PARAMETERS THAT AFFECT FLOODING IN VERTICAL CCF

A number of investigators have shown that flooding conditions depend strongly on the inlet liquid and gas flow rates. In general, it is observed that, the higher the inlet liquid flow rate is, the lower the gas flow rate will be required to produce flooding. Similarly, the higher the inlet gas flow rate is, the lower the liquid flow rate will be to provoke flooding. It is also shown that parameters, such as: the entrance/exit geometry, the tube length, the tube diameter, the liquid viscosity

and the surface tension, have an important effect on the flooding point.

Suzuki and Ueda (1977) reported that flooding occurs due to the interaction between the waves on the liquid film and the gas stream. They studied the effect of both the test section geometry and the fluid properties. The authors carried out the experiments in test sections having IDs of 10, 18, and 28.8 mm and lengths of 0.5, 1.0, 1.5, and 2.0 m. Fluids, having a viscosity of 9.0×10^{-4}, 2.0×10^{-3}, 5.1×10^{-3}, 1.0×10^{-2}, and $2.4 \times 10^{-2}\ Ns/m^2$ and a surface tensions of 5.5×10^{-2} and $4.7 \times 10^{-2}\ N/m$, are used to carry out the experiments. They found that, for a given liquid flow rate, the gas flow rate necessary to provoke flooding increases while increasing the tube diameter and, decreases, while increasing the tube length. Moreover, the gas flow rate required to produce flooding tends to increase while increasing the liquid viscosity. However, they could not find any correlation between the flooding conditions and the surface tension of the fluids.

Hewitt (1989) studied the effect of the tube length and the geometry of the entrance and the discharge on the flooding point. He observed that the formation of large waves near the liquid exit were responsible for provoking flooding. Thus, he concluded that the exit geometry of the test section, has a strong effect on the formation of waves, hence, on the flooding. He reported that, if the liquid is smoothly extracted around the tube periphery (exits without sharp edges), the waves grow continuously with length, leading to a length effect. In the case of sharp edged exits, or bell-mouth exits, the wave formation leading to the flooding is controlled near the liquid exit and the flooding occurs at much lower gas flow rates for a given liquid flow rate.

Monza *et al.*(2002) conducted experiments in vertical small ID (6, 7, 8, and 9 mm) tubes using smooth inlet and outlet conditions. The authors used air-water and air-kerosene as working fluids. They presented the flooding velocities as a function of liquid Reynolds' number ($Re_l = 4\Gamma/\nu$), where $\Gamma = \rho_l u_a vg \delta$ is the mass flow rate per unit width of surface and ν is the kinematic viscosity, and $u_a vg$ is the average horizontal velocity, and δ is the film thickness. At low Reynolds' numbers, the gas flow rate, at which flooding takes place, is inversely proportional to the liquid flow

rate or Re_l. In this region, they observed a decrease in the gas flow rate necessary to provoke flooding with decreasing both tube ID and liquid surface tension. At relatively higher liquid Reynolds' numbers, the gas flow rate at which flooding occurs tends to be proportional to Re_l. At higher liquid Reynolds' numbers, the gas flow rate required to provoke flooding has a tendency to be constant and independent of the liquid flow rate, but it shows a strong dependency on the tube diameter, i.e., increases with decreasing the tube ID.

2.1.4 VERTICAL CCF THROUGH OBSTRUCTIONS

Celata *et al.* (1989) performed counter-current air-water experiments with obstructions having perforation ratios (perforation ratio = orifice area/channel area) ranging from 0.36 to 1.00 and the equivalent diameters of the orifices from 12 to 20 *mm*. For the obstruction with a flow diameter of 14 *mm*, they used a complex equivalent geometry which has the same flow area but four symmetric holes with a flow diameter of 7 *mm* each. They reported that, for a given liquid flow rate, the presence of an obstruction diminishes the amount of gas required to trigger flooding. They also reported that the onset of flooding is characterized by a quick and significant increase in pressure drop across the test channel, which may go up to 5–6 times the value measured in the absence of flooding. After reaching this point, the pressure drop decreases as the gas velocity increases.

Tye (1998) carried out experiments to study the effect of obstructions on flooding. He observed that the gas flow rate, at the flooding point, decreases smoothly while increasing liquid flow rate. He also reported that, for a given liquid flow rate, the gas flow rate at the flooding point decreases with decreasing the orifice β ratio; $= D_{orifice}/D_{tube}$.

2.2 INCLINED AND HORIZONTAL CCF EXPERIMENTS

The problem of counter-current flow, and flooding in horizontal and inclined tubes, has received little attention compared to vertical counter-current flows. However,

the CCF and CCFL may take place in horizontal or inclined pipes, as well as, in more complex geometries such as the combination of a horizontal pipe with a vertical pipe. These geometries are similar to those encountered in CANDU reactors and, during a postulated lost of coolant accident (LOCA) when the emergency core cooling water is supplied to the reactor core, CCF may occur. Considering the importance of these geometries, in this section, the experiments carried out in such configurations will be discussed in more detail.

This section contains four parts and is devoted to presenting CCF experiments that have been carried using vertical-to-inclined and vertical-to-horizontal test sections. The first part presents the pressure drop experiments whereas, the second one discusses the parameters that influence the flooding conditions. The third part summarizes some CCF and CCFL, experiments carried out using complex test sections, and the last part of this section discusses the vertical-to-horizontal and vertical-to-inclined experiments, carried out with flow obstructions installed in the horizontal leg.

2.2.1 PRESSURE DROP IN INCLINED AND HORIZONTAL CCF

Lee and Bankoff (1983) studied the flooding in a stratified counter-current steam-water flow in nearly horizontal and inclined channels. They carried out the pressure drop experiments, for an inclination angle of 4.5°, with respect to the horizontal plane. The mass flow rate per unit width was kept constant at 2.19 $kg/m\,s$ while the gas flow rate was increased up to the onset of flooding. The liquid inlet temperature was varied from 39.5°C to 98°C. For a liquid inlet temperature of 39.5°C, they observed that the pressure drop is always in the negative region and decreases with increasing the vapour flow rate, reaching a minimum and then slightly increases. For a liquid inlet temperature of 71.3°C, the pressure drop lies in the negative region for low vapour mass flow rates; as the vapour mass flow rate increases the pressure drop rises sharply and becomes positive. For a liquid inlet temperature of 98°C, the pressure drop is in the positive region and increases with increasing vapour mass flow rate. The authors explained their results by using the

vapour phase momentum balance given by:

$$\Delta P_g = \rho_g g L \sin\theta + \int_0^L \frac{\tau_{ia} + \tau_{wg}}{(H-\delta)} dx - \int_{W_{g,out}}^{W_{g,in}} \frac{W_g}{\rho_g (H-\delta)^2} dW_g, \qquad (2.4)$$

where ρ_g is the gas density, L is the channel length, θ is the inclination angle, τ_{ia} is the adiabatic shear stress at the liquid-vapour interface, τ_{wg} is the shear stress between the vapour and the wall, H is the channel depth, δ is the mean film thickness, and $W_{g,in}$ and $W_{g,out}$ are the mass flow rates of vapour at the inlet and the outlet, respectively. In this equation, the first term on the right hand side is due to the gravity, the second term is due to the frictional pressure losses and the last one is due to the pressure gain caused by the deceleration of the flow.

Neglecting the gravity term in this equation, a balance between the frictional loss term and the pressure gain term is sustained. For the inlet temperature of liquid at 71.3°C, they argued that, because of the condensation rate, the total pressure drop is negative in the low steam flow region. However, when the steam flow approaches the flooding velocity, the frictional loss term rises sharply because of the built-up of roll waves. Near the flooding point, the total pressure drop exhibits a sharp increase and becomes positive. For a liquid inlet temperature of 39.5°C, the counter-current flow behaviour is the same, with the exception of the total pressure drop that is in the negative region due to the fact the condensation rate becomes dominant. In contrast to this, for a liquid inlet temperature of 98°C, the frictional loss term is dominant and the total pressure drop is in the positive region. The increase in total pressure drop at the low vapour flow rate is low; this drop increases as the vapour flow rate increases.

Zapke and Kröger (2000) measured the pressure drop of adiabatic gas-liquid counter-current flow in inclined and vertical ducts with a squared-edged gas inlet geometry. The duct height and width vary from 50 to 150 *mm* and from 10 to 20 *mm*, respectively. They observed that, at low gas flow rates, the two-phase pressure gradient depends on the gas Reynolds' number which is a function of the gas velocity, the gas density, the gas viscosity and the hydraulic diameter. However, at

higher gas flow rates, they reported that the two-phase pressure gradient depends on the densimetric gas Froude number (Fr_{hg}), which is defined as:

$$Fr_{hg} = \frac{\rho_g j_g^2}{gh\left(\rho_l - \rho_g\right)}, \tag{2.5}$$

where j_g is the superficial gas velocity, g is the gravitational acceleration and h is the duct height.

The authors observed that, at low to moderate air flow rates, the data correspond to the single-phase prediction and are correlated in terms of Re_g; this is due to the fact that large parts of the duct walls are dry during stratified flow and that there is no significant interaction on the gas-liquid interface. The characteristic length used to calculate the gas Reynold's number is the hydraulic diameter. As flooding is approached, due to the presence of vortices and the wavy interface, the pressure drop starts to rise. At higher gas flow rates, the pressure drop rises above the corresponding gas-only single-phase pressure drop, and the gas Froude number becomes the governing parameter, where the duct height is the important parameter.

2.2.2 OTHER PARAMETERS THAT AFFECT THE FLOODING IN INCLINED AND HORIZONTAL CCF

Lee and Bankoff (1983) carried out experiments for steam-water counter-current flow for two channel depths, 0.038 m and 0.076 m, and, for three inclination angles, 2.9, 4.5, and 33.5°, from the horizontal plane. They observed that the flooding characteristics vary from one geometrical condition to another; when the channel depth was 0.038 m, and the inclination angles were 4.5° and 33.5°, the onset of flooding was clearly marked by the formation of water slugs and bridging. Preliminary to slug formation, a rough thick liquid film develops, with well-developed roll waves superimposed on the interface, which caused considereable augmentation of the interfacial shear stress. The water slugs that form at the water exit propagate backwards with increasing steam flow rate, followed by a rupture of the interface

and bridging in the middle of the test channel. During the slug propagation, the flow could be characterized as an ocsillatory plug flow with continous entrainment of water droplets. However, for relatively high water flow rates, the transition to flooding takes place very rapidly with a small increase of the steam flow rate after the formation of water slugs. They argued that it was difficult to distinguish between the point of slug formation and the flooding threshold. For the channel depth of 0.076 m, and the inclination angles of 2.9 and 4.5°, roll waves also appear when the flooding point is approached. Similarly, slugs are formed at the water exit of the test section; however, the water slugs grow to a height of several times the mean liquid film thickness and a mist of water droplets is entrained from the crests of the water slugs. This results in an oscillatory slug flow. Since, in the former case, flooding occurs abruptly, the gas velocity needed to initiate flooding is much lower. They observed that, for moderate-inclinations (2.9° and 4.5°) or nearly horizontal flow, the dimensionless gas flooding velocity generally rises as the inclination angle decreases. The dimensionless gas flooding velocity is given by:

$$j^*_{mk} = j_k \left[\frac{\rho_k}{2gD_h \sin\theta \, (\rho_l - \rho_g)} \right]^{1/2}, \tag{2.6}$$

where j^*_m is the modified Wallis parameter, j_k is the superficial velocity of the k^{th} phase, and D_h is the hydraulic diameter.

Moreover, they studied the effect of the liquid inlet temperature and found that there are small differences between condensing steam-water and fully adiabatic two-phase flows.

Barnea *et al.* (1986) carried out experiments in inclined tubes to study the entrance effect on flooding by using porous and inner tube as liquid injector. For the porous liquid injector, they observed that flooding resulted from a local disturbance generated at the liquid entrance. For the inner tube liquid injector, the waves that form somewhere along the pipe were the main cause to trigger flooding. Beside their visual observations, they reported that, at low gas flow rates and at small and moderate inclination angles with respect to the horizontal plane, flooding takes

place at lower liquid flow rates when the porous wall liquid injector is used. At higher gas flow rates, the results for both liquid injectors are approximately the same, with a slight difference in the liquid flow rates required to initiate flooding. At inclination angles higher than 70°, and for moderate and high inlet liquid rates, the flooding results are the same for both types of liquid injectors.

2.2.3 CCF AND CCFL IN COMPLEX PIPE GEOMETRY TEST SECTIONS

Krowlewski (1980) performed experiments for air-water counter-current flow in vertical-to-horizontal and inclined-to-horizontal pipes, connected by a 90° or a 45° elbow. The experiments show that the gas flow rate required to provoke flooding in complex pipe geometries is smaller than that would be needed for a vertical tube.

Siddiqui *et al.* (1986) studied the flooding for air-water counter-current flows in a vertical-to-horizontal pipe connected with a 90° elbow. They carried out experiments by using pipes, having inside diameters ranging from 36.5 *mm* to 47 *mm*, and the horizontal length to diameter ratio ranging from 24 to 95, and elbow radius of curvatures ranging from square edge to 300 *mm*. They found that flooding is provoked by slugging at the hydraulic jump that is formed in the lower leg of the elbow, close to the bend. Similar to the results of Krowlewski (1980), the superficial gas velocities necessary to provoke flooding in such a system are much lower than those required for vertical pipes. They observed that the flooding gas velocities decrease with increasing both the tube diameter and the bend radius. They also reported that a slight upward inclination of 0.6° causes flooding at much lower gas flow rates, in turn an equal downward inclination causes an opposite effect.

Wan and Krishnan (1986) studied the effect of a slight inclination of the lower leg of the elbow on air-water CCFL, by using vertical-to-horizontal and vertical-to-slightly inclined pipes. For low liquid flow rates, their results agree quite well with those of Siddiqui *et al.* (1986), and with the predictions obtained with the correlation of Ardron and Banerjee (1986). For low gas flow rates, they observed

the formation of a hydraulic jump close to the elbow whereas, at higher liquid flow rates, the formation of slugs at the end of the horizontal pipe and the propagation of these slugs towards the upstream of the pipe was observed. In general, the results of Wan and Krishnan (1986), concerning the inclination of the lower leg, agree quite well with those of Siddiqui *et al.* (1986).

Wan (1986) performed experiments for counter-current steam and subcooled-water in a vertical-to-horizontal pipe. He reported that, as observed by Siddiqui *et al.* (1986) and Wan and Krishnan (1986) for air-water flow, the flooding occurred with the formation of water slugs in the horizontal leg.

Kawaji *et al.* (1989) carried out experiments for air-water counter-current flows in vertical-to-horizontal and vertical-to-downwardly inclined pipes containing elbows of varying angles (112.5, 135.0 and 157.5°). In vertical-to-horizontal pipes, at low liquid flow rates, their flooding data were in agreement with those of Siddiqui *et al.* (1989) and the predictions obtained with the correlation of Ardron and Banerjee (1986). At higher liquid flow rates, they observed that the flooding mechanism changed and, instead of taking place in the horizontal leg due to the hydraulic jump, it occured in the vertical leg, near the porous liquid injector, and the correlation failed in predicting the experimental trends. In vertical-to-downwardly inclined pipes, Kawaji *et al.* (1989) did not observe any hydraulic jump in the inclined section and they concluded that, for such a geometry, the flooding is initiated by slugging at low liquid flow rates and by liquid entrainment at high liquid flow rates.

2.2.4 CCF IN VERTICAL-TO-HORIZONTAL AND VERTICAL-TO-INCLINED PIPES CONTAINING FLOW OBSTRUCTIONS

Kawaji *et al.* (1993) studied the effect of elbows and obstructions on the flooding mechanism by placing orifices having β ratios of 0.55, 0.67, and 0.865 in one of the horizontal legs of double-vertical, double-horizontal and double-inclined test sections. They observed that, for a given superficial liquid velocity, the superficial gas velocity decreases with decreasing orifice β ratio.

Tye (1998) carried out experiments for vertical-to-horizontal counter-current flow with obstructions having β ratios of 0.55, 0.66, 0.72, 0.77, 0.83, 0.90, and 1.0. He obtained quite similar results to those of Siddiqui *et al.* (1986). He observed that the orifices, having β ratios of 0.90 and 0.83, have almost no effect on the flooding point, as compared to the case without an orifice ($\beta = 1.0$). However, for a constant liquid superficial velocity , the gas superficial velocity required to provoke flooding decreases with decreasing the β ratio. By comparing the flooding results obtained in a vertical-to-horizontal test section with those obtained in a vertical test section, Tye (1998) concluded that, for the same inlet liquid flow rate, flooding conditions in a vertical-to-horizontal test section are reached at a much higher inlet gas flow rate than in a vertical test section. The author also observed a plateau in the partial liquid delivery region. However, such a plateau does not exist in vetical test sections, as confirmed by Zabaras (1985) who observed that after the onset of flooding, there is a steep slope in the partial liquid delivery region.

2.3 CCFL MODELS

A number of analytical and empirical models have been developed for predicting flooding conditions. Most of the existing models have been developed for vertical CCF. In this section, CCFL models will be presented for vertical, vertical-to-horizontal and vertical-to-inclined flows.

2.3.1 CCFL MODELS FOR VERTICAL FLOWS

Models used for predicting the flooding limit can be divided into two categories: empirical and theoretical. The empirical models will be discussed in the following paragraphs and some theoretical models will be presented afterwards.

Two of the most popular empirical correlations are due to Wallis (1969) and to Pushkina and Sorokin (1969); the latter is often referred to as the Kutateladze number correlation. The Wallis correlation is written in terms of the non-

dimensional superficial velocity of the k^{th} phase given by:

$$j_k^* = j_k \left[\frac{\rho_k}{gD\left(\rho_l - \rho_g\right)} \right]^{1/2} \qquad \text{with} \qquad k = l, g. \tag{2.7}$$

The Wallis correlation has the general form given as:

$$j_g^{*\,1/2} + m\, j_l^{*\,1/2} = C, \tag{2.8}$$

where l represents the liquid phase and g the gas phase, j_k is the superficial velocity of the k^{th} phase, D is the diameter of the tube and m and C are constants that depend on the geometry of the channel, the inlet conditions, etc.. The value of m usually lies between 0.8 and 1.0, while C is between 0.7 and 1.0.

The non-dimensional superficial velocity j_k^* represents the balance between inertial forces and hydrostatic forces. In order to include the effect of surface tension forces, and to replace the diameter of the tube by a characteristic length, the Kutateladze number Kr_k given by:

$$Kr_k = j_k \left[\frac{\rho_k^2}{\sigma g\left(\rho_l - \rho_g\right)} \right]^{1/4}, \tag{2.9}$$

is used with $k = l, g$. The corresponding general form of the correlation based on the Kutateladze number is given by:

$$Kr_g^{1/2} + m\, Kr_l^{1/2} = C \tag{2.10}$$

Pushkina and Sorokin (1969) found that for large diameter tubes, the most appropriate values of m and C are $m = 0$ and $C = 1.79$. The Wallis correlation is recommended for small dimeter tubes (less than 50 mm), while the Kutateladze number correlation seems to be appropriate for larger diameter tubes.

McQuillan and Whalley (1985) presented a single correlation which is less sensitive to the size of the tube. This correlation is the Kutateladze number as a function of both *Bond* (Bo) and *Froude* (Fr) numbers, as well as, the viscosity ratio between

the liquid and the water considered as a reference fluid. It is given by the following formula:

$$Kr_g = 0.286 Bo^{0.26} Fr^{-0.22} \left(1 + \frac{\mu_l}{\mu_\omega}\right)^{-0.18}, \tag{2.11}$$

where μ_l is the viscosity of the liquid under consideration and μ_ω is the viscosity of the water. The Bond and Froude numbers are defined as:

$$Bo = \left[\frac{D^2 g\left(\rho_l - \rho_g\right)}{\sigma}\right], \tag{2.12}$$

$$Fr = \frac{Q_l}{P_\omega}\left[\frac{g(\rho_l - \rho_g)^3}{\sigma^3}\right]^{1/4}. \tag{2.13}$$

Moreover, McQuillan and Whalley (1985) compiled 2762 flooding data points that they used to test 17 empirical and 5 theoretical flooding correlations. They found that, among the five theoretical correlations: separate cylinders (Wallis, 1969), hanging film (Wallis and Kuo, 1976), potential flow (Imura *et al.*, 1977), separated flow (Bharathan *et al.*, 1978) and roll wave (Richter, 1981), the modified Bharathan correlation yielded the best predictions of the experimental data. The Bharathan correlation is written as:

$$\frac{2 f_\omega j_l^{*2}}{(1-\alpha)^2} + \frac{2 f_i j_g^{*2}}{\alpha^{2.5}} = (1-\alpha), \tag{2.14}$$

where α is the void fraction, and the wall and interfacial friction factors are $f_\omega = 0.005$ and $f_i = f_w + 14.6\,(1-\alpha)^{1.87}$, respectively. McQuillan and Whalley (1985) eliminated α from the Bharathan correlation, as well as, the interfacial friction factor by using the dimensionless film thickness given by:

$$\delta^* = 0.908 Re_f^{1/3} \tag{2.15}$$

for liquid film Reynolds' numbers less than 2064 and

$$\delta^* = 0.304 Re_f^{7/12} \tag{2.16}$$

for liquid film Reynolds' numbers greater than or equal to 2064. The liquid film Reynolds' number, Re_f, is defined as:

$$Re_f = \frac{\dot{m}_l}{P_\omega \mu_l}, \tag{2.17}$$

where $\dot{m}_l$ is the liquid mass flow rate, P_w is the wetted perimeter and μ_l is the liquid viscosity.

2.3.2 HORIZONTAL, INCLINED & VERTICAL-TO-HORIZONTAL CCFL MODELS

Since, for horizontal and inclined pipes, some investigators have observed that the formation of water slugs is responsible for triggering flooding, several slug formation models have been developed to predict flooding conditions. Most of these models are based on the stability analysis of a finite-amplitude wave. Among others, Kordyban and Ranov (1970) proposed a correlation for CCF having the following form:

$$\frac{j_g^*}{\alpha} + \left(\frac{\rho_g}{\rho_l}\right)^{1/2} \frac{j_l^*}{1-\alpha} = \left(\frac{\cot\vartheta}{2H\kappa}\right)^{1/2} \left[\frac{1}{\coth(\kappa h_g - 0.9) + 0.45\coth^2(\kappa h_g - 0.9)}\right]^{1/2} \tag{2.18}$$

where κ is the wave number, h_g is the gas height, ϑ is the inclination angle of the channel with respect to the horizontal plane, and j_k^* is a modified Wallis non-dimensional supeficial velocity given by:

$$j_k^* = j_k \left[\frac{\rho_k}{2gH\sin\vartheta(\rho_l - \rho_g)}\right]^{1/2} \quad \text{with} \quad k = l, g. \tag{2.19}$$

By introducing the most dangerous wave concept (i.e., the wave having the maximum amplitude that can be sustained by the flow) into the model of Kordyban and Ranov (1970), Mishima and Ishii (1980) obtained the following relation:

$$\frac{j_g^*}{\alpha} + \left(\frac{\rho_g}{\rho_l}\right)^{1/2} \frac{j_l^*}{1-\alpha} = 0.344(\alpha\cot\vartheta)^{1/2}. \tag{2.20}$$

Ardron and Banerjee (1986) developed a model and compared the predictions of the model with the data of Siddiqui *et al.* (1986). The authors assumed a one dimensional, steady, stratified and incompressible flow. They also neglected interphase mass transfer and surface tension effects. The pressure variations over the cross section of each phase were assumed to be due to hydrostatic forces only. Mass and momentum balance equations were written for the horizontal part of a tube. Boundary conditions were imposed at the crest of the hydraulic jump and at the water outlet. It was further assumed that when flooding takes place, the dimensionless superficial gas velocity at the crest of the hydraulic jump was given by: $0.2\alpha^{3/2} j_g$, while the critical flow condition ($d\alpha/dx \rightarrow \infty$) was satisfied at the water outlet. The balance equations were solved analytically and a system of algebraic equations was then obtained. The results, obtained from the numerical solution of this system of algebraic equations, were then fit to yield the following flooding correlation:

$$j_g^{*1/2} = 1.444 - 0.004 Lp \cosh\left[Lp^p K^q \left(j_l^{*1/2}\right)^r\right], \tag{2.21}$$

where $p = 0.057$, $q = -0.020$, $r = 0.70$, and

$$Lp = \frac{L(Re^*)^{-n}}{D}, \tag{2.22}$$

where $n = 0.2$, and

$$Re^* = \frac{D}{\nu_g}\left[\frac{gD(\rho_l - \rho_g)}{\rho_g}\right]^{1/2}, \tag{2.23}$$

$$K = \frac{\nu_g}{\nu_l}\left(\frac{\rho_g}{\rho_l}\right)^{1/2}, \tag{2.24}$$

and L is the distance between the crest of the hydraulic jump and the liquid outlet. The range of parameters for which this correlation is recommended are given as:

$$1 \leq Lp \leq 16,$$

$$0.5 \leq K \leq 1.8,$$

$$0 \leq J_l^{*1/2} \leq 0.6.$$

The predicted results using the correlation given by the Equation 2.21 differs from the numerical solution of the system of equations by less than 2%. It should be noted that this model does not apply for an inclination higher than the critical one, as described in the previous section. Furthermore, Andron and Banerjee's model fails to account for the observed effect of the radius of curvature of the bend on the flooding limit. For a downward inclination, the flow is supercritical in the lower limb, i.e., the average liquid velocity is higher than the propagation velocity of small surface waves ($Fr > 1$), this model is not valid in this case.

Having conducted experiments in vertical-to-horizontal and vertical-to-inlined pipes, as discussed in section 2.2.3, Kawaji *et al.* (1989) proposed a slugging correlation for low liquid flow rates, that is written as:

$$\frac{j_g}{\alpha} + \frac{j_l}{1-\alpha} = 0.5 \left[agD \cos\vartheta \frac{(\rho_l - \rho_g)}{\rho_g} \right]^{1/2}, \tag{2.25}$$

where ϑ is the inclination angle and

$$a = \left(1 - \frac{2\delta}{D}\right)^2. \tag{2.26}$$

Here, the liquid film thickness δ can be written by use of the Wallis correlation:

$$\frac{\delta}{D} = 0.063 j_l^{*2/3}. \tag{2.27}$$

For high liquid flow rates, Kawaji *et al.* (1989) proposed a correlation based on the liquid entrainment and carryover of droplets; the correlation has the following form:

$$\frac{j_g}{\alpha} + \frac{j_l}{1-\alpha} = \frac{2}{\sqrt{3}} \left[\frac{gD_d(\rho_l - \rho_g}{\rho_g C_d \sin\beta} \right]^{1/2}, \tag{2.28}$$

where the drag coefficient, C_d, is calculated by using the correlations applicable to a solid sphere, that is:

$$C_d = \begin{cases} 24/Re_d & Re_d < 1 \\ (24/Re_d)(1 + 0.15Re_d^{0.687}) & 1 < Re_d < 1000 \\ 0.44 & 1000 < Re_d > 2 * 10^5 \end{cases}, \tag{2.29}$$

where $Re_d = \rho_g(v_g + v_l)D_d/\mu_g$, and D_d is the droplet diameter which is calculated by using the Weber number given by:

$$We = \frac{\rho_l v_l^2 D_d}{\sigma}. \tag{2.30}$$

Tye (1998) developed a model to predict the flooding point in a test section containing vertical and horizontal legs using an extension of a model for the inception of entrainment applied at the crest of the hydraulic jump. He used the Ishii and Grolmez (1975) criterion for the inception of entrainment at the crest of the hydraulic jump. This criterion is based on the balance of drag and surface tension forces along the crest of a wave, that is:

$$F_d \geq F_\sigma, \tag{2.31}$$

where F_d is the drag force acting on the wave crest and F_σ is the retaining force of the surface tension. The drag force on the wave crest is calculated as:

$$F_d = C_d \lambda \eta \frac{\rho_g v_r^2}{2}, \tag{2.32}$$

where λ is the wave length, v_r is the relative velocity between the gas and the liquid phases ($v_r = v_g - v_l$), η is the wave amplitude, and the drag coefficient is given by an analogy to the drag deformed particles and is considered to be close to one ($C_d \approx 1$).

The retaining surface tension force is estimated as:

$$F_\sigma = C_s \lambda \sigma, \tag{2.33}$$

where C_s is an interfacial shape coefficient. Ishii and Grolmes (1975) suggested using a value lower or equal to 0.77 for this coefficient; $C_s \leq 0.77$.

Substituting equations 2.32 and 2.33 into equation 2.31, he obtained the entrainment criterion as follows,

$$\eta \frac{\rho_g v_r^2}{2} \geq \frac{C_s \sigma}{C_d}. \tag{2.34}$$

Starting with a guessed gas velocity, equation 2.34 is solved and the gas velocity is updated, until the inequality which defines the point of inception of entrainment is satisfied.

Tye (1998) also took into account the influence of the various size orifices on the flooding point by adding a correction term to calculate the liquid velocity. He named this term as an orifice offset height, and it is given by:

$$h_0 = \frac{1-\beta}{\beta} \frac{D}{2}, \tag{2.35}$$

where β is the orifice ratio and D is the inside diameter of the tube.

Tye (1998) compared the predictions of the model for both cases, with, and without an orifice placed in the horizontal leg with his experimental data, as well as with data of other investigators, among others, Siddiqui (1986), Kawaji (1991), Adron and Banerjee (1986) . The model predictions are, in general, in very good agreement with the experimental results.

2.4 STUDIES ON HORIZONTAL SLUG FLOW

The information on counter-current slug flows is very scarce or even nonexistent.

However, in this section, the experimental and theoretical studies carried out for co-current and counter-current slug flow in horizontal pipes will be presented.

2.4.1 CO-CURRENT HORIZONTAL SLUG FLOW EXPERIMENTS

Vermeulen and Ryan (1971) carried out experiments for slug flows in a 3.75 *cm* ID pipe, using air-water at atmospheric pressure conditions. They used two differential pressure transducers to determine the pressure gradient and the pressure fluctuations in the slug flow. The slug velocity, and the frequency, were determined by using photoconductive cell and electronic counter, as well as, a stopwatch. At higher flow rates they used the pressure data to determine the slug velocity and frequency. They found that there is a strong influence of the gas flow rate on the overall pressure drop rather than the liquid flow rate. At low air flow rate, the increase in pressure drop is quite small and linear; however, an increase in the gas flow rate causes the pressure drop to increase quite rapidly. Moreover, the authors also observed that, at low gas flow rates, the magnitude of pressure fluctuations was almost constant with increasing water flow rates. At high gas flow rates, increasing the water flow rate causes a maximum in pressure fluctuations; a further increase in the water flow rate causes the pressure fluctuations to decrease. Vermeulen and Ryan (1971) observed that the angle of tube inclination, within ± 7 degrees from the horizontal level, has little effect on the slug velocity. Similar to the pressure drop results, at low gas flow rates, increasing the water flow rate has an insignificant effect on slug velocity. At high gas flow rates, however, a maximum slug velocity is reached by increasing water flow rates, after which, a decrease is observed. At low gas and liquid flow rates, the slugs are long, about 30 to 45 *cm*, moving at a low velocity and their frequency is also low. An increase in the water flow rate increases the slug frequency, though increasing the gas flow rate causes a decrease in the slug frequency upto a point after which the slug frequency becomes almost constant. They observed a gradual change in slug frequency curves when the pipe was placed horizontally, however, the frequency curves became steeper when the pipe was inclined.

Fan *et al.* (1993) performed pressure drop experiments caused by the passage of stable and unstable slugs in a horizontal gas-liquid flow. Dukler and Hubbard (1975), Ruder *et al.* (1989) suggested that the stability of a slug requires that the picking up the liquid ahead of the slug should be balanced with liquid shed from the back. When the rate of accumulation of liquid into the slug exceeds the rate at which liquid is shed from the tail, the slug grows. As the liquid is lost from the tail, at a greater rate than it can be accumulated in the front, the slug decays. The phenomena is shown in Figure 2.4. The pressure profiles, associated with the passage of a slug, were measured using a pizoresistive pressure transducer. Fan *et al.* (1993) compared the experimental data with a model that considers the pressure drop as the sum of the contributions from the hydraulic jump in the front of the slug, the wall drag in the body of the slug, and a sudden change in the velocity of the liquid in the rear of the slug. They found that the average pressure drop increases with increasing the gas velocity. However, for high gas velocities, the average pressure drop increases with increasing the liquid velocity.

Andresussi *et al.* (1993) used local (optical) and cross-sectional (conductance) probes to characterize air-water slug flows under atmospheric conditions in horizontal 31 and 53 *mm* ID pipes. From local measurements, they obtained the radial void fraction distribution, the size of the dispersed bubbles and the aeration of the liquid layer under the Benjamine bubble. The cross sectional hold-up measurements allowed them to determine the slug lengths, frequencies, as well as, the length of the highly aerated mixing zone in the slug front. They compared the measured values of the liquid film hold-up at the tail of the slug and the slug frequency with the predictions of the model given by Dukler and Hubbard (1975). They found that measured slug lengths are quite independent of the flow rates. The length of the highly aerated mixing zone in front of the slug is large and, at high mixture velocities, can be extended up to one-half of the slug length. At intermediate mixture velocities ($5\,m/s < V_m < 10\,m/s$), there is a void gradient along the slug, whereas, at high mixture velocities, the aeration in the front and the tail of the slug is almost constant.

Jepson and Taylor (1993) collected data on slug frequency, slug length, liquid hold-up, translational slug velocity, as well as, pressure gradient for air-water flow in a 30 *cm* ID horizontal pipe. The authors used fast response pressure transducers, placed at 13.9 and 38.1 *m* from the mixer outlet, to measure pressure drop over a slug body, slug frequency, and slug translational velocity. The slug hold-up was measured, and the slug length was estimated, by the use of γ densitometer. The authors compared their data, with those collected by others, using small diameter ID tubes. As the pipe diameter is increased, the superficial liquid velocity should also be increased to attain slug flow. Figure 2.5 shows the slug parameters used in the article Jepson and Taylor(1993). Their observations can be summarized as follows:

- The slug frequency decreases with increasing the pipe diameter, as well as, with decreasing the superficial liquid velocity.

- The liquid film hold-up is limited to 24% as the superficial gas velocity is increased. However, at low superficial gas velocities, an increase in the superficial liquid velocity increases the film hold-up. As the superficial gas velocity increases, the limit in the liquid slug hold-up increases upto 38%. For all the cases tested, an increase in the pipe diameter causes a decrease in these limits. At lower superficial gas velocities, an increase in the superficial liquid velocity increases the slug hold-up.

- The ratio of the translational velocity to the mixture velocity, V_t/V_m, decreases continuously from 2.0 at low superficial gas velocities to 1.25 at high superficial gas velocities.

- The slug length increases with increasing the pipe diameter.

- The pressure gradient increases, with increasing the superficial gas and liquid velocities up to a point, where the slugs become extremely frothy. At this point, the pressure gradient starts decreasing. The authors explained that this drop is due to the high degree of aeration. Also, the pressure gradient

decreases, with increasing the pipe diameter, due to the fact that the frictional pressure drop decreases with increasing the pipe diameter.

2.4.2 MODELS AND CORRELATIONS FOR CO-CURRENT SLUG FLOW

The first realistic model of slug flow was developed by Dukler and Hubbard (1975). In the model, they assumed that liquid is scooped up at the slug front, accelerates to the slug velocity and then passes back through the slug. Even though this model provides a good understanding of the mechanisms that govern the formation of slugs, the model requires many parameters in order to perform the calculation.

Taitel and Dukler (1977) developed a model based on unsteady waves formed on a stratified film blocking the passage of the air to predict the slug frequency. However, they found that the theory is not able to predict the frequency if the flow in the liquid entry region, where slugs are formed, is not stratified.

Nicholson *et al.* (1978) proposed a model to predict the pressure gradient, liquid volume fraction, and slug length after having modified the model of Dukler and Hubbard (1975). Still, their model needs several empirical correlations. The physical phenomena behind their model is explained as: when unstable waves on the surface of the liquid phase grow in amplitude, they succeed in closing off, or bridging, the entire cross section of the pipe to form a slug of liquid. This slug is immediately accelerated by the gas behind it to an average stable translational velocity. Since the velocity of a liquid particle within the slug is lower than the observed translational velocity of the overall slug, there is a constant mass flux moving through the main body of the slug. Liquid is added to the slug at its leading edge from the preceding liquid film and, simultaneously, the liquid is dropped off or shed at the back of the slug to create a new liquid film beneath the propelling gas bubble (Benjamin bubble). As a result of wall shear stress, the liquid, in the trailing film, begins to decelarate immediately upon being shed. The deceleration continues until either a succeeding slug scoops up the film or a stable velocity is

reached, which is maintained by interfacial shear at the boundary between the film and the gas bubble above it. The length of the liquid slugs becomes stable when the liquid pick-up rate, at the leading edge, becomes equal to the liquid shedding rate at the slug tail.

They found that, in the low pressure gradient region, the predicted pressures are higher than the measured values. They explained that these differences are due to the fact that the model does not include any specific provision for the observed behaviour of the elongated bubble (Benjamin bubble), at the end of the slug, which penetrates back into the liquid slugs. The presence of this bubble might reduce the frictional pressure gradient in the liquid slug over the penetration length. In general, the predicted values of pressure gradient agree well with the data. Moreover, they calculated the liquid volume fraction with the available frequency data, and the predictions of the model are in good agreement with the data. They found that slug lengths are quite sensitive to the small changes in the frequency.

Kordyban (1969) carried out two-phase flow experiments in a horizontal rectangular channel. The author, also, filmed the experiments with a camera capable of collecting 64 frames per second. Moreover, he developped a model and used the experimental data in the model to estimate the transition from stratified to slug flow. The model requires the liquid depth, the wave length and the height of waves. He measured the liquid level and wave height by the use of platinum wire liquid level gauges which operate on the principale of variation of electrical conductivity with the water level between the two parallel wires. The author also used a 3 needle gauge for liquid level calibrations. The pressure fluctuations and the aerodynamic pressure over the waves were measured by a strain gauge type transducer at the pressure taps located at the top wall of the channel. He used a band pass filter for spectral analysis of the waves and pressure fluctuations. As a result, he obtained spectral density as a function of frequency by using a variable band pass filter between the signal output and the voltmeter. Finally, he calculated the wave length from the peaks of the spectral density curves. The wave length is written as which has the following form:

$$\lambda = \frac{c + u_l}{f}, \tag{2.36}$$

where f is the frequency that corresponds to the peak value of the spectral density and $c + u_l$ is the the wave speed. In presence of a liquid flow, the velocity is calculated as:

$$c + u_l = \frac{\rho_g u_g + \rho_l u_l}{\rho_l + \rho_g} + \left[\frac{g}{k} \frac{\rho_l - \rho_g}{\rho_l + \rho_g} + \frac{\sigma_l}{\rho_l + \rho_g} - \frac{\rho_l \rho_g}{\rho_l + \rho_g} (u_g - u_l)^2 \right]^{1/2}. \tag{2.37}$$

where σ_l is the surface tension of the liquid and k is the wave number.

Kordyban (1969) measured the wave height and the aerodynamic pressure over the waves by the use of an oscillograph, connected simultaneously to the liquid level gauge and the pressure transducer. In the oscillograph record, the low pressure peak corresponds to the crest of the wave, while a high pressure peak correspond to the back side of the wave. The total wave height, that was the height from trough to crest, was determined from the record of the oscillograph and the calibration curves for the liquid level gauges. The aerodynamic pressure, at the back of the wave, was calculated from the oscillograph recording; it represents the difference between the low pressure peak, near the crest of the wave, and the high peak falling at the back side of the wave. He used the pressure measurements in the calculation of Jeffreys' β_j coefficient which is a criterion for the wave growth. This coefficient is calculated as follows:

$$\beta_j = \frac{p_2}{\rho_g (u_g - c)^2 ak}. \tag{2.38}$$

Jeffreys (1925) argued that β_j should be lower than unity and probably below 0.5; Kordyban (1969) found $\beta_j \approx 0.6$. He concluded that a high value of the coefficient indicates a rapid growth of waves and that was the case he observed from the photographs.

The wave speed was determined by measuring the position of the wave crest at successive values of time. The values were taken from one reel of the 64 frames

per second film. However, he could not find any other works to compare with his data.

Kordyban (1969) proposed that the transition to slug flow takes place due to a type of Kelvin-Helmholtz instability, i.e., the instability which occurs when the suction, due to aerodynamic pressure at the wave crest, overcomes the downward acceleration of the wave, which is given by:

$$\frac{g}{k}\frac{\rho_l - \rho_g}{\rho_l + \rho_g} + \frac{\sigma_l}{\rho_l + \rho_g}k < \frac{\rho_l \rho_g}{\rho_l + \rho_g}\left(u_g - u_l\right)^2. \tag{2.39}$$

Contrary to the usual case of Kelvin-Helmoltz instability, the author proposed the amplitude dependent instability which has the following form:

$$\frac{F_g F_l}{\frac{\rho_l}{\rho_g}F_l + F_g}\left(u_g - u_l\right)^2 \geq g\left(1 - \frac{\rho_g}{\rho_l}\right)\eta - \frac{\sigma_l}{\rho_l}\frac{\partial^2 \eta}{\partial x^2}, \tag{2.40}$$

where η is the wave amplitude, F_g and F_l are given by:

$$F_l = k\eta \coth k\left(h_l + \eta\right) - 1/2k^2\eta^2 \coth^2 k\left(h_l + \eta\right),$$
$$F_g = k\eta \coth k\left(h_g - \eta\right) + 1/2k^2\eta^2 \coth^2 k\left(h_g - \eta\right).$$

Taking into account that there is a limit for deep-water waves to attain a maximum height, Kordyban (1969) proposed a limiting amplitude for waves to be described as:

$$k\eta \coth k\left(\eta + h_l\right) \rightarrow 1.$$

The author argued that deep-water waves were responsible for the formation of the slugs. Then he suggested that the transition to slug flow takes place when

$$\left(u_g - u_l\right)^2 \geq \frac{\rho_l}{\rho_g}\frac{g}{k}\frac{1}{\coth\left(kh_g - 0.9\right) + 0.45\coth^2\left(kh_g - 0.9\right)}. \tag{2.41}$$

Kordyban (1969) compared the predictions of his theory with the known flow pattern maps, i.e., Baker(1954), Schicht(1969). He concluded that there was a good agreement between the predictions of the theory and the flow patterns.

Kordyban (1985) carried out a photographic study allowing him to observe that, prior to the slug formation, small waves appear on the crest of large waves, and that a slug results from the rapid growth of one of these waves, which are of wavelet type. He proposed that the appearance of these wavelets is related to the initiation of a Kelvin-Helmholtz flow instability. Thus, slugs form as a result of local instabilities at the wave crest, rather than the instability of the whole wave; in this case the author obtained the following instability criterion,

$$(\rho_l - \rho_g)\, g = K_c \rho_g v \frac{v_g h_g}{(h_g - \eta)^2}, \tag{2.42}$$

where K_c is a constant, having a value larger than unity, and he estimated this value to be 1.80, h_g is the mean depth of air passage, and v is the velocity where the amplitude of the wave is η. The author concluded that, for a liquid of smaller surface tension, this mechanism is still valid, but for a liquid of greater surface tension, it might be possible that the instability of the whole wave would take place before the formation of the wavelets at the crest.

Tronconi (1990) developed a model to predict the slug frequency by assuming that the slug frequency is one half of the frequency of the unstable wave precursor of slugs. Taking the proportionality constant in the model of Mishima and Ishii (1980) to be of 1/2, he obtained an equation for slug frequency given by:

$$w = 0.61 \frac{\rho_g}{\rho_l} \frac{u_g}{h_g}. \tag{2.43}$$

He compared the predictions of this equation with the available data. He found that a decrease in pipe diameter results in an increase in the slug frequency. Moreover, he observed a maximum in the frequency at low gas flow rates in small diameter pipes. This might be associated with the laminar-turbulent transition of

the gas flow in the inlet region. The prediction of the model for intermittent flow, in very small tubes, is limited by the liquid surface tension. He found that the influence of liquid viscosity is weak when the stratified liquid flow is turbulent at the entrance. However, he observed a noticeable increment in the frequency when the liquid viscosity is increased up to $50 \times 10^{-3} Pa\,s$.

Crowley *et al.* (1992) used the one-dimensional wave theory to predict the transition velocity. They compared the predictions of the model with those of Taitel and Dukler (1976). For low gas densities and velocities, their model was able to predict better the experiments. The comparison of the predictions of the model with the experimental data, obtained for different working fluids, including hydrocarbons, water, and Freon, having higher gas densities ($\approx 15 - 30\,kg/m^3$), shows a good capability of this model in predicting the experiments. Crowley *et al.* (1992) also extended their analysis by using the method of characteristics to simulate the wave growth, the wave decay and the wave interaction. They explained the formation of slugs as follows: when a new slug is formed, an additional pressure drop between the upstream and downstream side of the slug, is required. This pressure feeds back to the inlet of the pipe by acoustic waves through the gas (which travel upstream) provoking a change in the inlet conditions. This new "disturbance" eventually rises to form a slug and the cycle repeats.

2.4.3 COUNTER-CURRENT HORIZONTAL SLUG FLOW EXPERIMENTS

Wallis and Dobson (1973) conducted experiments for co-current, as well as, counter-current air-water slug flow in a horizontal channel. They also investigated the slugging phenomena under stationary water conditions. They observed that the onset of slugging is reached in several ways, by increasing the air or water flow rates or by changing the channel slope. Once slugging is initiated, the liquid flow rate in the channel drops dramatically and the water is carried over by the exhaust air (flooding). The void fraction data obtained for co-current and counter-current flow fell very close to those obtained with stationary water (Figure 2.6). They found that the transition from stratified to slug, or plug flow in a horizontal rect-

angular channel, occurs at a value of relative velocity between the phases given by:

$$(v_g - v_l) = 0.5\sqrt{gh_g\left(\rho_l - \rho_g\right)/\rho_g}. \tag{2.44}$$

Assuming that $v_g \gg v_l$ in stratified flow, they approximated the results with a relationship given by:

$$j_g^* = 0.5\alpha^{3/2}. \tag{2.45}$$

Chun *et al.* (1995) conducted experiments to measure the wave height and investigate the transition criterion from wavy to slug flow in horizontal air-water counter-current flows. They used two different test section geometries: a 0.05 m ID and 8.28 m long pipe, and a 0.1 $\times$ 0.1 m cross-sectional area and 7.98 m in long duct. They measured the height of waves and the depth of water by attaching rulers to the test sections at 7 locations for the pipe and 11 locations for the square duct. They repeated the experiments five times to obtain average values. They observed a slight increase in the dimensionless wave height, η/D, when the water flow rate is increased.

2.4.4 MODELS AND CORRELATIONS FOR HORIZONTAL COUNTER-CURRENT FLOW

Johnston (1985) carried out experiments using Kerosene and a zinc chloride solution as working fluids flowing counter-currently in three different diameter pipes, having inclinations ranging from horizontal to 18°. He also modified the instability criterion of Taitel and Dukler (1976) to compare it with his data. He proposed a stability criterion given by:

$$\underbrace{F^2\left[\frac{1}{C_2^2}\frac{U_g^2\left(d\overline{A}_l/d\overline{h}_l\right)}{A_g}\right]}_{STAB} \geq 1, \tag{2.46}$$

where F is a modified Froude number given by:

$$F = \sqrt{\rho_g / (\rho_l - \rho_g)} \frac{j_g}{\sqrt{Dg \cos \alpha}}, \tag{2.47}$$

and

$$\frac{d\overline{A}_l}{d\overline{h}_l} = \sqrt{1 - \left(2\overline{h}_l - 1\right)^2}. \tag{2.48}$$

Here, $C_2 = \left(1 - \overline{h}_l / D\right)$ is a parameter reflecting the position of the interfacial boundary, and $\overline{A}_l$ is the non-dimensional cross-sectional area of the liquid phase calculated as:

$$\overline{A}_l = 0.25 \left[\pi - \cos^{-1}\left(2\overline{h}_l - 1\right) + \left(2\overline{h}_l - 1\right)\sqrt{1 - \left(2\overline{h}_l - 1\right)^2}\right], \tag{2.49}$$

and $\overline{A}_g$ is the non-dimensional cross-sectional area of the gas phase given by:

$$\overline{A}_g = 0.25 \left[\cos^{-1}\left(2\overline{h}_l - 1\right) - \left(2\overline{h}_l - 1\right)\sqrt{1 - \left(2\overline{h}_l - 1\right)^2}\right]. \tag{2.50}$$

Based on this stability criterion and the experimental study, the author concluded that:

- A transition from stratified to slug flow in counter-current flows can be predicted with a stability criterion which is based on the growth and collapse of interfacial waves.

- The experimental results show that the stability criterion is less than 17% to that expected from theoretical considerations.

- At fairly gentle inclinations (horizontal to 1.8°) this criterion is influenced by: viscous forces, inlet conditions and gravity. At steeper inclinations, the stability was predominantly affected by the gravitational force; the larger the inclination, the larger the stability number.

Johnston (1985) also observed that, as the inclination of the test section increases, the gravity tends to suppress the growth of the choking wave, thereby making the system more stable.

Chun *et al.* (1995) developed a transition criterion for a horizontal air-water counter-current slug flow, using a total energy balance over a wave crest. This balance can be expressed by the sum of the increase of the net kinetic energy over the wave crest (ΔE_K) and the work done by the shear stress on the front surface of the wave crest (W_t). They obtained the following transition criterion:

$$v_{g,\,cr} = \sqrt{\frac{\rho_l g h_g C_{p,\,cr}}{\rho_g}\,\frac{\sqrt{4/\pi + f_i} - 1}{4/\pi + f_i - 1}}, \tag{2.51}$$

where the geometric factor $C_{p,cr}$ is given as:

$$C_{p,\,cr} = 1 + \frac{32}{9\pi}\frac{D\eta_{cr}}{S_i^2}\left(\frac{D_{h,g}}{D_{h,l}}\right)^2\left(1 - \frac{2h_l}{D}\right), \tag{2.52}$$

and $(D_{h,g}/D_{h,l})^2$ is the ratio of hydraulic diameters of gas and liquid, ρ_g and ρ_l are the densities of gas and liquid, respectively, and h_g is the gas height. The gas-liquid interfacial friction factor f_i is given by:

$$f_i = 0.01(3X)^{(0.8+X)/4}, \tag{2.53}$$

and X is calculated as:

$$X = 0.02\left(\frac{v_r}{\sqrt{gD}}\right)^{2/3} Re_r^{1/3}\left(\frac{D_{h,l}}{D + D_{h,l}}\right)^2. \tag{2.54}$$

Here, $v_r = v_g - v_l$ is the relative velocity between the phases, g is the gravitational constant, and η is the wave amplitude.

They compared the predictions of the model with their experimental data. They showed that the predictions of the wave height model were in good agreement with the data, while the agreement between the predictions based on the transition criterion with the data were within $\pm 8\%$.

As has already been shown that the co-current slug flow has been widely studied; co-current slug flow experiments have been carried out to measure the slug frequency, the void fraction, the slug propagation velocity, the pressure drop and pressure fluctuations over the slug. Among other researchers, Taitel and Dukler (1977), Kordyban (1969), Crowley *et al.* (1992) developed models to predict the transition from stratified to co-current slug flow. These investigators, also, with the others, such as, Dukler and Hubbard (1975), Nicholson *et al.* (1978), developed models to predict the characteristic parameters of the co-current slug flow; i.e., the slug frequency, the slug propagation velocity, etc.. However, the amount of available information regarding the counter-current horizontal slug flow is so rare. Wallis and Dobson (1973), Chun *et al.* (1995) performed experiments and Johnston (1985) and Chun *et al.*(1995) developed models to study the transition from stratified or wavy to counter-current slug flow.

This review shows that slugging in co-current flows occurs due to the Kelvin-Helmholtz instability. This is not necessary the case for counter-current flows in pipes containing obstructions. Thus, it is our intention to perform counter-current slug flow experiments in a geometry similar to a typical feeder pipe encountered in CANDU nuclear power reactors, i.e., vertical-to-horizontal connected with an elbow, including flow obstructions in the horizontal leg. It is also, the aim of this research to develop a model for the formation of a slug in a counter-current flow, taking into account the flow obstructions. Since, to the best of author's knowledge, no studies has been carried out for the counter-current slug flow in such a geometry, the predictions of the model will be compared only with the experiments carried out for this research. In the following chapters, the experiments performed to study the charateristic parameters of a slug will be discussed. Next, the model and the predictions of the model will be presented.

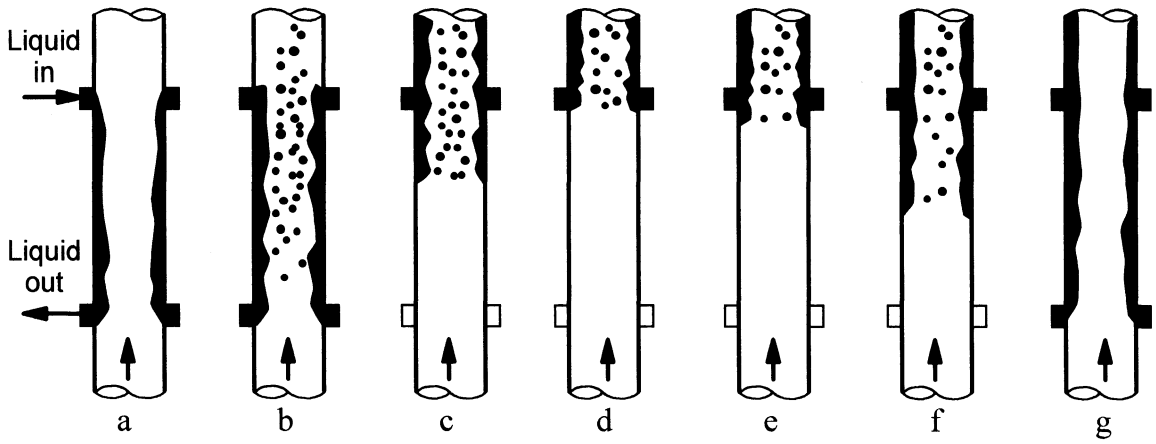

Figure 2.1: Flow transitions in vertical counter-current annular flow.

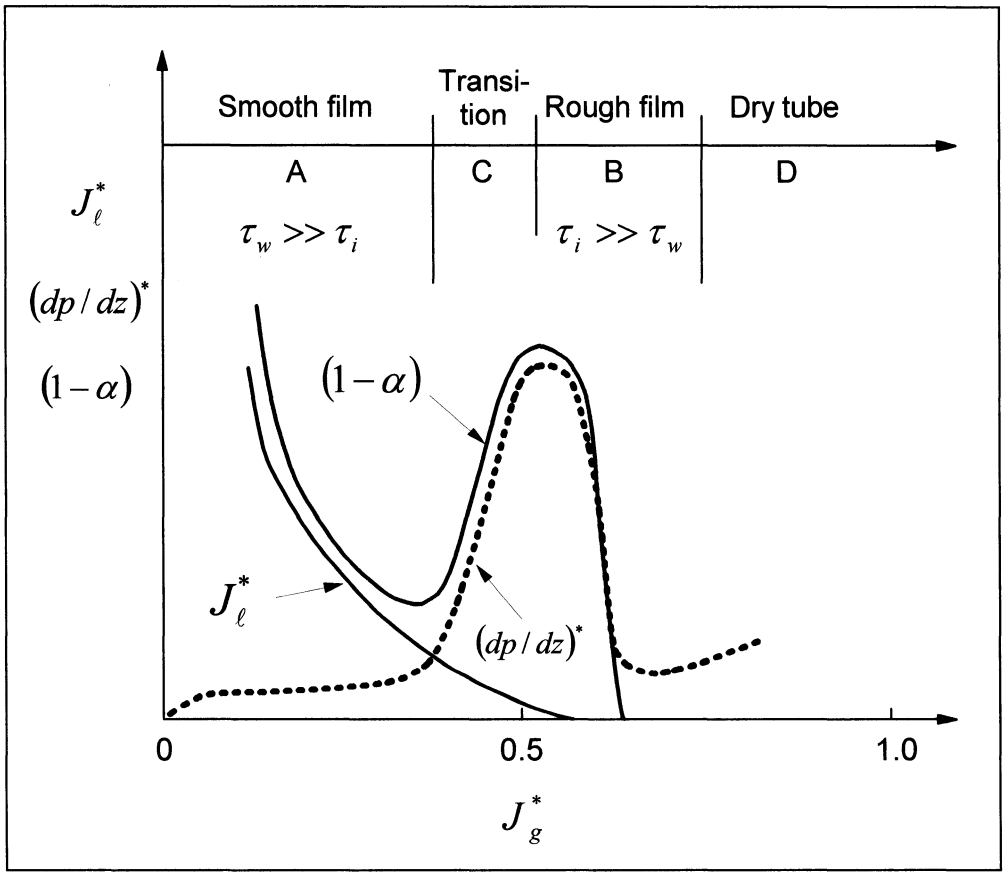

Figure 2.2: Qualitative variations of non-dimensional superficial liquid velocity, liquid hold-up and non-dimensional pressure gradient with non-dimensional superficial gas velocity (Bharathan *et al.*, 1983).

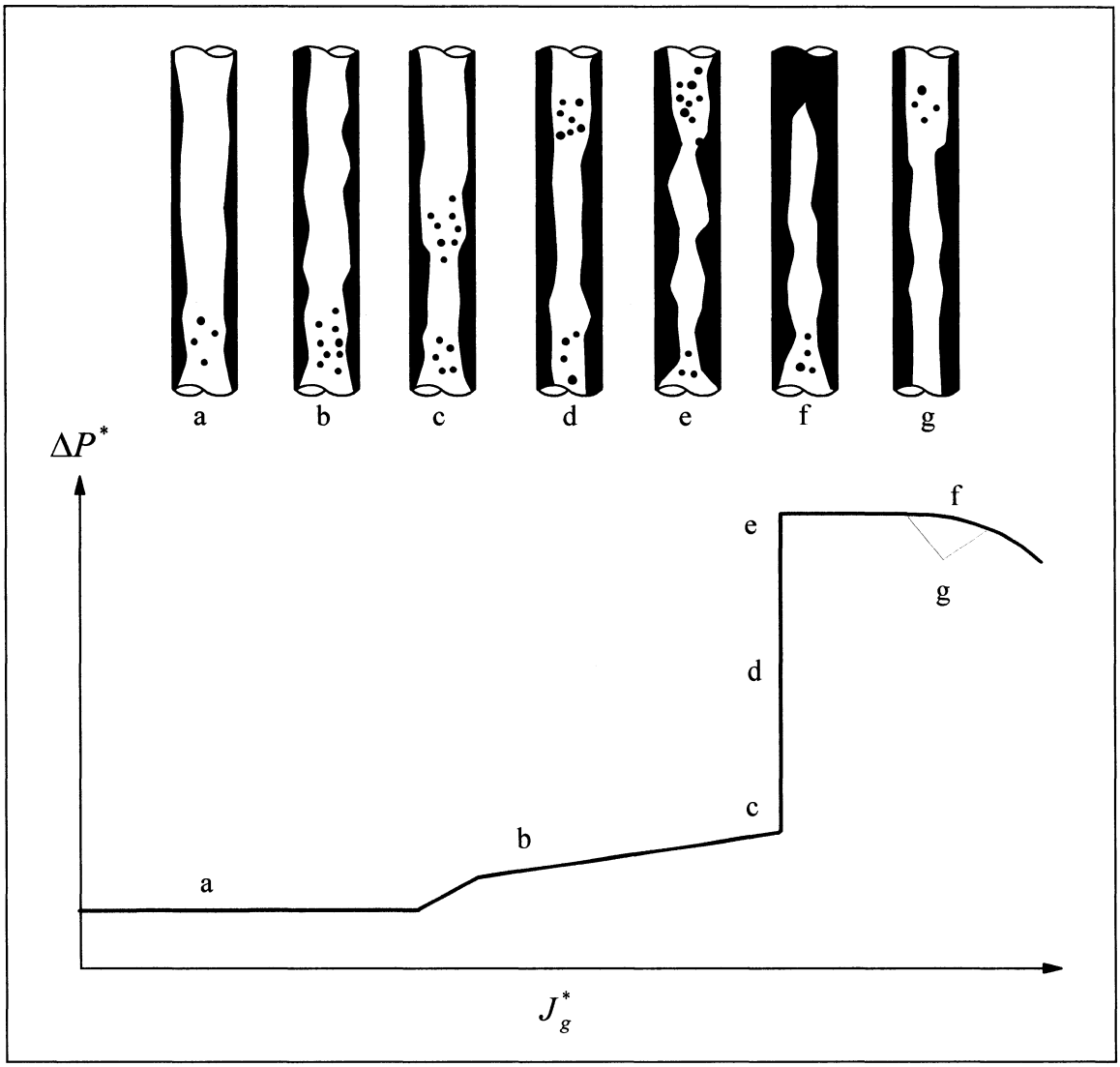

Figure 2.3: Pressure drop variation vs. gas flow rate in counter-current flow with upper-plenum injection (Hawley and Wallis, 1982).

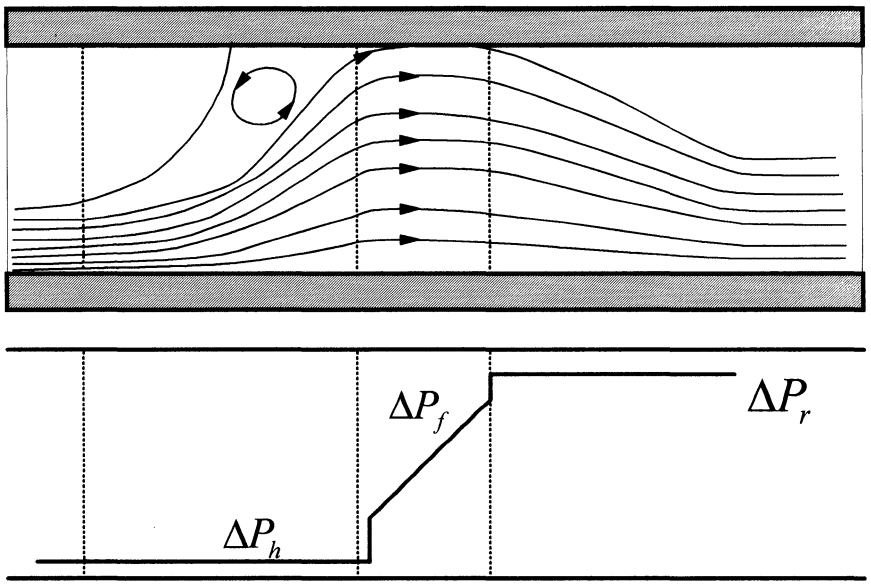

Figure 2.4: Idealized pressure profile with the sketch of a stable slug (Fan *et al.*, 1993).

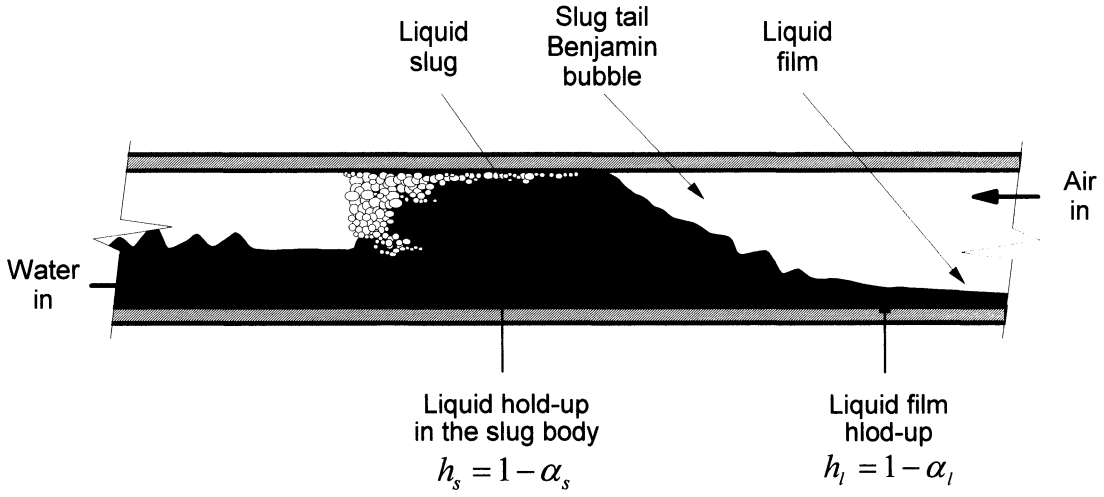

Figure 2.5: The description of slug parameters used in Jepson and Taylor (1993).

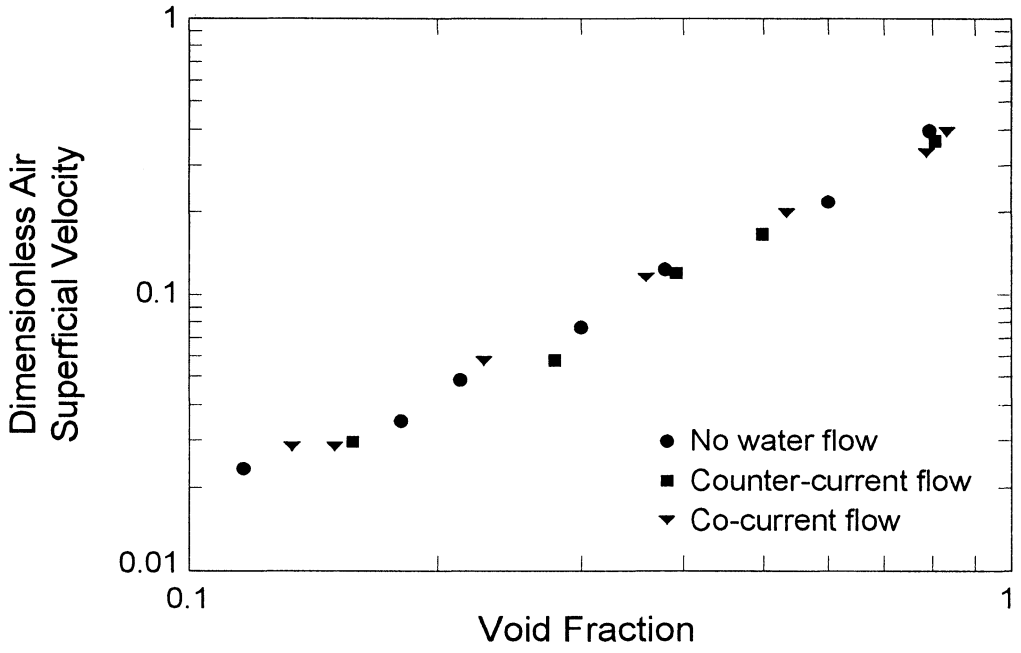

Figure 2.6: The onset of "Slugging" in a 2.5 × 2.5 cm^2 horizontal channel (Wallis and Dobson, 1973).

CHAPTER 3

COUNTER-CURRENT TWO PHASE FLOW TEST FACILITY

The CCF test facility, shown in Figure 3.1, can support vertical test sections, as well as, test sections containing vertical and horizontal legs. This system consists of a constant head water tank, a pump, a calming section, a bank of water turbine-type flow meters and air rotameters, and the test section. The water flow rate, supplied to the test section by the pump connected to the constant head water tank, is controlled in two steps: a coarse control that is done using a set of valves and a by-pass circuit at the pump outlet, and a fine control that is done using a set of two different size parallel needle valves, located close to the test section. During the experiments, the temperature of the water is kept constant at $20\pm0.5°C$.

3.1 TEST SECTION

Figure 3.2 shows a schematic diagram of the CCF test section. The test assembly consists of an upper and a lower plenum, and vertical and horizontal legs connected by an elbow. The test section, that has a geometry similar to a typical feeder pipe encountered in CANDU nuclear power reactors, consists of 2.02 m long vertical and 3.30 m long horizontal legs. The horizontal leg contains flanges in which an orifice may be placed. The vertical and horizontal legs are connected by an opaque 90° PVC elbow. These legs are centered in the elbow by two Plexiglas collars and are sealed using O-rings; Figure 3.3 shows the details of this assembly. In order to allow flow visualization, both the vertical and the horizontal legs are manufactured from 63.5 mm ID transparent Plexiglas tubes. The vertical leg is supported by an aluminum I-beam and the test section is positioned vertically, using adjustable supports. The horizontal leg is also supported by an aluminum I-beam using 6 adjustable supports. The horizontally placed I-beam is supported by 3 adjustable

tubular steel legs bolted to the floor. The major parts of the test section are:

- *The upper plenum*: is used as a two-phase flows collector/separator system.
- *The porous wall water injector*: consists of a 63.5 mm I.D. tube with 800, 1 mm holes on the wall.
- *The lower plenum*: contains the liquid outlet including a water level control system and the air inlet system. The level control system consists of a 3.45 kPa (0.5 $psid$) differential pressure transducer, used as a liquid level transducer. The level control system is capable of maintaining the water level in the lower plenum constant ($\pm 1\, cm$) through a wide range of liquid flow rates.
- *The orifices*: are made of 1.5 mm thick stainless steel plates without a chamfered edge. Orifices with β ratios ($= D_{orifice}/D_{tube}$) of 0.83, 0.77, 0.72, and 0.66 have been used to carry out the present experiments.

Flanges located at two axial positions in the horizontal leg are used to insert orifices of different sizes. The water is injected in the upper part of the test section, just below the upper plenum (see Figure 3.2). Filtered air obtained from the mains of the laboratory is used as the gas phase. The air is injected through the lower plenum. The level of the water is kept constant by using the level controller in the lower plenum within ± 1 cm under all transient flow conditions encountered during the experiments. The dimensions of the test section, as well as the location of the flanges, are given in Figure 3.2.

3.2 INSTRUMENTATION

The test section is instrumented to measure the inlet liquid and gas flow rates, inlet flow temperatures, absolute pressures, and void fractions. The liquid flow rate is measured using "Flow Technology" turbine flow meters covering a range of 0.05 to 4.54 m^3/h having an accuracy better than 1% of the reading. The gas flow rate is measured using a set of five "Brooks" rotameters, covering a range of 0.085 to 132.5 $m^3/h \pm 2\%$ of the full scale, at an outlet pressure of 2 bar. The temperature of the air is measured using a K-type thermocouple installed near the air entrance to the lower plenum (Figure 3.1). The absolute pressure in the lower plenum

is measured using a 1.4 *bar* "Sensotec" pressure transducer with an accuracy of 0.25% of full scale. The void fraction measurement system, also used as the slug detection system, consists of three mobile capacitance probes (Teyssedou and Tye, 1999). Each probe consists of two electrodes manufactured using a 0.06 mm thick metallic foil deposited on a Plexiglas collar; the topology of these probes is shown in Figure 3.4. It is important to note that, with the proposed arrangement of the electrodes, one of them is connected to ground and is simultaneously used as a Faraday electrostatic shield for the second one. Each void probe, with its associated electronics module and anti-alias filters, was calibrated under steady state conditions. For the calibration, a small test section 0.15 m in length, with the same ID, wall thickness, and material (Plexiglas) as that used for the CCF test section shown in Figure 3.2 where the probes were finally installed, was used. Due to the extent of the slugs observed in some experiments and to the formation of a highly perturbed region close to the elbow in other experiments, the position of the probes with respect to the elbow, as well as the distances between the probes were not the same for all the experiments. The following distances between the probes were used during the experiments: 0.20, 0.35, and 0.40 m while the distance of the first probe to the elbow was maintained constant at 0.19 m. The calibration curve of the three probes are shown in Figure 3.5. With the optimization of the geometry of the electrodes used for each probe, it was possible to obtain an almost linear response of the apparatus for void fractions of up to 70%. The scattering of the calibration points for each probe is quite possibly due to the fact that it was almost impossible to manufacture electrodes having exactly the same geometry. The position of the probes installed in the horizontal leg with respect to the elbow, is shown in Figure 3.2. The output of these modules, as well as the output of the pressure transducer located in the lower plenum, are connected to a Data Acquisition System (DAS). The DAS has a 16-bit analog to digital conversion unit, and is connected to a PC. The DAS is capable of collecting 66 000 data points (13 200 $\times$ 5 Channels) per run with a sampling time of 20 ms. In order to minimize the amount of data, and to avoid aliasing of the signals, the sampling time was selected after a careful analysis of the void signals using a HP spectrum analyzer.

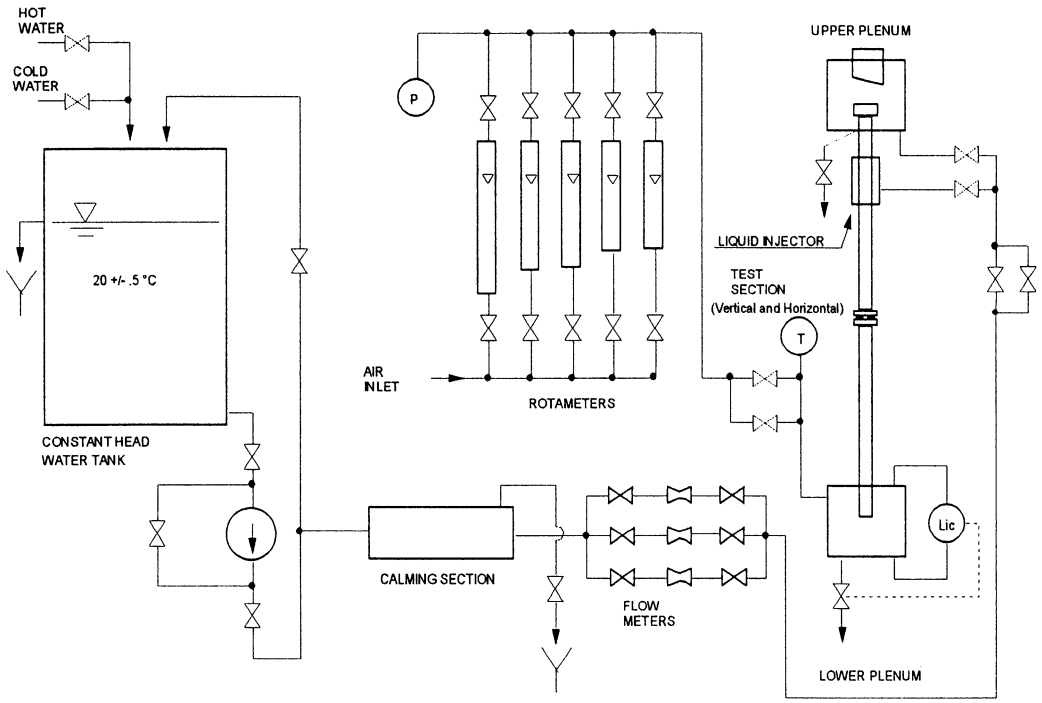

Figure 3.1: Test facility.

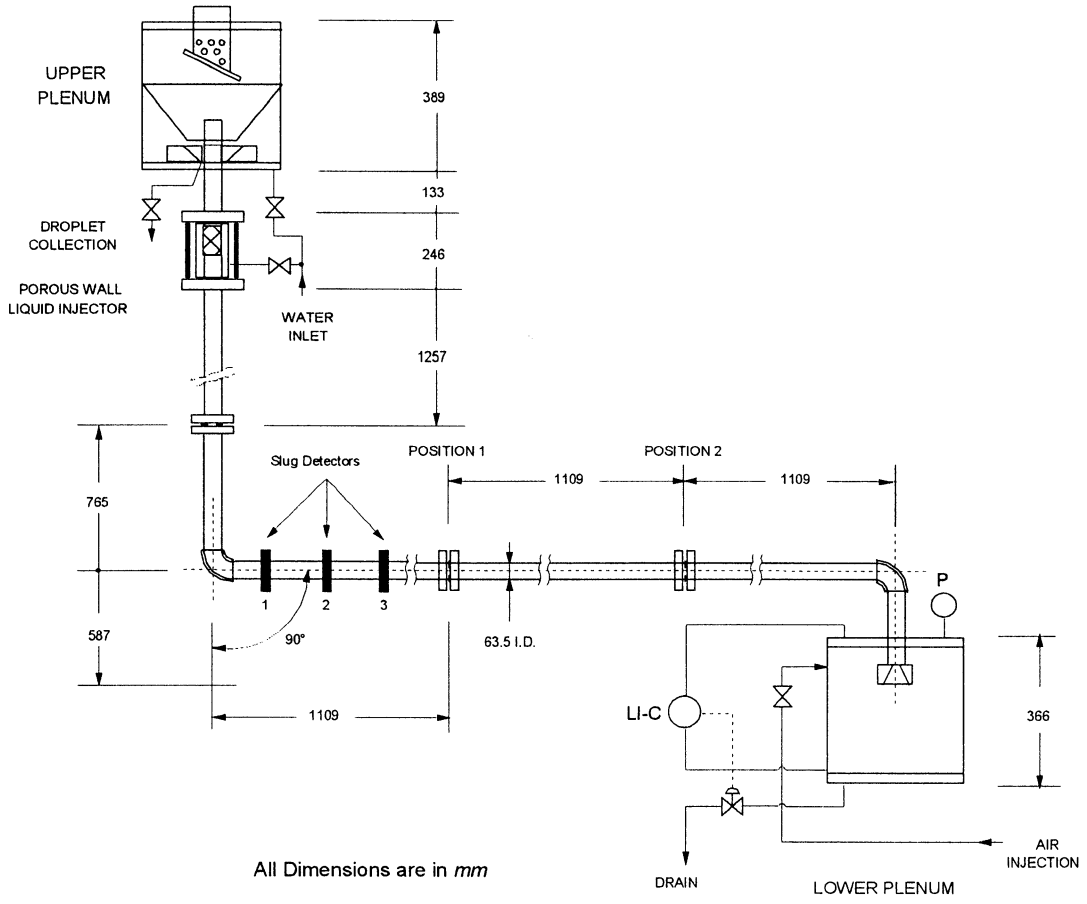

Figure 3.2: CCF Test section.

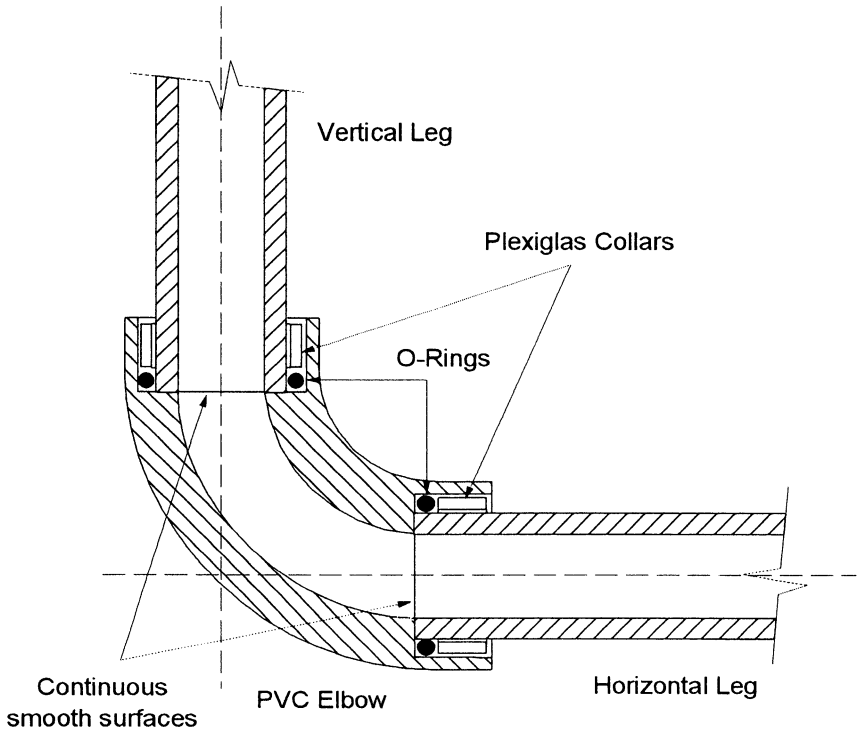

Figure 3.3: Details of the elbow assembly.

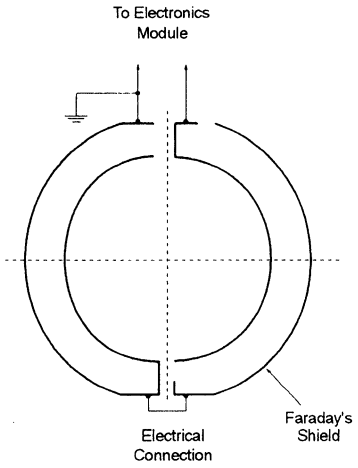

Figure 3.4: Topology of the electrodes.

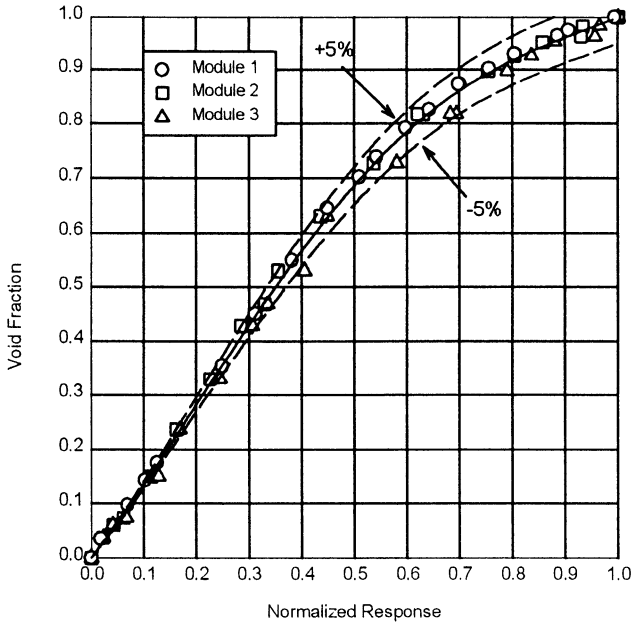

Figure 3.5: Void gauges calibration curves.

CHAPTER 4

EXPERIMENTAL CONDITIONS AND PROCEDURES

This chapter is divided into two parts. The first part describes the experimental conditions and procedures used to carry out flooding and slugging experiments. The second part presents the conditions and the procedures used to carry out experiments that were devoted to the characterization of the wave propagation under counter-current flow conditions. These experiments provided data on the initial wave propagation conditions required to model the slug formation in the horizontal leg. The experimental results are given in Chapter 5, while the wave model is presented in chapter 7.

4.1 FLOODING AND SLUGGING EXPERIMENTS

The range of the inlet liquid flow rate changes from 0.4 to 2.5 m^3/h and the inlet gas flow rate changes from 0 to 29 m^3/h. The corresponding superficial velocities are $0.035 - 0.219\ m/s$ and $0 - 2.543\ m/s$, respectively, where the superficial velocity of k-phase is defined as:

$$j_k = \frac{Q_k}{A}, \quad k = l, g, \tag{4.1}$$

where Q_k is the volumetric flow rate of phase k and A is the cross section area of the tube.

The β ratios ($= D_{orifice}/D_{tube}$) of the orifices, used in this research, are 0.83, 0.77, 0.72, and 0.66. Each of these orifices is first inserted at Position 1 and then at Position 2 in the horizontal leg (see Figure 3.2). Some experiments were also conducted without orifices.

For a given orifice size (β =0.66, 0.72, 0.77, and 0.83) and position in the horizontal leg, as well as a given inlet liquid flow rate, the gas flow rate was slowly increased

increased up to the moment that a difference between the inlet and delivered liquid flow rates was observed. These flow conditions were considered as the point of onset of flooding. Moreover, it should be noted that the onset of flooding was determined as the intersection point between the curve fittings of full and partial liquid delivery data (Bédard, 1997). Simultaneously, the visual observation of the flow, in conjunction with the void fraction signals produced by the slug detector probes, permitted the onset of slugging in the horizontal leg to be determined. After reaching the onset of flooding and slugging conditions, the inlet gas flow rate was increased in order to cover the entire partial liquid delivery region. Furthermore, for each orifice the experiments were repeated for inlet liquid flow rates ranging from 0.4 to 2.5 m^3/h.

For each pair of liquid and gas flow rates, the signals produced by three slug detector probes, as well as the signal produced by the pressure transducer used to measure the absolute pressure in the lower plenum, were collected simultaneously. After having finished the experiments, these signals were post processed using a FORTRAN program that allows the Fast Fourier Transform (FFT), the mean value of the void fraction and pressure signals, the Probability Density Function (PDF) and the cross–correlation of the signals to be determined. The calibration curve presented in Figure 3.5, in conjunction with the normalized response of each void fraction probe, were used to determine the average void fraction at different locations in the horizontal run. The cross–correlation and the distance between the electrodes were used to calculate the slug propagation velocity.

The capability of the hardware and software used to collect and treat the data was determined according to the following procedure. A function generator was connected to one of the channels of the DAS. Sinusoidal signals, covering a range of 0.2 to 5.0 Hz and having a constant amplitude of 4 Volt peak to peak ($Vp-p$), were applied to one of the DAS channels and collected with a sampling rate of 20 ms. A two channel "Gould" digital oscilloscope (100 Ms/s) and a "Fluke" frequency counter were simultaneously used to monitor the incoming signals to the DAS. The collected signals were then numerically mixed with a Gaussian noise,

normal distribution. The mixed signals were treated by the FFT software and the intensity of the noise was subsequently increased up to a level that the fundamental frequency of the sinusoidal signal was not able to be detected by the FFT processor. Figure 4.1 shows the distribution function of a void fraction signal collected during an experiment carried out using an orifice having a β ratio of 0.77 installed at Position 1 in the horizontal leg (see Figure 3.2). The same figure also shows the distribution function of a 0.2 Hz sinusoidal signal, after being mixed with a Gaussian noise having an amplitude of 30 $Vp-p$. This noise amplitude represents the upper limit where the peak of the fundamental frequency, produced by the signal generator, can still be detected. Under this limiting condition, it was determined that the Signal to Noise Ratio (SNR) of the technique used to treat the data, is $\approx 18\ dB\ (= 20\log(30/4))$, for a constant and the same coupling impedance. The spectra of both the void fraction and pressure signals, obtained from the same experiment, i.e., $\beta = 0.77$, $Q_l = 1.1\ m^3/h$ and $Q_g = 16.8\ m^3/h$, are shown in Figure 4.2. It is interesting to note the similarity that exists in the frequency components of these two signals. In both cases, the predominant frequency of the slugs is close to 0.2 Hz.

4.2 WAVE PROPAGATION EXPERIMENTS

Wave propagation experiments were performed, in order to obtain the initial conditions required by the slug model that will be discussed in detail in Chapter 7. During these experiments, a digital video SONY-DCR-TRV17 camera, with a circular polarizer (COKIN Polarizer V-30), was used to collect images of travelling waves. An edge detection technique was then used to obtain the wave amplitude. At the end of this chapter, the general concept of the edge detection technique will be discussed .

A Carl Zeiss 30 mm objective was installed in the camera. This camera has an optical zoom of 10x and a numerical zoom of 120x. The camera was placed at a distance of 85 cm from the test section. A photo-flood with a blue spectra lamp was used as the illumination source.

was used as the illumination source.

The wave propagation experiments were carried out using the same test section that was used to carry out the slug flow experiments. In order to increase the optical contrast of the liquid film, a blue dye (625 *ml* of concentrated dye mixed to 3.785 l of water) was added to the inlet water. A very low and constant flow rate of dye was used, in such a way that the overall water flow rate was not perturbed.

4.2.1 EXPERIMENTAL CONDITIONS

Since the wave amplitudes obtained from these experiments would be used as the initial conditions for the wave propagation model, the wave propagation experiments were carried out without any obstruction. The reflections from the orifice were simulated using a reflection coefficient. The reflection coefficient is obtained by using simple physical relation from optics. For this calculation, the incident wave is replaced by inlet liquid flow rate, and the transmitted and the reflected waves are replaced by partial liquid delivery and reflected liquid flow rates, respectively. The conservation of energy in optics gives the value of unity to the sum of the reflection and transmision coefficients. For the present research, the conservation of mass was taken into account. Defining the transmision coefficient, as a ratio of partial liquid delivery to full liquid delivery, one can write the reflection coefficient as follows:

$$\gamma = \frac{\text{full liquid delivery} - \text{partial liquid delivery}}{\text{full liquid delivery}}. \tag{4.2}$$

Equation 4.2 is also used for the calculation of the reflection coefficient in the case of the without obstruction, since the incident waves are reflected from the second elbow (see Figure 3.2). The partial liquid delivery data used in this equation were obtained from the Bédard's Master's thesis (1997). Note that Bédard's experimental conditions were reproduced to carry out these calculations. It must be also pointed out that the partial liquid delivery is a function of the gas flow rate (Bédard, 1997). Figures 4.3 – 4.7 show the reflection coefficient as a function of the inlet liquid flow rate and the orifice β ratio.

Table 4.1 summarizes the matrix of the experimental conditions used to carry out this part of the work. These experimental conditions are given as a function of the inlet liquid and gas volumetric flow rates and the corresponding superficial velocities.

Table 4.1 Experimental conditions for the wave propagation.

β	$Q_{l,inlet}$ (m^3/h)	Q_g (m^3/h)	$j_{l,inlet}$ (m/s)	j_g (m/s)	$j_{l,delivery}$ (m/s)
1.0	0.8	31.503	0.070	2.763	0.0605
1.0	1.1	22.227	0.096	1.950	0.0830
1.0	1.5	16.626	0.132	1.458	0.1127
1.0	1.8	11.376	0.158	0.998	0.1380

4.2.2 EXPERIMENTAL PROCEDURES

For a given inlet liquid flow rate, the gas flow rate was increased until disturbed waves were seen to occur at the surface of the flowing water. This procedure was then repeated for the entire flow rates given in Table 4.1. Each case was recorded with the digital camera. The Adobe Premiere software (version 6.0) was then used to extract a series of individual frames from each recorded film. An edge detection macro of Matlab, in conjugation with a program written in Matlab (given in Appendix E), were used to obtain the wave amplitude information from each frame.

It was observed that the so-called Sobel 3×3 operator was better than the other edge detector operators, i.e., Roberts, Prewitt, Log, Zero-Crossing, and Canny, as well as, the edge detection macro that we wrote based on the Gaussian Distribution. The performance of some edge detectors has been studied by William Pratt (1991) and the comparison of these detectors taken from his study are demonstrated in Figure 4.8. In these figures, the signal-to-noise ratio is defined as $\text{SNR} = (h/\sigma_n)^2$, where h is the edge height and σ_n is the noise standard deviation. The edge detection threshold can be scaled linearly with the signal-to-noise ratio

under the condition that $P_F = 1 - P_D$, where P_D is the probability of correct edge detection and P_F is the probability of false edge detection. These probabilities can be given as follows:

$$P_D = \int_{tr}^{\infty} p(G|edge)dG, \tag{4.3a}$$

$$P_F = \int_{tr}^{\infty} p(G|no-edge)dG. \tag{4.3b}$$

where tr is the edge detection threshold and $p(G|edge)$ and $p(G|no-edge)$ are the conditional probability densities of the edge gradient $G(j,k)$.

For an image with a SNR=100, the threshold is about 10% of the peak gradient value. In the figure, it is apparent that the capability of the edge detection increases as signal-to-noise ratio (SNR) increases, and Sobel and Prewitt 3×3 operators are superior to the Roberts 2×2 operators. The Prewitt operator is better than the Sobel operator for a vertical edge whereas, for a diagonal edge, the Sobel operator is superior.

The edge gradient generation is one of the techniques used to detect edges in an image. This is a first order derivative edge detection and there are two fundamental methods for generating first order derivative edge gradients:

- *orthogonal gradient generation*: generates the gradients in two orthogonal directions in an image,
- *edge template gradient generation*: uses a set of directional derivatives.

Since it is easier and efficient to use the orthogonal gradient generation, only the first method is used for this research, and this will be described in the following paragraphs.

The gradient along the line normal to the edge slope can be computed in terms of the derivatives along orthogonal axes according to the following equation:

$$G(x,y) = \frac{\partial F(x,y)}{\partial x}\cos\theta + \frac{\partial F(x,y)}{\partial y}\sin\theta, \tag{4.4}$$

where $F(x,y)$ is an image field.

The generation of an edge gradient $G(j,k)$ in the discrete domain can be described in terms of a row edge gradient $G_R(j,k)$ and a column edge gradient $G_C(j,k)$. Thus, the spatial gradient can be computed as:

$$G(j,k) = \left\{[G_R(j,k)]^2 + [G_C(j,k)]^2\right\}^{1/2}. \tag{4.5}$$

There are several ways to generate the discrete gradient. The simplest of all is to form the difference of pixels along rows and columns in the image. The row gradient is defined as:

$$G_R(j,k) = F(j,k) - F(j,k-1), \tag{4.6}$$

and the column gradient is:

$$G_C(j,k) = F(j,k) - F(j+1,k). \tag{4.7}$$

Diagonal edge gradients can be obtained by forming differences of diagonal pairs of pixels and this is the basis of *ROBERTS cross-difference operator* which is defined as:

$$G(j,k) = \left\{[G_1(j,k)]^2 + [G_2(j,k)]^2\right\}^{1/2}, \tag{4.8}$$

where $G_1(j,k)$ and $G_2(j,k)$ are given by:

$$G_1(j,k) = F(j,k) - F(j+1,k+1) \tag{4.9}$$

and

$$G_2(j,k) = F(j,k+1) - F(j+1,k). \tag{4.10}$$

The other way to generate the discrete gradient is to form the pixel difference in a way that the row and column gradients become:

$$G_R(j,k) = F(j,k+1) - F(j,k-1) \tag{4.11}$$

and

$$G_C(j,k) = F(j-1,k) - F(j+1,k). \tag{4.12}$$

The disadvantage of this method is that the separated pixel difference gradient generation method is highly sensitive to small luminance fluctuations in the image. Therefore, another technique is used to avoid this problem. Two dimensional gradient formation operators can be used to perform differentiation in one coordinate direction and perform spatial averaging in the orthogonal direction. Prewitt has introduced a 3x3 pixel edge gradient operator described by the pixel numbering convention which can be represented as:

$$\begin{matrix} A_0 & A_1 & A_2 \\ A_7 & F(j,k) & A_3 \\ A_6 & A_5 & A_4 \end{matrix}$$

The row and column edge gradients are defined as:

$$G_R(j,k) = \frac{1}{K+2}\left[(A_2 + KA_3 + A_4) - (A_0 + KA_7 + A_6)\right] \tag{4.13}$$

and

$$G_C(j,k) = \frac{1}{K+2}\left[(A_0 + KA_1 + A_2) - (A_6 + KA_5 + A_4)\right], \tag{4.14}$$

where $K = 1$.

The *Sobel edge detector* differs from the Prewitt edge detector in that the values of north, south, east and west pixels are doubled, i.e., $K = 2$. The motivation for this weighing is to give equal importance to each pixel in terms of its contribution to the spatial gradient.

Consequently, the row and the column gradients can be expressed by the convolution relationships:

$$G_R(j,k) = F(j,k) \otimes H_R(j,k) \tag{4.15}$$

and

$$G_C(j,k) = F(j,k) \otimes H_C(j,k), \tag{4.16}$$

where $H_R(j,k)$ and $H_C(j,k)$ are 3×3 row and column impulse response arrays, and they are defined for several cases in Figure 4.9.

The finite convolution can be written as:

$$G(j,k) = \sum_{m=j-1}^{j+1} \sum_{n=k-1}^{k+1} F(m,n)H(m,n). \tag{4.17}$$

After forming the edge gradient in the manner discussed above, the important step is to compare the gradient to a threshold value to determine if an edge exists. In the *Matlab Edge Detection Macro*, the threshold value is calculated, based on the RMS estimate of noise. For this research, after obtaining an idea of the threshold value from this estimate, several threshold values were tested beyond this calculated RMS value, and the best one was chosen as a threshold. This value was entered as a constant (=0.04) and used to treat all the frames collected for the experiments.

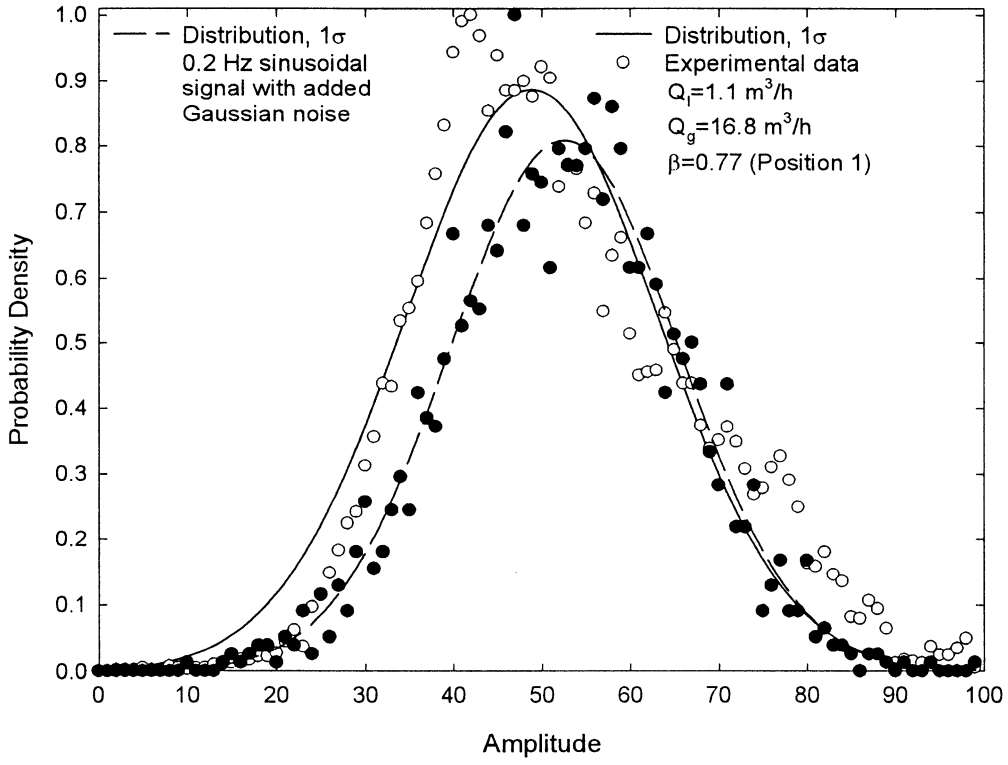

Figure 4.1: Distribution functions.

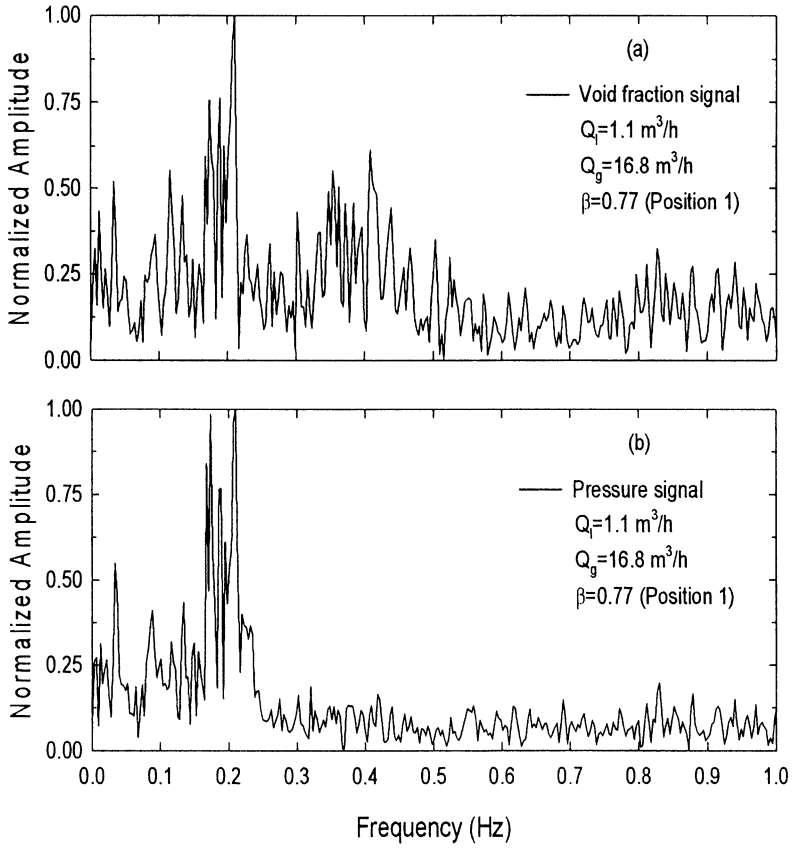

Figure 4.2: Typical power spectra of void fraction and pressure signals.

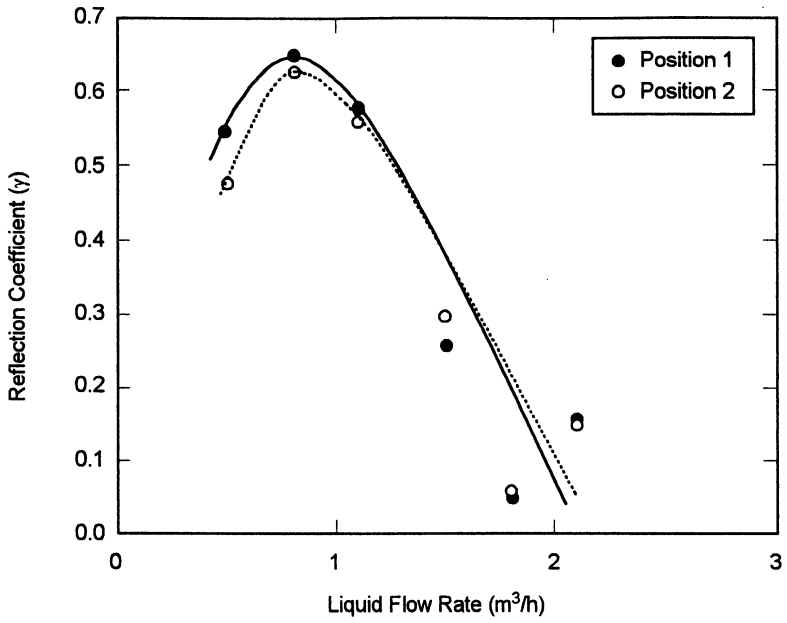

Figure 4.3: Reflection coefficient vs. inlet liquid flow rate for orifice β=0.66.

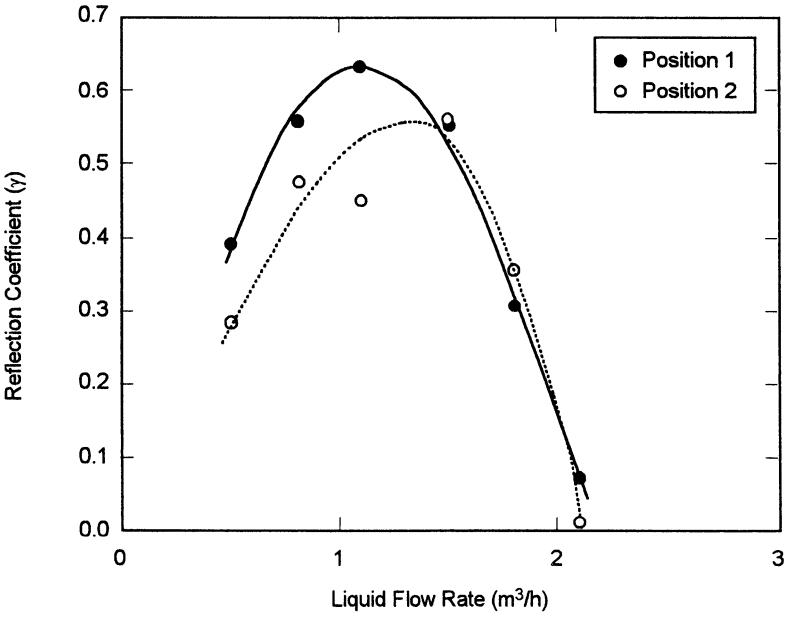

Figure 4.4: Reflection coefficient vs. inlet liquid flow rate for orifice β=0.72.

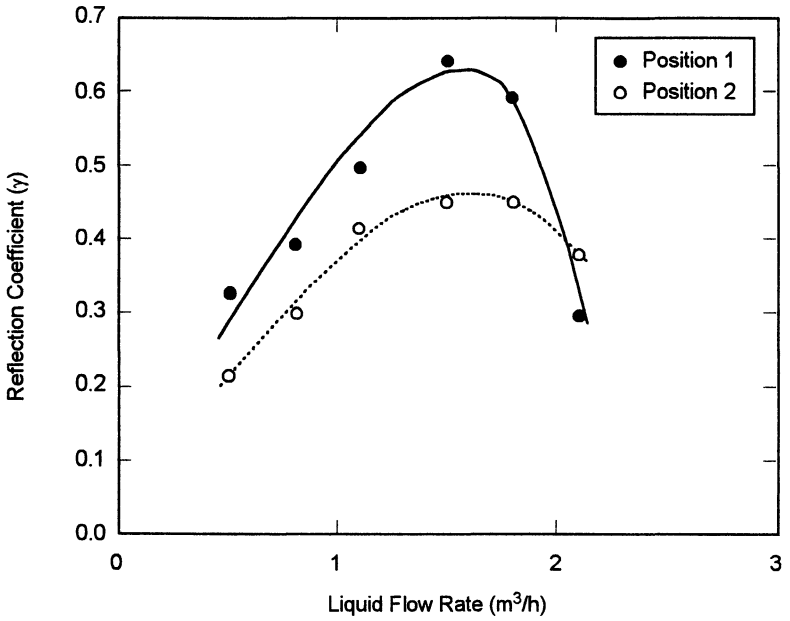

Figure 4.5: Reflection coefficient vs. inlet liquid flow rate for orifice β=0.77.

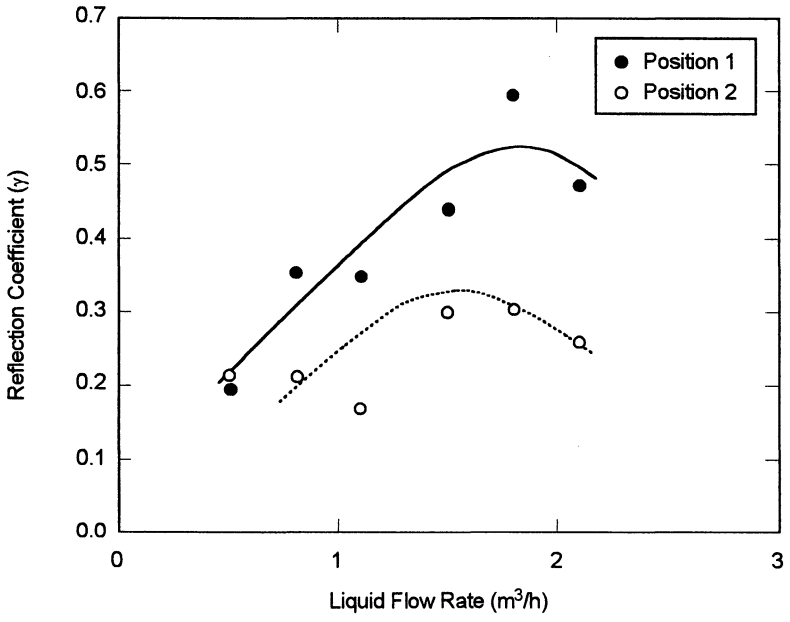

Figure 4.6: Reflection coefficient vs. inlet liquid flow rate for orifice β=0.83.

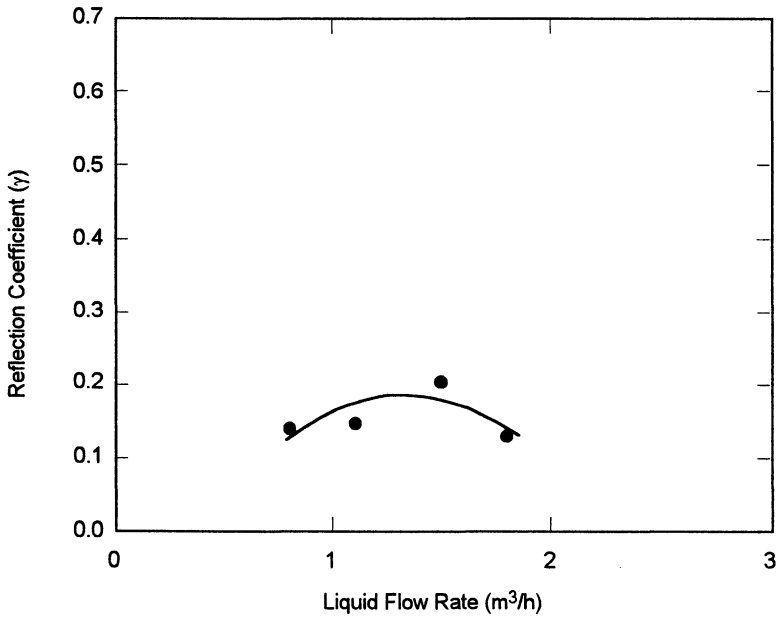

Figure 4.7: Reflection coefficient vs. inlet liquid flow rate for orifice β=1.0.

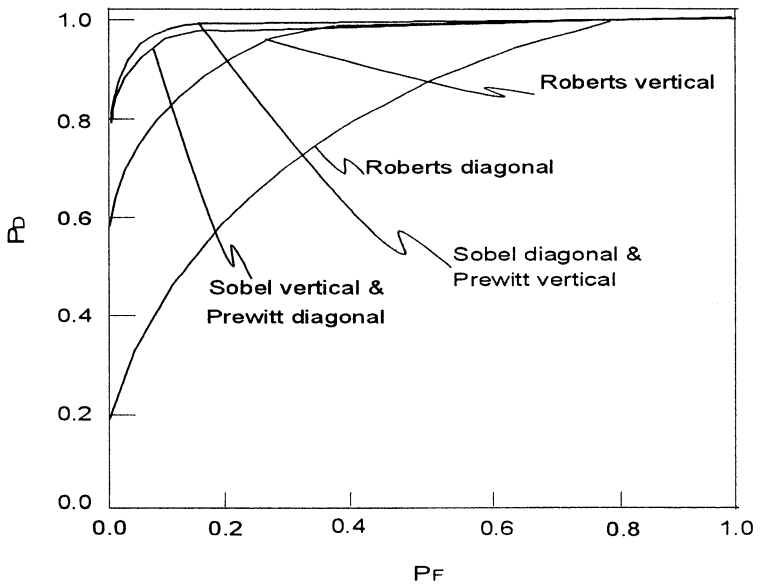

(a) SNR = 10.0

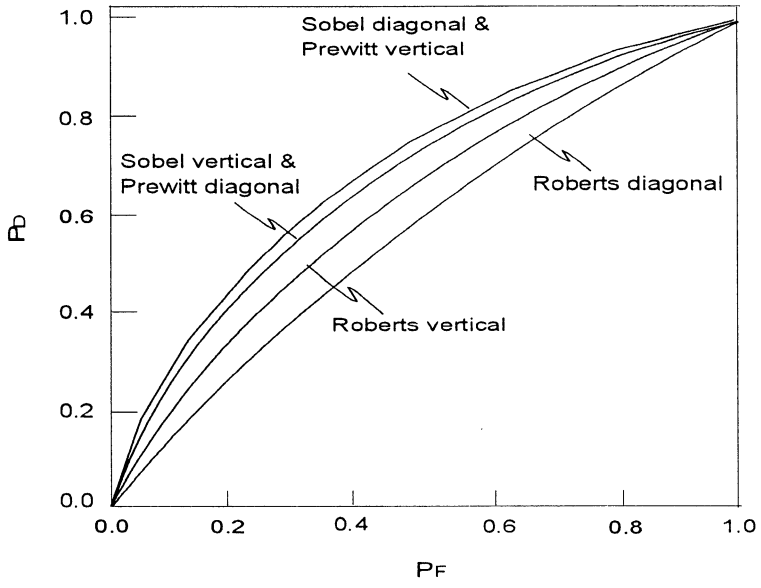

(b) SNR = 1.0

Figure 4.8 Probability of detection versus probability of false detection for 2×2 and 3×3 operators (Pratt, 1991).

Operator	Row Gradient	Column Gradient
pixel difference	$\begin{bmatrix} 0 & 0 & 0 \\ 0 & 1 & -1 \\ 0 & 0 & 0 \end{bmatrix}$	$\begin{bmatrix} 0 & -1 & 0 \\ 0 & 1 & 0 \\ 0 & 0 & 0 \end{bmatrix}$
seperated pixel difference	$\begin{bmatrix} 0 & 0 & 0 \\ 0 & 1 & -1 \\ 0 & 0 & 0 \end{bmatrix}$	$\begin{bmatrix} 0 & -1 & 0 \\ 0 & 1 & 0 \\ 0 & 0 & 0 \end{bmatrix}$
Roberts	$\begin{bmatrix} 0 & 0 & -1 \\ 0 & 1 & 0 \\ 0 & 0 & 0 \end{bmatrix}$	$\begin{bmatrix} -1 & 0 & 0 \\ 0 & 1 & 0 \\ 0 & 0 & 0 \end{bmatrix}$
Prewitt	$\frac{1}{3}\begin{bmatrix} 1 & 0 & -1 \\ 1 & 0 & -1 \\ 1 & 0 & -1 \end{bmatrix}$	$\frac{1}{3}\begin{bmatrix} -1 & -1 & -1 \\ 0 & 0 & 0 \\ 1 & 1 & 1 \end{bmatrix}$
Sobel	$\frac{1}{4}\begin{bmatrix} 1 & 0 & -1 \\ 2 & 0 & -2 \\ 1 & 0 & -1 \end{bmatrix}$	$\frac{1}{4}\begin{bmatrix} -1 & -2 & -1 \\ 0 & 0 & 0 \\ 1 & 2 & 1 \end{bmatrix}$
Frei − Chen	$\frac{1}{2+\sqrt{2}}\begin{bmatrix} 1 & 0 & -1 \\ \sqrt{2} & 0 & -\sqrt{2} \\ 1 & 0 & -1 \end{bmatrix}$	$\frac{1}{2+\sqrt{2}}\begin{bmatrix} -1 & -\sqrt{2} & -1 \\ 0 & 0 & 0 \\ 1 & \sqrt{2} & 1 \end{bmatrix}$

Figure 4.9: Impulse response arrays for 3×3 orthogonal differential gradient edge operators (Pratt, 1991).

CHAPTER 5

EXPERIMENTAL RESULTS

The results obtained for the slug flow and the wave propagation experiments are presented in this chapter. The slug flow experimental results including the average void fraction, the slug frequency, the slug propagation velocity and a comparison between the onset of flooding and the onset of slugging are presented in the first part of this chapter. Afterwards, the results obtained from the wave propagation experiments will be discussed.

5.1 SLUG FLOW EXPERIMENTS

Four different orifices without chamfered edges and having β ratios of 0.66, 0.72, 0.77 and 0.83 were used to carry out the CCF slugging experiments. The experiments were repeated by changing the position of the orifices with respect to the elbow in the horizontal leg; these positions are indicated as Position 1 and Position 2 in Figure 3.2. Experiments were also carried out without orifices installed in the horizontal leg. The data have been analysed in order to obtain the onset of flooding and slugging, the slug propagation velocity, the slug frequency, and the average void fraction as a function of both the liquid and gas superficial velocities.

It is important to point out that, for all the cases studied, it was visually observed that, for a given liquid flow rate, a hydraulic jump forms in the horizontal leg and propagates towards the elbow as the gas flow rate is increased. A further increase in the gas flow rate causes the hydraulic jump to enter into the elbow and liquid droplets are entrained above the elbow in the vertical leg. Under this condition, the flooding takes place and it is simultaneously accompanied by the formation of slugs in the horizontal leg. Once the flooding is triggered, a pulsating column is formed in the vertical leg. This pulsating column, under the same onset of flooding conditions, subsequently provokes high amplitude waves that travel along

the horizontal leg toward the orifice. This visual observation is schematically presented in Figure 5.1. The waves that are formed close to the elbow, and propagate downstream in the horizontal leg are then partially reflected by the orifice. Figure 5.2 shows the entrained droplets above the elbow, i.e., the onset of entrainment, and Figure 5.3 shows the formation of a pulsating column in the vertical leg. Figures 5.4 and 5.5 show a wave, produced by the pulsating column and traveling downstream toward the orifice. These waves travel along the horizontal leg and, depending on the orifice size, a partial reflection occurs at the orifice (Figure 5.6). Figure 5.7 shows a photo of two waves traveling in opposite directions, with the reflected wave produced by the orifice located at Position 1 in the horizontal leg. Incident and reflected waves travelling in opposite directions are able to interact mutually , i.e., wave interference occurs. Each time an incident wave interacts constructively with a reflected one, and the resulting amplitude becomes equal to the tube ID blocking the passage of the gas; a slug of liquid is then formed (Figure 5.8).

5.1.1 THE ONSET OF FLOODING AND THE ONSET OF SLUGGING

The first part of this section discusses the comparison of the onset of flooding and that of slugging, whereas the second and the third parts discuss the effect of the size of the obstruction and its location with respect to the elbow on the onset of flooding and the onset of slugging. The last part of this section is devoted to the presention of the results obtained from the experiments carried out without any obstruction installed in the horizontal leg.

Figures 5.9a-b show the comparison of the onset of flooding and that of slugging data for obstructions having β ratios of 1.0, 0.83, 0.77, 0.72, and 0.66. These results are also presented in Appendix A in the form of tables. The onset of flooding results presented in these figures were taken from Bédard (1997). For his research, he used the same test section that we have used to carry out the slugging experiments. In these figures, the solid and the empty symbols correspond to the experiments conducted for flooding and slugging, respectively. Figure 5.9a

shows the results for the cases where the obstructions were installed at Position 1, and Figure 5.9b shows those for Position 2. As can be observed, with the exception of the experiments carried out without an orifice ($\beta = 1.0$), the points that correspond to the onset of flooding and slugging seem to be quite close. It is important to mention that some of the experimental points do not appear in Figures 5.9a. and 5.9b. because they are hidden by points corresponding to the same values of superficial velocities. Thus, when an orifice is installed in the horizontal leg, and for the conditions used during the present experiments (both the liquid and the gas flow rates are kept constant for each experiment), flooding is simultaneously accompanied by the formation of slugs in the horizontal leg. Siddiqui *et al.* (1986) and Kawaji *et al.* (1991) have observed that at high liquid flow rates a hydraulic jump formed in the horizontal leg close to the elbow and that flooding was caused by slugging which simultaneously occured at this point.

Figures 5.9a and 5.9b also show that for a constant value of the superficial gas velocity, the required liquid flow rate necessary to provoke flooding and/or slugging decreases by increasing the severity of the obstruction. As discussed in the previous section, the constructive interaction between the incident and the reflected waves depends on their amplitudes; thus, the greater the severity of the obstruction the higher will be the amplitude of the reflected waves. This may explain the fact that, for a constant superficial liquid velocity, the gas flow rate necessary (i.e., gas superficial velocity) to form the slugs decreases as the severity of the obstruction increases. The interaction between the incident and reflected waves maintains the formation of slugs over almost the entire partial liquid delivery region. Approaching zero liquid penetration conditions, the thickness of the liquid film is considerably reduced, diminishing the propagation of high amplitude waves up to a point where the formation of slugs completely disappears.

A comparison of Figures 5.9a and 5.9b shows that both the onset of flooding and the onset of slugging seem to be independent of the location of the orifice with respect to the elbow. Similarly to Siddiqui *et al.* (1986) and Kawaji *et al.* (1993), before flooding starts taking place, the formation of a hydraulic jump close to the

elbow has been observed. When the gas flow rate is subsequently increased, the hydraulic jump moves toward the elbow and flooding occurs immediately after the hydraulic jump disappears inside the elbow. Wan and Krishnan (1986) and Siddiqui *et al.* (1986), for low liquid flow rates in a horizontal test section, observed that flooding occurred when the hydraulic jump was dragged towards the elbow. Kawaji *et al.* (1991), however, observed that for moderate liquid flow rates, the location of the hydraulic jump moves towards the exit of the horizontal pipe, away from the elbow. Under such a condition, they observed that the flooding mechanism changes to slugging occuring close to the end of the horizontal pipe.

For the experiments carried out without an orifice installed in the horizontal leg a slight difference between flooding and slugging conditions is observed (see Figures 5.9a-b). Similarly to the experiments carried out with an orifice installed in the horizontal leg, the onset of flooding is accompanied by the formation of a pulsating column in the vertical leg. The waves produced by the pulsating column now travel downstream to the second elbow located close to the lower plenum (see Figure 3.2). Due to the distance that separates the two elbows, the reflected waves from the second elbow are in general of very low amplitude. Diminishing the amplitude of the incident and reflected waves prevents a constructive interference having the required amplitude for bridging the pipe to occur. By increasing the gas flow rate above that required to produce flooding, it is, however, observed that two different kinds of slugs start forming in the horizontal leg. The first kind are very short ones that form close to or even inside the first elbow. The second kind of slugs are very long (occupying almost 2/3 of the horizontal leg) and are formed immediately upstream of the second elbow (close to the lower plenum). Therefore, it is apparent that the hydrodynamic mechanisms that govern the formation of slugs when an orifice is installed in the horizontal leg are different than those when there is no orifice installed in the horizontal leg.

5.1.2 SLUG FREQUENCY

The slug frequency as a function of the gas and liquid superficial velocities is deter-

mined for each orifice size and position with respect to the elbow by post-processing the signals produced by the electrodes with the use of a FORTRAN program that allows Fast Fourier Transform (FFT) to be determined. The normalized spectra obtained after processing the signals are analyzed and the first highest peak encountered within each spectral record is considered as the predominant frequency of the slugs. It is important to remark that, for very low frequencies, the first peak obtained from the FFT also corresponded to the same frequency determined by timing the formation of the slugs using a chronometer.

Figures 5.10a-i show the best fits of the predominant slug frequency as a function of the superficial gas velocity. It should be noted that the experimental conditions and determined slug frequencies are also presented in Appendix B. In general, it is observed that for both positions and for all the orifices tested, the frequency decreases with increasing superficial gas velocity. It can also be seen that for a given superficial gas velocity and a given orifice β ratio, the slug frequency is much higher if an orifice is located closer to the elbow, for example Position 1 in Figure 3.2. Furthermore, the predominant slug frequency increases with decreasing orifice β ratios.

As discussed before, it was observed that the slugs are formed by a constructive interference between waves that propagate in opposite directions. Large amplitude waves are generated by a pulsating column that forms above the elbow after reaching the onset of flooding condition. These waves are partially reflected by the orifice; thus, the mutual interaction of the incident and the reflected waves brings about the bridging of the tube. This type of wave interaction can explain the fact that the predominant frequency decreases both with increasing superficial gas velocity and the size of the orifice. The increase in the superficial gas velocity increases the amount of entrained liquid, thus reducing the water level in the channel. In turn, the increase in the orifice size decreases the probability that the waves will be reflected. As the incident waves travel along the horizontal leg, their amplitude gradually decreases; thus, when the orifice is located farther away from the elbow, the probability of the incident and reflected waves to bridge the tube

decreases and results in a lower slugging frequency.

Figure 5.10i shows the predominant slug frequency for the experiments carried out without orifice ($\beta = 1.0$). Two different regions are distinguished in this figure. The first region, where most of the data are concentrated, shows a quite low frequency that decreases with increasing superficial gas velocity. These data points correspond to quite long slugs that form at the second elbow located closer to the lower plenum (see Figure 3.2). It is apparent that the slug frequencies in this region are coherent with those observed for the orifice having the highest β ratio (=0.83). The second region, characterized by a huge scattering in the data, corresponds to very short, high frequency, slugs that are formed closer to or even inside the first elbow (Figure 3.2). Most of these slugs were detected by one of the void probes that was kept at a constant and short distance from this elbow.

In the open literature, there is no available slug frequency data that have been collected for vertical-to-horizontal counter-current flow with orifices installed in the horizontal leg. Most of the existing studies are concerned with slugging in co-current two-phase flows. A comparison of the present data with those presented for co–current flows by Dukler and Hubbard (1975), for superficial gas velocities lower than 2 m/s, shows a similar trend, i.e., the slug frequency decreases with increasing superficial gas velocity. For superficial gas velocities higher than 2 m/s, however, their data shows that the slug frequency increases at a very low pace with increasing J_g. It is important to remark that the slug frequencies obtained during the present work are much lower than those obtained by Dukler and Hubbard. There are several reasons for this difference: Dukler and Hubbard used a much smaller tube ID, they applied much higher liquid flow rates and the experiments were carried out under co-current flow conditions. In a similar study, Jepson and Taylor (1993) have shown that increasing the tube inside diameter decreases the slug frequency, because a higher inside diameter decreases the probability of a wave to bridge the tube. Note that Jepson and Taylor carried out the experiments for co-current flows at a much higher superficial velocities than those used in the present work, i.e., $2 < J_g < 14\ m/s$.

5.1.3 AVERAGE VOID FRACTION

The average void fraction ($= \Delta V_g / \Delta V_{total}$) as a function of the gas and liquid superficial velocities is determined for each orifice size and position with respect to the elbow as follows: the signals produced by the electrodes are normalized and then the calibration curves given in Figure 3.5 are used to obtain void fraction values. These values are averaged in time. Figure 5.11a-i show the average void fraction as a function of the superficial gas velocity for all the cases studied. The same figure also shows the regression lines of the data. For all the cases studied, a single function having the form given by $a + b e^{-1.5}$, was used to fit the data. It should be also noted that the experimental conditions and the average void fraction are presented in Appendix C. Except for the experiments carried out without orifice (Figure 5.11i), it can be observed that for superficial gas velocities higher than 0.5 m/s an almost unique asymptotic value of the average void fraction close to 80% is reached. This asymptotic value seems to be independent of the size of the orifice and its position with respect to the elbow. This constant value can be explained by a complex relationship of slug frequency, slug length and slug void content. As a matter of fact, it has been observed that, for a given superficial gas velocity, the lower the β ratio the higher the slug frequency. In addition, orifices having small β ratios produce shorter slugs with a much higher void content. The relationship between these factors results in a time average void fraction which is almost constant for all the orifices tested during the present study. For superficial gas velocities lower than 0.5 m/s, it has been observed that both the frequency of the slugs and the length of the slugs increases. In general, very low superficial gas velocities correspond to quite high inlet liquid flow rates (Bédard, 1997) which in turn provoke the formation of quite long slugs. It must be pointed out that during this work the slug lengths were not measured; thus, the aforementioned analysis is based on visual observations of the phenomena (the experiments were recorded with a video camera that allowed us to view the experiments in slow motion reducing, in this way, any "subjective" appreciation of some of the features described in the thesis).

Figure 5.11i shows the average void fraction obtained for the experiments carried out without an orifice. In general, a huge scattering in the data is observed; the asymptotic value (if there is any) seems to be slightly higher than that observed for the experiments carried out with an orifice installed in the horizontal leg. The scattering in the data is due to the fact that, as has been mentioned before, two different types of slugs are formed when there is no orifice installed in the pipe: very long slugs generated closer to the second elbow and very fast shorter ones formed quite close to the first elbow. The fact that longer slugs trap more gas, i.e., more void content, may explain the higher average void fraction observed for this case (β=1.0). It is important to note that similar trends were observed by Wallis and Dobson (1973) and Woods and Hanratty (1996) who conducted the experiments in a 0.095 m ID, 26.5 m long pipe with air and water flowing co-currently. Moreover, Wallis and Dobson found that the void fraction was also independent of the liquid flow rate, and as has been observed in the present work.

5.1.4 SLUG PROPAGATION VELOCITY

As has been mentioned in the experimental conditions and procedures (Section 4.1), the slug propagation velocities were determined by cross-correlating the signals produced by the slug detection probes in conjunction with the distance between these probes. For the present experiments, three probes were placed at different locations between the elbow and the first flange used to install the orifice (Position 1 in Figure 3.2). Due to the extent of the slugs observed in some experiments and to the formation of a highly perturbed region close to the elbow in other experiments, the position of the probes with respect to the elbow, as well as the distances between the probes were not the same for all the experiments. The following distances between the probes were used during the experiments: 0.20, 0.35, and 0.40 m while the distance of the first probe to the elbow was maintained constant at 0.19 m. Due to the thickness of the probes (Teyssedou and Tye, 1999) it is quite difficult, if not impossible, to determine the effective distance between them. In all the cases, it has been considered that this distance cannot be determined with an accuracy better than a half of the thickness of a probe, i.e.,

12 *mm*.

The data on the slug propagation velocity as a function of the superficial gas velocity, β ratios, and liquid flow rates are shown in Figures 5.12a-c as well as are given in Appendix D in the form of tables. For the range of the experimental conditions, it is, in general, observed that the slug propagation velocity depends on neither the orifice's size nor the position of the orifice with respect to the elbow. It is also observed that the liquid flow rate does not affect the slug propagation velocity. Further, the slug propagation velocity decreases, almost linearly, with the superficial gas velocity and this trend can be shown with a simple best fit of the data by using a simple linear regression curve given by $V_s = 0.821 - 0.151\, J_g$. It is important to mention that this regression is valid for the experimental data obtained with an orifice installed in the horizontal leg at both locations.

A balance of pressure forces (assuming that frictional forces between the slug and the pipe are much smaller than the pressure forces, the frictional forces between the slug and the pipe are neglected) shows that the driving force that keeps the slug moving is a function of the pressure difference between the slug head and tail (see Figure 5.13). . Assuming the atmospheric pressure P_{atm} (considered as constant) acts on the slug head, then the slug movement must be controlled by the effective pressure exerted by the air on its tail, P_g. In turn, this pressure is equal to the gas pressure at the lower plenum (see Figure 3.2) minus the pressure drop essentially due to the interfacial drag at the liquid-gas interface. At this point, it is important to consider the fact that during the whole slugging process, a non negligible amount of liquid is still delivered (the region before reaching the zero liquid penetration point in Figure 5.1). This liquid flows downstream towards the lower plenum, passing through the orifice which fixes its height in this region, i.e., liquid content in the slug tail. Furthermore, in the slug tail region, the interfacial friction depends on the relative velocity of the two phases flowing counter-currently. Data collected by Bédard (1997) for the entire partial liquid delivery region up to the zero liquid penetration point, was used to evaluate the product of the interfacial area per unit length and the square of the relative velocities between the phases; the results are

shown in Figures 5.14a,b. It is apparent that this product, which should control the interfacial drag and consequently the driving force applied to the slug, increases with increasing superficial gas velocity. Orifices having β ratios of 0.66, 0.72, and 0.77 are characterized by almost the same interfacial drag. However, for $\beta = 0.83$, a substantial difference is observed for superficial gas velocities lower than 1.5 m/s. There are two possible reasons for this departure. First, it is important to mention that these conditions (i.e., higher β ratios and low gas flow rates) correspond to the highest inlet liquid flow rates applied during the experiments; thus, the delivered liquid flow rate was much higher and consequently the collection method used was less accurate. Even though a systematic error introduced in the liquid collection procedure can explain the jump observed for a superficial gas velocity close to 1.5 m/s, it cannot entirely explain the results presented in Figure 5.14a-b. It is important to mention that the interfacial area per unit length (A in Figures 5.14a-b) as well as the cross-sectional areas occupied by the phases are calculated based on the liquid height that corresponds to the minimum value required for a given orifice to allow the liquid to pass trough. For higher β ratios, however, the interfacial area calculated in this way as well as the cross-sectional area occupied by each phase becomes unrealistic; thus, the results presented in Figure 5.14 must be considered only as qualitative. As has already been mentioned, due to the fact that the amount of delivered liquid greatly increases with decreasing gas flow rate (Bédard, 1997), the results shown in Figure 5.14 can be affected by the precision of the measurements carried out under such flow conditions. In general, Figure 5.14 can be used to show the fact that the drag force exerted by the liquid on the gas phase in the slug tail region, increases with increasing superficial gas velocity. Consequently, increasing the superficial gas velocity, increases the interfacial friction pressure losses, that in turn reduces the effective driving force applied to the slug. The same figure also shows that the interfacial drag force seems to be almost independent of the orifice size and its position in the horizontal leg. This observation can be used to explain the fact that for a given superficial gas velocity a unique slug propagation velocity, independent of the orifice size and position, is observed in Figure 5.12. In addition, an increase in the gas pressure loss reduces the driving force acting on the slug; thus, the slug propagation velocity

must decrease with increasing superficial gas velocity as shown in Figure 5.12. It is important to mention that similar trends were observed by Jepson and Taylor (1993) for higher superficial gas velocities in co-current two-phase flows.

In Figure 5.12c, it is interesting to observe two different regions of slug propagation velocity, as it was observed for the predominant frequency for the experiments without obstruction. As discussed in Section 5.1.2, the formation of two types of slug observed for experiments carried out without an orifice ($\beta = 1.00$) conjunction with the drag force in the slug tail zone can be used explain the phenomena in this region.

5.2 WAVE PROPAGATION EXPERIMENTS WITHOUT SLUGGING

Wave propagation experiments were carried out without any obstructions installed in the horizontal leg. These experiments were devoted in obtaining the profile of incidents waves. These profiles are required as initial conditions for the model that is presented in Chapter 7. For a given liquid flow rate, the gas flow rate is slowly increased close to the onset of flooding conditions, *by taking care that flooding does not occur.* These flow conditions, i.e., inlet and gas flow rates (for flow conditions, see Section 4.2.1 and Table 4.1), are then kept constant while a sequence of video films of the flow are collected. The details of the experimental conditions and procedures were presented in Section 4.2. After filming each experiment, the images were transfered to the computer. A MATLAB edge detection macro and a program written in MATLAB were used to detect the wave amplitudes. The MATLAB programs are given in Appendix E. As explained in Section 4.2.2, the Sobel edge detection technique was considered to be the most appropriate. Since the macro of this edge detection technique can be found in the MATLAB package, it is not given in Appendix E.

Figure 5.15 shows the comparison of several edge detection methods, i.e.; Sobel, Prewitt, Roberts, Laplacian, Zero-Crossing and Canny. The Sobel, Prewitt, Roberts and Canny edge detection techniques obtain the edges at those points where the gradient of the image is maximum. The Laplacian and Zero-Crossing

methods find edges by looking for zero-crossings after the filteration of the image.

Figures 5.16 – 5.19 show the comparison of typical edge detection results with the photographic image of the flow that corresponds to the same image frame used to determine the wave profile. The corresponding experimental conditions are given in the figures. The length of the edge detection region is 63.5 cm, and it corresponds to the distance between the labels across which the edge detection technique was applied. This distance corresponds to the length that can be captured by the video camera without introducing any noticeable deformation to the image; otherwise, the aspect ratio of the image started to be altered. It is interesting to see the performance of the edge detection. These figures are taken as a basis for providing the initial conditions to the model which will be presented in the next chapter.

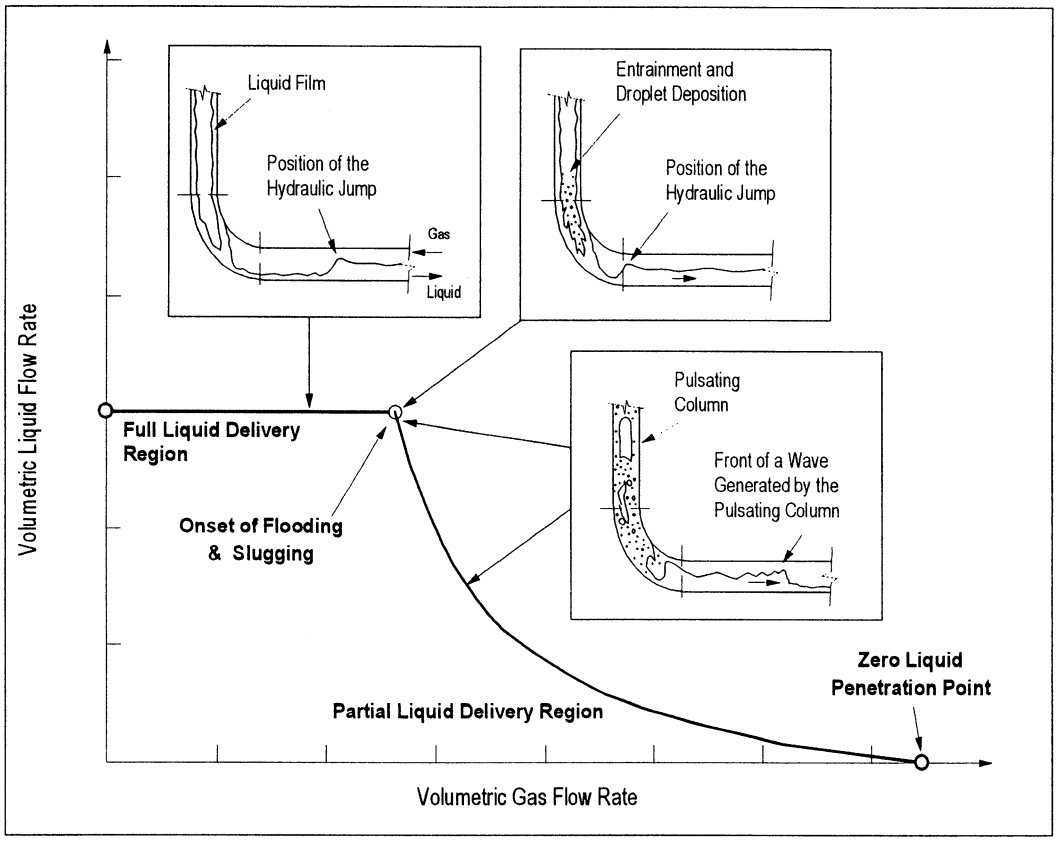

Figure 5.1: Phenomenological results.

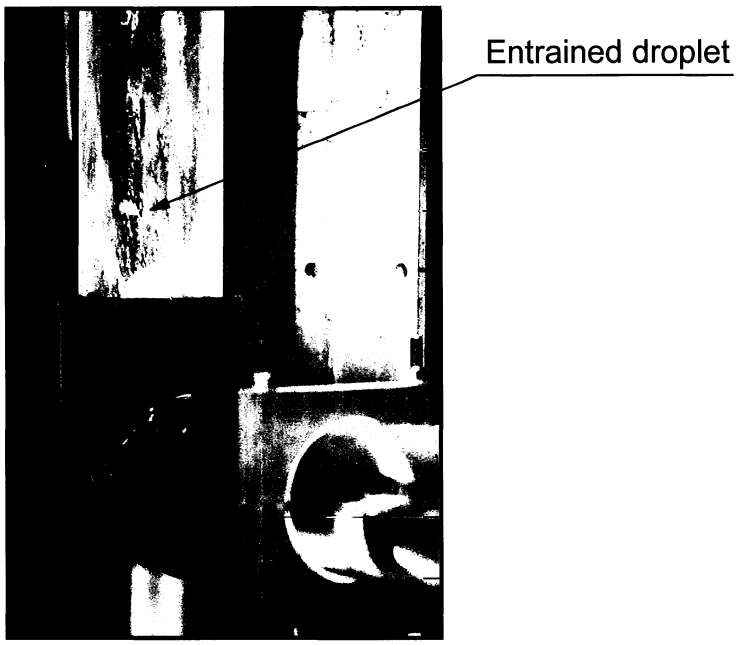

Figure 5.2: Onset of entrainment above the elbow (Tye, 1998).

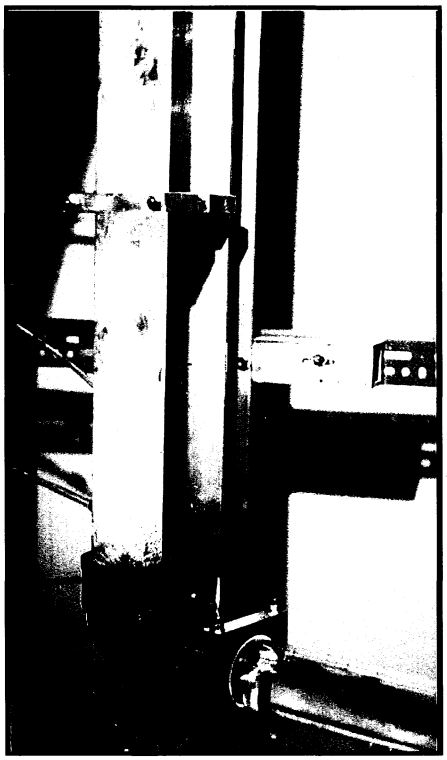

Figure 5.3: Pulsating column in the vertical leg (Tye, 1998).

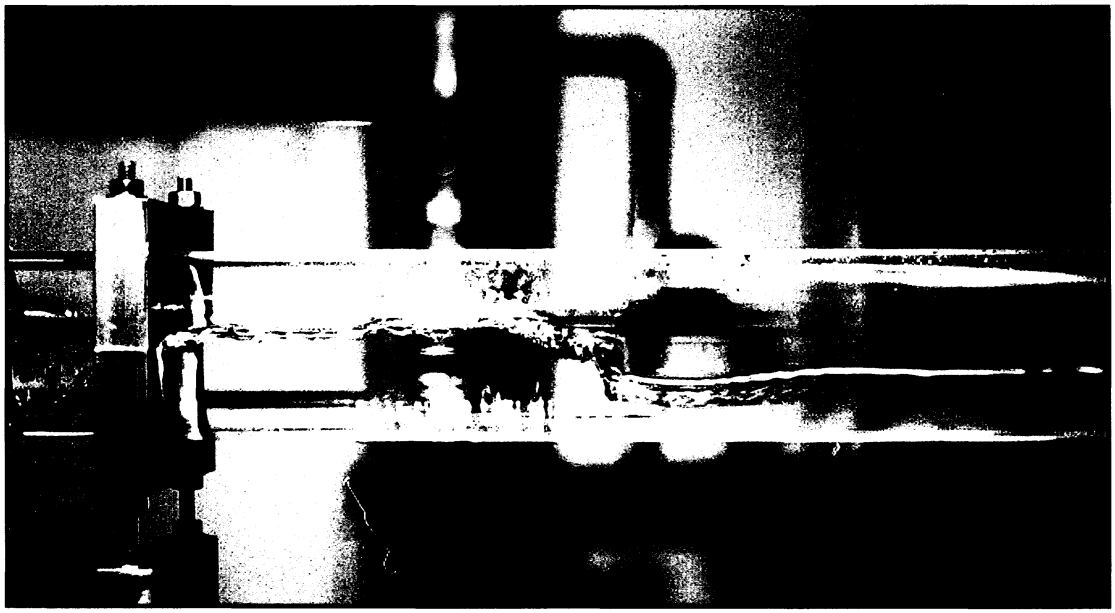

Figure 5.4: Wave formed by the pulsating column (Tye, 1998).

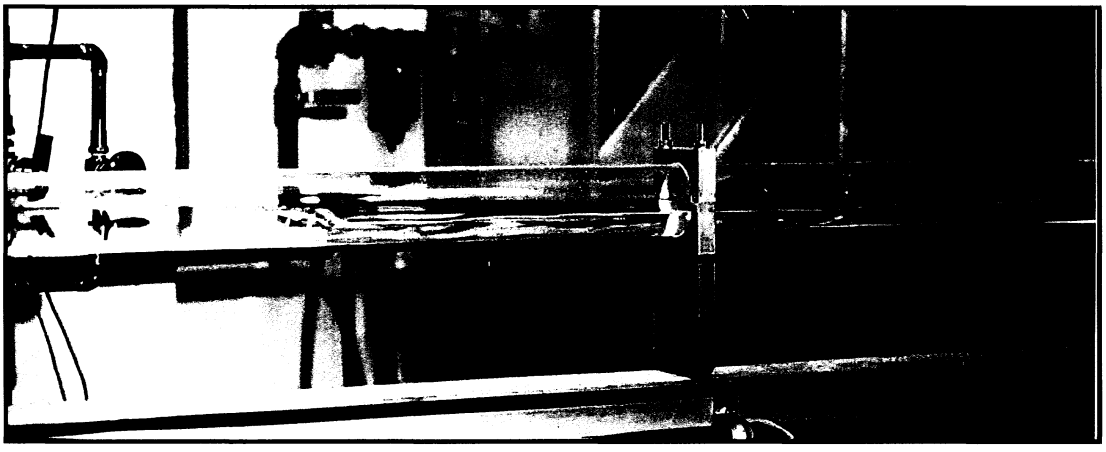

Figure 5.5: Wave formed by the pulsating column traveling towards the orifice (Tye, 1998).

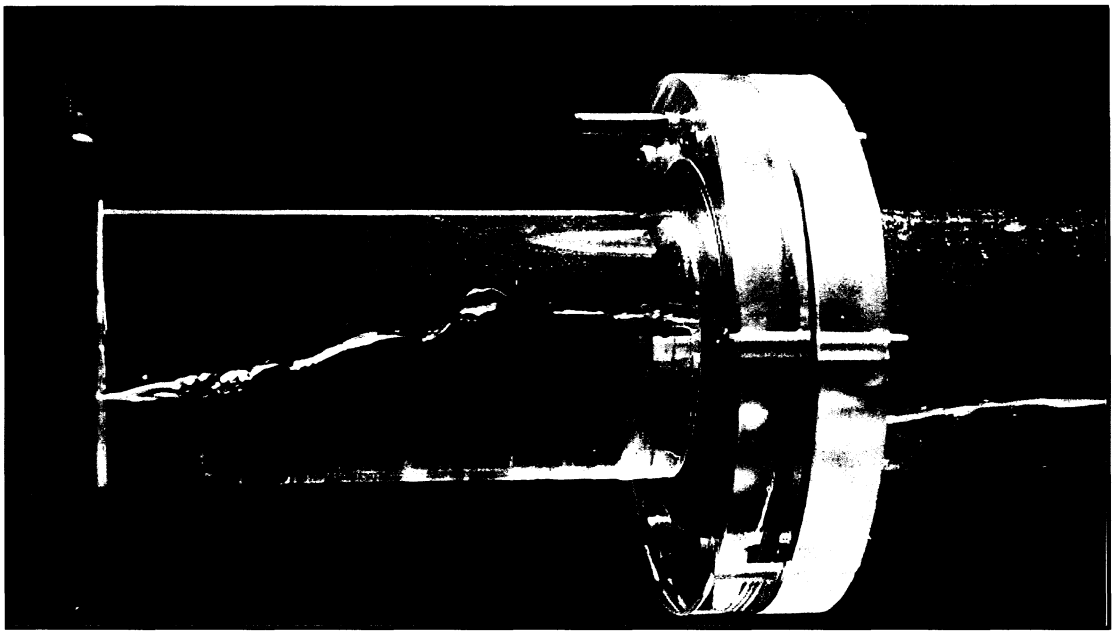

Figure 5.6: Wave reflected from the orifice (Tye, 1998).

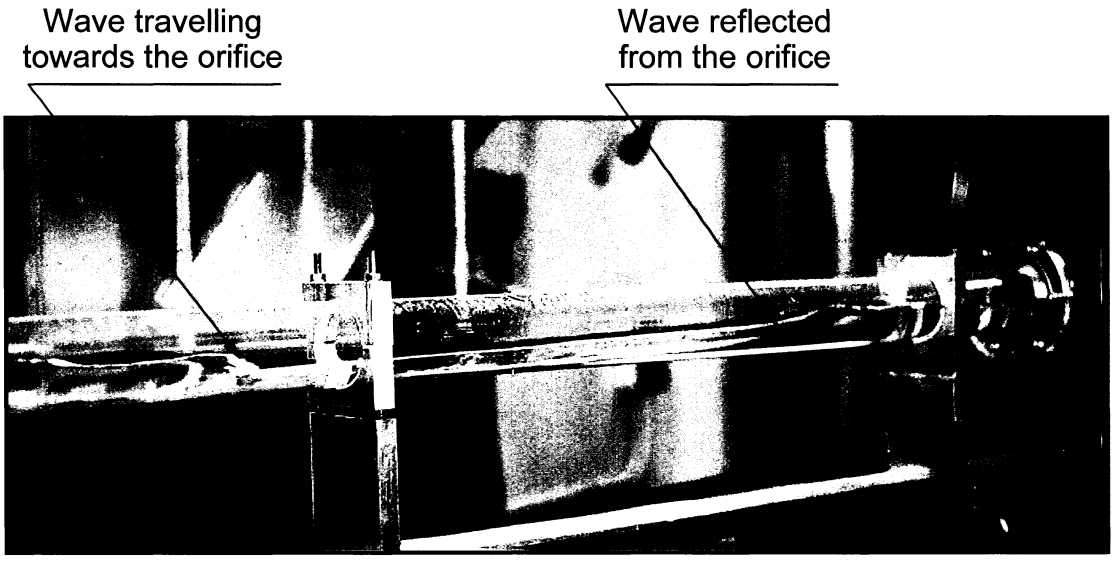

Figure 5.7: Wave travelling towards the orifice and wave reflected from the orifice (Tye, 1998).

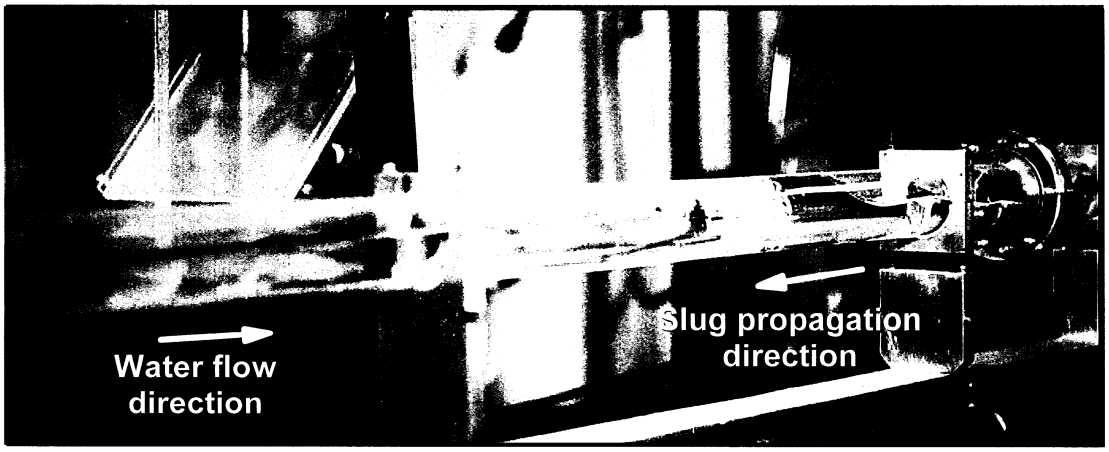

Figure 5.8: Liquid slug formed in the horizontal leg (Tye, 1998).

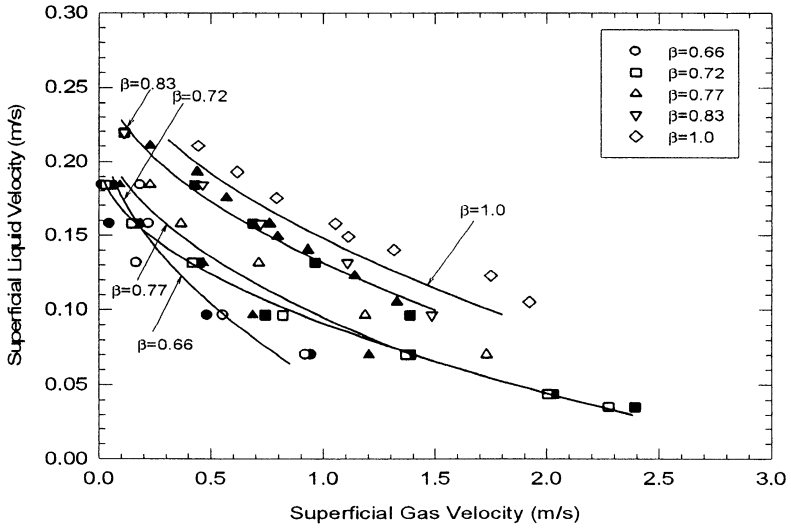

Figure 5.9a: j_l vs. j_g at the onset of flooding and at the onset of slugging presented by solid and empty symbols, respectively, Position 1.

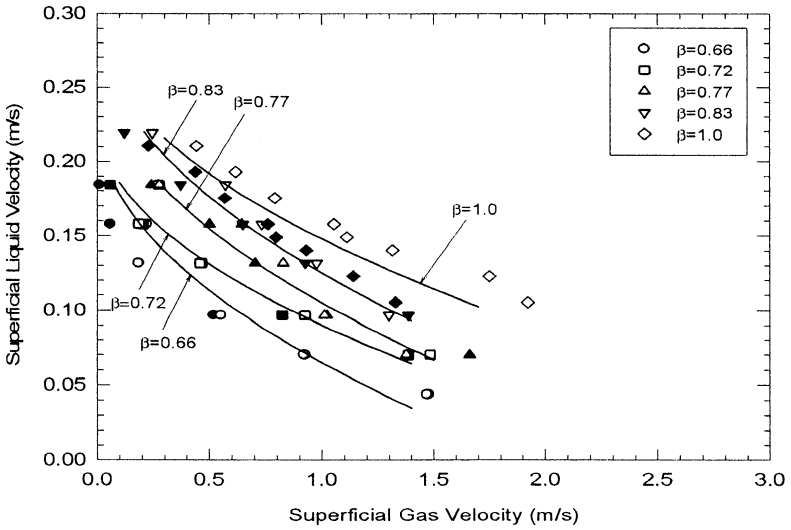

Figure 5.9b: j_l vs. j_g at the onset of flooding and at the onset of slugging presented by solid and empty symbols, respectively, Position 2.

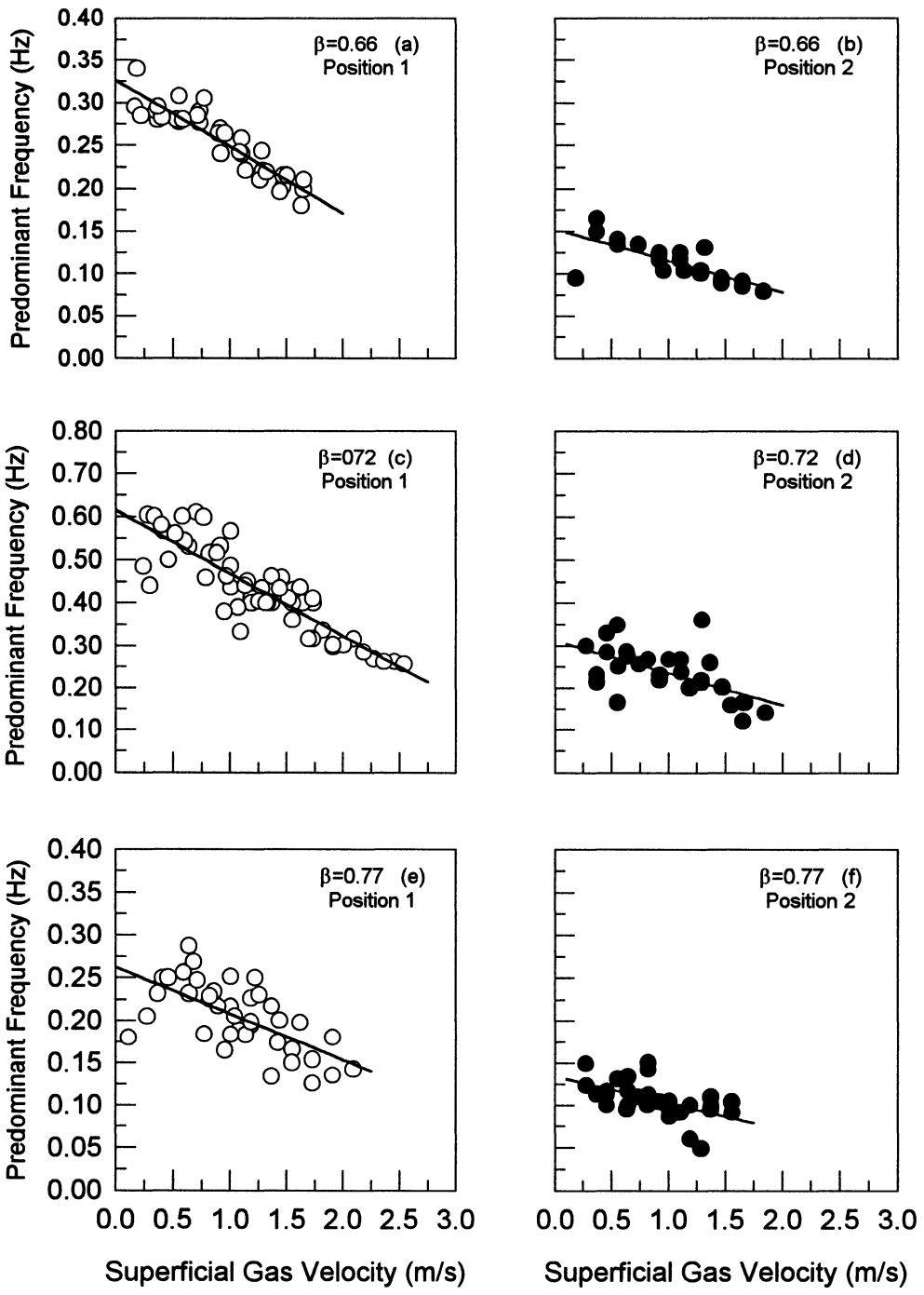

Figure 5.10.a-f: Predominant slug frequency vs. superficial gas velocity.

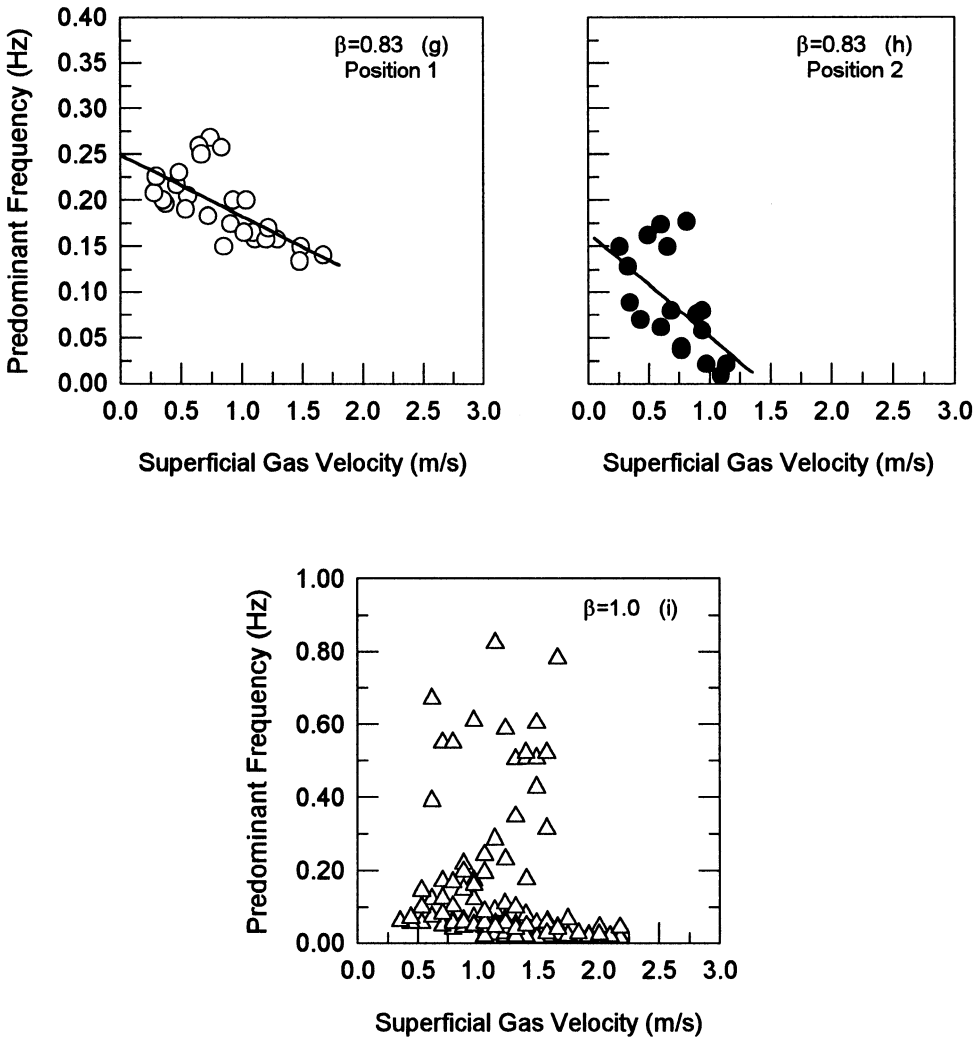

Figure 5.10.g-i: Predominant slug frequency vs. superficial gas velocity.

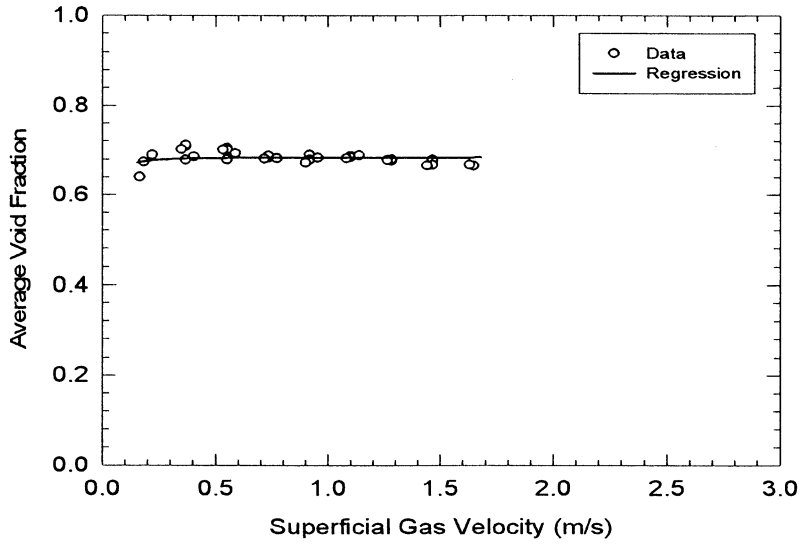

Figure 5.11a: Average void fraction vs. superficial gas velocity, for $\beta = 0.66$, Position 1.

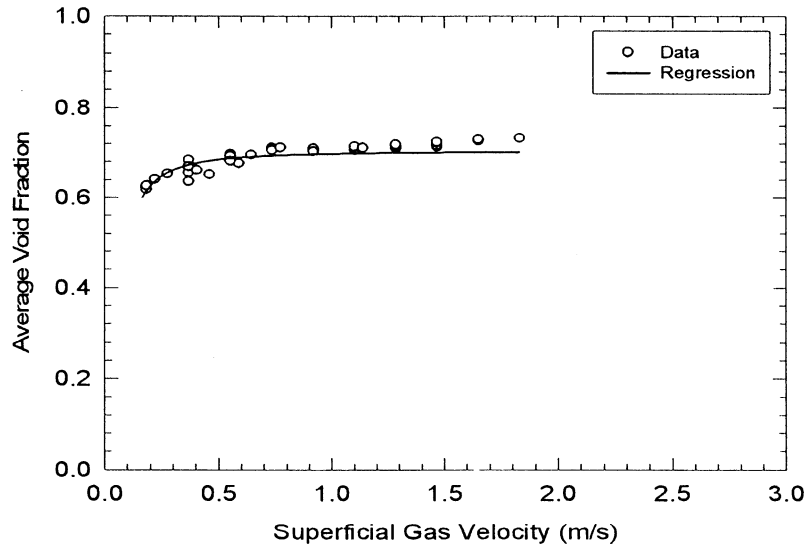

Figure 5.11b: Average void fraction vs. superficial gas velocity, for $\beta = 0.66$, Position 2.

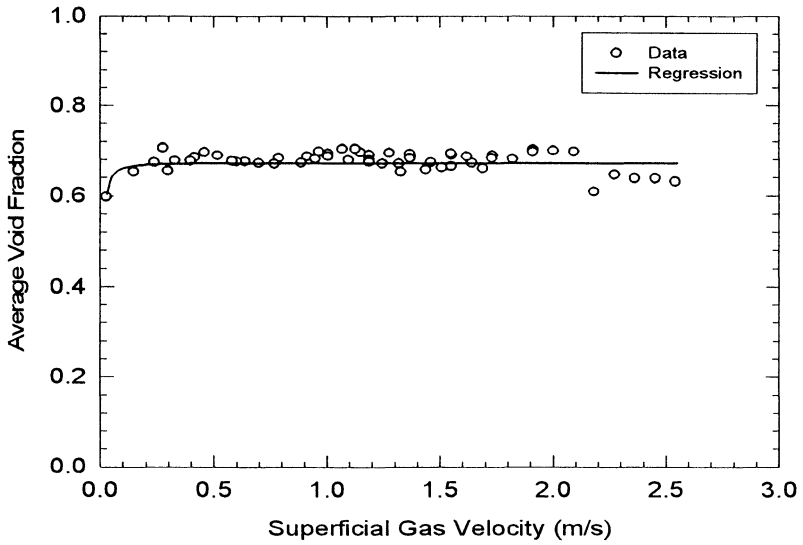

Figure 5.11c: Average void fraction vs. superficial gas velocity, for $\beta = 0.72$, Position 1.

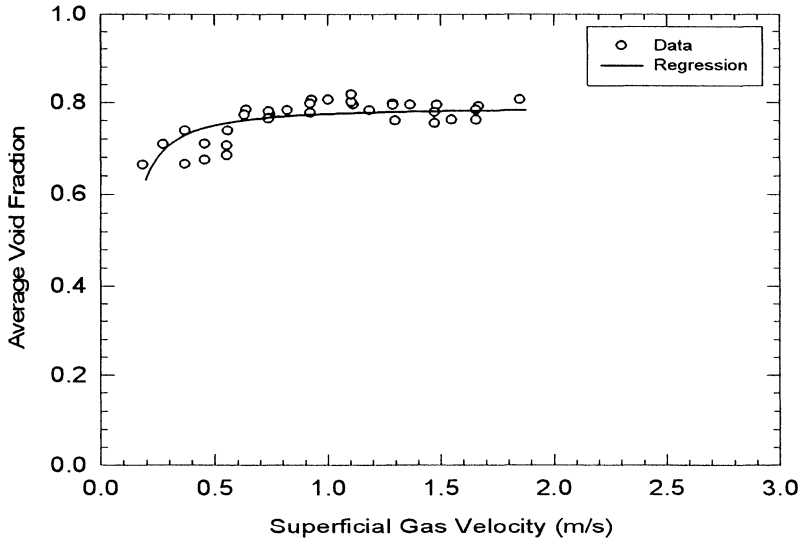

Figure 5.11d: Average void fraction vs. superficial gas velocity, for $\beta = 0.72$, Position 2.

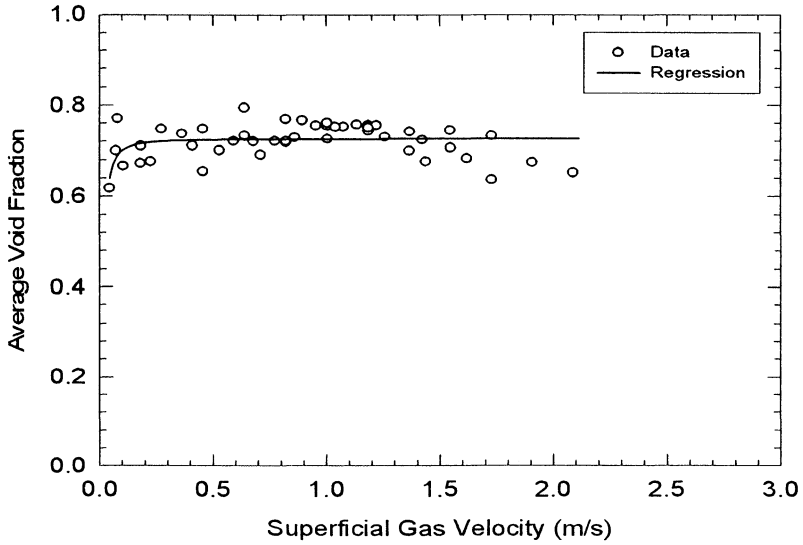

Figure 5.11e: Average void fraction vs. superficial gas velocity, for $\beta = 0.77$, Position 1.

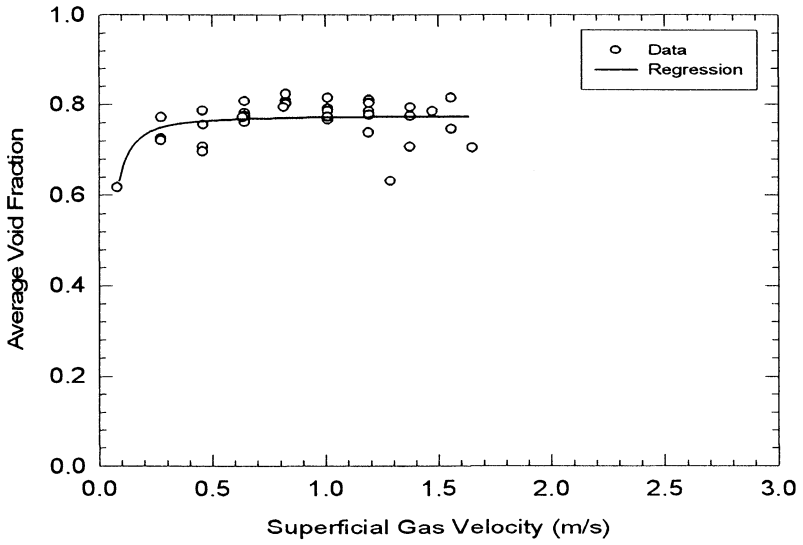

Figure 5.11f: Average void fraction vs. superficial gas velocity, for $\beta = 0.77$, Position 2.

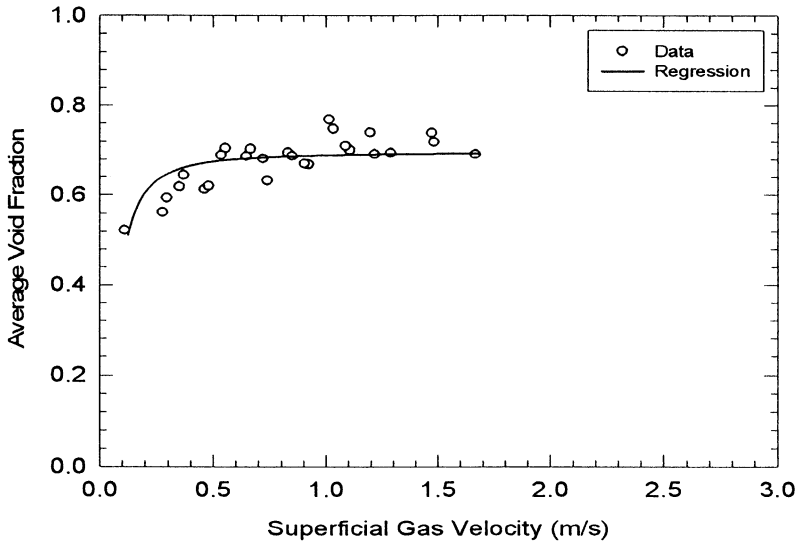

Figure 5.11g: Average void fraction vs. superficial gas velocity, for $\beta = 0.83$, Position 1.

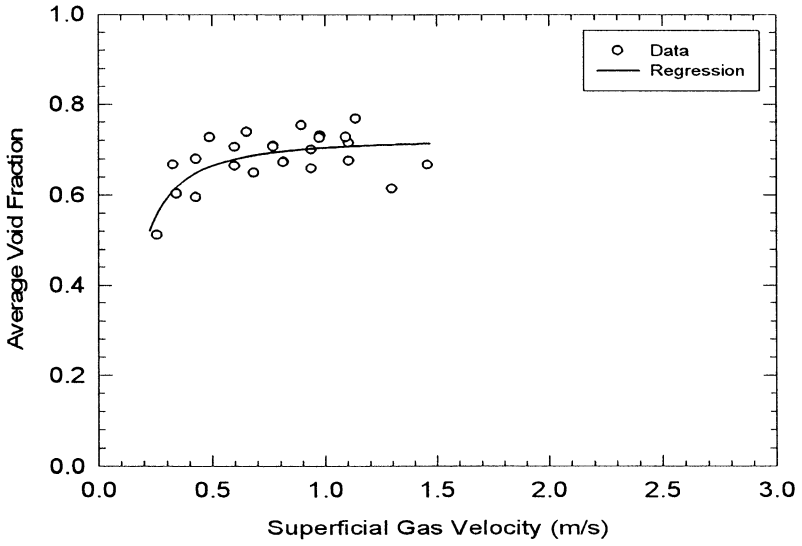

Figure 5.11h: Average void fraction vs. superficial gas velocity, for $\beta = 0.83$, Position 2.

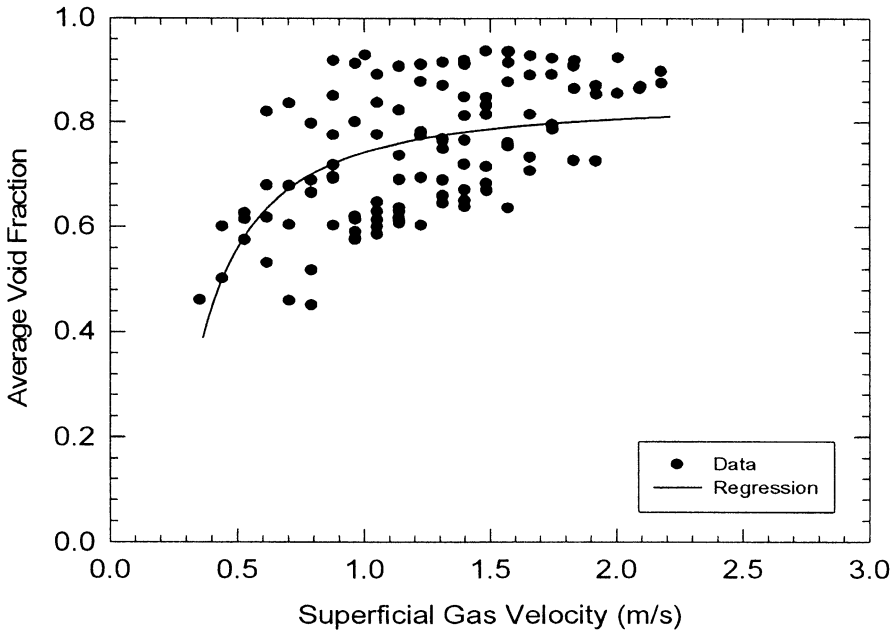

Figure 5.11i: Average void fraction vs. superficial gas velocity, for $\beta = 1.00$.

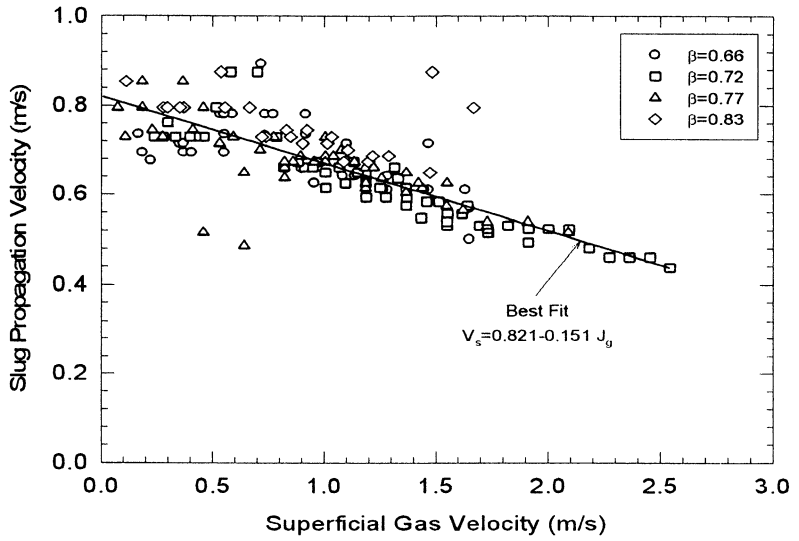

Figure 5.12a: Slug propagation velocity vs. superficial gas velocity, Position 1.

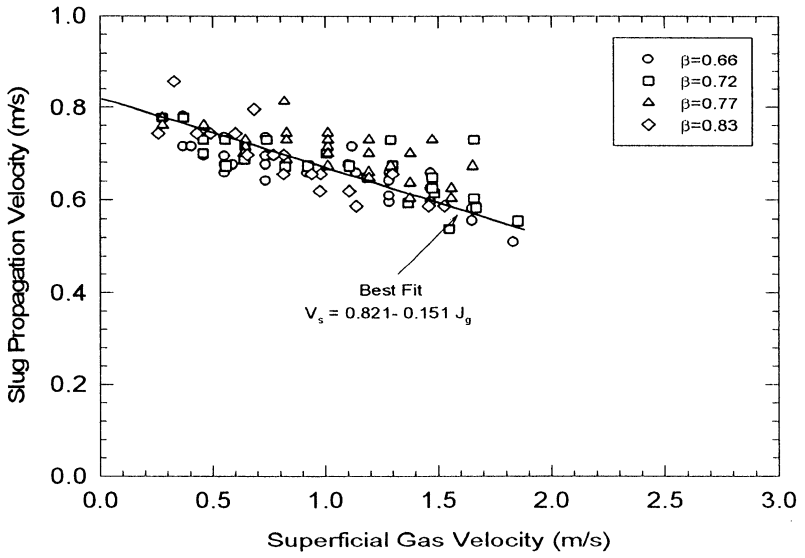

Figure 5.12b: Slug propagation velocity vs. superficial gas velocity, Position 2.

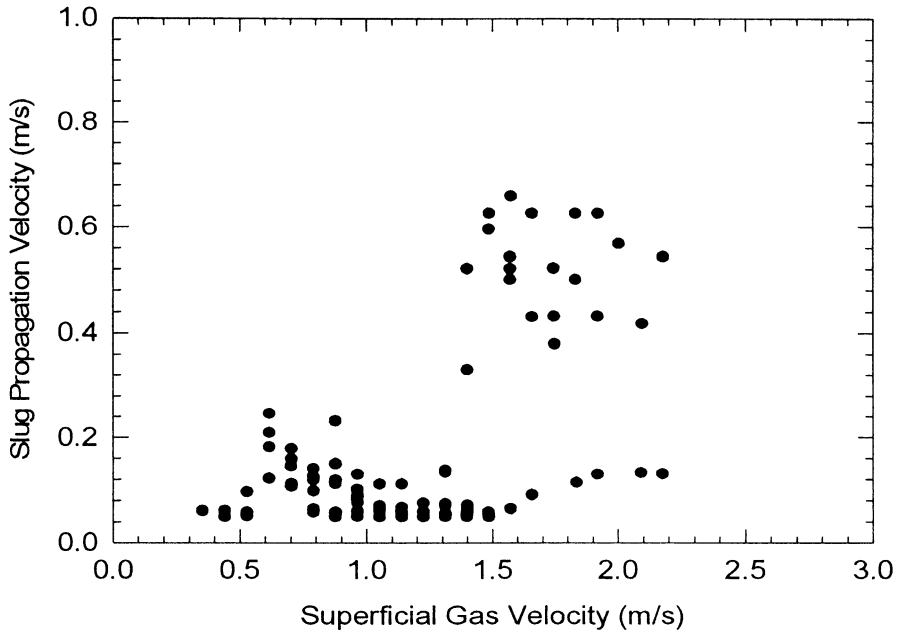

Figure 5.12c: Slug propagation velocity vs. superficial gas velocity, for $\beta = 1.00$.

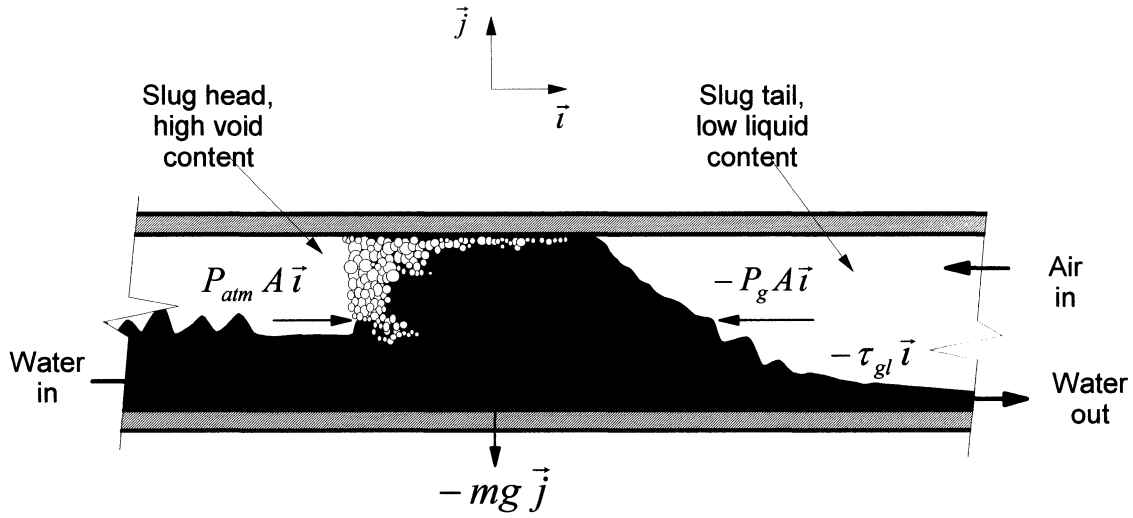

Figure 5.13: Forces acting on a liquid slug.

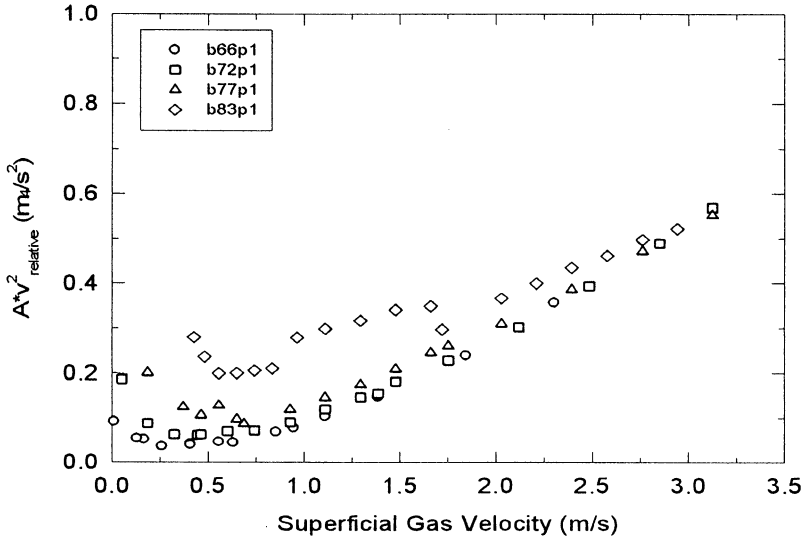

Figure 5.14a Interfacial drag term for Position 1.

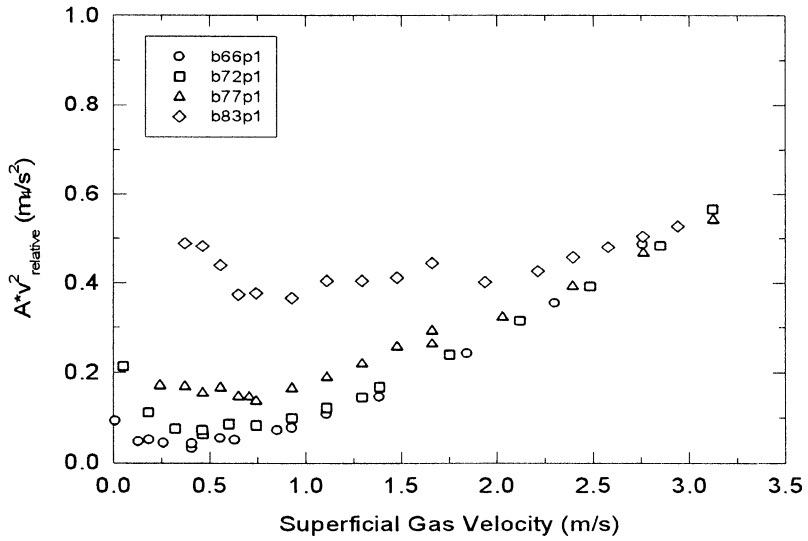

Figure 5.14b Interfacial drag term for Position 2.

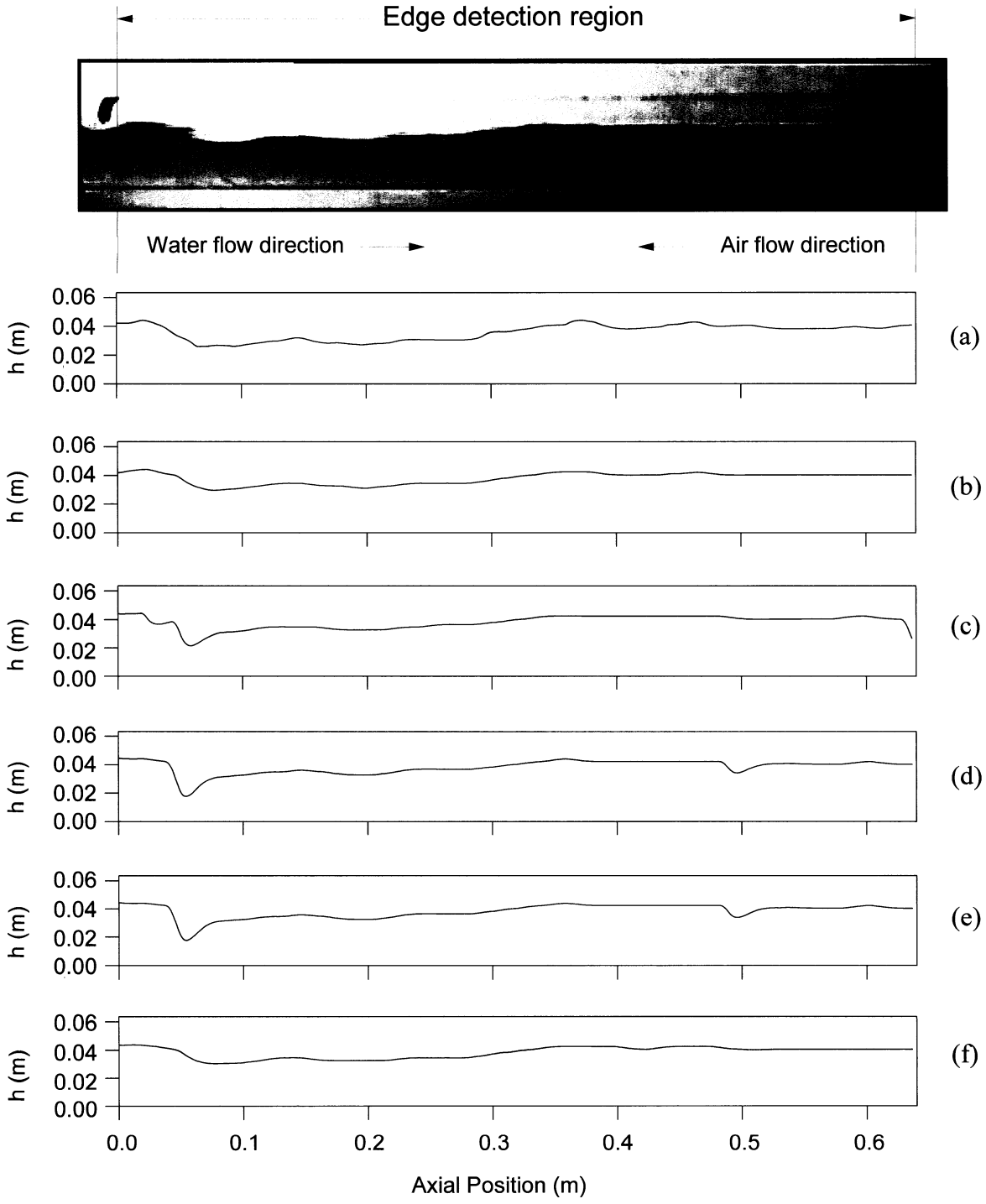

Figure 5.15: Comparison of edge detection methods: (Sobel (a), Prewitt (b), Roberts (c), (Laplacian (d), Zero-cross (e), Canny (f)).

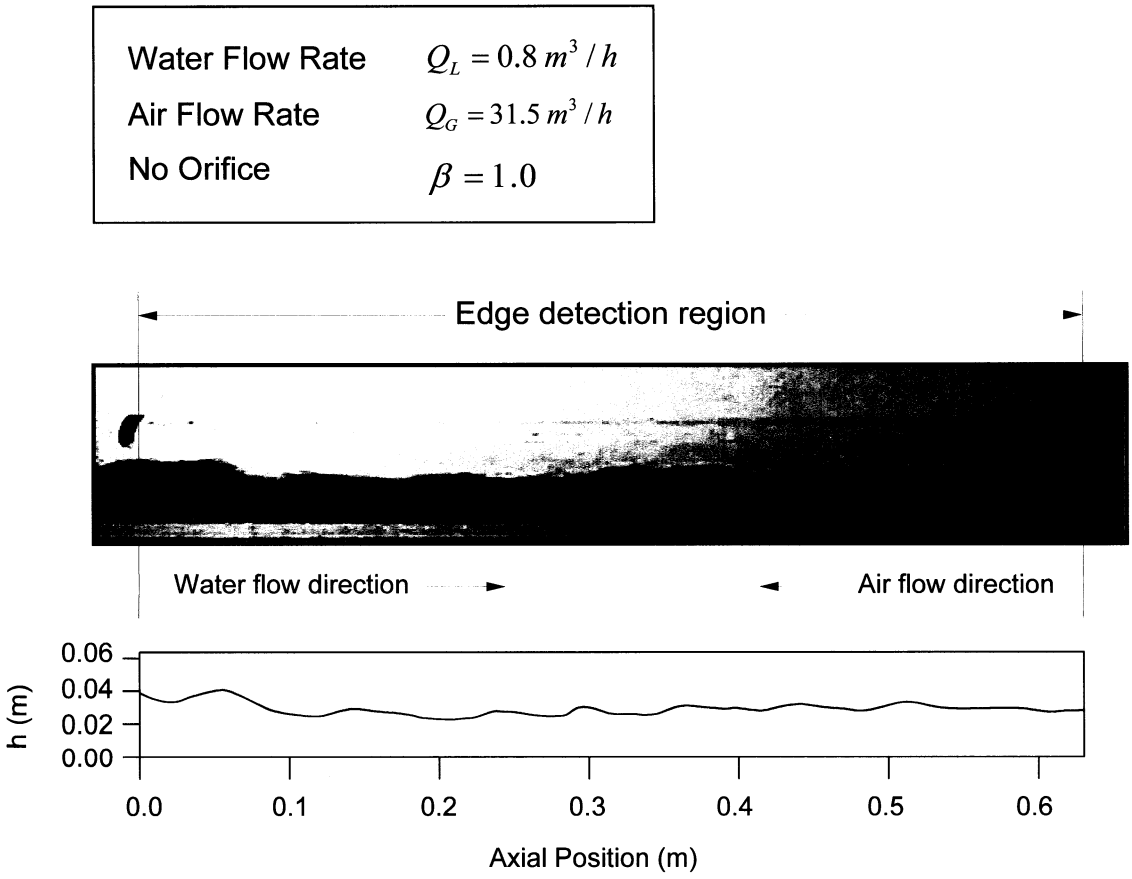

Figure 5.16: Comparison of a frame with the output of Sobel's edge detection method.

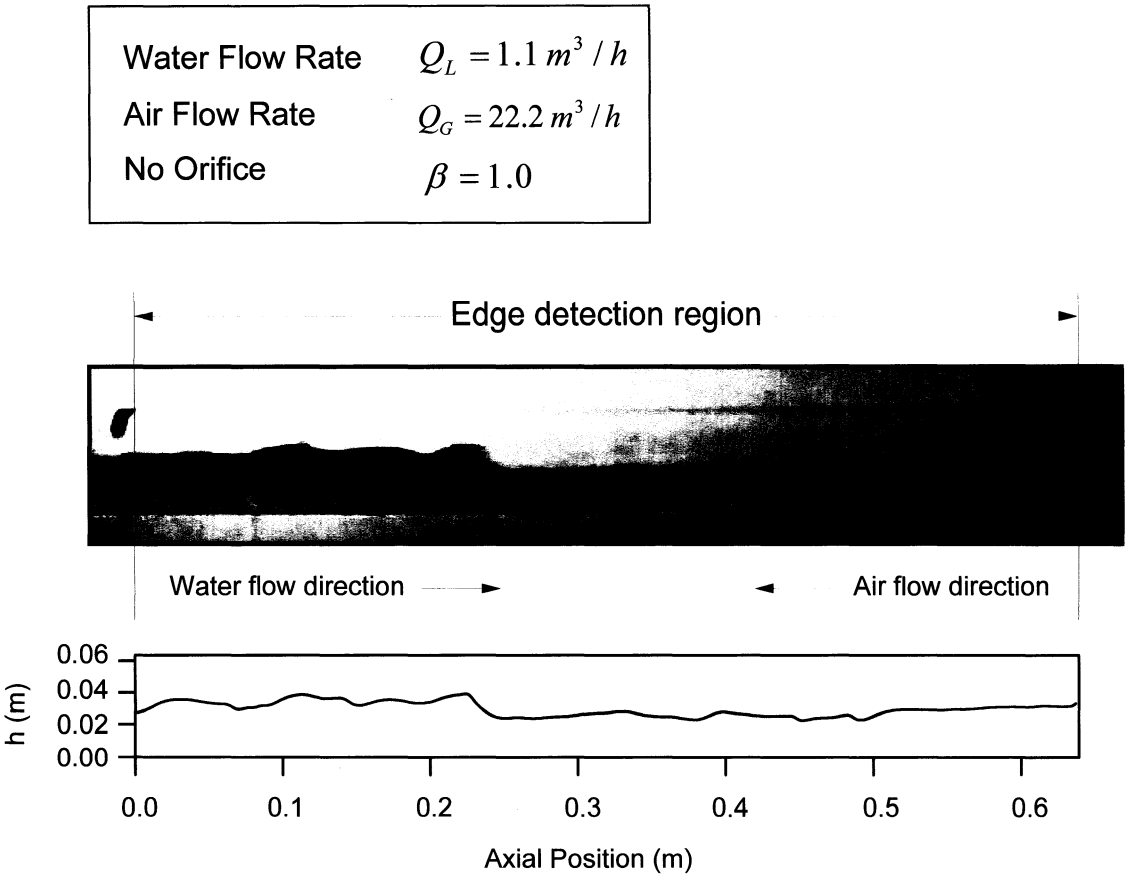

Figure 5.17: Comparison of a frame with the output of Sobel's edge detection method.

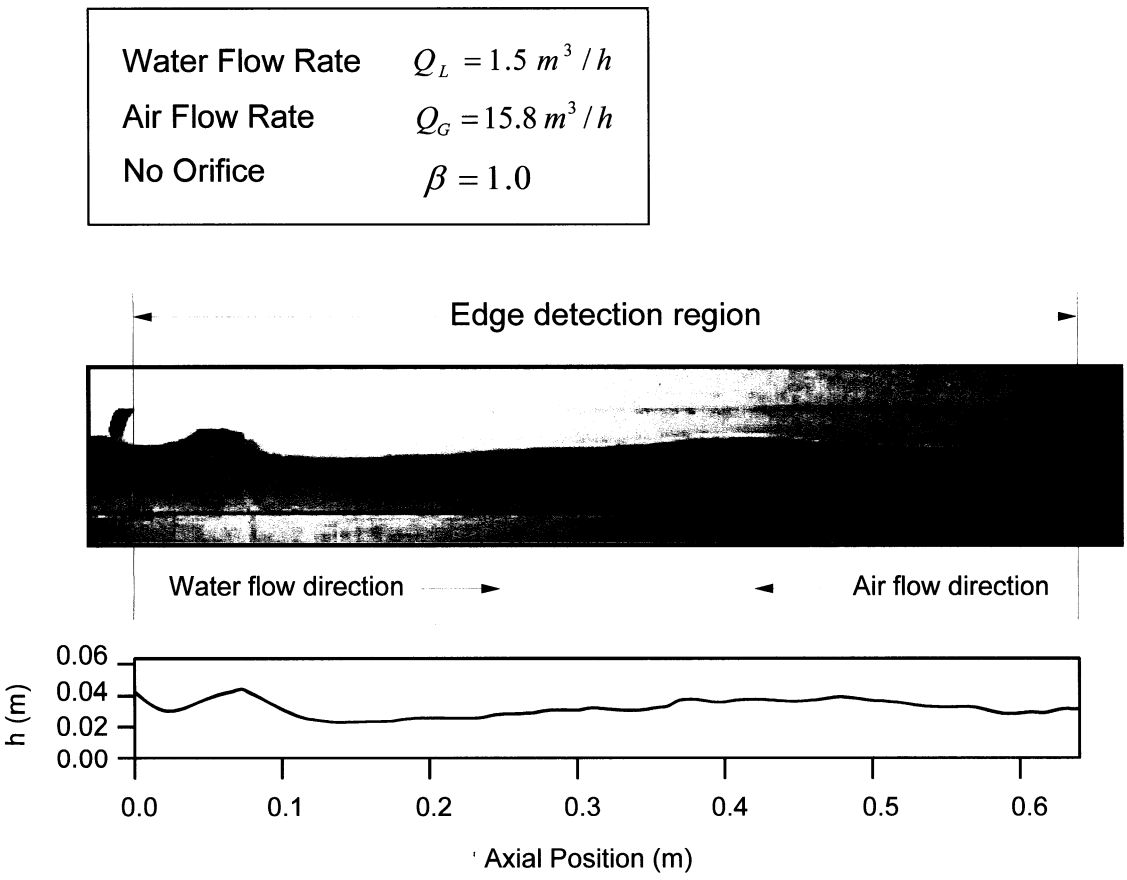

Figure 5.18: Comparison of a frame with the output of Sobel's edge detection method.

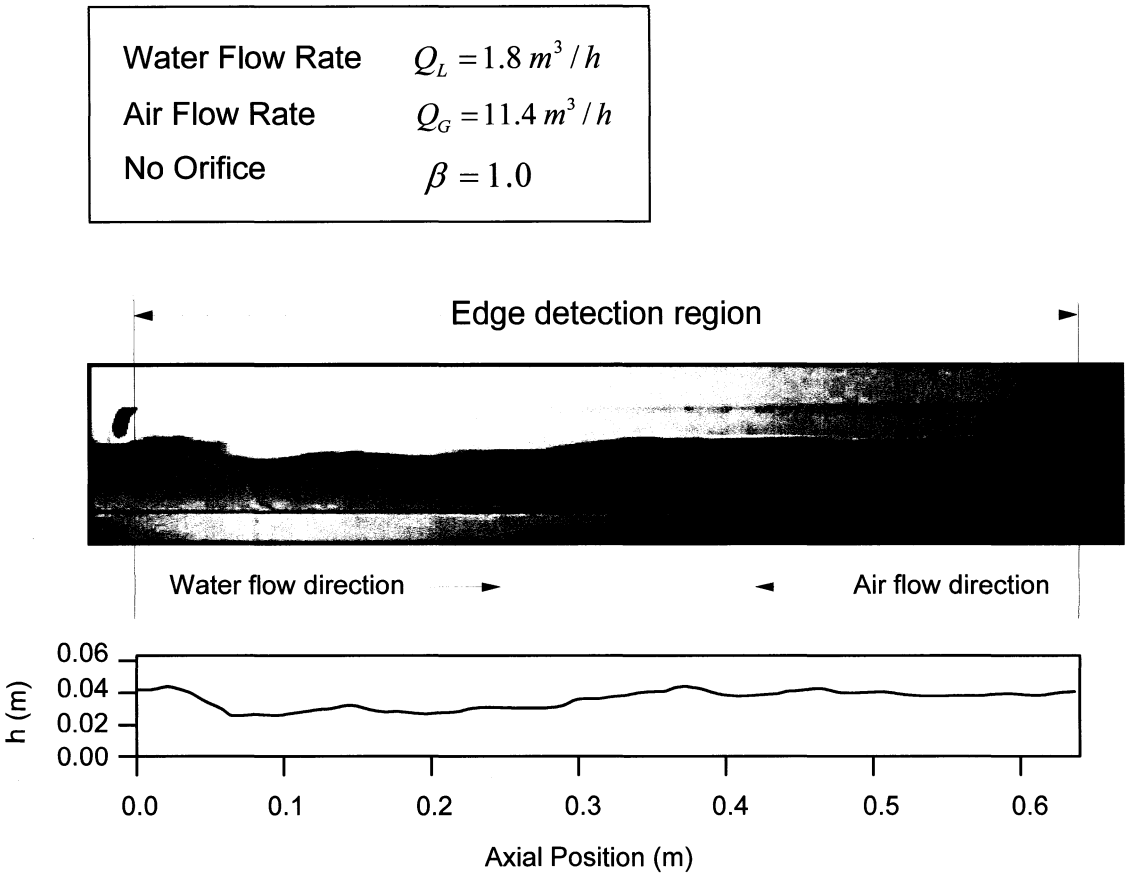

Figure 5.19: Comparison of a frame with the output of Sobel's edge detection method.

CHAPTER 6

THE THEORY BEHIND THE MODEL

In this chapter, several water wave theories will be discussed in order to enlighten the basic concepts of the model which will be presented in Chapter 7. The water waves can be divided into two categories: hyperbolic and dispersive. In the first section of this chapter, hyperbolic waves without making any distinction of linearity and nonlinearity will be discussed. In the second section, the dispersive waves which give birth to solitons will be presented; these theoretical aspects are important for the model developed during this research.

6.1 HYPERBOLIC WAVES

Hyperbolic waves are formulated mathematically in terms of partial differential equations. The equations used to describe this type of waves depend only on the form of the equations, independently, whether explicit solutions can be obtained. In this group, dissipative type of waves can also be found. Since the dissipation arises from a physical system that incoparates some frictional behaviour, such as fluid viscosity, dissipative term will be discussed in the next section after presenting the momentum equation.

A prototype for hyperbolic waves is often taken to be the wave equation given by:

$$\frac{\partial^2 \varphi}{\partial t^2} = c_0^2 \nabla^2 \varphi, \tag{6.1}$$

with

$$\nabla^2 = \frac{\partial^2}{\partial x^2} + \frac{\partial^2}{\partial y^2} + \frac{\partial^2}{\partial z^2}.$$

If the waves propagate along x axis, we can write

$$\frac{\partial \varphi}{\partial t} - c_0 \frac{\partial \varphi}{\partial x} = 0, \tag{6.2a}$$

$$\frac{\partial \varphi}{\partial t} + c_0 \frac{\partial \varphi}{\partial x} = 0. \tag{6.2b}$$

Under this classification of hyperbolic waves, one can also identify linear and nonlinear waves. Since the hyperbolic waves are not relevant to this study, the linear and nonlinear hyperbolic waves will not be discussed in too much detail. Nevertheless, in the following sections, the equations that describe hyperbolic waves will be discussed. In general, these are the equations of hydrodynamics: the continuity equation, the momentum equation, and the energy equation. Depending on the cases studied, these equations are used in combination of two or three.

6.1.1 THE CONTINUITY EQUATION

The continuity principle, known as well as the mass conservation equation, expresses the conservation of matter, i.e., fluid matter in a given space cannot be created or destroyed. In the case of an incompressible homogeneous fluid, the continuity principle can also be expressed by the conservation of volume.

The mass conservation equation gives a relationship between the velocity ($\mathbf{u}$), the density (ρ), the space coordinates (x, y, z) and time (t). Thus, the continuity equation can be written in the differential form as:

$$\frac{\partial \rho}{\partial t} + \nabla \cdot (\rho \mathbf{u}) = 0. \tag{6.3}$$

If the choice of coordinates is the right-handed rectangular Cartesian system, the nabla operator and the fluid velocity can be expressed in the following form:

$$\nabla = \left(\frac{\partial}{\partial x}, \frac{\partial}{\partial y}, \frac{\partial}{\partial z} \right),$$

$$\mathbf{u} \equiv (u, v, w).$$

6.1.2 THE MOMENTUM CONSERVATION EQUATION

The momentum principle expresses the relationship between the applied forces ($\mathbf{F}$) on a unit volume of matter of density ρ and the inertia forces of this unit volume of matter, as it is given by Newton's Second Law. The *inertia forces* are due to the natural tendency of bodies to resist any change in their motion. On the other hand, we can distinguish two types of applied forces in fluid mechanics: *body forces*, which are more or less the same for all fluid particles and have their source exterior to the fluid, and *local forces*, which are the forces exerted on a fluid element by other nearby fluid elements.

To cause the motion of a constant mass m, or more generally, to change the state of an existing motion, it is necessary to apply to this mass a force ($\mathbf{F}$), which causes an acceleration $d\mathbf{u}/dt$ such that $\mathbf{F} = m(d\mathbf{u}/dt)$. Here, the mass ($m$) corresponds to that of a unit of volume of fluid; therefore, $m \equiv \rho$. Hence, the fundamental equation of momentum has the form $\mathbf{F} = \rho(d\mathbf{u}/dt)$. The three components along the three coordinate axes x, y, z are $\rho(du/dt)$, $\rho(dv/dt)$, $\rho(dw/dt)$, respectively. Two types of inertia forces may be distinguished, depending on the type of acceleration or elementary motion considered: (1) *local acceleration* which corresponds to a variation of the translation velocity or the derivative of velocity with respect to time and (2) *convective acceleration* which corresponds to a variation of velocity associated to the deformation and rotation of a fluid particle, i.e., derivative of velocity with respect to space. The local acceleration characterizes any unsteady motion resulting from a change in the translatory motion of a fluid particle imposed by external forces $\mathbf{F}$, whereas the convective acceleration characterizes any nonuniform flow resulting from any linear or angular deformation, or from a change in the rotation of fluid particles, imposed by the external forces $\mathbf{F}$. The components of the acceleration term can be given by:

$$\rho\left(\frac{\partial u}{\partial t} + u\frac{\partial u}{\partial x} + v\frac{\partial u}{\partial y} + w\frac{\partial u}{\partial z}\right),$$

$$\rho\left(\frac{\partial v}{\partial t} + u\frac{\partial v}{\partial x} + v\frac{\partial v}{\partial y} + w\frac{\partial v}{\partial z}\right),$$

$$\rho\left(\frac{\partial w}{\partial t}+u\frac{\partial w}{\partial x}+v\frac{\partial w}{\partial y}+w\frac{\partial w}{\partial z}\right). \tag{6.4}$$

Body forces result from an external field (such as gravity) which acts on each element of the considered volume in a given direction. In some studies, such as tidal motion and oceanic circulation, the gravity acceleration must be considered as radial. In the case of gravity action, the body force per unit of volume is simply equal to the fluid weight ρg, where g is the acceleration due to the gravity. This force is independent of the motion. Taking the vertical axis z as positive upward along the normal to the earth's surface, the components x, y, z of the gravity force are: $\Omega_x = -\partial(\rho g z)/\partial x = 0$, $\Omega_y = -\partial(\rho g z)/\partial y = 0$, $\Omega_z = -\partial(\rho g z)/\partial z = -\rho g$, and $\Omega = gz$.

Local forces result from forces acting on the outside of the considered volume. In the case of a fluid particle, they are caused by molecular forces. They decrease very quickly away from the boundaries of the particle of fluid, and their action is limited to a very thin layer. In practice, if the fluid is a continuous medium, this layer can be considered infinitesimally thin. The local forces can be divided into two: (1) *normal forces* – due to pressure, and (2) *shearing forces* – due to viscosity. These two kinds of forces also exist within the particle, but are always balanced in pairs and their sum is zero.

Pressure forces result from the normal components of the molecular forces near the boundary of the considered volume. However, shear stresses are present because of fluid viscosity and are caused by the transfer of molecular momentum. The friction force (τ) is assumed to be proportional to the coefficient of viscosity (μ) and the rate of angular deformation; thus, friction forces can be expressed as:

$$\mu\left(\frac{\partial^2 \mathbf{u}}{\partial x^2}+\frac{\partial^2 \mathbf{u}}{\partial y^2}+\frac{\partial^2 \mathbf{u}}{\partial z^2}\right)=\mu\nabla^2\mathbf{u}. \tag{6.5}$$

The momentum conservation equation is obtained by equating the applied forces to the inertia force for a unit volume of fluid. Different forms of the momentum

equation corresponding to a number of cases are encountered in hydrodynamics. The Navier-Stokes equations are used to represent most of the problems encountered in fluid mechanics. They are second-order differential equations because of the frictional terms, and nonlinear because of the convective inertia term. The components of the Navier-Stokes are given by:

$$\overbrace{\underbrace{\rho\left(\frac{\partial u}{\partial t}+u\frac{\partial u}{\partial x}+v\frac{\partial u}{\partial y}+w\frac{\partial u}{\partial z}\right)}_{\text{Local acceleration}}\overbrace{}^{\text{Convective acceleration}}}^{\text{Inertia Forces}} = \overbrace{\underbrace{-\frac{\partial p}{\partial x}}_{\text{Pressure}}\underbrace{}_{\text{Gravity}}\overbrace{+\mu\left(\frac{\partial^2 u}{\partial x^2}+\frac{\partial^2 u}{\partial y^2}+\frac{\partial^2 u}{\partial z^2}\right)}^{\text{Friction}}}^{\text{Applied Forces}}$$

$$\rho\left(\frac{\partial v}{\partial t}+u\frac{\partial v}{\partial x}+v\frac{\partial v}{\partial y}+w\frac{\partial v}{\partial z}\right) = -\frac{\partial p}{\partial y} + \mu\left(\frac{\partial^2 v}{\partial x^2}+\frac{\partial^2 v}{\partial y^2}+\frac{\partial^2 v}{\partial z^2}\right)$$

$$\rho\left(\frac{\partial w}{\partial t}+u\frac{\partial w}{\partial x}+v\frac{\partial w}{\partial y}+w\frac{\partial w}{\partial z}\right) = -\frac{\partial p}{\partial z} - \rho g + \mu\left(\frac{\partial^2 w}{\partial x^2}+\frac{\partial^2 w}{\partial y^2}+\frac{\partial^2 w}{\partial z^2}\right). \tag{6.6}$$

6.1.3 THE ENERGY CONSERVATION EQUATION

The energy conservation equation expresses the fact that the rate of change of total internal energy in an infinitesimal volume must be balanced by the heat flux, the heat generation, and the heat lost in the considered volume and the workdone to/by the volume.

Alternatively, for water waves of an adiabatic flow, the mechanical energy equation can be expressed as a balance between the rate of change of the mechanical energy and the flow of energy transported by the velocity field, together with the contribution from the rate of work of pressure forces. Thus, the energy equation can be written in the following form:

$$\frac{\partial}{\partial t}\left(\frac{1}{2}\rho\mathbf{u}\cdot\mathbf{u}+\rho\Omega\right)+\nabla\cdot\left\{\mathbf{u}\left(\frac{1}{2}\rho\mathbf{u}\cdot\mathbf{u}+P+\rho\Omega\right)\right\}=0. \tag{6.7}$$

Since the energy equation is not used for the development of the present model, further details in the energy equation will not be introduced in this document.

6.2 BOUNDARY CONDITIONS

The boundary conditions will be presented under two categories: kinematic and dynamic. The kinematic conditions require a statement that the moving surface is a surface of the fluid; that is, it is always composed of fluid particles. The bottom condition is a special case for the kinematic conditions, under which the movement of the fluid particles are defined by the solid boundary. The kinematic conditions do not involve the action of forces, however, the dynamic condition does. The dynamic condition is also defined at the free surface by writing a pressure balance equation.

Kinemtic Condition

The free surface is represented by:

$$z = h(x, y, t),$$

which can also be written in the form,

$$z - h(x, y, t) = 0. \tag{6.8}$$

A surface $F(x, y, z, t) =$ constant, which moves with the fluid, so that it always contains the same fluid particles, must satisfy:

$$\frac{DF}{Dt} = 0. \tag{6.9}$$

Here,

$$\frac{D}{Dt} = \frac{\partial}{\partial t} + u\frac{\partial}{\partial x} + v\frac{\partial}{\partial y} + w\frac{\partial}{\partial z}. \tag{6.10}$$

From Equations 6.8 and 6.9, we have:

$$\frac{D}{Dt}\left[z - h(x, y, t)\right] = 0. \tag{6.11}$$

Equation 6.11 is the kinematic condition which is satisfied by those fluid particles that move with the fluid surface. Knowing that

$$\frac{Dz}{Dt} = w, \tag{6.12}$$

we can write the kinematic condition as follows:

$$w = \frac{\partial h}{\partial t} + \left(u\frac{\partial h}{\partial x} + v\frac{\partial h}{\partial y} \right) \qquad \text{on} \quad z = h(x, y, t). \tag{6.13}$$

Equation 6.13 shows that the evaluation of $h(x, y, t)$ is necessary to define the velocity field.

Bottom Condition

In the same manner, for an inviscid fluid, the bottom kinematic condition constitutes a boundary that is defined as a surface that moves with the fluid. The impermeable bed of the channel can be represented by:

$$z = b(x, y, t),$$

or

$$z - b(x, y, t) = 0. \tag{6.14}$$

For a fluid surface, we can write:

$$\frac{D}{Dt}\left[z - b(x, y, t)\right] = 0. \tag{6.15}$$

Thus, the bottom kinematic condition can be expressed, in a similar way to the free surface kinematic condition, in the following form:

$$w = \frac{\partial b}{\partial t} + \left(u\frac{\partial b}{\partial x} + v\frac{\partial b}{\partial y} \right) \qquad \text{on} \quad z = b(x, y, t). \tag{6.16}$$

If the bottom surface, b, does not depend on x and y, and for a steady flow, Equation 6.16 becomes:

$$w = 0 \qquad \text{on} \quad z = 0. \tag{6.17}$$

Dynamic Condition

In the absence of the viscous forces, the dynamic condition can be derived from the momentum equation given in the following form:

$$\frac{D}{Dt}(\rho u) = -\nabla P + \mathbf{F}, \tag{6.18}$$

where $\mathbf{F}$ is the body force represented by a conservative force field: $\mathbf{F} = -\rho\nabla\Omega$ for some potential function $\Omega(x, y, x, t)$, where the negative sign is used to show that the force is directed to the region where the gradient of the potential function decreases. Thus, for an incompressible fluid with ρ = constant, the momentum equation is given by:

$$\frac{D\mathbf{u}}{Dt} = -\nabla\left(\frac{P}{\rho} + \Omega\right). \tag{6.19}$$

From Equations 6.12 and 6.19, we have,

$$\frac{\partial \mathbf{u}}{\partial t} + (\mathbf{u}\cdot\nabla)\,\mathbf{u} = -\nabla\left(\frac{P}{\rho} + \Omega\right). \tag{6.20}$$

Knowing that

$$(\mathbf{u}\cdot\nabla)\,\mathbf{u} = \nabla\frac{1}{2}\mathbf{u}\cdot\mathbf{u} - \mathbf{u}\times\nabla\times\mathbf{u}, \tag{6.21}$$

for an incompressible, irrotational and potential flow, where $\nabla\times\mathbf{u} = 0$, we can write the momentum equation in the following form:

$$\frac{\partial \mathbf{u}}{\partial t} + \nabla\frac{1}{2}\mathbf{u}\cdot\mathbf{u} = -\nabla\left(\frac{P}{\rho} + \Omega\right). \tag{6.22}$$

In the case of potential flow, we can also associate the velocity to a potential function, that is:

$$\mathbf{u} = \nabla\varphi,$$

where φ is the velocity potential. Thus, the momentum equation is expressed as:

$$\frac{\partial}{\partial t}(\nabla\varphi) + \nabla\frac{1}{2}\mathbf{u}\cdot\mathbf{u} = -\nabla\left(\frac{P}{\rho} + \Omega\right). \tag{6.23}$$

Expressing $\Omega = gz$, where g is the gravitational acceleration, and z is measured positive upwards, the momentum equation becomes,

$$\nabla\left(\frac{\partial\varphi}{\partial t} + \frac{1}{2}\mathbf{u}\cdot\mathbf{u} + \frac{P}{\rho} + gz\right) = 0. \tag{6.24}$$

The integration of Equation 6.24 gives:

$$\frac{\partial\varphi}{\partial t} + \frac{1}{2}\mathbf{u}\cdot\mathbf{u} + \frac{P}{\rho} + gz = f(t), \tag{6.25}$$

where $f(t)$ is an arbitrary function of integration.

For a dynamic boundary condition, considering that the pressure at the surface is equal to the atmospheric pressure, $P = P_a$ on $z = h(x, y, t)$, the continuity of pressure requires that,

$$\frac{\partial\varphi}{\partial t} + \frac{1}{2}\mathbf{u}\cdot\mathbf{u} + \frac{P_a}{\rho} + gh = f(t) \qquad \text{on} \qquad z = h. \tag{6.26}$$

It is supposed that, somewhere (as $|x, y| \to \infty$), the fluid is stationary with $P = P_a$ and $h = h_\circ$ = constant; thus, the following equation is obtained:

$$f(t) = \frac{P_a}{\rho} + gh_\circ.$$

Finally, the momentum conservation equation is written as:

$$\frac{\partial\varphi}{\partial t} + \frac{1}{2}\mathbf{u}\cdot\mathbf{u} + g\left(h - h_\circ\right) = 0 \qquad \text{on} \qquad z = h. \tag{6.27}$$

This equation constitutes the surface-pressure condition.

All the boundary conditions derived in this section will be used in the following section for the derivation of nonlinear dispersive wave equations: the Korteweg–de Vries equation and the Boussinesq system of equations.

6.3 DISPERSIVE WAVES

Dispersive waves can be defined through a dispersion relation whenever oscillations in space are coupled with oscillations in time. This means that they involve wave packets where the wave velocity is a function of frequency. Contrary to the hyperbolic waves, the dispersive waves are based on solutions rather than on a particular equation. Depending on these solutions, one can distinguish linear and nonlinear dispersive waves. In the following sections, boundary conditions, linear and nonlinear water waves, particularly solitons pertaining to the nonlinear dispersive wave family, will be discussed in details.

6.3.1 LINEAR DISPERSIVE WAVES

For convenience, we will use $\eta(x, y, t)$ instead of $h(x, y, t)$, which was used in the derivation of boundary conditions in Section 6.2. Here, η is the deviation of water surface from the undisturbed water level ($h_\circ = \text{const}$). Thus, the relation between η and h can be given by:

$$h = \eta + h_\circ. \tag{6.28}$$

For small perturbations on water surface, initially at rest, $\eta(x, y, t)$ and $\varphi(x, y, z, t)$ are small; therefore, the governing equations may be linearized. Substituting the velocity potential into Equation 6.13, the linearized free surface condition can be obtained as:

$$\frac{\partial \eta}{\partial t} = \frac{\partial \varphi}{\partial z}, \tag{6.29}$$

and from Equation 6.27, the dynamic condition is written as:

$$\frac{\partial \varphi}{\partial t} + g\eta = 0. \tag{6.30}$$

Equations 6.29 and 6.30 can be arranged in a way that $\eta(x, y, t)$ can be eliminated from these equations. The resulting equation takes the following form:

$$\frac{\partial^2 \varphi}{\partial t^2} + g\frac{\partial \varphi}{\partial z} = 0 \qquad \text{on} \qquad z = h_\circ. \tag{6.31}$$

For an inviscid, incompressible flow, the use of velocity potential in the continuity equation leads to the Laplace's equation given in the following form:

$$\frac{\partial^2 \varphi}{\partial x^2} + \frac{\partial^2 \varphi}{\partial y^2} + \frac{\partial^2 \varphi}{\partial z^2} = 0, \qquad 0 < z < h_\circ. \tag{6.32}$$

From Equation 6.16, for the case that the bottom surface is independent of time, that is $z = b(x, y)$, the bottom condition, as a function of the velocity potential, is expressed as:

$$\frac{\partial \varphi}{\partial z} = u\frac{\partial b}{\partial x} + v\frac{\partial b}{\partial y}. \tag{6.33}$$

After obtaing a solution for φ, the surface is calculated from the dynamic condition given by the Equation 6.30, that yields:

$$\eta(x, y, t) = -\frac{1}{g}\frac{\partial \varphi}{\partial t}(x, y, z = h_\circ, t). \tag{6.34}$$

Notice that starting from here, the following vectorial notations will be used: $\mathbf{x} = (x, y)$ and $\mathbf{k} = (k_x, k_y)$, the dependency on z, if there is any, will be shown explicitly. In the case of water waves, the waves propagate horizontally; thus, the elementary sinusoidal solutions take the following form:

$$\eta = Ae^{i(\mathbf{k}\cdot\mathbf{x} - \omega t)} \tag{6.35}$$

and

$$\varphi = Z(z)e^{i(\mathbf{k}\cdot\mathbf{x} - \omega t)}, \tag{6.36}$$

where $\mathbf{k}$ is the wave number, ω is the frequency and A is the amplitude. In the elementary solution, $\mathbf{k}$, ω and A are constants.

These equations represent an oscillatory behaviour in x, y and t but not in z. From Laplace's equation, the form of φ, given by Equation 6.36, is a solution provided that $Z(z)$ satisfies the following equation:

$$Z'' - k^2 Z = 0, \qquad k = |\mathbf{k}| = (k_x^2 + k_y^2)^{1/2}. \tag{6.37}$$

For a water channel of constant depth $h_\circ$, the boundary condition on $z = 0$ requires that $Z'(z) = 0$. Hence

$$Z \propto \cosh kz.$$

From Equations 6.34 to 6.36, the following equation is obtained:

$$A = \frac{i\omega}{g} Z(0), \tag{6.38}$$

where A is the amplitude of η. Thus, the amplitude of φ is obtained as:

$$Z(z) = -\frac{ig}{\omega} A \frac{\cosh kz}{\cosh kh_\circ}. \tag{6.39}$$

Finally, Equation 6.36 becomes:

$$\varphi = -\frac{ig}{\omega} A \frac{\cosh kz}{\cosh kh_\circ} e^{i(\mathbf{k}\cdot\mathbf{x} - \omega t)}. \tag{6.40}$$

Alternatively, this equation can be written in the following form:

$$\varphi(x, y, z, t) = A_\circ e^{i(\mathbf{k}\cdot\mathbf{x} - \omega t)}, \tag{6.41}$$

where $A_\circ = -(ig/\omega) A (\cosh k(z) / \cosh kh_\circ)$.

From Equations 6.31 and 6.40, we obtain the dispersion relation in the following form:

$$\omega^2 - gk \tanh kh_\circ = 0,$$

and its solution is,

$$\omega = \sqrt{gk \tanh kh_\circ}. \tag{6.42}$$

In general, the dispersion relation may be obtained from the real roots of the following equation:

$$\omega = f(k). \tag{6.43}$$

There can be a number of such solutions, with different functions $f(k)$ (the so-called, modes). In linear problems, the modes can be superposed to make up a complete solution. The real part of the solution of Equation 6.41 is given as:

$$\Re\varphi = |A_\circ| \cos\theta. \tag{6.44}$$

where $\theta = \mathbf{k} \cdot \mathbf{x} - \omega t$ is the phase. Any particular phase surface, moving with normal velocity ω/k in the direction of $\mathbf{k}$, propagates with a speed, called the phase velocity. This velocity is given by:

$$\mathbf{c} = \frac{\omega}{k}\hat{\mathbf{n}}, \tag{6.45}$$

where $\hat{\mathbf{n}}$ is the unit vector in the $\mathbf{k}$ direction. For any particular mode $\omega = f(k)$, the phase velocity is a function of k. This means that, as time evolves, the different component modes *disperse*, with the result that a single concentrated hump disperses into a whole oscillatory train of waves having different wave numbers, and each traveling with its own speed. However, the wave packet propagates with a group velocity. The group velocity is given by:

$$C(k) = \frac{d(f(k))}{dk}. \tag{6.46}$$

In a similar sense, the energy also propagates with the group velocity. It is the group velocity which plays the dominant role in propagation phenomena. On the other hand, *for hyperbolic waves, where the dispersion is assumed not to take place, the group velocity and the phase velocity are the same and equals to a constant.*

Here, it is worth to mention about the gravity waves, since the speed of gravity waves will be used for the non-dimensionalization of the velocity field in the KdV

and the Boussinesq equations. Gravity waves belong to the family of water waves, under which two categories are found: gravity and capillary waves. The important parameter, used to classify water waves is the critical wave length, λ_{cr}, which is defined as:

$$\lambda_{cr} = 2\pi \left(\frac{\sigma}{g\rho} \right)^{1/2}$$

where g is the gravitational acceleration, σ is the surface tension, and ρ is the water density. When the wave length of waves is larger than this critical value, they are called "Gravity Waves"; when the value is smaller than this critical value, the surface tension becomes dominant and they are categorized under the "Capilary Waves".

For shallow water, where the wavelength is much greater than the depth of the channel ($kh_\circ \ll 1$), we can write $\tanh kh_\circ \simeq kh_\circ$, which leads to the following formulas for the phase velocity and group velocity (see Equations 6.45 and 6.46):

$$c = \frac{\omega}{k} = \frac{\sqrt{gh_\circ k^2}}{k} = \sqrt{gh_\circ} \tag{6.47}$$

and

$$C(k) = \frac{d\omega}{dk} = \frac{1}{2} \frac{2gh_\circ k}{\sqrt{gh_\circ k^2}} = \sqrt{gh_\circ}. \tag{6.48}$$

Since the two velocities (group and phase) are the same, and they are independent of k, the waves are not dispersive. Therefore, we can conclude that gravity waves are not dispersive due to the outcome of Equations 6.47 and 6.48.

6.3.2 NONLINEAR DISPERSIVE WAVES (KORTEWEG–DE VRIES EQUATION)

The balance between the nonlinearity and the dispersion leads to the existence of solitons!

Before discussing solitons, the description of solitary waves and the historical development of solitons will be presented.

A *solitary wave* was first observed on the Edinburgh to Glasgow canal by J. Scott Russell in 1834. After his initial observation, Russell performed a number of laboratory experiments to investigate the nature of solitary waves by dropping a weight at one end of a water channel. He found that the volume of water displaced was the volume of water in the wave and, by careful measurement, he showed that the wave moved at a speed, $c_\circ$, given by:

$$c_\circ^2 = g\,(h_0 + a)\,, \tag{6.49}$$

where $h_\circ$ is the undisturbed depth of the water, and a is the amplitude of the wave. From this equation, it is clear that higher waves (that is, larger a) travel faster. He also performed experiments to generate waves of depression by raising the weight from the bottom of the channel. He found, however, that an initial depression became a train of oscillatory waves whose lengths increased while their amplitudes decreased with time.

Assuming that the wavelength of a solitary wave is greater than the depth of the undisturbed water (long wave, or shallow water assumption; $\delta = h_\circ/\lambda \to 0$), Boussinesq (1871) and Rayleigh (1876) attempted to give a mathematical description to the solitary wave. As a result, they confirmed the speed of the wave given by Russell's formula (6.49) and also showed that the wave profile could be represented by the sech^2 function.

Thus, a solitary wave which is the result of the observation that gravity waves having permanent shape and considerable amplitude, can propagate on the surface of the water. It has a hump profile over the surface and drops smoothly back to undisturbed surface level far ahead and far behind the wave. This is an example of a stable nonlinear wave solution; it does not become multi-valued and has a permanent shape. This type of wave propagates at a constant speed.

On the other hand, when more than one solitary wave appear in the solution, they are called solitons. In another word, a soliton becomes a solitary wave when it is infinitely separated from all other solitons.

A soliton, however, is not precisely defined, but it is used to describe any solution

of a nonlinear equation or system which (i) represents a wave having permanent shape, (ii) is localized, decaying or becoming constant at infinity, and (iii) may interact strongly with other solitons so that after the interaction it retains its shape, almost as if the principle of superposition were valid. Zabusky and Kruskal (1965) were the first researchers who named these kinds of waves as "solitons" to emphasize that a soliton shows a "particle" nature after a collision, keeping its initial shape after the collision. However, they observed that solitons were phase-shifted after a collision.

A packet of waves of nearly the same wave lengthes propagates with the group velocity, however, the individual components in the wave packet move through the packet with their phase velocity. High-wave components of a general solution travel faster than the short-wave components, and, thereby, the components disperse.

In contrast to dispersion, non-linearity leads to the concentration of a disturbance. The balance between the dispersive effects ($\partial^3 u/\partial x^3$) and the concentrating effects ($u\partial u/\partial x$) leads to the existence of the solitary wave.

In 1895, Korteweg and de Vries developed a theory for weakly nonlinear and dispersive right moving solitons traveling in a shallow water. Before giving the Korteweg–de Vries (KdV) equation and the expansion of this theory to the left and right moving solitons (Boussinesq equation), two important parameters which are used in the derivation of KdV and Boussinesq equations will be introduced. The first parameter is known as the *amplitude* ($\varepsilon = a/h_\circ$), and the second one is *shallowness* ($\delta = h_\circ/\lambda$). The amplitude parameter is given by the ratio of the wave amplitude to the water depth, and the shallowness parameter is given by the ratio of the water depth to the wavelength. The equations given below are derived from Johnson (1997).

For the derivation of the Boussinesq and KdV equations, it is convenient to non-dimensionalise and scale the continuity and momentum eqautions as well as the boundary conditions. The non-dimensionalisation is carried out using convenient length and time scales. The parameters that will be used for non-

dimensionalisation and scaling are: the undisturbed water depth, $h_\circ$, and the wavelength of surface waves. In order to define a time scale, a suitable velocity scale is needed. Since the long wave approximation is used for the derivation of Boussinesq and KdV equations, the propagation of long waves will be considered; this leads to the use of the speed of gravitational waves, which is given by $(gh_\circ)^{1/2}$.The characteristic speed, i.e., the speed of gravitational waves, and the wavelength, λ, define a typical time associated with the horizontal wave propagation, this is $\lambda/\left(gh_\circ\right)^{1/2}$.

It should be noted that the non-dimensional x and y are measured in the units of the wave length, λ, whereas the non-dimensional z is measured in the units of the undisturbed water depth, $h_\circ$. The characteristic speed, i.e., the speed of gravity waves, $c_\circ = (gh_\circ)^{1/2}$, is used to define the scale for the horizontal velocity components, u and v, but the vertical velocity component, w, is treated differently, so that the continuity equation is consistent with the boundary conditions. Thus, the vertical velocity component is scaled with $(gh_\circ)^{1/2}\, h_\circ/\lambda$.

The surface wave, itself, leads to the introduction of a further parameter a, which is a typical wave amplitude. The free surface, $z = h(x, y, t)$, can be written as:

$$z(x, y, t) = h(x, y, t) = h_\circ + a\eta(x, y, t), \tag{6.50}$$

where the function $\eta(x, y, t)$ is a non-dimensional quantity. The bottom surface can be written as, $z(x, y, t) = b(x, y, t)$ and it is constant.

Note that in order to simplify the mathematical notation, in the rest of this thesis the dimensional variables will be identified by a prime ($'$). In turns, variables without a prime will be considered as non-dimensional quantities. The non-dimensional variables used for the derivation of the governing equations are:

$$x \to \frac{x'}{\lambda}, \quad y \to \frac{y'}{\lambda}, \quad z \to \frac{z'}{h_\circ}, \quad t \to \frac{t'}{(\lambda/\sqrt{gh_\circ})}, \tag{6.51}$$

Furthermore, two additional conversion of variables for both scaling and unidirectional transformation of the conservation equations will be also introduced.

In order to maintain the homogenity of the notation, please note that the variables will be kept unchanged.

$$u \rightarrow \frac{u'}{\sqrt{gh_\circ}}, \quad v \rightarrow \frac{v'}{\sqrt{gh_\circ}}, \quad w \rightarrow \frac{w'}{\left(h_\circ\sqrt{gh_\circ}/\lambda\right)}, \tag{6.52}$$

The pressure is given by:

$$P'(x', y', z', t') = P'_a + \rho g\left(h_\circ - z'\right) + \rho g h_\circ p(x', y', z', t'), \tag{6.53}$$

where P_a is the atmospheric pressure (=constant), $\rho g\left(h_\circ - z\right)$ is the hydrostatic pressure distribution. The pressure scale, $\rho g h_\circ$ is based on the pressure at the depth, $h_\circ$. The pressure variable, $p(x', y', z', t')$, is a measure of the deviation from the hydrostatic pressure distribution.

Rewriting Equation 6.53 at the free surface, $z'(x', y', t') = h_\circ + a\eta$, we have

$$P'(x', y', z', t') - P'_a = -\rho g h_\circ \frac{a}{h_\circ}\eta + \rho g h_\circ p(x', y', z', t'), \tag{6.54}$$

or

$$0 = \rho g h_\circ \left(p(x', y', z', t') - \varepsilon\eta\right). \tag{6.55}$$

The non-dimensionalisation of this equation leads to:

$$p(x, y, z, t) - \varepsilon\eta = 0. \tag{6.56}$$

From Equations 6.50 and 6.51, the free surface of the liquid is obtained as:

$$h_\circ z = h_\circ\left(1 + \frac{a}{h_\circ}\eta\right). \tag{6.57}$$

Dividing Equation 6.57 by $h_\circ$, we obtain the non-dimensional free surface as:

$$z = 1 + \left(a/h_\circ\right)\eta,$$

Knowing that $\varepsilon = a/h_\circ$, we can write

$$z = 1 + \varepsilon\eta. \tag{6.58}$$

Similarly, the bottom surface can be expressed as:

$$z = const, \tag{6.59}$$

where the contant corresponds to a dimensional constant value divided by $h_\circ$.

For an inviscid flow, from the Euler's equation, the momentum equation in the x direction is written as follows:

$$\rho\left(\frac{\partial u'}{\partial t'} + u'\frac{\partial u'}{\partial x'} + v'\frac{\partial u'}{\partial y'} + w'\frac{\partial u'}{\partial z'}\right) = -\frac{\partial p'}{\partial x'}. \tag{6.60}$$

This equation can be written in terms of non-dimensional variables in the following form:

$$\frac{\partial\left(c_\circ u\right)}{\partial\left(\frac{\lambda}{c_\circ}t\right)} + c_\circ u\frac{\partial\left(c_\circ u\right)}{\partial\left(\lambda x\right)} + c_\circ v\frac{\partial\left(c_\circ u\right)}{\partial\left(\lambda y\right)} + c_\circ\frac{h_\circ}{\lambda}w\frac{\partial\left(c_\circ u\right)}{\partial\left(h_\circ z\right)} = -\frac{1}{\rho}\frac{\partial\left(\rho c_\circ^2 p\right)}{\partial\left(\lambda x\right)}. \tag{6.61}$$

Thus, the non-dimensional momentum equation in the x direction becomes:

$$\frac{\partial u}{\partial t} + u\frac{\partial u}{\partial x} + v\frac{\partial u}{\partial y} + w\frac{\partial u}{\partial z} = -\frac{\partial p}{\partial x}. \tag{6.62}$$

Similarly, the momentum equation in the y direction is written as:

$$\frac{\partial v}{\partial t} + u\frac{\partial v}{\partial x} + v\frac{\partial v}{\partial y} + w\frac{\partial v}{\partial z} = -\frac{\partial p}{\partial y}. \tag{6.63}$$

The dimensional form of the momentum equation in the z direction is written as:

$$\rho\left(\frac{\partial w'}{\partial t'} + u'\frac{\partial w'}{\partial x'} + v'\frac{\partial w'}{\partial y'} + w'\frac{\partial w'}{\partial z'}\right) = -\frac{\partial p'}{\partial z'}. \tag{6.64}$$

This equation can be written in terms of non-dimensional variables in the following form:

$$\frac{\partial\left(\frac{h_\circ c_\circ}{\lambda}w\right)}{\partial\left(\frac{\lambda}{c_\circ}t\right)} + c_\circ u\frac{\partial\left(\frac{h_\circ c_\circ}{\lambda}w\right)}{\partial(\lambda x)} + c_\circ v\frac{\partial\left(\frac{h_\circ c_\circ}{\lambda}w\right)}{\partial(\lambda y)} + c_\circ\frac{h_\circ}{\lambda}w\frac{\partial\left(\frac{h_\circ c_\circ}{\lambda}w\right)}{\partial(h_\circ z)}$$

$$= -\frac{1}{\rho}\frac{\partial\left(\rho c_\circ^2 p\right)}{\partial(h_\circ z)}. \tag{6.65}$$

The simplification of this equation yields,

$$\left(\frac{h_\circ}{\lambda}\right)^2\left(\frac{\partial w}{\partial t} + u\frac{\partial w}{\partial x} + v\frac{\partial w}{\partial y} + \frac{\partial w}{\partial z}\right) = -\frac{\partial p}{\partial z}$$

or

$$\delta^2\left(\frac{\partial w}{\partial t} + u\frac{\partial w}{\partial x} + v\frac{\partial w}{\partial y} + \frac{\partial w}{\partial z}\right) = -\frac{\partial p}{\partial z}, \tag{6.66}$$

where $\delta = h_\circ/\lambda$.

From Equations 6.62, 6.63, and 6.66, the components of the non-dimensional momentum equation are in the following form:

$$\frac{Du}{Dt} = -\frac{\partial p}{\partial x}, \quad \frac{Dv}{Dt} = -\frac{\partial p}{\partial y}, \quad \delta^2\frac{Dw}{Dt} = -\frac{\partial p}{\partial z}, \tag{6.67}$$

where

$$\frac{D}{Dt} \equiv \frac{\partial}{\partial t} + \left(u\frac{\partial}{\partial x} + v\frac{\partial}{\partial y} + w\frac{\partial}{\partial z}\right).$$

For an incompressible, irrotational and inviscid flow, the continuity equation written in primary variables, i.e., Equation 6.3, can be written as follows:

$$\frac{\partial u'}{\partial x'} + \frac{\partial v'}{\partial y'} + \frac{\partial w'}{\partial z'} = 0, \tag{6.68}$$

and in the non-dimensional form is obtained as:

$$\frac{\partial(c_\circ u)}{\partial(\lambda x)} + \frac{\partial(c_\circ v)}{\partial(\lambda y)} + \frac{\partial\left(\frac{h_\circ c_\circ}{\lambda}w\right)}{\partial(h_\circ z)} = 0,$$

or

$$\frac{\partial u}{\partial x} + \frac{\partial v}{\partial y} + \frac{\partial w}{\partial z} = 0. \tag{6.69}$$

The surface kinematic condition, from Equation 6.13, can be written in the following non-dimensional form:

$$\frac{c_o h_o}{\lambda} w = \frac{\partial (h_o + a\eta)}{\partial \left(\frac{\lambda}{c_o} t\right)} + c_o u \frac{\partial (h_o + a\eta)}{\partial (\lambda x)} + c_o v \frac{\partial (h_o + a\eta)}{\partial (\lambda y)},$$

or

$$\frac{c_o h_o}{\lambda} w = \frac{c_o}{\lambda} \frac{\partial \left(\frac{h_o}{h_o} a\eta\right)}{\partial t} + \frac{c_o}{\lambda} u \frac{\partial \left(\frac{h_o}{h_o} a\eta\right)}{\partial x} + \frac{c_o}{\lambda} v \frac{\partial \left(\frac{h_o}{h_o} a\eta\right)}{\partial y}.$$

Finally, we have

$$w = \varepsilon \left(\frac{\partial \eta}{\partial t} + u \frac{\partial \eta}{\partial x} + v \frac{\partial \eta}{\partial y} \right) \qquad \text{on} \quad z = 1 + \varepsilon\eta, \tag{6.70}$$

whereas the dynamic condition, in the non-dimensional form, has already been obtained from Equation 6.56 as:

$$p = \varepsilon\eta \qquad \text{on} \quad z = 1 + \varepsilon\eta. \tag{6.71}$$

The bottom condition, similarly to the surface kinematic condition, from Equation 6.17, in non-dimensional form yields:

$$w = 0 \qquad \text{on} \quad z = 0. \tag{6.72}$$

As Equations 6.70 and 6.71 show, the vertical velocity component, w, and the pressure, p, at the free surface, where $z = 1 + \varepsilon\eta$, are proportional to ε. As $\varepsilon \to 0$, $w \to 0$, $p \to 0$, and there is no disturbance at the free surface. Thus, a set of scaled variables will be defined in a way that they will be consistent with both the boundary conditions and the governing equations. Please note that in order to maintain the homogenity of the notation, after scaling variables, we will use the same notation. Therefore, the scaled variables are given as follows:

$$p \to \varepsilon p, \qquad u \to \varepsilon u, \qquad v \to \varepsilon v \quad \text{and} \quad w \to \varepsilon w. \tag{6.73}$$

Then, the momentum equation in the x direction is given by:

$$\frac{\partial(\varepsilon u)}{\partial t}+\varepsilon u\frac{\partial(\varepsilon u)}{\partial x}+\varepsilon v\frac{\partial(\varepsilon u)}{\partial y}+\varepsilon w\frac{\partial(\varepsilon u)}{\partial z}=-\frac{\partial(\varepsilon p)}{\partial x}.$$

Thus, the component of the momentum equation in the x direction can be written as:

$$\frac{\partial u}{\partial t}+\varepsilon\left(u\frac{\partial u}{\partial x}+v\frac{\partial u}{\partial y}+w\frac{\partial u}{\partial z}\right)=-\frac{\partial p}{\partial x}. \tag{6.74}$$

Finally, Equation 6.74 becomes

$$\frac{Du}{Dt}=-\frac{\partial p}{\partial x}, \tag{6.75}$$

where we redefine the operator D/Dt as follows:

$$\frac{D}{Dt}=\frac{\partial}{\partial t}+\varepsilon\left(u\frac{\partial}{\partial x}+v\frac{\partial}{\partial y}+w\frac{\partial}{\partial z}\right).$$

Similarly, other components of the momentum equation are given by:

$$\frac{Dv}{Dt}=-\frac{\partial p}{\partial y}, \tag{6.76}$$

and

$$\delta^2\frac{Dw}{Dt}=-\frac{\partial p}{\partial z}. \tag{6.77}$$

The contunity equation is obtained in the following form:

$$\frac{\partial(\varepsilon u)}{\partial x}+\frac{\partial(\varepsilon v)}{\partial y}+\frac{\partial(\varepsilon w)}{\partial z}=0. \tag{6.78}$$

The scaled form of this equation becomes:

$$\frac{\partial u}{\partial x}+\frac{\partial v}{\partial y}+\frac{\partial w}{\partial z}=0. \tag{6.79}$$

From Equation 6.70, we have the kinematic condition given in the following form:

$$w = \frac{\partial \eta}{\partial t} + \varepsilon \left(u \frac{\partial \eta}{\partial x} + v \frac{\partial \eta}{\partial y} \right) \qquad \text{on} \quad z = 1 + \varepsilon\eta. \tag{6.80}$$

From Equation 6.71, the dynamic condition is:

$$p = \eta \qquad \text{on} \quad z = 1 + \varepsilon\eta. \tag{6.81}$$

The bottom condition simply yields,

$$w = 0 \qquad \text{on} \quad z = 0. \tag{6.82}$$

Assuming that the problem is independent of the y direction, the following equations will be derived for the x and z variables. In order to obtain a balance between the nonlinearity and the dispersion, the square of the shallowness (δ) and amplitude (ε) parameters are chosen to be of the same order, namely, $\delta^2 = O(\varepsilon)$ as $\varepsilon \to 0$. Thus, a second scaling of variables is necessary. Please note that in order to maintain the homogenity of the notation, after scaling variables, we will use the same notation. Therefore, the region of interest is defined by scaling the following independent variables:

$$x \to \frac{\delta}{\varepsilon^{1/2}} x, \qquad t \to \frac{\delta}{\varepsilon^{1/2}} t, \qquad w \to \frac{\varepsilon^{1/2}}{\delta} w. \tag{6.83}$$

The momentum equation in the x direction is given by:

$$\frac{\partial u}{\partial \left(\frac{\delta}{\varepsilon^{1/2}} t \right)} + \varepsilon \left[u \frac{\partial u}{\partial \left(\frac{\delta}{\varepsilon^{1/2}} x \right)} + \frac{\varepsilon^{1/2}}{\delta} w \frac{\partial u}{\partial z} \right] = - \frac{\partial p}{\partial \left(\frac{\delta}{\varepsilon^{1/2}} x \right)}. \tag{6.84}$$

Alternatively, Equation 6.84 can be written as:

$$\frac{\partial u}{\partial t} + \varepsilon \left(u \frac{\partial u}{\partial x} + w \frac{\partial u}{\partial z} \right) = - \frac{\partial p}{\partial x}. \tag{6.85}$$

Similarly, the momentum equation in the z direction is given by:

$$\delta^2 \left\{ \frac{\partial\left(\frac{\varepsilon^{1/2}}{\delta}w\right)}{\partial\left(\frac{\delta}{\varepsilon^{1/2}}t\right)} + \varepsilon \left[u\frac{\partial\left(\frac{\varepsilon^{1/2}}{\delta}w\right)}{\partial\left(\frac{\delta}{\varepsilon^{1/2}}x\right)} + \frac{\varepsilon^{1/2}}{\delta}w\frac{\partial\left(\frac{\varepsilon^{1/2}}{\delta}w\right)}{\partial z} \right] \right\} = -\frac{\partial p}{\partial z}. \tag{6.86}$$

The simplification of Equation (6.86) leads to the following equation:

$$\varepsilon \left[\frac{\partial w}{\partial t} + \varepsilon \left(u\frac{\partial w}{\partial x} + w\frac{\partial w}{\partial z} \right) \right] = -\frac{\partial p}{\partial z}. \tag{6.87}$$

Substituting Equation 6.83 into Equation 6.78, the contunity equation is obtained in the following form:

$$\frac{\partial(\varepsilon u)}{\partial\left(\frac{\delta}{\varepsilon^{1/2}}x\right)} + \frac{\partial\left(\frac{\varepsilon^{1/2}}{\delta}w\right)}{\partial z} = 0,$$

or

$$\frac{\partial u}{\partial x} + \frac{\partial w}{\partial z} = 0. \tag{6.88}$$

From Equation 6.80, the kinematic condition can be written as:

$$\frac{\varepsilon^{1/2}}{\delta}w = \frac{\partial \eta}{\partial\left(\frac{\delta}{\varepsilon^{1/2}}t\right)} + \varepsilon u\frac{\partial \eta}{\partial\left(\frac{\delta}{\varepsilon^{1/2}}x\right)} \qquad \text{on} \quad z = 1 + \varepsilon\eta. \tag{6.89}$$

Simplifying Equation 6.89, we have,

$$w = \frac{\partial \eta}{\partial t} + \varepsilon u\frac{\partial \eta}{\partial x}. \tag{6.90}$$

The dynamic condition is,

$$p = \eta \qquad \text{on} \quad z = 1 + \varepsilon\eta, \tag{6.91}$$

Since the bottom condition does not change, then:

$$w = 0 \qquad \text{on} \quad z = 0. \tag{6.92}$$

The outcome of this transformation is to replace δ^2 by ε in the momentum equation, namely, in the z direction. The next step is to seek a first approximation for the governing equations, as $\varepsilon \to 0$.

The momentum equation in the z direction and the dynamic condition at the free surface lead to,

$$p(x,z,t) = \eta(x,t), \qquad 0 \leq z \leq 1. \tag{6.93}$$

The momentum equation in the x direction becomes:

$$\frac{\partial u}{\partial t} = -\frac{\partial p}{\partial x}. \tag{6.94}$$

After taking the derivation of Equation 6.93 with respect to x, and substituting it into Equation (6.94), we have:

$$\frac{\partial u}{\partial t} = -\frac{\partial \eta}{\partial x}. \tag{6.95}$$

From Equation 6.88, the integration of the continuity equation over z yields:

$$w = -z\frac{\partial u}{\partial x}, \tag{6.96}$$

which also satisfies the bottom condition, that is, $w(z)\big|_{z=0} = 0$.

The kinematic condition in conjunction with Equation 6.96 yield,

$$\frac{\partial \eta}{\partial t} = -\frac{\partial u}{\partial x}. \tag{6.97}$$

From Equations 6.95 and 6.97, the wave equation is obtained in the following form:

$$\frac{\partial^2 \eta}{\partial t^2} - \frac{\partial^2 \eta}{\partial x^2} = 0. \tag{6.98}$$

As it has been already mentioned, the KdV equation has a particular interest for representing the right moving waves. Therefore, retaining the waves moving only in the $+x$ direction, we can introduce a new variable such that:

$$\xi = x - t. \tag{6.99}$$

However, an asymptotic expansion, which is based on the classical wave equation with high order non-linear and dispersive terms, leads to oscillations in the solution as $t\,(\text{or}\,x) \rightarrow \infty$. Thus, defining the new variables as follows:

$$\xi = x - t \equiv O(1), \qquad \text{and} \qquad \tau = \varepsilon t \equiv O(1), \tag{6.100}$$

one can expect that the solution will be stable. Please note that in order to maintain the homogenity of the notation, after uni-directional transformation of the variables, we will use the same notation. The transformation, i.e., Equation 6.100, will be applied to the governing equations, by using the following identities:

$$\frac{\partial \xi}{\partial x} = 1, \quad \frac{\partial \xi}{\partial t} = -1, \quad \frac{\partial \tau}{\partial x} = 0, \quad \frac{\partial \tau}{\partial t} = \varepsilon.$$

Thus, for any dependent variable, i.e, s, we can write the total differential as:

$$\frac{\partial s}{\partial x} = \frac{\partial s}{\partial \xi}\frac{\partial \xi}{\partial x} + \frac{\partial s}{\partial \tau}\frac{\partial \tau}{\partial x}$$

and

$$\frac{\partial s}{\partial t} = \frac{\partial s}{\partial \xi}\frac{\partial \xi}{\partial t} + \frac{\partial s}{\partial \tau}\frac{\partial \tau}{\partial t}$$

The introduction of the change of variables into the momentum equation results in:

$$-\frac{\partial u}{\partial \xi} + \varepsilon\left(\frac{\partial u}{\partial \tau} + u\frac{\partial u}{\partial \xi} + w\frac{\partial u}{\partial z}\right) = -\frac{\partial p}{\partial \xi}, \tag{6.101}$$

for the x component, and

$$\varepsilon\left[-\frac{\partial w}{\partial \xi} + \varepsilon\left(\frac{\partial w}{\partial \tau} + u\frac{\partial w}{\partial \xi} + w\frac{\partial w}{\partial z}\right)\right] = -\frac{\partial p}{\partial z}, \tag{6.102}$$

for the z component.

The continuity equation is given by:

$$\frac{\partial u}{\partial \xi} + \frac{\partial w}{\partial z} = 0, \tag{6.103}$$

with the kinematic condition,

$$w = -\frac{\partial \eta}{\partial \xi} + \varepsilon\left(\frac{\partial \eta}{\partial \tau} + u\frac{\partial \eta}{\partial \xi}\right) \quad \text{on} \qquad z = 1 + \varepsilon\eta, \tag{6.104}$$

and the dynamic condition

$$p = \eta \quad \text{on} \qquad z = 1 + \varepsilon\eta, \tag{6.105}$$

as well as the bottom condition

$$w = 0 \qquad \text{on} \quad z = 0. \tag{6.106}$$

The solution given as an asymptotic expansion must satisfy the limit conditions. Here, the asymptotic expansion is defined with respect to the parameter, ε, as follows:

$$q(\xi, \tau, z; \varepsilon) \sim \sum_{n=0}^{\infty} \varepsilon^n q_n(\xi, \tau, z), \quad \eta(\xi, \tau; \varepsilon) \sim \sum_{n=0}^{\infty} \varepsilon^n \eta_n(\xi, \tau), \tag{6.107}$$

where q_n represents u, w and p. This equation satisfies $u \to 0$, $w \to 0$, and $p \to 0$ with $\varepsilon \to 0$.

Therefore, the momentum equation in the x direction, in which we substitute the ε expansion up to the first order in ε^n can be written in the following form:

$$\begin{aligned}\left(-\varepsilon^0 \frac{\partial u_0}{\partial \xi} - \varepsilon^1 \frac{\partial u_1}{\partial \xi} - \ldots\right) + \varepsilon \left(\varepsilon^0 \frac{\partial u_0}{\partial \tau} + \varepsilon^1 \frac{\partial u_1}{\partial \tau} + \ldots\right) + \varepsilon \left(\varepsilon^0 u_0 + \varepsilon^1 u_1 + \ldots\right) \\ \times \left(\varepsilon^0 \frac{\partial u_0}{\partial \xi} + \varepsilon^1 \frac{\partial u_1}{\partial \xi} + \ldots\right) + \varepsilon \left(\varepsilon^0 w_0 + \varepsilon^1 w_1 + \ldots\right) \left(\varepsilon^0 \frac{\partial u_0}{\partial z} + \varepsilon^1 \frac{\partial u_1}{\partial z} + \ldots\right) \\ = -\left(\varepsilon^0 \frac{\partial p_0}{\partial \xi} + \varepsilon^1 \frac{\partial p_1}{\partial \xi} + \ldots\right).\end{aligned} \tag{6.108}$$

The leading order is obtained as:

$$\varepsilon^0 \left(-\frac{\partial u_0}{\partial \xi} + \frac{\partial p_0}{\partial \xi}\right) = 0,$$

or

$$\frac{\partial u_0}{\partial \xi} = \frac{\partial p_0}{\partial \xi}, \tag{6.109}$$

and the next order term is:

$$\varepsilon \left(-\frac{\partial u_1}{\partial \xi} + \frac{\partial u_0}{\partial \tau} + u_0 \frac{\partial u_0}{\partial \xi} + w_0 \frac{\partial u_0}{\partial z} + \frac{\partial p_1}{\partial \xi}\right) = 0,$$

or simply,

$$-\frac{\partial u_1}{\partial \xi} + \frac{\partial u_0}{\partial \tau} + u_0 \frac{\partial u_0}{\partial \xi} + w_0 \frac{\partial u_0}{\partial z} + \frac{\partial p_1}{\partial \xi} = 0. \tag{6.110}$$

Similarly, the momentum equation in the z direction is written in the following form:

$$\varepsilon\left(-\varepsilon^0\frac{\partial w_0}{\partial \xi}-\varepsilon^1\frac{\partial w_1}{\partial \xi}-\ldots\right)+\varepsilon^2\left(\varepsilon^0\frac{\partial w_0}{\partial \tau}+\varepsilon^1\frac{\partial w_1}{\partial \tau}+\ldots\right)+\varepsilon^2\left(\varepsilon^0u_0+\varepsilon^1u_1+\ldots\right)$$
$$\times\left(\varepsilon^0\frac{\partial w_0}{\partial \xi}+\varepsilon^1\frac{\partial w_1}{\partial \xi}+\ldots\right)+\varepsilon^2\left(\varepsilon^0w_0+\varepsilon^1w_1+\ldots\right)\left(\varepsilon^0\frac{\partial w_0}{\partial z}+\varepsilon^1\frac{\partial w_1}{\partial z}+\ldots\right)$$
$$=-\left(\varepsilon^0\frac{\partial p_0}{\partial z}+\varepsilon^1\frac{\partial p_1}{\partial z}+\ldots\right). \tag{6.111}$$

The leading order is obtained as:

$$\varepsilon^0\left(-\frac{\partial p_0}{\partial z}\right)=0,$$

or

$$\frac{\partial p_0}{\partial z}=0, \tag{6.112}$$

and the next order term is as follows:

$$\varepsilon\left(-\frac{\partial w_0}{\partial \xi}+\frac{\partial p_1}{\partial z}\right)=0,$$

or simply,

$$\frac{\partial w_0}{\partial \xi}=\frac{\partial p_1}{\partial z}. \tag{6.113}$$

The application of the asymptotic expansion solution to the continuity equation results in:

$$\left(\varepsilon^0\frac{\partial u_0}{\partial \xi}+\varepsilon^1\frac{\partial u_1}{\partial \xi}-\ldots\right)+\left(\varepsilon^0\frac{\partial w_0}{\partial z}+\varepsilon^1\frac{\partial w_1}{\partial z}+\ldots\right)=0, \tag{6.114}$$

where the leading order is obtained as:

$$\varepsilon^0\left(\frac{\partial u_0}{\partial \xi}+\frac{\partial w_0}{\partial z}\right)=0,$$

or

$$\frac{\partial u_0}{\partial \xi}+\frac{\partial w_0}{\partial z}=0, \tag{6.115}$$

and the next order term is:

$$\varepsilon\left(\frac{\partial u_1}{\partial \xi}+\frac{\partial w_1}{\partial z}\right)=0,$$

or simply,

$$\frac{\partial u_1}{\partial \xi}+\frac{\partial w_1}{\partial z}=0. \tag{6.116}$$

The same expansion solution is used to determine the kinematic condition, that is:

$$\begin{aligned}\left(\varepsilon^0 w_0+\varepsilon^1 w_1+...\right)=&\left(-\varepsilon^0\frac{\partial \eta_0}{\partial \xi}-\varepsilon^1\frac{\partial \eta_1}{\partial \xi}-...\right)+\varepsilon\left(\varepsilon^0\frac{\partial \eta_0}{\partial \tau}+\varepsilon^1\frac{\partial \eta_1}{\partial \tau}+...\right)\\&+\varepsilon\left(\varepsilon^0 u_0+\varepsilon^1 u_1+...\right)\left(\varepsilon^0\frac{\partial \eta_0}{\partial \xi}+\varepsilon^1\frac{\partial \eta_1}{\partial \xi}+...\right),\end{aligned} \tag{6.117}$$

where the leading order is obtained as:

$$\varepsilon^0\left(w_0+\frac{\partial \eta_0}{\partial \xi}\right)=0,$$

or

$$w_0=-\frac{\partial \eta_0}{\partial \xi}, \tag{6.118}$$

and the next order term is written as follows:

$$\varepsilon\left(w_1+\frac{\partial \eta_1}{\partial \xi}-\frac{\partial \eta_0}{\partial \tau}-u_0\frac{\partial \eta_0}{\partial \xi}\right)=0,$$

or simply,

$$w_1=-\frac{\partial \eta_1}{\partial \xi}+\frac{\partial \eta_0}{\partial \tau}+u_0\frac{\partial \eta_0}{\partial \xi}. \tag{6.119}$$

The application of the asymptotic expansion to the dynamic condition gives:

$$\left(\varepsilon^0 p_0+\varepsilon^1 p_1+...\right)=\left(\varepsilon^0\eta_0+\varepsilon^1\eta_1-...\right). \tag{6.120}$$

The leading order is obtained as:

$$\varepsilon^0\left(p_0-\eta_0\right)=0,$$

or

$$p_0 = \eta_0. \tag{6.121}$$

The next order term is as follows:

$$\varepsilon\left(p_1 - \eta_1\right) = 0,$$

or simply,

$$p_1 = \eta_1. \tag{6.122}$$

Finally, the bottom condition is given by:

$$\left(\varepsilon^0 w_0 + \varepsilon^1 w_1 + ...\right) = 0. \tag{6.123}$$

Thus, the leading order and the first order terms are obtained, respectively, as:

$$w_0 = 0, \tag{6.124}$$

and

$$w_1 = 0. \tag{6.125}$$

The leading order results can be summarized as follows:

$$\frac{\partial u_0}{\partial \xi} = \frac{\partial p_0}{\partial \xi}, \qquad \frac{\partial p_0}{\partial z} = 0, \qquad \frac{\partial u_0}{\partial \xi} + \frac{\partial w_0}{\partial z} = 0, \tag{6.126}$$

for momentum and mass conservation equations,

$$p_0 = \eta_0 \qquad \text{and} \qquad w_0 = -\frac{\partial \eta_0}{\partial \xi} \qquad \text{on} \qquad z = 1, \tag{6.127}$$

for dynamic and kinematic conditions, and

$$w = 0 \qquad \text{on} \qquad z = 0, \tag{6.128}$$

for the bottom condition.

Equations 6.126, 6.127, and 6.128 yield the following conclusion:

$$p_0 = \eta_0, \qquad u_0 = \eta_0, \qquad w_0 = -z\frac{\partial \eta_0}{\partial \xi}, \qquad 0 \leq z \leq 1. \tag{6.129}$$

The boundary conditions, i.e., dynamic and kinematic, need to be investigated in more detail for $z = 1 + \varepsilon\eta$. Therefore, by using Taylor expansions of u, w and p, the two boundary conditions with $z = 1 + \varepsilon\eta$ are rewritten when $\varepsilon \to 0$, i.e., $z \to 1$, in the following form:

$$p_0 + \varepsilon\eta_0 \frac{\partial p_0}{\partial z} + \varepsilon p_1 = \eta_0 + \varepsilon\eta_1 + O(\varepsilon^2), \tag{6.130}$$

and

$$w_0 + \varepsilon\eta_0 \frac{\partial w_0}{\partial z} + \varepsilon w_1 = \frac{\partial \eta_0}{\partial \xi} - \varepsilon \frac{\partial \eta_1}{\partial \xi} + \varepsilon \left(\frac{\partial \eta_0}{\partial \tau} + u_0 \frac{\partial \eta_0}{\partial \xi} \right) + O(\varepsilon^2). \tag{6.131}$$

From Equation 6.110, the first order term for the the x component of the momentum equation is given by:

$$-\frac{\partial u_1}{\partial \xi} + \frac{\partial u_0}{\partial \tau} + u_0 \frac{\partial u_0}{\partial \xi} + w_0 \frac{\partial u_0}{\partial z} = -\frac{\partial p_1}{\partial \xi}, \tag{6.132}$$

and the z component of the momentum equation is,

$$\frac{\partial w_0}{\partial \xi} = \frac{\partial p_1}{\partial z}. \tag{6.133}$$

We can also write the next order term for the continuity equation as:

$$\frac{\partial u_1}{\partial \xi} + \frac{\partial w_1}{\partial z} = 0. \tag{6.134}$$

with the boundary conditions from Equation 6.130,

$$p_1 + \eta_0 \frac{\partial p_0}{\partial z} = \eta_1 \qquad \text{on} \quad z = 1, \tag{6.135}$$

and from Equation 6.131,

$$w_1 + \eta_0 \frac{\partial w_0}{\partial z} = -\frac{\partial \eta_1}{\partial \xi} + \frac{\partial \eta_0}{\partial \tau} + u_0 \frac{\partial \eta_0}{\partial \xi} \qquad \text{on} \quad z = 1. \tag{6.136}$$

Also, the bottom condition is given by:

$$w_1 = 0 \qquad \text{on} \quad z = 0 \tag{6.137}$$

From Equations 6.126 and 6.129, we obtain

$$\frac{\partial u_0}{\partial z} = 0, \qquad \frac{\partial p_0}{\partial z} = 0, \qquad \frac{\partial w_0}{\partial z} = -\frac{\partial \eta_0}{\partial \xi}. \tag{6.138}$$

Equations 6.129 and 6.133 lead to:

$$\frac{\partial p_1}{\partial z} = -z\frac{\partial^2 \eta_0}{\partial \xi^2},$$

or

$$p_1 = -\frac{z^2}{2}\frac{\partial^2 \eta_0}{\partial \xi^2} + F, \tag{6.139}$$

where F is an arbitrary integral function.

In order to obtain the arbitrary integral function F, the dynamic condition on $z = 1$ is applied to Equations 6.135, 6.138 and 6.139. Thus, the arbitrary integral function is given by:

$$F = \eta_1 + \frac{1}{2}\frac{\partial^2 \eta_0}{\partial \xi^2}, \tag{6.140}$$

and from Equations 6.139 and 6.140, the pressure is given by:

$$p_1 = \frac{1}{2}\left(1 - z^2\right)\frac{\partial^2 \eta_0}{\partial \xi^2} + \eta_1. \tag{6.141}$$

Since $\partial u_0/\partial z = 0$, Equations 6.132 and 6.134 lead to

$$\frac{\partial w_1}{\partial z} = -\frac{\partial u_1}{\partial \xi} = -\frac{\partial p_1}{\partial \xi} - \frac{\partial u_0}{\partial \tau} + u_0\frac{\partial u_0}{\partial \xi}. \tag{6.142}$$

Substituting Equations 6.141 and 6.129 into Equation 6.142, we have

$$\frac{\partial w_1}{\partial z} = -\frac{\partial u_1}{\partial \xi} = -\frac{\partial \eta_1}{\partial \xi} - \frac{1}{2}\left(1 - z^2\right)\frac{\partial^3 \eta_0}{\partial \xi^3} - \frac{\partial \eta_0}{\partial \tau} - \eta_0\frac{\partial \eta_0}{\partial \xi}, \tag{6.143}$$

or

$$w_1 = -\left(\frac{\partial \eta_1}{\partial \xi} + \frac{\partial \eta_0}{\partial \tau} + \eta_0\frac{\partial \eta_0}{\partial \xi} + \frac{1}{2}\frac{\partial^3 \eta_0}{\partial \xi^3}\right)z + \frac{1}{6}z^3\frac{\partial^3 \eta_0}{\partial \xi^3}. \tag{6.144}$$

The surface boundary condition ($z = 1$) yields

$$w_1\big|_{z=1} = -\left(\frac{\partial \eta_1}{\partial \xi} + \frac{\partial \eta_0}{\partial \tau} + \eta_0 \frac{\partial \eta_0}{\partial \xi} + \frac{1}{2}\frac{\partial^3 \eta_0}{\partial \xi^3}\right) + \frac{1}{6}\frac{\partial^3 \eta_0}{\partial \xi^3}. \tag{6.145}$$

On the other hand, from Equations 6.136 and 6.138, we also have

$$w_1\big|_{z=1} = -\frac{\partial \eta_1}{\partial \xi} + \frac{\partial \eta_0}{\partial \tau} + 2\eta_0 \frac{\partial \eta_0}{\partial \xi}. \tag{6.146}$$

Since Equation 6.145 must be equal to Equation 6.146, equating these equations gives:

$$2\frac{\partial \eta_0}{\partial \tau} + 3\eta_0 \frac{\partial \eta_0}{\partial \xi} + \frac{1}{3}\frac{\partial^3 \eta_0}{\partial \xi^3} = 0. \tag{6.147}$$

This equation is known as the *Korteweg–de Vries equation* (KdV). The dispersion relation can also be obtained for Equation 6.147. Knowing that

$$\frac{\partial}{\partial \xi} = \frac{\partial}{\partial x}\frac{\partial x}{\partial \xi} + \frac{\partial}{\partial t}\frac{\partial t}{\partial \xi},$$

and

$$\frac{\partial}{\partial \tau} = \frac{\partial}{\partial x}\frac{\partial x}{\partial \tau} + \frac{\partial}{\partial t}\frac{\partial t}{\partial \tau},$$

we can write Equation 6.147 in terms of x and t under the following form, where x and t are non-dimensional scaled variables:

$$2\left[\frac{1}{\varepsilon}\left(\frac{\partial}{\partial x} + \frac{\partial}{\partial t}\right)\eta_0\right] + 3\eta_0 \frac{\partial \eta_0}{\partial x} + \frac{1}{3}\frac{\partial^3 \eta_0}{\partial x^3} = 0. \tag{6.148}$$

Since we are interested in a linear dispersion relation, the non-linear term $\eta_0\,(\partial \eta_0/\partial x)$ in Equation 6.148 is neglected, then:

$$\frac{\partial \eta_0}{\partial x} + \frac{\partial \eta_0}{\partial t} + \frac{\varepsilon}{6}\frac{\partial^3 \eta_0}{\partial x^3} = 0. \tag{6.149}$$

At this point, a back transformation by using Equation 6.83 can be carried out. This back transformation allows us to write the equations in terms of the non-dimensional values of x and t as, that is:

$$x \rightarrow \frac{\varepsilon^{1/2}}{\delta}x \qquad\qquad t \rightarrow \frac{\varepsilon^{1/2}}{\delta}t \tag{6.150}$$

Substituting these variables into Equation 6.149, we obtain:

$$\frac{\partial \eta_0}{\left(\frac{\varepsilon^{1/2}}{\delta}\right)\partial x} + \frac{\partial \eta_0}{\left(\frac{\varepsilon^{1/2}}{\delta}\right)\partial t} + \frac{\varepsilon}{6}\frac{\partial^3 \eta_0}{\left(\frac{\varepsilon^{1/2}}{\delta}\right)^3 \partial x^3} = 0,$$

or

$$\frac{\partial \eta_0}{\partial x} + \frac{\partial \eta_0}{\partial t} + \frac{\delta^2}{6}\frac{\partial^3 \eta_0}{\partial x^3} = 0. \tag{6.151}$$

In order to get a solution by using primary variables (x', t'), a second back transformation is required. For this back transformation, the following variables are used:

$$x \rightarrow \frac{x'}{\lambda}, \qquad t \rightarrow \frac{c_\circ}{\lambda}t', \qquad \text{and} \qquad \eta \rightarrow \frac{\eta'}{h_\circ}. \tag{6.152}$$

Substituting these variables into Equation 6.151, we obtain:

$$\frac{\left(\frac{1}{h_\circ}\right)\partial \eta_0'}{\left(\frac{1}{\lambda}\right)\partial x'} + \frac{\left(\frac{1}{h_\circ}\right)\partial \eta_0'}{\left(\frac{c_\circ}{\lambda}\right)\partial t'} + \frac{\delta^2}{6}\frac{\left(\frac{1}{h_\circ}\right)^3 \partial^3 \eta_0'}{\left(\frac{1}{\lambda}\right)^3 \partial x'^3} = 0,$$

or

$$\frac{\partial \eta_0'}{\partial x'} + \frac{1}{c_\circ}\frac{\partial \eta_0'}{\partial t'} + \frac{\delta^2}{6}\frac{\lambda^2}{h_\circ^2}\frac{\partial^3 \eta_0'}{\partial x'^3} = 0. \tag{6.153}$$

Since $\delta = h_\circ/\lambda$, Equation 6.153 becomes

$$\frac{\partial \eta_0'}{\partial x'} + \frac{1}{c_\circ}\frac{\partial \eta_0'}{\partial t'} + \frac{1}{6}\frac{\partial^3 \eta_0'}{\partial x'^3} = 0. \tag{6.154}$$

Since the amplitude is given by,

$$\eta_0' = A\exp\left(ik'x' - i\omega' t'\right),$$

Equation 6.154 takes the following form:

$$ik' + \frac{1}{c_\circ}\left(-i\omega'\right) + \frac{1}{6}\left(ik'\right)^3 = 0,$$

or it can be written as:

$$\omega' = c_\circ k' - \frac{1}{6}c_\circ k'^3. \tag{6.155}$$

For the dispersive correction term, that is $\left(1/6\right)\left(\partial^3\eta_0'/\partial x'^3\right)$ in Equation 6.154, with the use of $\left(\partial\eta'/\partial t' \simeq -c_\circ\partial\eta'/\partial x'\right)$, which is obtained after substituting Equations 6.35 and 6.40 into Equation 6.2, we have

$$\frac{\partial\eta_0'}{\partial t'} + c_\circ\frac{\partial\eta_0'}{\partial x'} - \frac{1}{6}\frac{\partial^3\eta_0'}{\partial t'\,\partial x'^2} = 0. \tag{6.156}$$

This equation is obtained for the waves propagating only in the $+x$ direction. In order to describe the waves moving in both directions, we have to derive the conservation equations as it was proposed by Boussinesq (1872).

6.3.3 NONLINEAR DISPERSIVE WAVES (BOUSSINESQ SYSTEM OF EQUATIONS)

In this section, the Boussinesq system of equations will be derived at the surface of the liquid.Afterwards, the same system of equations will be averaged over the height of a channel. In his pioneering study of solitary waves, Boussinesq (1872) found that the assumption of $\varepsilon = O(\delta^2) \ll 1$ provides a well balanced role between ε and δ for solitary waves to exist. Therefore, while deriving the Boussinesq system of equations, the asymptotic expansion will be applied to δ instead to ε. The derivation of the equations presented in this section is based on the study of Wu (1998). Thus, the following non-dimensional variables will be used rather than what was presented before in Section 6.3.2 (Equations 6.51 and 6.52).

$$\eta \to \frac{\eta'}{h_\circ}, \qquad w \to \frac{w'}{c_\circ}, \qquad \varphi \to \frac{\varphi'}{c_\circ\lambda}, \tag{6.157}$$

where we use the same notation as before, that is the prime used to identify dimensional (primary) variables. Considering once again a potential flow, $\mathbf{u} = \nabla\varphi$ where φ is the velocity potential function, the non-dimensional velocity components in the x and z directions can be written in terms of the velocity potential as:

$$c_\circ u = \frac{\partial\left(c_\circ\lambda\varphi\right)}{\partial\left(\lambda x\right)}, \qquad c_\circ w = \frac{\partial\left(c_\circ\lambda\varphi\right)}{\partial\left(h_\circ z\right)},$$

or

$$u = \frac{\partial \varphi}{\partial x}, \qquad w = \delta^{-1}\frac{\partial \varphi}{\partial z}. \tag{6.158}$$

The free surface of the liquid can be expressed as:

$$z'(x', t') = h_\circ(1 + \eta(x', t')),$$

which means that dimensional value of η' is measured in the same units oh $h_\circ$. Thus, the non-dimensional form of the free surface of the liquid is given as:

$$z(x, t) = 1 + \eta(x, t). \tag{6.159}$$

The continuity equation in a non-dimensional form is written as:

$$\frac{\partial (c_\circ u)}{\partial (\lambda x)} + \frac{\partial (c_\circ w)}{\partial (h_\circ z)} = 0,$$

or

$$\delta\frac{\partial u}{\partial x} + \frac{\partial w}{\partial z} = 0. \tag{6.160))}$$

We can also write the continuity equation in terms of the velocity potential as:

$$\delta^2\frac{\partial^2 \varphi}{\partial x^2} + \frac{\partial^2 \varphi}{\partial z^2} = 0. \tag{6.161))}$$

The non-dimensional momemtum equation in the x direction is given by:

$$\frac{\partial (c_\circ u)}{\partial \left(\frac{\lambda}{c_\circ} t\right)} + c_\circ u\frac{\partial (c_\circ u)}{\partial (\lambda x)} + c_\circ w\frac{\partial (c_\circ u)}{\partial (h_\circ z)} = -\frac{1}{\rho}\frac{\partial \left(\rho c_\circ^2 p\right)}{\partial (\lambda x)},$$

or

$$\frac{\partial u}{\partial t} + u\frac{\partial u}{\partial x} + \delta^{-1} w\frac{\partial u}{\partial z} = -\frac{\partial p}{\partial x}. \tag{6.162}$$

Similarly, the non-dimensional momentum equation in the z direction becomes:

$$\frac{\partial (c_\circ w)}{\partial \left(\frac{\lambda}{c_\circ} t\right)} + c_\circ u\frac{\partial (c_\circ w)}{\partial (\lambda x)} + c_\circ w\frac{\partial (c_\circ w)}{\partial (h_\circ z)} = -\frac{1}{\rho}\frac{\partial \left(\rho c_\circ^2 p\right)}{\partial (h_\circ z)},$$

or

$$\frac{\partial w}{\partial t} + u\frac{\partial w}{\partial x} + \delta^{-1} w\frac{\partial w}{\partial z} = -\delta^{-1}\frac{\partial p}{\partial z}. \tag{6.163}$$

The free surface condition can be written as:

$$c_\circ w = \frac{\partial\left(h_\circ \eta\right)}{\partial\left(\frac{\lambda}{c_\circ} t\right)} + c_\circ u \frac{\partial\left(h_\circ \eta\right)}{\partial\left(\lambda x\right)},$$

or

$$w = \delta \frac{\partial \eta}{\partial t} + \delta u \frac{\partial \eta}{\partial x}. \tag{6.164}$$

For the bottom condition, we have

$$w = 0. \tag{6.165}$$

Assuming that the pressure at the surface is equal to the atmospheric $P' = P_a$, the dynamic boundary condition is given by:

$$P_a = P_a + \rho g h_\circ \left(1 - \frac{z'}{h_\circ}\right) + \rho g h_\circ p, \qquad \text{with} \qquad z' = h_\circ \left(1 + \eta\right))$$

then:

$$p(x, z, t)\big|_{z=1+\eta} = \eta. \tag{6.166}$$

As discussed before, the equations will be averaged over the heigth of the channel. The continuity equation (Equation 6.160) can be averaged in the following form:

$$\int_0^{1+\eta} \delta \frac{\partial u}{\partial x} dz + \int_0^{1+\eta} \frac{\partial w}{\partial z} dz = 0. \tag{6.167}$$

Rewriting this equation at the integral boundaries by using the Leibnitz theorem for the first term, we have

$$\delta \frac{\partial}{\partial x} \int_0^{1+\eta} u dz - \delta \frac{\partial \eta}{\partial x} u\big|_{z=1+\eta} + w\big|_{z=1+\eta} - w\big|_{z=0} = 0. \tag{6.168}$$

Substituting the free surface and bottom boundary conditions, i.e., Equations 6.164 and 6.165, into Equation 6.168 the following equation is obtained:

$$\delta \frac{\partial}{\partial x} \left[\frac{1+\eta}{1+\eta} \int_0^{1+\eta} u dz\right] - \delta \frac{\partial \eta}{\partial x} u\big|_{z=1+\eta} + \delta \frac{\partial \eta}{\partial t} + \delta \frac{\partial \eta}{\partial x} u\big|_{z=1+\eta} - 0 = 0. \tag{6.169}$$

Rearranging Equation 6.169, the continuity equation becomes:

$$\frac{\partial \eta}{\partial t} + \frac{\partial}{\partial x}\left[(1+\eta)\,\bar{u}\right] = 0, \tag{6.170}$$

where $\bar{u} = \bar{u}(x,t)$ is the average value of the velocity component u, that is:

$$\bar{u} = \frac{1}{1+\eta}\int_0^{1+\eta} u dz. \tag{6.171}$$

From Equation 6.162, the momentum equation in the x direction at the free liquid surface can be written as follows:

$$\left.\frac{\partial u}{\partial t}\right|_{z=1+\eta} + u\left.\frac{\partial u}{\partial x}\right|_{z=1+\eta} + \delta^{-1}\left(\delta\frac{\partial \eta}{\partial t} + \delta\frac{\partial \eta}{\partial x}u\right)\left|_{z=1+\eta}\right.\left.\frac{\partial u}{\partial z}\right|_{z=1+\eta} = -\left.\frac{\partial p}{\partial x}\right|_{z=1+\eta}. \tag{6.172}$$

Rearranging this equation, we have:

$$\left.\frac{\partial u}{\partial t}\right|_{z=1+\eta} + \left.\frac{\partial \eta}{\partial t}\frac{\partial u}{\partial z}\right|_{z=1+\eta} + u\left.\frac{\partial u}{\partial x}\right|_{z=1+\eta} + \left.\frac{\partial \eta}{\partial x}u\frac{\partial u}{\partial x}\right|_{z=1+\eta} = -\left.\frac{\partial p}{\partial x}\right|_{z=1+\eta}. \tag{6.173}$$

The material derivative at the free liquid surface can be given by:

$$\hat{D} = \frac{\partial}{\partial t} + \hat{u}\frac{\partial}{\partial x}, \qquad \text{where} \qquad \hat{u} = u(x,z,t)\Big|_{z=1+\eta} = \hat{u}(x,t), \tag{6.174}$$

Note that $\hat{u}$ represents the velocity component of the fluid particles that move with η; thus, $\hat{u}$ is independent of η and z.

Therefore, the x component of momentum equation is written as:

$$\hat{D}\hat{u} = -\left.\frac{\partial p}{\partial x}\right|_{z=1+\eta}. \tag{6.175}$$

In the same manner, from Equation 6.163, the momentum equation in the z direction can be written at the free liquid surface in the following form:

$$\left.\frac{\partial w}{\partial t}\right|_{z=1+\eta} + u\left.\frac{\partial w}{\partial x}\right|_{z=1+\eta} + \delta^{-1}\left(\delta\frac{\partial \eta}{\partial t} + \delta\frac{\partial \eta}{\partial x}u\right)\left|_{z=1+\eta}\right.\left.\frac{\partial w}{\partial z}\right|_{z=1+\eta} = -\delta^{-1}\left.\frac{\partial p}{\partial z}\right|_{z=1+\eta}. \tag{6.176}$$

Rearranging Equation 6.176, we have

$$\left.\frac{\partial w}{\partial t}\right|_{z=1+\eta} + \left.\frac{\partial \eta}{\partial t}\frac{\partial w}{\partial z}\right|_{z=1+\eta} + \left. u\frac{\partial w}{\partial x}\right|_{z=1+\eta} + \left.\frac{\partial \eta}{\partial x}u\frac{\partial w}{\partial z}\right|_{z=1+\eta} = -\delta^{-1}\left.\frac{\partial p}{\partial z}\right|_{z=1+\eta}. \tag{6.177}$$

Taking into account that the fluid particles move with η, w becomes independent of z; thus, $\hat{w} = w(x,z,t)\Big|_{z=1+\eta} = \hat{w}(x,t)$. Under this condition, substituting the material derivatives (Equation 6.174) into Equation 6.176, the following momentum equation in the z direction is obtained:

$$\hat{D}\hat{w} = -\delta^{-1}\left.\frac{\partial p}{\partial z}\right|_{z=1+\eta}. \tag{6.178}$$

From Equation 6.164, the liquid free surface condition can be also written in the following form:

$$\hat{w} = \delta\hat{D}\eta. \tag{6.179}$$

Substituting this equation into Equation 6.178, we have

$$\delta^2\hat{D}\hat{D}\eta = -\left.\frac{\partial p}{\partial z}\right|_{z=1+\eta}. \tag{6.180}$$

From the dynamic boundary condition (Equation 6.166) the pressure gradient in the x direction, at the liquid free surface is given by:

$$\left.\frac{\partial p}{\partial x}\right|_{z=1+\eta} + \left.\left(\frac{\partial p}{\partial z}\frac{\partial \eta}{\partial x}\right)\right|_{z=1+\eta} = \frac{\partial \eta}{\partial x}. \tag{6.181}$$

Rearranging this equation, we have

$$-\left.\frac{\partial p}{\partial x}\right|_{z=1+\eta} = \left.\left(\frac{\partial p}{\partial z}\frac{\partial \eta}{\partial x}\right)\right|_{z=1+\eta} - \frac{\partial \eta}{\partial x}. \tag{6.182}$$

Substituting Equations 6.180 and 6.182 into Equation 6.175, the following equation is obtained:

$$\hat{D}\hat{u} + \frac{\partial \eta}{\partial x} = -\delta^2\hat{D}^2\eta\frac{\partial \eta}{\partial x}. \tag{6.183}$$

The next step consists in obtaining the momentum equation averaged over the height of the channel. This means that Equation 6.183 should be averaged over the height of the channel (z). Before introducing further derivations, it is convenient to consider the material derivative averaged over the channel height, which can be written as:

$$\bar{D} = \frac{\partial}{\partial t} + \bar{u}\frac{\partial}{\partial x}. \tag{6.184}$$

Substituting Equation 6.184 into Equation 6.170, the continuity equation is obtained as follows:

$$\bar{D}\eta = -(1+\eta)\frac{\partial \bar{u}}{\partial x}. \tag{6.185}$$

In order to obtain a convergent solution, that is $\eta \to 0$ and $u \to 0$ and taking into account that for a potential flow $\mathbf{u} = \nabla\varphi$ with $z \approx 1$, the following second order asymptotic series expansion for the velocity potential is proposed:

$$\varphi(x,z,t;\delta) = \sum_{n=0}^{\infty} \frac{(-1)^n}{(2n!)}\delta^{2n} z^{2n} \frac{\partial^{2n}}{\partial x^{2n}}\varphi_0(x,t;\delta). \tag{6.186}$$

writing 6.186 explicitly leads to

$$\varphi(x,z,t;\delta) = \varphi_0(x,t;\delta) + \frac{(-1)}{2}\delta^2 z^2 \frac{\partial^2}{\partial x^2}\varphi_\circ(x,t;\delta) + O(\delta^4). \tag{6.187}$$

Subsituting Equation 6.187 into Equation 6.158, the $u(x,z,t)$ velocity component can be written as:

$$u(x,z,t) = \frac{\partial}{\partial x}\left[\varphi_0(x,t;\delta) + \frac{(-1)}{2}\delta^2 z^2 \frac{\partial^2}{\partial x^2}\varphi_0(x,t;\delta) + O(\delta^4)\right]. \tag{6.188}$$

Writing this equation at the free liquid surface where $z = 1+\eta$ and $u \neq f(\eta)$, we obtain:

$$\hat{u}(x,t) = \frac{\partial}{\partial x}\varphi_0(x,t;\delta) + \frac{(-1)}{2}\delta^2 (1+\eta)^2 \frac{\partial^3}{\partial x^3}\varphi_0(x,t;\delta) + O(\delta^4). \tag{6.189}$$

Introducing a new variable, $u_0(x,t) = \partial\varphi_0(x,t;\delta)/\partial x$ into Equation 6.189, the velocity component $u(x,t)$ at the free liquid surface becomes:

$$\hat{u}(x,t) = u_0(x,t) + \frac{(-1)}{2}\delta^2 (1+\eta)^2 \frac{\partial^2}{\partial x^2} u_0(x,t) + O(\delta^4). \tag{6.190}$$

Note that this equation can be also written as:

$$\hat{u}(x,t) = \sum_{n=0}^{\infty} \delta^{2n} A_n u_0(x,t), \tag{6.191}$$

where A_n are the operators that apply on u_0 and they have the following forms:

$$A_0 = 1, \qquad A_1 = \frac{(-1)}{2}(1+\eta)^2 \frac{\partial^2}{\partial x^2}, \text{ etc.} \tag{6.192}$$

An equation for u_0 can be also written similarly to Equation 6.191 in the following form:

$$u_0(x,t) = \sum_{n=0}^{\infty} \delta^{2n} J_n \hat{u}(x,t). \tag{6.193}$$

where J_n are the operators that apply on $\hat{u}$.

Substituting Equation 6.191 into Equation 6.193, the following equation is obtained:

$$u_0(x,t) = \sum_{n=0}^{\infty}\sum_{m=0}^{\infty} \delta^{2n+2m} J_n A_m u_0(x,t). \tag{6.194}$$

By keeping only second order terms, this equation is written as:

$$u_0(x,t) = J_0 A_0 u_0(x,t) + \delta^2 J_1 A_0 u_0(x,t) + \delta^2 J_0 A_1 u_0(x,t) + O(\delta^4). \tag{6.195}$$

It is obvious that in order to verify this identity, the operators must be:

$$J_0 A_0 = 1, \qquad J_1 A_0 + J_0 A_1 = 0, \tag{6.196}$$

which results in:

$$J_0 = 1, \qquad J_1 = -A_1. \tag{6.197}$$

Starting from Equation 6.187, a similar mathematical treatment can be carried out to write the averaged velocity, $\bar{u}(x,t)$. Such a treatment yields:

$$\bar{u}(x,t) = \frac{\partial}{\partial x}\varphi_0(x,t;\delta) + \frac{(-1)}{2}\delta^2 \left(\frac{1}{1+\eta} \int_0^{1+\eta} z^2 dz \right) \frac{\partial^3}{\partial x^3}\varphi_0(x,t;\delta) + O(\delta^4). \tag{6.198}$$

Rearranging this equation, we obtain:

$$\bar{u}(x,t) = \frac{\partial}{\partial x}\varphi_0(x,t;\delta) + \frac{(-1)}{2}\delta^2 \frac{1}{3}(1+\eta)^2 \frac{\partial^3}{\partial x^3}\varphi_0(x,t;\delta) + O(\delta^4). \tag{6.199}$$

Rewriting Equation 6.199 in terms of u_0, we have

$$\bar{u}(x,t) = u_0(x,t) + \frac{(-1)}{6}\delta^2 (1+\eta)^2 \frac{\partial^2}{\partial x^2}u_0(x,t) + O(\delta^4). \tag{6.200}$$

Alternatively, this equation can be written as:

$$\bar{u}(x,t) = \sum_0^\infty \delta^{2n} B_n u_0(x,t), \tag{6.201}$$

with

$$B_0 = 1, \qquad B_1 = \frac{(-1)}{6}(1+\eta)^2 \frac{\partial^2}{\partial x^2}. \tag{6.202}$$

Also, it is easy to see that $B_1 = 1/3\, A_1$. The zero order term of the velocity component, $u(x,z,t)$, can be written in terms of the averaged velocity, $\bar{u}(x,t)$ in the following form:

$$u_0(x,t) = \sum_{n=0}^\infty \delta^{2n} K_n \bar{u}(x,t). \tag{6.203}$$

Substituting Equation 6.201 into Equation 6.203, we obtain the following equation:

$$u_0(x,t) = \sum_{n=0}^\infty \sum_{m=0}^\infty \delta^{2n+2m} K_n B_m u_0(x,t). \tag{6.204}$$

Explicitly, this equation can be written as:

$$u_0(x,t) = K_0 B_0 u_0(x,t) + \delta^2 K_1 B_0 u_0(x,t) + \delta^2 K_0 B_1 u_0(x,t) + O(\delta^4). \tag{6.205}$$

Therefore, the following conditions must be satisfied,

$$K_0 B_0 = 1, \qquad K_1 B_0 + K_0 B_1 = 0, \tag{6.206}$$

which results in

$$K_0 = 1, \qquad K_1 = -B_1. \tag{6.207}$$

From Equations 6.191 and 6.203, the following equation for the velocity component, u, at the free surface is obtained:

$$\hat{u}(x,t) = \sum_{n=0,\, n'=0}^{\infty} \delta^{2n+2n'} A_n K_{n'} \bar{u}(x,t). \tag{6.208}$$

This equation can be explicitly written as:

$$\hat{u}(x,t) = A_0 K_0 \bar{u}(x,t) + \delta^2 A_0 K_1 \bar{u}(x,t) + \delta^2 A_1 K_0 \bar{u}(x,t) + O(\delta^4). \tag{6.209}$$

By using Equations 6.192, 6.202 and 6.207, then Equation 6.209 can be written in the following form:

$$\hat{u}(x,t) = \bar{u}(x,t) + \delta^2 \frac{2}{3} A_1 \bar{u}(x,t) + O(\delta^4). \tag{6.210}$$

Subsituting the value of A_1, from Equation 6.192, we obtain the relationship between the velocity component at the free liquid surface and the average value of the same velocity component, that is:

$$\hat{u}(x,t) = \bar{u}(x,t) - \delta^2 \frac{1}{3} (1+\eta)^2 \frac{\partial^2}{\partial x^2} \bar{u}(x,t) + O(\delta^4). \tag{6.211}$$

In order to obtain Equation 6.183 in terms of averaged terms, the relation between two material derivatives can be established as:

$$\hat{D}\hat{u} - \bar{D}\bar{u} = \bar{D}\left(\hat{u} - \bar{u}\right) + \left(\hat{D} - \bar{D}\right)\hat{u}. \tag{6.212}$$

Subsituting Equation 6.211 into the first term on the right hand side of Equation 6.212, we obtain the following equation:

$$\bar{D}\left(\hat{u} - \bar{u}\right) = \bar{D}\left(-\delta^2 \frac{1}{3} (1+\eta)^2 \frac{\partial^2}{\partial x^2} \bar{u}(x,t) + O(\delta^4)\right), \tag{6.213}$$

which results in

$$\bar{D}\left(\hat{u}-\bar{u}\right)=-\frac{1}{3}\delta^2\left(1+\eta\right)^2\bar{D}\frac{\partial^2}{\partial x^2}\bar{u}(x,t)-\frac{1}{3}\delta^2\left[\bar{D}\left(1+\eta\right)^2\right]\frac{\partial^2}{\partial x^2}\bar{u}(x,t)+O(\delta^4). \tag{6.214}$$

Since $\bar{D}=\partial/\partial t+\bar{u}(\partial/\partial x)$, Equation 6.214 becomes:

$$\begin{aligned}\bar{D}\left(\hat{u}-\bar{u}\right)=&-\frac{1}{3}\delta^2\left(1+\eta\right)^2\frac{\partial}{\partial t}\frac{\partial^2}{\partial x^2}\bar{u}(x,t)-\frac{1}{3}\delta^2\left[\frac{\partial}{\partial t}\left(1+\eta\right)^2\right]\frac{\partial^2}{\partial x^2}\bar{u}(x,t)\\&-\frac{1}{3}\delta^2\left(1+\eta\right)^2\bar{u}\frac{\partial}{\partial x}\frac{\partial^2}{\partial x^2}\bar{u}(x,t)-\frac{1}{3}\delta^2\bar{u}\left[\frac{\partial}{\partial x}\left(1+\eta\right)^2\right]\frac{\partial^2}{\partial x^2}\bar{u}(x,t)+O(\delta^4).\end{aligned} \tag{6.215}$$

Rearranging the terms in Equation 6.215, we have:

$$\bar{D}\left(\hat{u}-\bar{u}\right)=-\frac{1}{3}\delta^2\left(1+\eta\right)^2\bar{D}\frac{\partial^2}{\partial x^2}\bar{u}(x,t)+\frac{2}{3}\delta^2\left(1+\eta\right)^2\frac{\partial\bar{u}(x,t)}{\partial x}\frac{\partial^2}{\partial x^2}\bar{u}(x,t)+O(\delta^4). \tag{6.216}$$

Knowing that $\hat{D}=\partial_t+\hat{u}\partial_x$ and $\bar{D}=\partial_t+\bar{u}\partial_x$, we can write the second term on the right hand side of Equation 6.212 in the following form:

$$\left(\hat{D}-\bar{D}\right)\hat{u}=\left(\hat{u}-\bar{u}\right)\frac{\partial}{\partial x}\hat{u}. \tag{6.217}$$

Subsituting Equation 6.211 into Equation 6.217, we obtain the following equation:

$$\left(\hat{D}-\bar{D}\right)\hat{u}=\left(-\frac{1}{3}\delta^2\left(1+\eta\right)^2\frac{\partial^2}{\partial x^2}\bar{u}(x,t)\right)\frac{\partial\hat{u}}{\partial x}. \tag{6.218}$$

Substituting Equation 6.211 into Equation 6.218 in the place of $\hat{u}$, we have

$$\begin{aligned}\left(\hat{D}-\bar{D}\right)\hat{u}=&-\frac{1}{3}\delta^2\left(1+\eta\right)^2\frac{\partial^2}{\partial x^2}\bar{u}(x,t)\\&\times\frac{\partial}{\partial x}\left[\bar{u}(x,t)-\delta^2\frac{1}{3}\left(1+\eta\right)^2\frac{\partial^2}{\partial x^2}\bar{u}(x,t)+O(\delta^4)\right].\end{aligned} \tag{6.219}$$

The second term inside the bracket can be neglected, otherwise the equation becomes highly non-linear. Thus, Equation 6.219 becomes:

$$\left(\hat{D}-\bar{D}\right)\hat{u}\equiv-\frac{1}{3}\delta^2\left(1+\eta\right)^2\frac{\partial^2}{\partial x^2}\bar{u}(x,t)\frac{\partial}{\partial x}\bar{u}(x,t)+O(\delta^4). \tag{6.220}$$

Substituting Equations 6.216 and 6.220 into 6.212, we obtain the following equation:

$$\hat{D}\hat{u} - \bar{D}\bar{u} = -\frac{1}{3}\delta^2 (1+\eta)^2 F[\bar{u}] + O(\delta^4), \tag{6.221}$$

where $F[\bar{u}]$ is given by:

$$F[\bar{u}] = \bar{D}\frac{\partial^2}{\partial x^2}\bar{u} + \frac{\partial^2}{\partial x^2}\bar{u}\frac{\partial}{\partial x}\bar{u} - 2\frac{\partial}{\partial x}\bar{u}\frac{\partial^2}{\partial x^2}\bar{u}. \tag{6.222}$$

By the use of Equation 6.211, the right hand side of Equation 6.183 can be written in terms of averaged operators in the following form:

$$\begin{aligned}\delta^2\hat{D}^2\eta\frac{\partial}{\partial x}\eta =& \delta^2\left[\frac{\partial}{\partial t} + \bar{u}\frac{\partial}{\partial x} - \frac{1}{3}\delta^2(1+\eta)^2\frac{\partial^2}{\partial x^2}\bar{u}\frac{\partial}{\partial x}\right] \\ &\times\left[\frac{\partial}{\partial t} + \bar{u}\frac{\partial}{\partial x} - \frac{1}{3}\delta^2(1+\eta)^2\frac{\partial^2}{\partial x^2}\bar{u}\frac{\partial}{\partial x}\right]\eta\times\frac{\partial\eta}{\partial x}.\end{aligned} \tag{6.223}$$

By neglecting higher order non-linear terms, i.e., the last terms in the brackets, Equation 6.221 becomes:

$$\delta^2\hat{D}^2\eta\frac{\partial}{\partial x}\eta = \delta^2\bar{D}^2\eta\frac{\partial}{\partial x}\eta + O(\delta^4). \tag{6.224}$$

By using the continuity equation (Equation 6.185), the $\bar{D}^2\eta = \bar{D}\bar{D}\eta$ term can be written as:

$$\bar{D}^2\eta = \bar{D}\left[-(1+\eta)\frac{\partial\bar{u}}{\partial x}\right], \tag{6.225}$$

which results in

$$\bar{D}^2\eta = (1+\eta)\frac{\partial\bar{u}}{\partial x}\frac{\partial\bar{u}}{\partial x} - (1+\eta)\bar{D}\frac{\partial\bar{u}}{\partial x}, \tag{6.226}$$

or

$$\bar{D}^2\eta = -(1+\eta)G[\bar{u}], \tag{6.227}$$

with $G[\bar{u}]$ given by:

$$G[\bar{u}] = \bar{D}\left(\frac{\partial\bar{u}}{\partial x}\right) - \left(\frac{\partial\bar{u}}{\partial x}\right)^2. \tag{6.228}$$

Substituting Equations 6.221, 6.222, 6.227 and 6.228 into Equation 6.183, we obtain the following equation:

$$\bar{D}\bar{u} + \frac{\partial\eta}{\partial x} = \frac{1}{3}\delta^2(1+\eta)^2 F[\bar{u}] + \delta^2(1+\eta)G[\bar{u}]\times\frac{\partial\eta}{\partial x}. \tag{6.229}$$

Noting that $F[\bar{u}] = \partial G[\bar{u}]/\partial x$, we can write:

$$\bar{D}\bar{u} + \frac{\partial \eta}{\partial x} = \frac{\delta^2}{3}\frac{1}{1+\eta}\frac{\partial}{\partial x}\left[(1+\eta)^3 G[\bar{u}]\right]. \tag{6.230}$$

The substitution of Equation 6.228 into Equation 6.230 and writing $\bar{D}$ explicitly results in:

$$\frac{\partial \bar{u}}{\partial t} + \bar{u}\frac{\partial \bar{u}}{\partial x} + \frac{\partial \eta}{\partial x} = \frac{\delta^2}{3}\frac{1}{1+\eta}\frac{\partial}{\partial x}\left\{(1+\eta)^3\left[\frac{\partial}{\partial x}\frac{\partial}{\partial t}\bar{u} + \bar{u}\frac{\partial^2 \bar{u}}{\partial x^2} - \left(\frac{\partial \bar{u}}{\partial x}\right)^2\right]\right\} + O(\delta^4). \tag{6.231}$$

Note that, on the right hand side of this equation, there is only one linear term, i.e., $\delta^2/3\left(\partial^2/\partial x^2\right)\left(\partial/\partial t\right)\bar{u}$. Thus, by neglecting higher order non-linear terms, the following equation is obtained:

$$\frac{\partial \bar{u}}{\partial t} + \bar{u}\frac{\partial \bar{u}}{\partial x} + \frac{\partial \eta}{\partial x} = \frac{\delta^2}{3}\frac{\partial^3}{\partial x^2\,\partial t}\bar{u}. \tag{6.232}$$

Using Equations 6.51, 6.52 and 6.157, we can write the dimensional form of this equation as follows:

$$\frac{\partial u'}{\partial t'} + u'\frac{\partial u'}{\partial x'} + g\frac{\partial \eta'}{\partial x'} = \frac{h_\circ^2}{3}\frac{\partial^3}{\partial x'^2\,\partial t'}u'. \tag{6.233}$$

and the dimensional form of the continuity equation (Equation 6.170) is also obtained as follows:

$$\frac{\partial \eta'}{\partial t'} + \frac{\partial}{\partial x'}\left[(h_\circ + \eta')\,u'\right] = 0. \tag{6.234}$$

6.3.4 CONCLUDING REMARKS ON THE KORTEWEG–DE VRIES AND BOUSSINESQ EQUATIONS

In this section, the derivation of the KdV equation from the Boussinesq system will be discussed. We will start with non-dimensional continuity and Boussinesq equations as given in the previous section. The non-dimensional continuity equation is given by:

$$\frac{\partial \eta}{\partial t} + \frac{\partial}{\partial x}\left[(1+\eta)\,\bar{u}\right] = 0. \tag{6.235}$$

The non-dimensional Boussinesq equation (Equation 6.232) for $\delta = 1$ yields:

$$\frac{\partial \bar{u}}{\partial t} + \bar{u}\frac{\partial \bar{u}}{\partial x} + \frac{\partial \eta}{\partial x} = \frac{1}{3}\frac{\partial^3}{\partial x^2\,\partial t}\bar{u}, \tag{6.236}$$

where both x and η are measured in the same units of $h_\circ$.

As it is mentioned before, the KdV equation is obtained only for the waves moving in one direction. This allows us to use the uni-directional approximation which can be given by $\partial/\partial t = -\partial/\partial x$ for non-dimensional variables. On the other hand, we have already shown that $\partial/\partial t = -c_\circ \partial/\partial x$ for the dimensional x and t.

Taking into account this approach, the system of equations (Equations 6.235 and 6.236) can be written, respectively, in the following form:

$$-\frac{\partial \eta}{\partial x} + \frac{\partial \bar{u}}{\partial x} + \frac{\partial}{\partial x}(\eta\bar{u}) = 0 \tag{6.237}$$

and

$$-\frac{\partial \bar{u}}{\partial x} + \frac{1}{2}\frac{\partial \bar{u}^2}{\partial x} + \frac{\partial \eta}{\partial x} = \frac{1}{3}\frac{\partial^3 \bar{u}}{\partial x^3}. \tag{6.238}$$

This system suggests that there is a relation between u and η, and it can be written as follows:

$$\bar{u} = f(\eta) \approx \eta + \alpha\frac{\partial \eta}{\partial x} + \beta\frac{\partial^2 \eta}{\partial x^2} + \gamma\eta^2 + \cdots, \tag{6.239}$$

where α, β, and γ are unknown constants. If we substitute Equation (6.239) into the system of equations (Equation 6.237 and 6.238), we obtain that this system is self-consistent with $\alpha = 0$, $\beta = 1/6$, $\gamma = -1/4$. Therefore, we can write:

$$\bar{u} \approx \eta + \frac{1}{6}\frac{\partial^2 \eta}{\partial x^2} - \frac{1}{4}\eta^2 \tag{6.240}$$

and

$$\frac{\partial \bar{u}}{\partial x} \approx \frac{\partial \eta}{\partial x} + \frac{1}{6}\frac{\partial^3 \eta}{\partial x^3} - \frac{1}{2}\eta\frac{\partial \eta}{\partial x}. \tag{6.241}$$

Substituting Equations 6.240 and 6.241 into Equation 6.235, we obtain:

$$\frac{\partial \eta}{\partial t} + \frac{\partial \eta}{\partial x} + \frac{3}{2}\eta\frac{\partial \eta}{\partial x} + \frac{1}{6}\frac{\partial^3 \eta}{\partial x^3} = 0, \tag{6.242}$$

where we neglect the highly non-linear dispersive terms. This is the KdV equation written in the laboratory frame of reference. This equation can be rewritten for the moving frame by use of the same transformation proposed in Equation 6.100, with $\varepsilon = 1$. This leads to the following equation:

$$\frac{\partial \eta}{\partial \tau} + \frac{3}{2}\eta \frac{\partial \eta}{\partial \xi} + \frac{1}{6}\frac{\partial^3 \eta}{\partial \xi^3} = 0, \tag{6.243}$$

which results in the same equation given by Equation 6.147.

In the next chapter, the model based on these concepts and these equations will be presented.

CHAPTER 7

MODEL FOR THE FORMATION OF SLUGS

The aim of this reasearch is to develop a phenomenological model capable of predicting the formation of slugs in a test section containing both a vertical and a horizontal leg in which an obstruction is placed. Visual observations of the counter-current slug flow were relied on to guide us in the model development.

The first section of this chapter gives the equations and the approximations used in the model, as well as, the initial and the boundary conditions. The second section presents the predictions of the model and comparison with the experimental data already presented in Chapter 5.

7.1 THE SLUG FLOW MODEL

The development of the proposed model is based on visual observations of the slug formation phenomena in a test section containing an obstruction in the horizontal leg. As discussed in Chapter 5, the formation of slugs are caused by the inference of two waves which propagate in opposite directions. Thus, the model development is focused on the wave theory, in particularly the soliton theory. In the following section, a model based on the soliton theory will be presented. Afterwards, the initial and the boundary conditions determined from the frame images collected under the experimental conditions described in Section 4.2, will be presented.

7.1.1 THE GOVERNING EQUATIONS

In the previous chapter, the KdV and the Boussinesq equations were derived for right moving, and left and right moving waves, respectively. However, the slug model requires a solution of two solitons moving in opposite directions. For such

a model, the KdV equation becomes insufficient since it is uni-directional. Instead in order to gain more control on the equations and robust numerical stability, the Boussinesq system of equations, and a solution described by Whitham (1974; Chapter 13, Section 11) and Peregrine (1966) are proposed. This solution comprises a combination of mass and momentum equations. The proposed technique solves the mass and the momentum equations separately, instead of solving them together as it is the case for the Boussinesq equation (Equation 6.232).

The same nondimensional variables defined in Section 6.3.2. are used in this chapter. Thus, the continuity equation is written in the following form:

$$\frac{\partial \eta}{\partial t} + \frac{\partial}{\partial x}\left[(1+\eta)\,u\right] = 0. \tag{7.1}$$

If we measure x in the units of $h_\circ$, and t in the units of $h_\circ/c_\circ$, from Equation 6.233, we can write:

$$\frac{\partial u}{\partial t} + u\frac{\partial u}{\partial x} + \frac{\partial \eta}{\partial x} = \frac{1}{3}\frac{\partial^3 u}{\partial x^2 \partial t}\,. \tag{7.2}$$

Note that u represents the average velocity over a plane normal to the wave propagation direction (see Section 6.3.3).

Peregrine (1966) studied numerically the KdV equation as well as the mass and momentum consevation equations for a unidirectional propagation of a soliton. He found that straightforward finite difference approximations were stable for the KdV equation and unstable for the separate form of the conservation equations. He proposed a numerical scheme for the conservation of mass and momentum equations. Therefore, this numerical scheme has been used for solving the present model. The continuity equation is initially used to calculate the amplitude for an advanced time step. Then, this amplitude is used to solve the momentum equation which yields the averaged horizontal velocity. Substituting this horizontal velocity into the continuity equation, a new corrected amplitude is obtained.

Please note that the time steps will be denoted by j, and the space steps by i and * denotes non-corrected amplitude values. Therefore, the continuity equation used

to calculate the wave amplitude $\eta^*_{i,j+1}$ is given as:

$$\frac{\eta^*_{i,j+1}-\eta_{i,j}}{\Delta t}+\left[1+\frac{1}{2}\left(\eta^*_{i,j+1}+\eta_{i,j}\right)\right]\frac{u_{i+1,j}-u_{i-1,j}}{2\Delta x}+u_{i,j}\frac{\eta_{i+1,j}-\eta_{i-1,j}}{2\Delta x}=0\,. \tag{7.3}$$

The discretized momentum equation is written as:

$$\begin{aligned}\frac{u_{i,j+1}-u_{i,j}}{\Delta t}&+u_{i,j}\frac{u_{i+1,j+1}-u_{i-1,j}+u_{i+1,j}-u_{i-1,j}}{4\Delta x}\\&+\frac{\eta^*_{i+1,j+1}-\eta^*_{i-1,j+1}+\eta_{i+1,j}-\eta_{i-1,j}}{4\Delta x}\\&=\frac{1}{3}\frac{u_{i+1,j+1}-2u_{i,j+1}+u_{i-1,j+1}-u_{i+1,j}+2u_{i,j}-u_{i-1,j}}{\Delta x^2\Delta t}\end{aligned} \tag{7.4}$$

and the discretized form of the continuity equation required to obtain the corrected wave amplitude $\eta_{i,j+1}$ is written as:

$$\begin{aligned}\frac{\eta_{i,j+1}-\eta_{i,j}}{\Delta t}&+(1+\eta_{i,j})\frac{u_{i+1,j+1}-u_{i-1,j+1}+u_{i+1,j}-u_{i-1,j}}{4\Delta x}\\&+\frac{1}{2}\left(u_{i,j+1}+u_{i,j}\right)\frac{\eta_{i+1,j}-\eta_{i-1,j}}{2\Delta x}=0\,.\end{aligned} \tag{7.5}$$

The FORTRAN program used for solving this system of equation as well as to predict the interference of the two solitons, is given in the Appendix F.

7.1.2 THE INITIAL AND BOUNDARY CONDITIONS

As already mentioned above, the initial conditions are obtained from the frames of the films collected during the wave propagation experiments. The conditions and the procedure used for these experiments have been given in Section 4.2. After processing the images using the edge detection technique, the profile of a probable incident wave is saved and then prepared as an input file for the soliton program.

In this program, the values of Δx and Δt are taken as 0.5 and 0.004 respectively. Since the ratio of Δx to Δt gives the propagation velocity of the perturbations, the values for Δx and Δt have been chosen after some comparisons of the predictions of the model with the frame images. Such a comparison is given in Figures 7.1-7.4. The frame images presented in these figures were obtained from an experiment

carried out under the following condition: $Q_l = 0.80\,m^3/h$, $Q_g = 31.50\,m^3/h$ and $\beta = 1.0$. Figures 7.1a-d show the propagation of a wave with time, i.e, $t_1 = 0.033\,s$, $t_2 = 0.133\,s$, etc. Each figure shows a frame image above and a figure below in which a comparison of the edge detection result with the prediction the model has been presented. In these figures, the edge detection result and the prediction of the model have been presented in the non-dimensional form, i.e., $[(h_0 + \eta) - h_0]/h_0)$, where h_o is the average liquid height. It is interesting to observe the similarity that exists between the predictions of the model and the wave profiles obtained from the film frames. The photos in Figures 7.1c-d also show a number of two or three wave components of the packet. Thus, it is visually observed that while a wave packet starts propagating along the tube, a wave packet decomposition takes place, i.e., waves with different frequencies in the wave packet starts moving at their own speeds. Therefore, the wave components of the packet starts moving at a lower pace than the wave packet. Finally, they are separated from the packet keeping the number of the wave components in the wave packet constant.

The boundary conditions were obtained from the *forward and backward difference approximations* that were applied to the space derivative on the first and last nodes of the discretized space respectively. The generalized form of the second forward difference approximation is expressed as:

$$\left.\frac{dy}{dx}\right|_{x=x_1} = \frac{-3y_1 + 4y_2 - y_3}{2\Delta x}$$

$$\left.\frac{d^2y}{dx^2}\right|_{x=x_1} = \frac{y_1 - 2y_2 + y_3}{(\Delta x^2)}, \tag{7.6}$$

whereas the backward difference is expressed by:

$$\left.\frac{dy}{dx}\right|_{x=x_n} = \frac{y_{n-2} - 4y_{n-1} + 3y_n}{2\Delta x}$$

$$\left.\frac{d^2y}{dx^2}\right|_{x=x_n} = \frac{y_{n-2} - 2y_{n-1} + y_n}{(\Delta x^2)}. \tag{7.7}$$

A general form of the forward and backward schemes, discretized in space and in

time is shown in Figure 7.2. Thus, the wave amplitude at the first node results in:

$$\left[1+\frac{1}{4}\frac{\Delta t}{\Delta x}\left(4u_{2,j}-u_{3,j}-3u_{1,j}\right)\right]\eta^{*}_{1,j+1}=\eta_{1,j}-\frac{1}{2}\frac{\Delta t}{\Delta x}u_{1,j}\left(4\eta_{2,j}-\eta_{3,j}-3\eta_{1,j}\right)$$
$$-\frac{1}{2}\frac{\Delta t}{\Delta x}\left(1+\frac{1}{2}\eta_{1,j}\right)\left(4u_{2,j}-u_{3,j}-3u_{1,j}\right). \quad (7.8)$$

and at the last node yields:

$$\left[1+\frac{1}{4}\frac{\Delta t}{\Delta x}\left(3u_{n,j}-4u_{n-1,j}+u_{n-2,j}\right)\right]\eta^{*}_{n,j+1}$$
$$=\eta_{n,j}-\frac{1}{2}\frac{\Delta t}{\Delta x}u_{n,j}\left(3\eta_{n,j}-4\eta_{n-1,j}+\eta_{n-2,j}\right)$$
$$-\frac{1}{2}\frac{\Delta t}{\Delta x}\left(1+\frac{1}{2}\eta_{n,j}\right)\left(3u_{n,j}-4u_{n-1,j}+u_{n-2,j}\right). \quad (7.9)$$

In the same manner, the boundary conditions for the averaged horizontal velocity at the first node is written as:

$$\left(1+\frac{2}{3\Delta x^{2}}-\frac{1}{2}\frac{\Delta t}{\Delta x}u_{1,j}\right)u_{1,j+1}+\left(-\frac{2}{3\Delta x^{2}}+\frac{1}{2}\frac{\Delta t}{\Delta x}u_{1,j}\right)u_{2,j+1}$$
$$=\left(1-\frac{1}{3\Delta x^{2}}+\frac{3}{4}\frac{\Delta t}{\Delta x}u_{1,j}\right)u_{1,j}+\left(\frac{2}{3\Delta x^{2}}+\frac{\Delta t}{\Delta x}u_{1,j}\right)u_{2,j}$$
$$+\left(-\frac{1}{3\Delta x^{2}}+\frac{1}{4}\frac{\Delta t}{\Delta x}u_{1,j}\right)u_{3,j}+\frac{3}{4}\frac{\Delta t}{\Delta x}\left(\eta_{1,j}+\eta^{*}_{1,j+1}\right)$$
$$-\frac{\Delta t}{\Delta x}\left(\eta_{2,j}+\eta^{*}_{2,j+1}\right)+\frac{1}{4}\frac{\Delta t}{\Delta x}\left(\eta_{3,j}+\eta^{*}_{3,j+1}\right) \quad (7.10)$$

and at the last node a similar approach yields:

$$\left(\frac{1}{2}+\frac{1}{3\Delta x^{2}}+\frac{1}{4}\frac{\Delta t}{\Delta x}u_{n,j}\right)u_{n,j+1}-\left(\frac{1}{3\Delta x^{2}}+\frac{1}{4}\frac{\Delta t}{\Delta x}u_{n,j}\right)u_{n-1,j+1}$$
$$=\left(1-\frac{1}{3\Delta x^{2}}+\frac{3}{4}\frac{\Delta t}{\Delta x}u_{n,j}\right)u_{n,j}+\left(\frac{2}{3\Delta x^{2}}+\frac{\Delta t}{\Delta x}u_{n,j}\right)u_{n-1,j}$$
$$+\left(-\frac{1}{3\Delta x^{2}}+\frac{1}{4}\frac{\Delta t}{\Delta x}u_{n,j}\right)u_{n-2,j}-\frac{3}{4}\frac{\Delta t}{\Delta x}\left(\eta_{n,j}+\eta^{*}_{n,j+1}\right)$$
$$+\frac{\Delta t}{\Delta x}\left(\eta_{n-1,j}+\eta^{*}_{n-1,j+1}\right)-\frac{1}{4}\frac{\Delta t}{\Delta x}\left(\eta_{n-2,j}+\eta^{*}_{n-2,j+1}\right). \quad (7.11)$$

The explicit form of the corrected wave amplitude at the first node can be written as:

$$\eta_{1,j+1} = \eta_{1,j} - \frac{1}{4}\frac{\Delta t}{\Delta x}\left(u_{1,j} + u_{1,j+1}\right)\left(4\eta_{2,j} - \eta_{3,j} - 3\eta_{1,j}\right) - \frac{1}{4}\frac{\Delta t}{\Delta x}\left(1 + \eta_{1,j}\right)\left(4u_{2,j} - u_{3,j} - 3u_{1,j}\right) + 4u_{2,j} - u_{3,j} - 3u_{1,j} \quad (7.12)$$

and at the last node results in:

$$\eta_{n,j+1} = \eta_{n,j} - \frac{1}{4}\frac{\Delta t}{\Delta x}\left(u_{n,j} + u_{n,j+1}\right)\left(3\eta_{n,j} - 4\eta_{n-1,j} + \eta_{n-2,j}\right) - \frac{1}{4}\frac{\Delta t}{\Delta x}\left(1 + \eta_{n,j}\right)\left(3u_{n,j} - 4u_{n-1,j} + u_{n-2,j}\right) + 3u_{n,j} - 4u_{n-1,j} + u_{n-2,j}. \quad (7.13)$$

Equations 7.6 and 7.7 are solved by using the limit conditions given by Equations 7.8-7.13.

7.2 THE PREDICTIONS OF THE MODEL

As it was discussed in Section 5.2, and shown in Figures 5.4-5.8, the slugs are formed as a result of the interference of the two waves. This observation has also been used to formulate a model for slug formation. These figures guided us to conclude that the slug formation phenomenon takes place by following three steps;

1. An incident wave formed by the pulsating column propagates towards the orifice; thus, in the model a soliton whose profile was taken from the image frame was generated. It propagates towards the obstruction. Here, it should be noted that, the obstructions were placed at different locations in the horizontal leg in order to investigate the effect of the orifice location on the slug formation dynamics (Chapter 5). The locations of the flange for accomadating the obstructions are 1.1 m (Position 1) and 2.2 m (Position 2) away from the first elbow (see Figure 3.2). Moreover, for the case without obstruction a 3.3 m long horizontal test section was simulated.

2. A partial reflection of the incident wave takes place at the orifice. The reflection of the wave was carried out by using a coefficient given by Equation 4.2

(see Section 4.2.1). Moreover, the profile of this reflected wave was obtained whenever the incident soliton hit the obstruction.

3. The last step provides us the interference of the two solitons traveling in opposite directions.

In the program, for a given liquid flow rate, the initial profile of the incident wave is kept as constant; then the reflected wave is added to the incident one. In reality this step is a combination of the first and the second steps. Ultimately, this last step is achieved whenever the incident soliton interfere with the reflected one. We assume that a slug forms whenever an interaction occurs and the amplitude of this interaction reaches the inside diameter of the pipe. Therefore, further calculations are not required.

Some typical results are presented in Figures 7.3 - 7.6. Other results are shown in Figures G-1 G-36 in Appendix G.

7.2.1 SLUG FREQUENCY

The frequency for the formation of slugs is calculated due to the sequential periodicity of the interference of the two waves as shown in the Figures 7.3 - 7.6. Thus, we assume that whenever an incident wave propagates towards the orifice and is reflected back from the orifice leading an interference, this phenomenon takes place sequentially, and puts a upper limit on the frequency. This means that each slug will be followed immediately by a new slug precursor. It is obvious that this is not realistic. We should expect to see a time delay between the formation of a slug and a slug precursor. It is clear that this time delay should be added to the calculated period. The total lag time can be given by:

$$T = T_i + T_r + T_{ir}, \tag{7.14}$$

where T_i is the time interval necessary for an incident wave to propagate up to the orifice, T_r is the time interval necessary for an incident wave to be reflected, T_{ir} is the time interval for the incident and the reflected waves to interfere.

Since the time delay between the formation of successive incident waves is not known, this delay is not taken into account in Equation 7.14. Consequently, this will affect the frequency calculation which is obtained as:

$$f = \frac{1}{T}. \tag{7.15}$$

Since the frequency is inversely proportional to the period, an increase in the period will result in a decrease in the frequency. That is why we stated that the predicted frequency should be considered as the upper frequency limit; thus in reality a lower frequency should be expected.

Figures 7.7 to 7.15 show the frequency comparison of the predicted frequencies with the experimental data presented in Chapter 5 (for β ratios and orifice positions with respect to the elbow).

These figures show that the model can predict the results quite well, in particular for the experiments carried out with the orifice placed at Position 2. The difference between predicted and measured frequencies are possible due to the time delay between a slug and its precursor wave, that was not included in these simulations. However, it should be noted that the model predicts a frequency jump at the highest superficial gas velocity. This can be explained by the fact that the taller is the wave, the faster it travels. Consequently, this results in a shorter time necessary for taller waves to reach the obstruction. In turn, this affects the first term in the period equation (Equation 7.14). As this term becomes smaller, the period also becomes smaller. Consequently, the frequency becomes higher. As shown by the figures presented in the in Appendix G, the wave profiles obtained for $Q_l = 0.8\ m^3/h$, which corresponds to highest gas flow rate, are the most pronounced compared to those obtained for other inlet liquid flow rate conditions.

Moreover, it must be emphasized that the time period, T, was obtained from slugs generated by precursor waves that correspond to experiments carried out without orifices. It must be expected a difference if the precursor waves are obtained with orifices.

7.2.2 SLUG PROPAGATION VELOCITY

Figure 7.16 shows a scheme of a slug used for the calculation of the slug propagation velocity. Taking into account the velocity distribution shown in this figure, the slug propagation velocity is calculated from a mass conservation equation that yields:

$$u = \frac{v_1 A_1 + v_2 A_2 - v_3 A_3}{A}, \tag{7.16}$$

where u is the velocity of center of volume, v_1 and v_2 are the horizontal velocity components of the flow in the slug. A_1, A_2 are the corresponding flow cross-sectional areas; v_3 is the horizontal velocity component of the flow that enters into the control volume and A_3 is its corresponding cross-section area.

In order to calculate the slug propagation velocity using Equation 7.16, we used the predicted averaged horizontal velocity component for v_1 and the gravitational wave velocity (given by the equation 6.49) for v_2. Since we do not know the horizontal velocity component of the flow that enters into the control volume, we did not take it into acount in Equation 7.16. Consequently, higher velocity values must be expected from the calculations. These results are shown in Figures 7.17 - 7.26. The comparison shows that the model predictions follow the same tendency as that observed from the experiments (Figure 7.26). Moreover, it should be noted that these predictions depend on neither the position nor the obstruction size as shown by the experimental data.

To the best of the author's knowledge, there is no such a work neither experimental nor theoretical on the characterization of slugs in vertical to horizontal counter-current flow with obstructions. Thus, the present model was compared only with the counter-current slug flow experimental results obtained by using the same experimental facility (Onder, 1998).

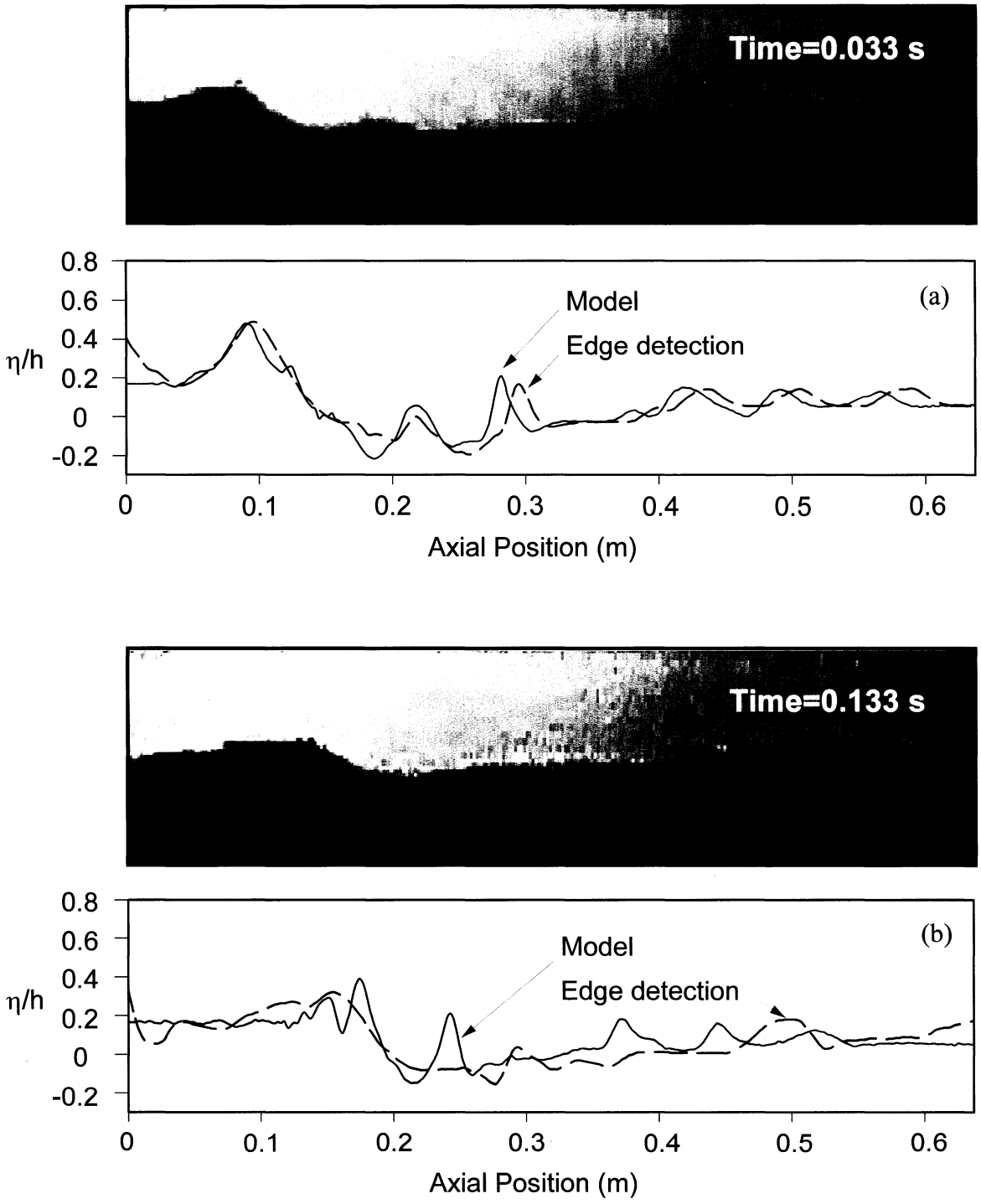

Figure 7.1a.b: Comparison of predicted propagation waves with edge detection data $\left(Q_l = 0.8\,m^3/h, Q_g = 31.5\,m^3/h, \beta = 1.0\right)$.

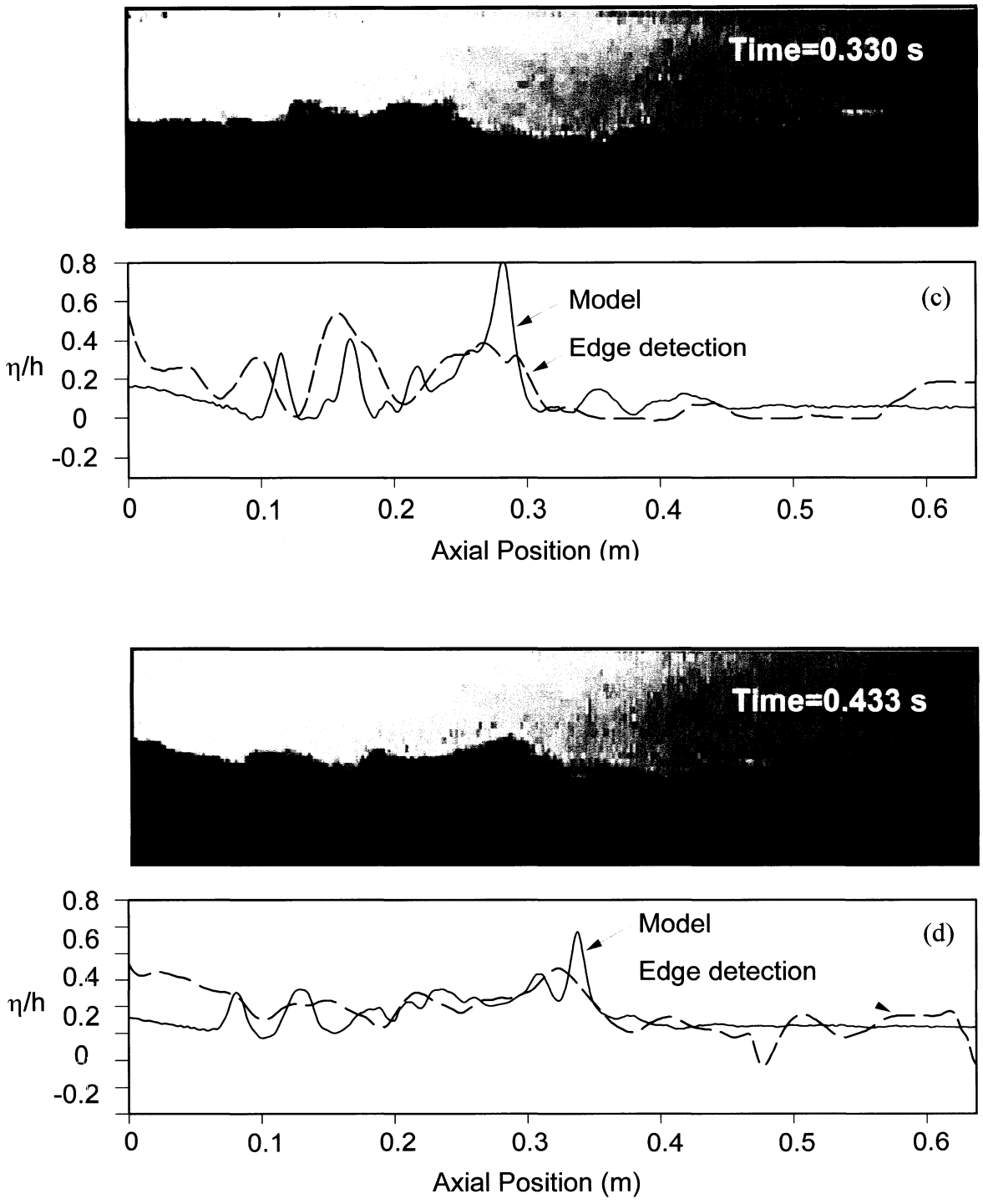

Figure 7.1c.d: Comparison of predicted propagation waves with edge detection data $\left(Q_l = 0.8\,m^3/h, Q_g = 31.5\,m^3/h, \beta = 1.0\right)$.

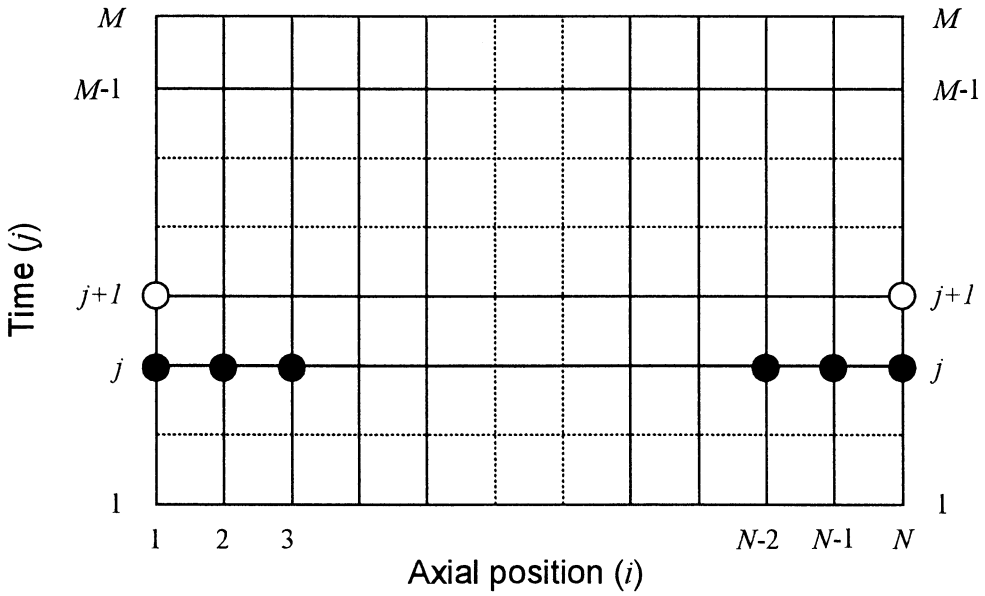

Figure 7.2 Forward and backward difference approximation.

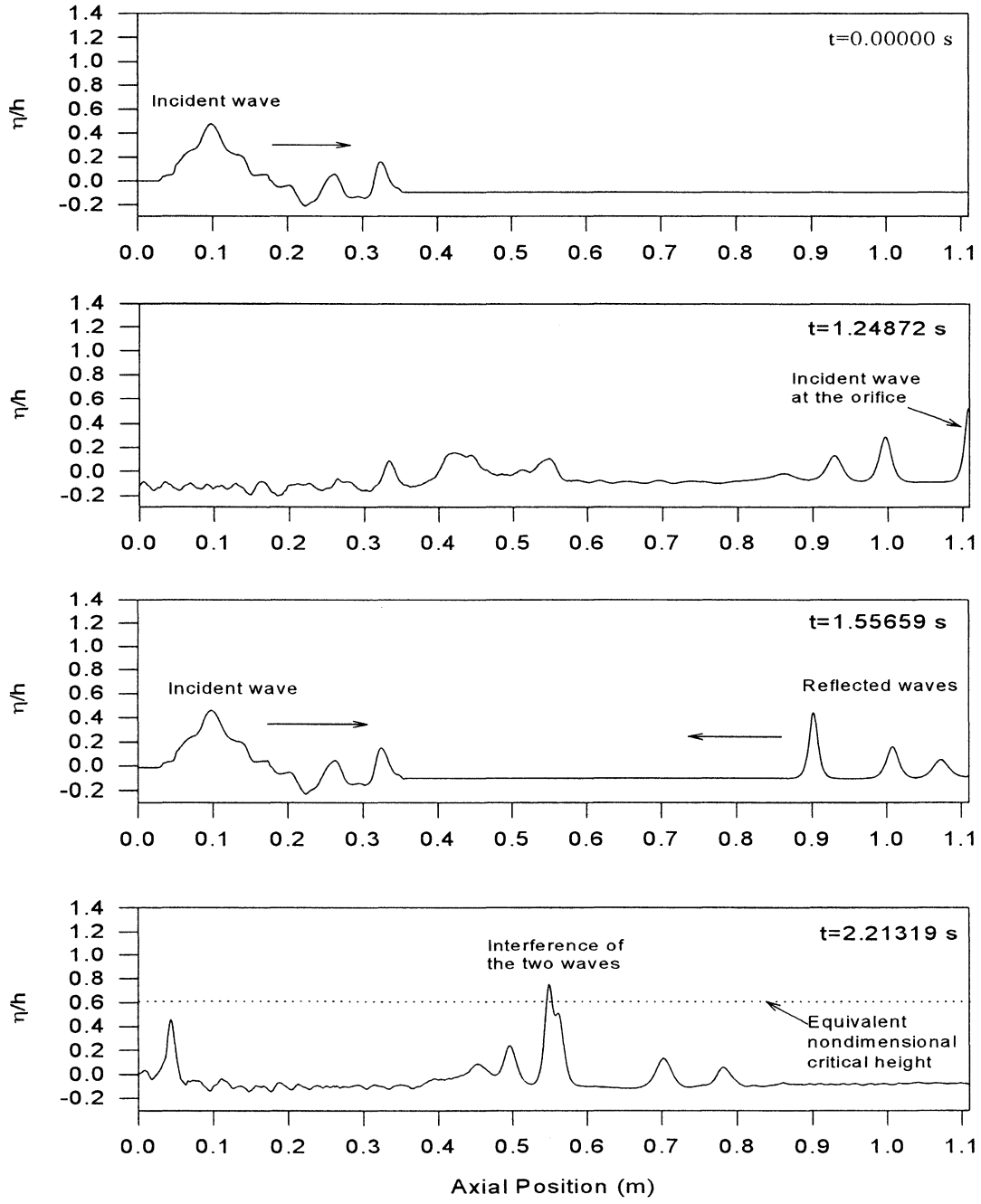

Figure 7.3: Prediction of the formation of a slug ($\beta = 0.66$, Position 1, $Q_l = 0.8\,m^3/h$, $Q_g = 31.5\,m^3/h$).

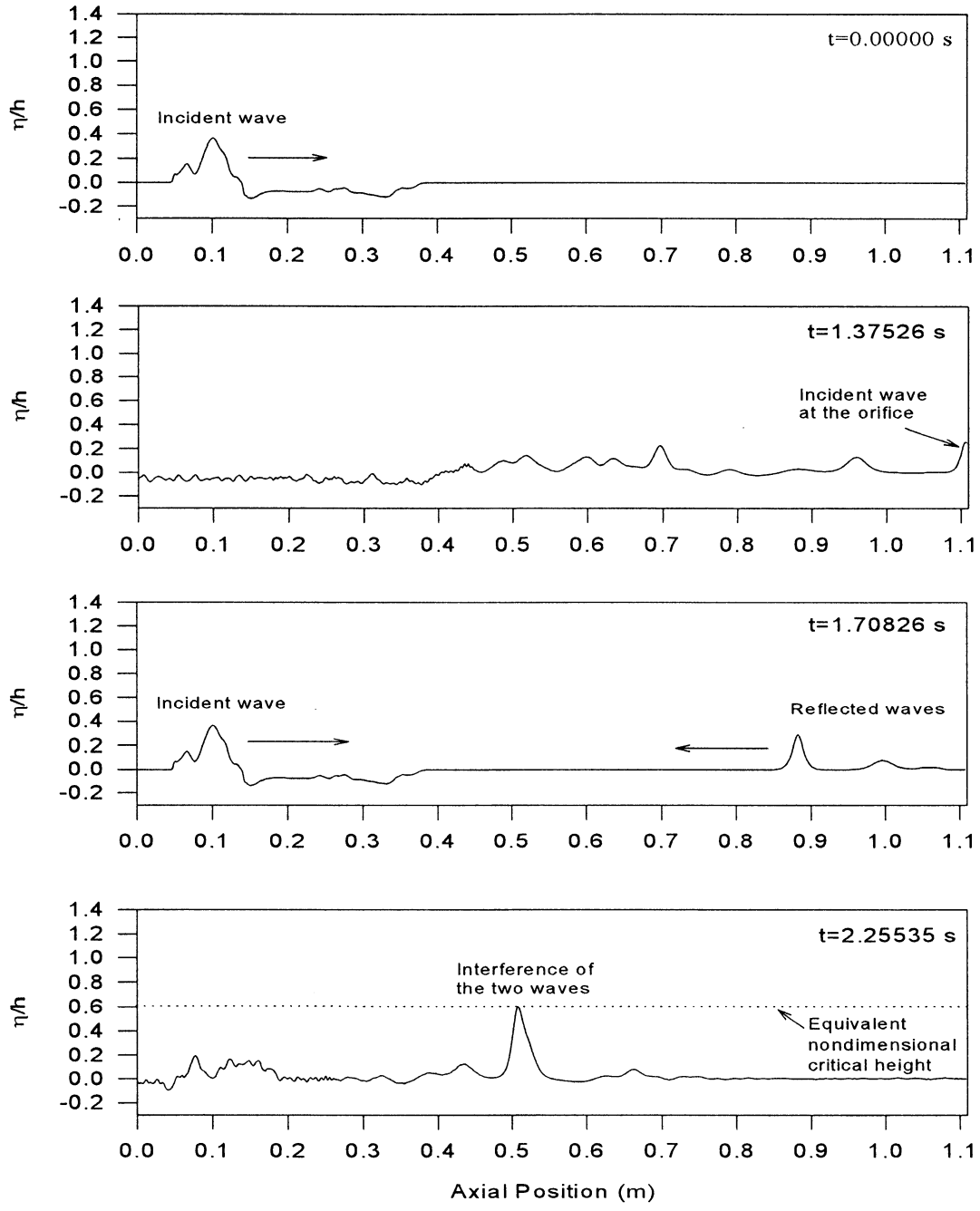

Figure 7.4: Prediction of the formation of a slug ($\beta = 0.66$, Position 1, $Q_l = 1.1\,m^3/h$, $Q_g = 22.2\,m^3/h$).

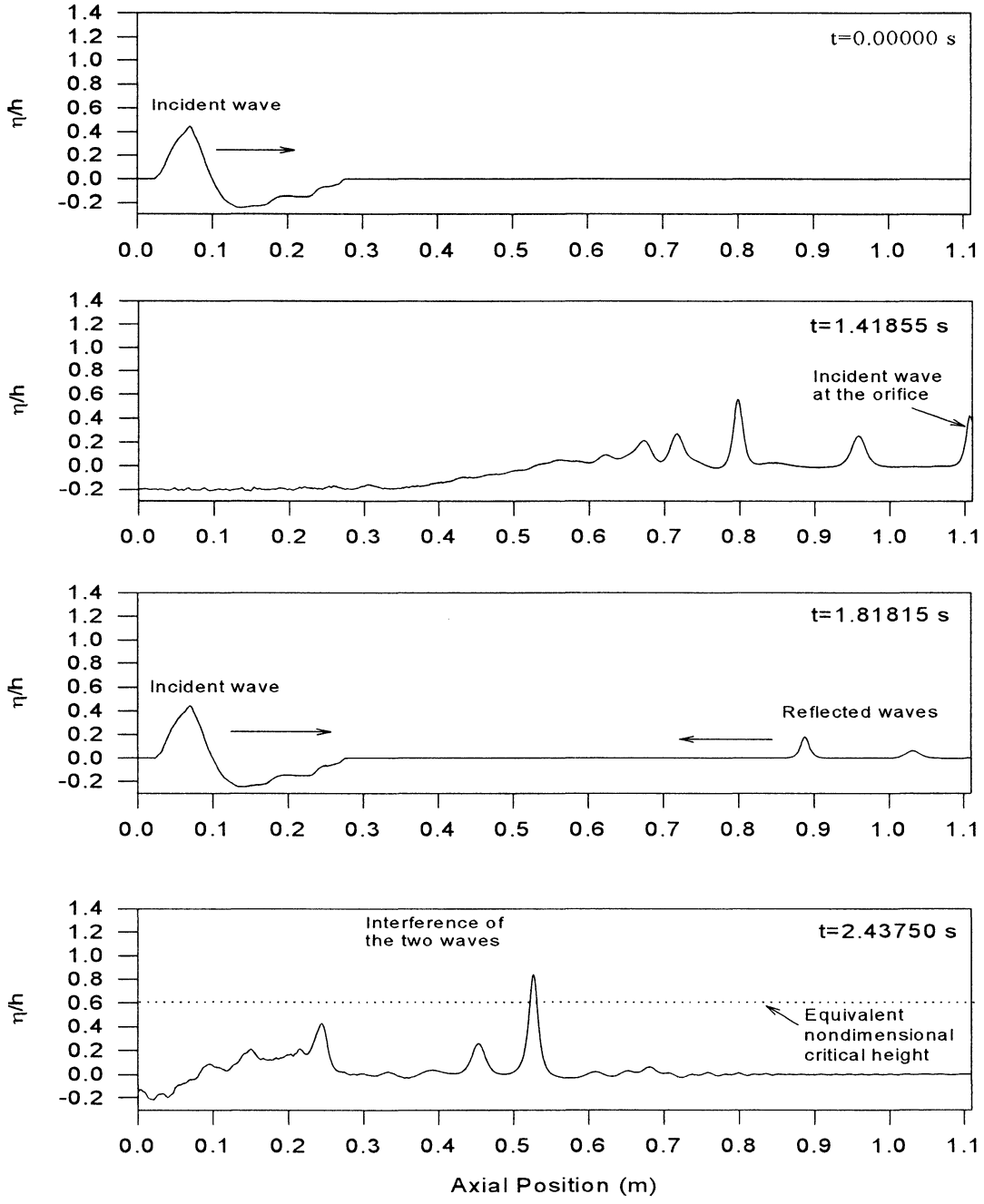

Figure 7.5: Prediction of the formation of a slug ($\beta = 0.66$, Position 1, $Q_l = 1.5\,m^3/h$, $Q_g = 15.8\,m^3/h$).

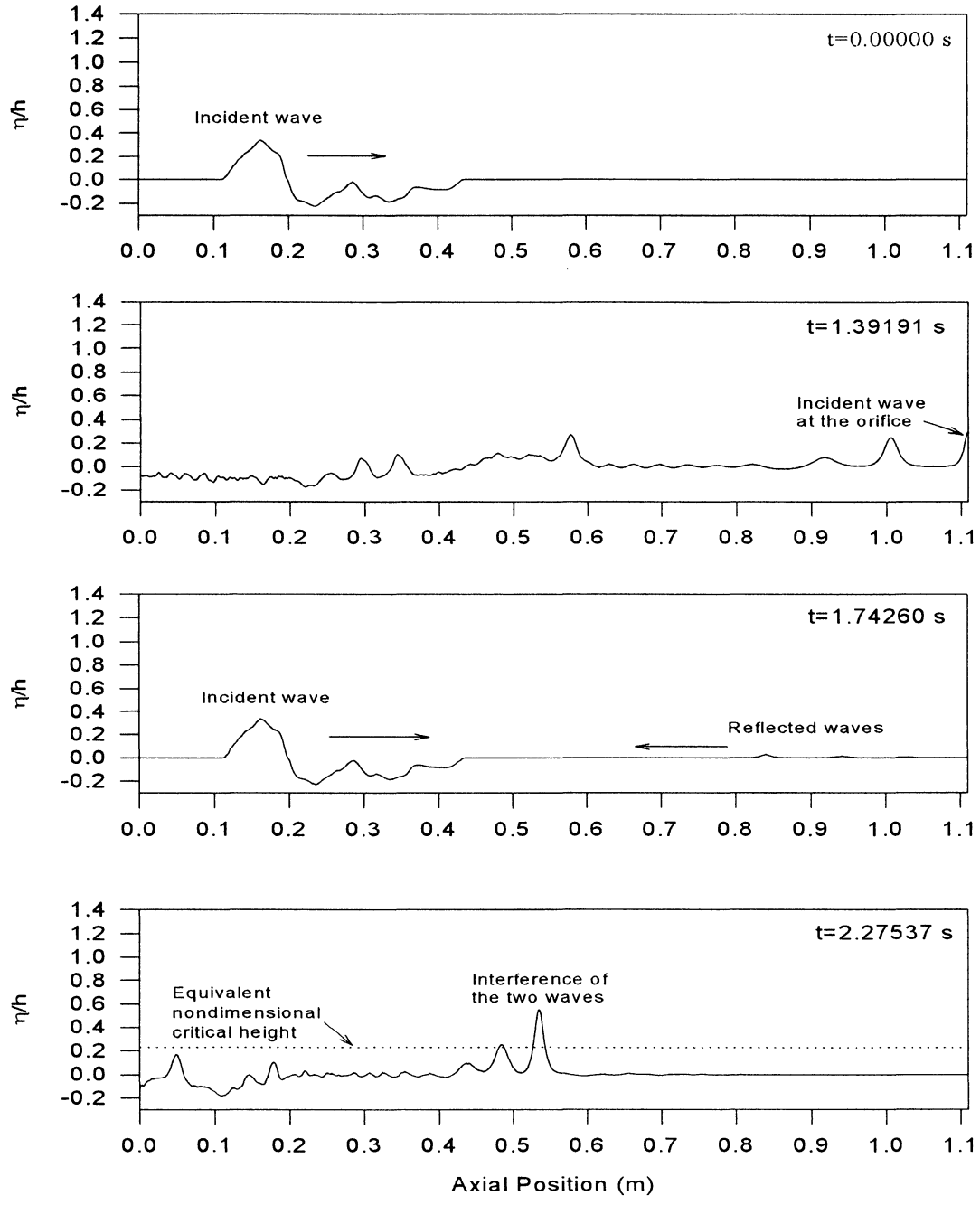

Figure 7.6: Prediction of the formation of a slug ($\beta = 0.66$, Position 1, $Q_l = 1.8\,m^3/h$, $Q_g = 11.4\,m^3/h$).

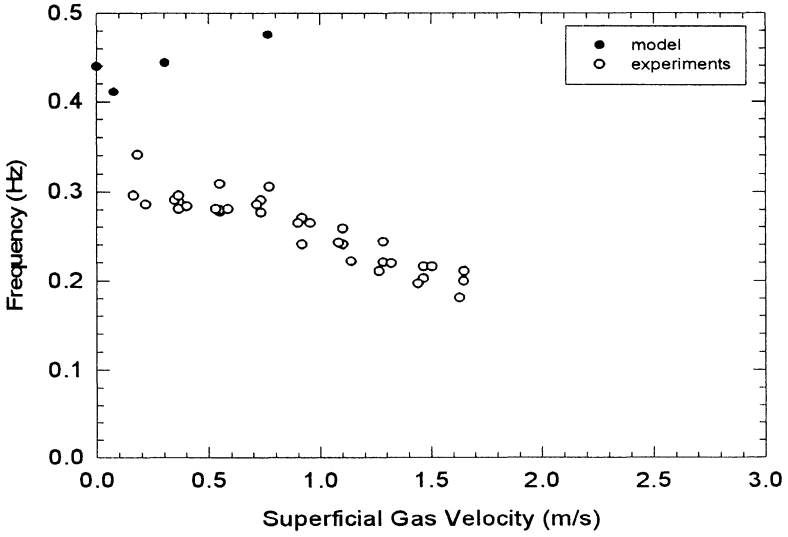

Figure 7.7: Comparison of the model prediction with slug frequency data ($\beta = 0.66$, Position 1).

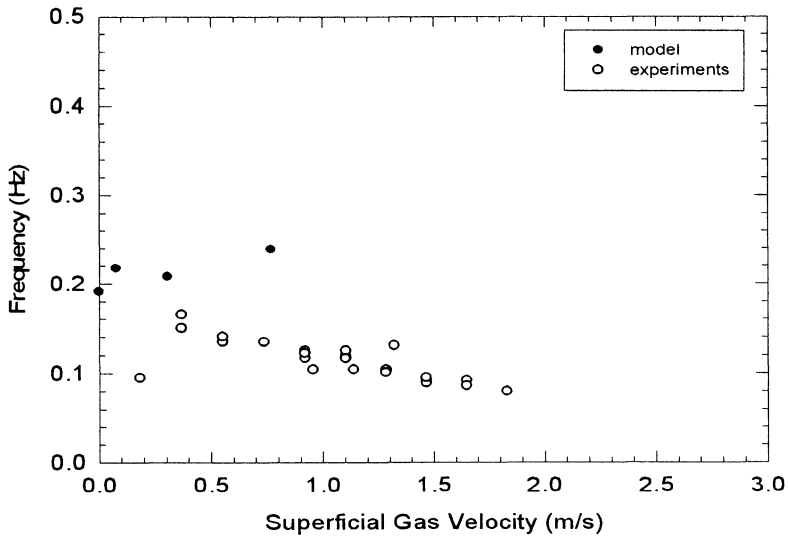

Figure 7.8: Comparison of the model prediction with slug frequency data ($\beta = 0.66$, Position 2).

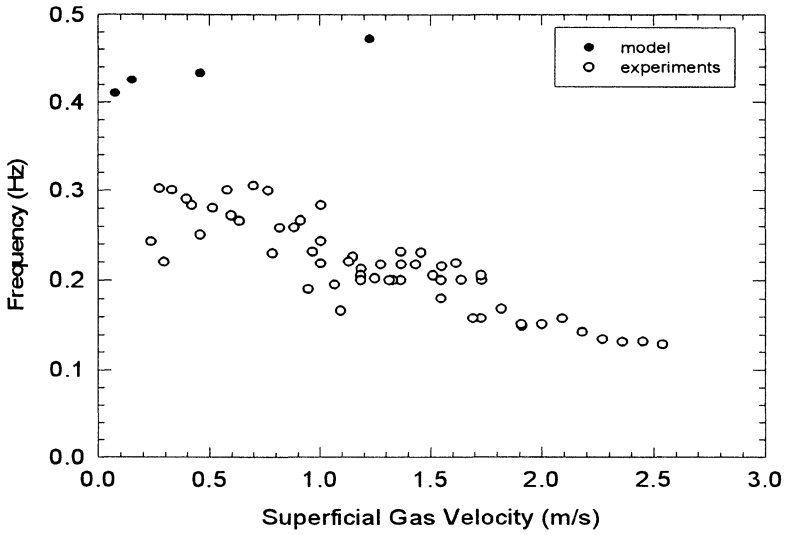

Figure 7.9: Comparison of the model prediction with slug frequency data ($\beta = 0.72$, Position 1).

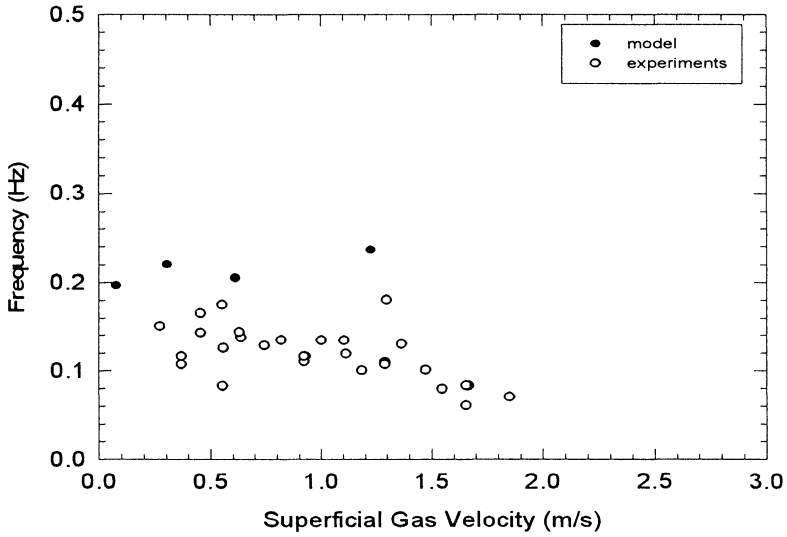

Figure 7.10: Comparison of the model prediction with slug frequency data ($\beta = 0.72$, Position 2).

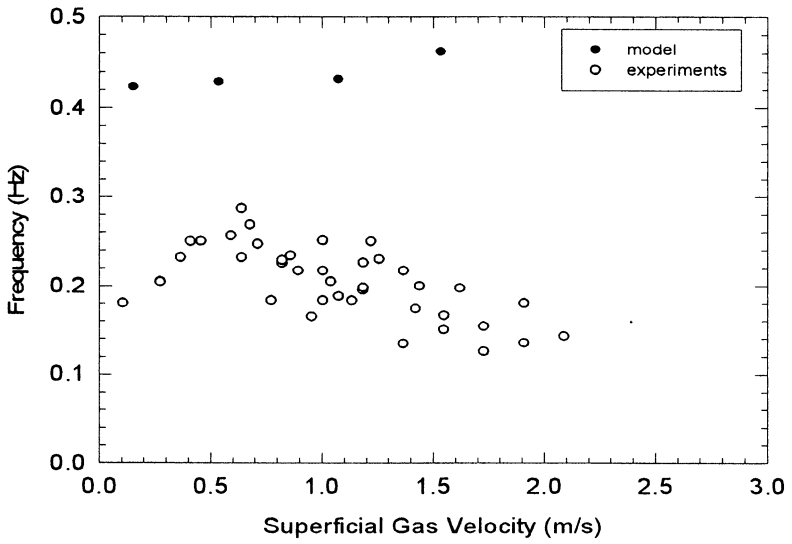

Figure 7.11: Comparison of the model prediction with slug frequency data ($\beta = 0.77$, Position 1).

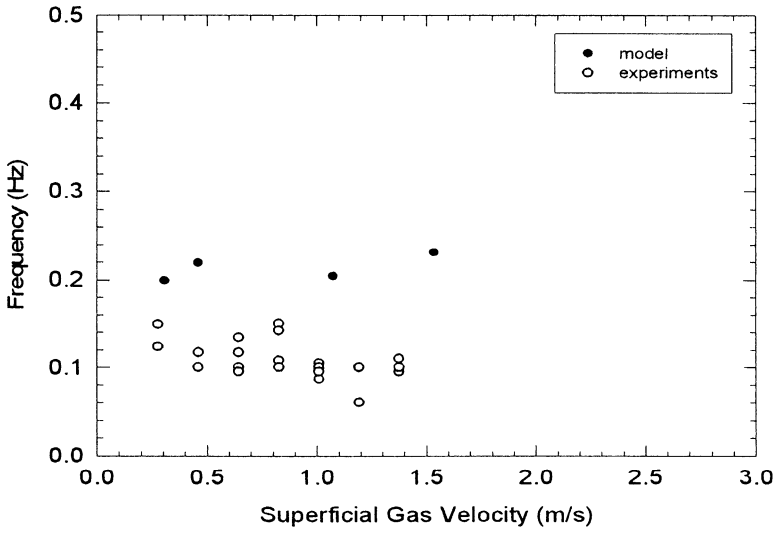

Figure 7.12: Comparison of the model prediction with slug frequency data ($\beta = 0.77$, Position 2).

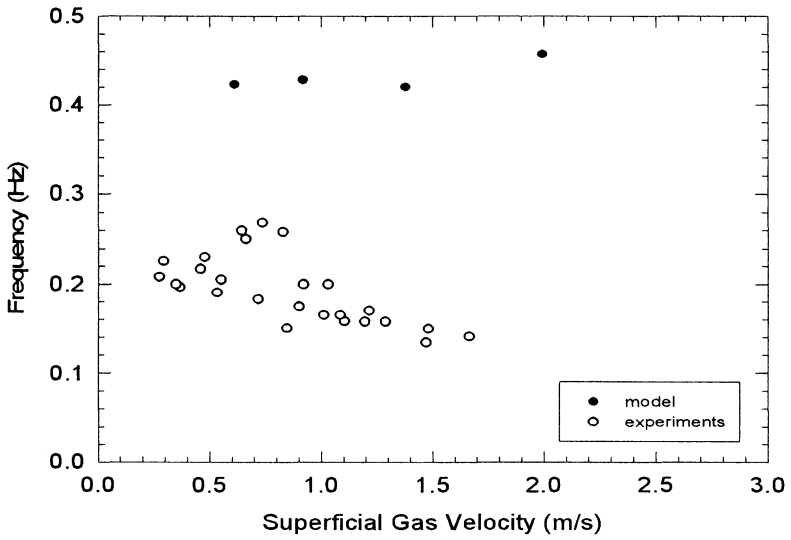

Figure 7.13: Comparison of the model prediction with slug frequency data ($\beta = 0.83$, Position 1).

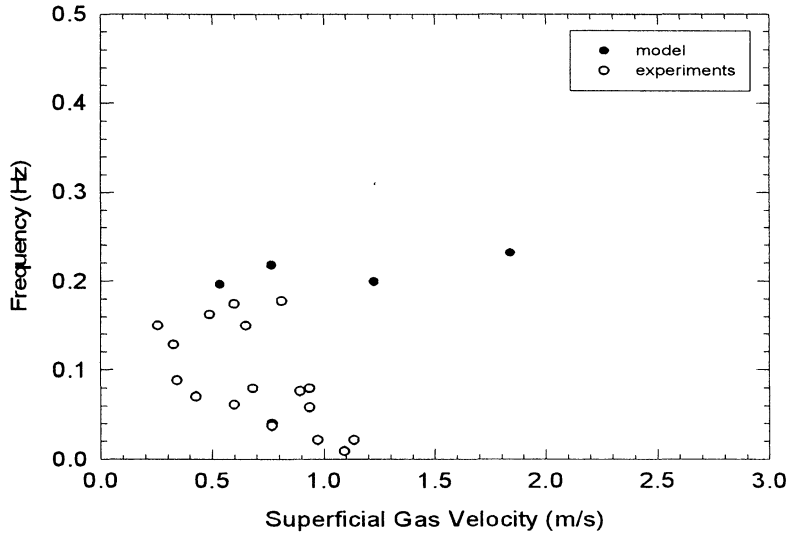

Figure 7.14: Comparison of the model prediction with slug frequency data ($\beta = 0.83$, Position 2).

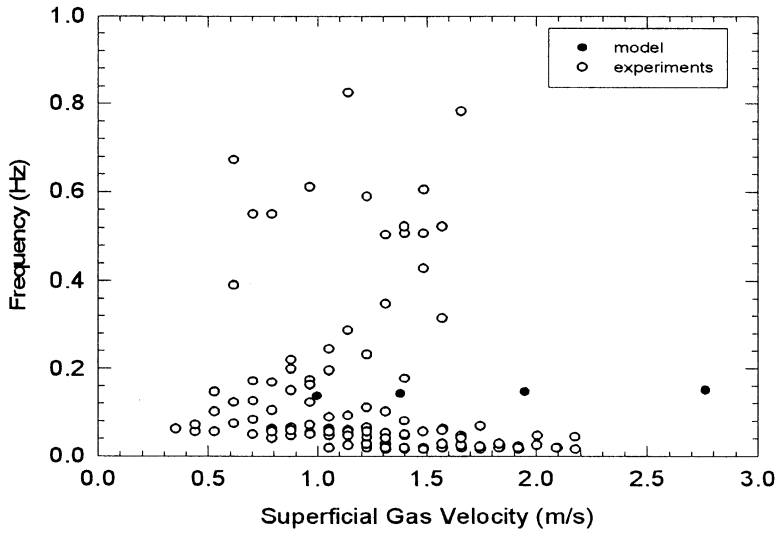

Figure 7.15: Comparison of the model prediction with slug frequency data ($\beta = 1.00$).

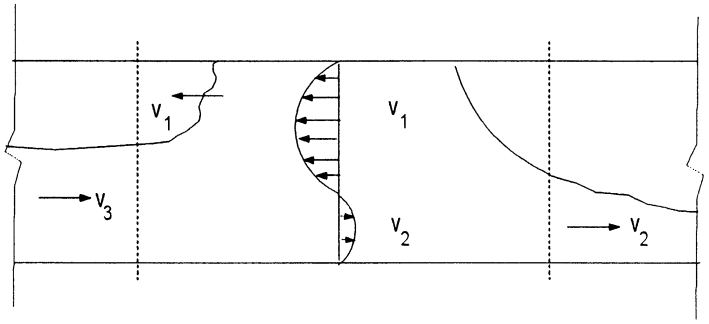

Figure 7.16: The slug scheme used for modeling the slug propagation velocity.

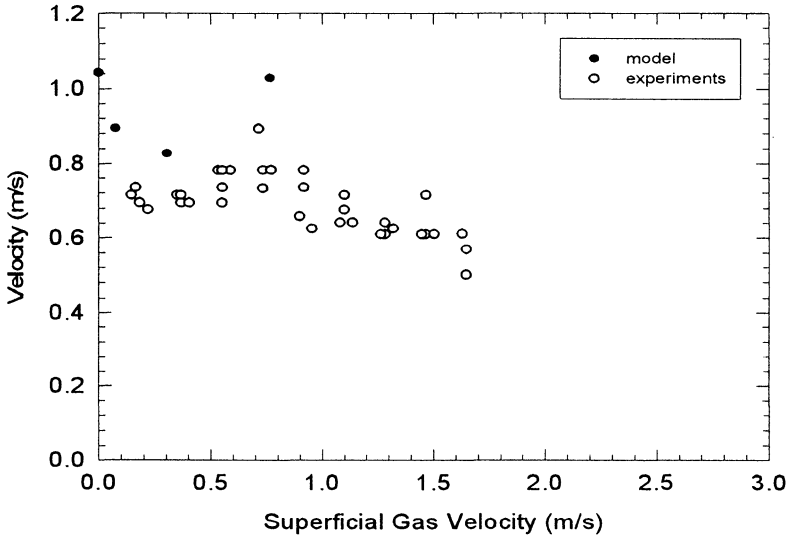

Figure 7.17: Comparison of the model prediction with data of slug propagation velocity ($\beta = 0.66$, Position 1).

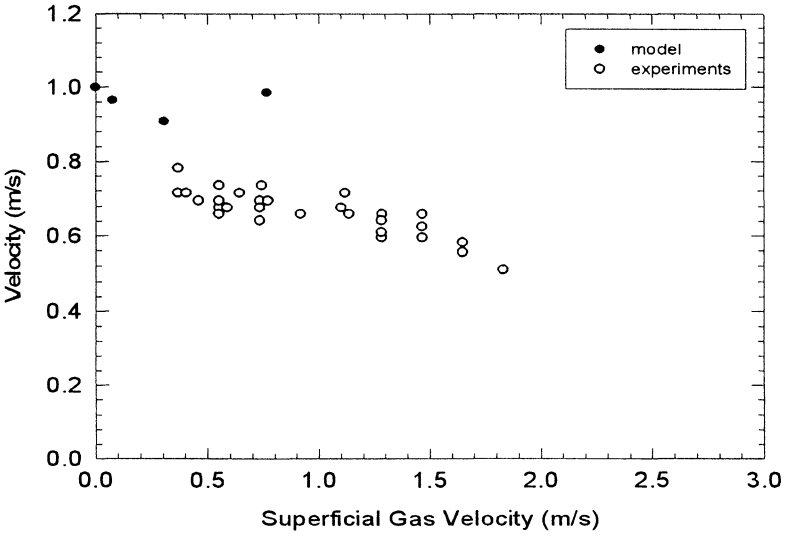

Figure 7.18: Comparison of the model prediction with data of slug propagation velocity ($\beta = 0.66$, Position 2).

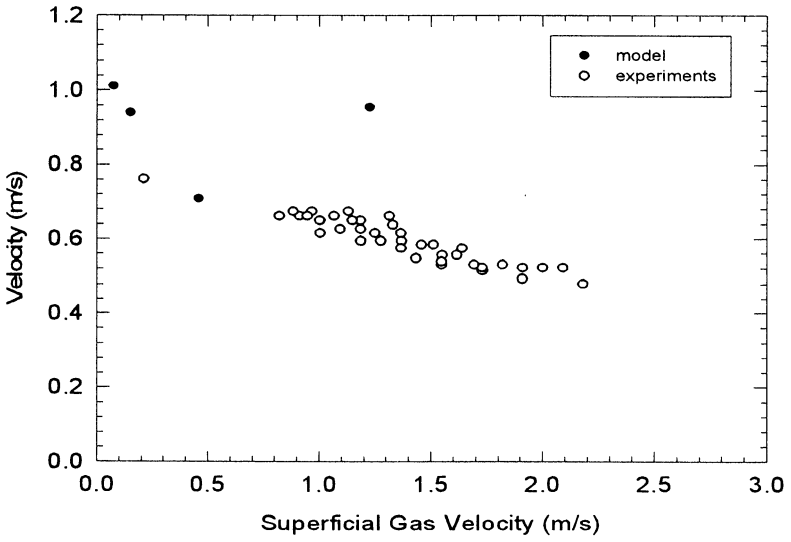

Figure 7.19: Comparison of the model prediction with data of slug propagation velocity ($\beta = 0.72$, Position 1).

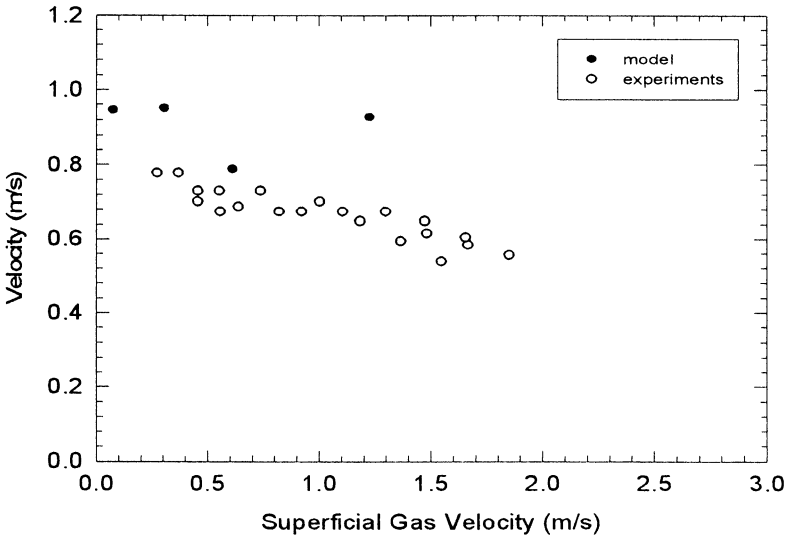

Figure 7.20: Comparison of the model prediction with data of slug propagation velocity ($\beta = 0.72$, Position 2).

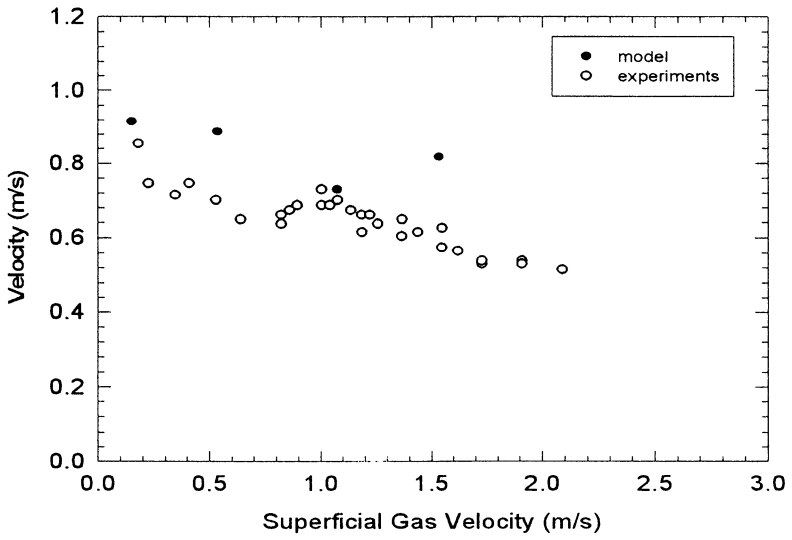

Figure 7.21: Comparison of the model prediction with data of slug propagation velocity ($\beta = 0.77$, Position 1).

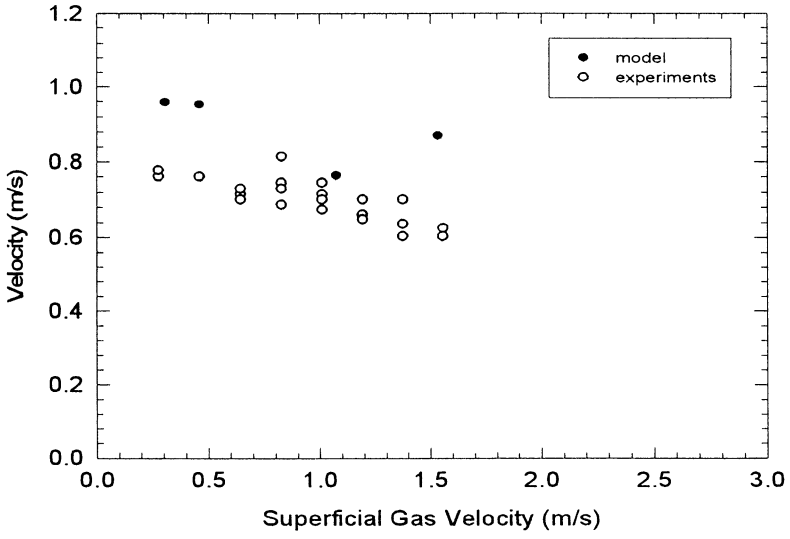

Figure 7.22: Comparison of the model prediction with data of slug propagation velocity ($\beta = 0.77$, Position 2).

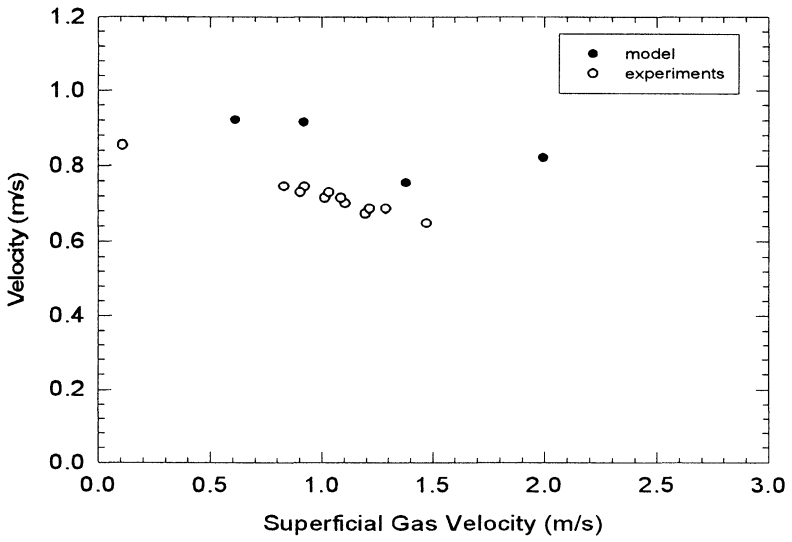

Figure 7.23: Comparison of the model prediction with data of slug propagation velocity ($\beta = 0.83$, Position 1).

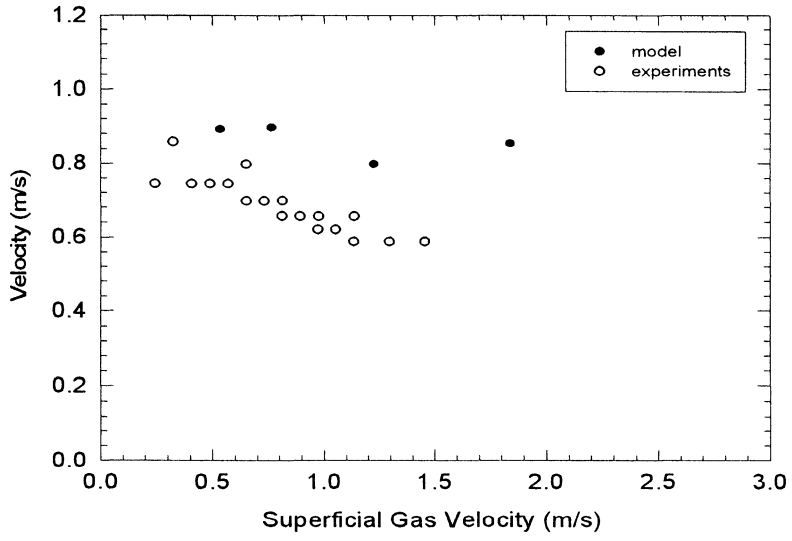

Figure 7.24: Comparison of the model prediction with data of slug propagation velocity ($\beta = 0.83$, Position 2).

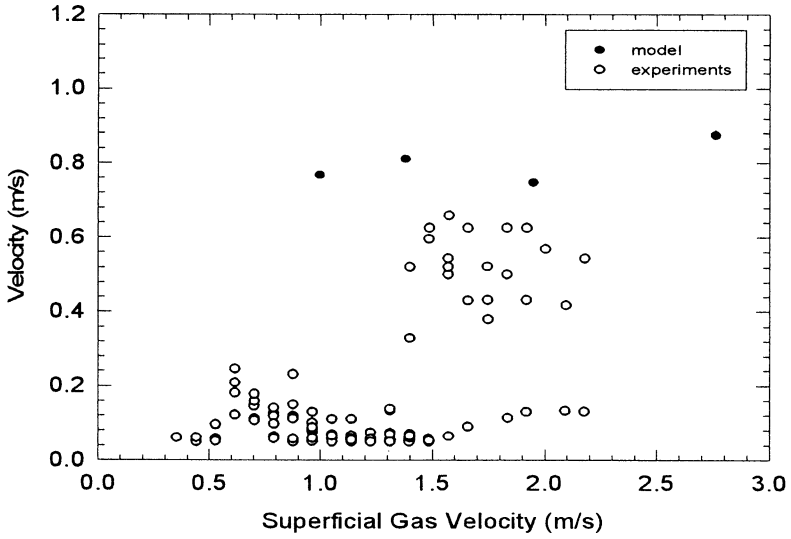

Figure 7.25: Comparison of the model prediction with data of slug propagation velocity ($\beta = 1.00$).

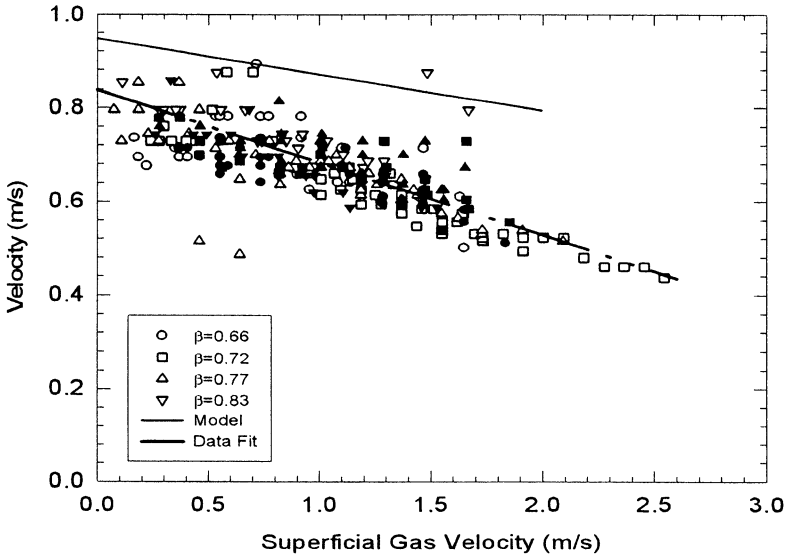

Figure 7.26: The comparison of the slug propagation velocity as predicted by the model with the experimental results (in the figure, empty symbols represent the experiments carried out with the orifice located at Position 1 and the solid symbols with the orifice located at Position 2).

CHAPTER 8

CONCLUSIONS AND RECOMMENDATIONS

The comparison of the experimental results of Zabaras (1985) with those of Tye (1998) shows that the partial liquid delivery region, i.e., from the onset of flooding to the zero penetration point, in vertical tubes is much smaller than in vertical-to-horizontal ones. Therefore, the study of the partial liquid delivery in vertical-to-horizontal tubes becomes important. Since the slugging phenomena occur in this flow region, their comprehension is absolutely required. Moreover, it must be pointed out that slugging conditions correspond to intermittent emergency cooling of the reactor core. Thus, a better understanding of the slugging phenomena in pipes having the same geometry as the header-feeder system in CANDU reactors will help to improve safety analysis.

In this thesis, a model has been presented to predict the formation of a slug in a tubular test section containing both a vertical and a horizontal leg in which an obstruction is placed. Contrary to the concept of the formation of a co-current slug, based on the Kelvin-Helmholtz instability, counter-current slugs, in the test section described as above, are formed as a result of the interference of two solitons. The model is based on the visual observations of the phenomena that can be summarized as follows: starting at the flooding point, a pulsating column forms in the vertical leg; this pulsating column provokes the formation of high amplitude waves in the elbow. These waves propagate downstream in the horizontal leg until they reach the orifice. At this location, they are partially reflected backward towards the elbow. When an incident and a reflected waves encounter one to the other, a constructive interference takes place. This interference provokes a sudden increase in the amplitude that can reach the inside diameter of the pipe. Under such a condition it has been visually observed that a slug is formed in the horizontal leg. It is important to mention that the continuos pulsating column

in the vertical leg maintains the generation of incident waves in the horizontal leg. During the experiments, it was also visually observed that two or three wave components of the packet can start lagging with respect to the wave front. Along the tube, these components start moving at a lower pace than the wave packet. Finally, they are separated from the packet keeping the number of the components in the wave packet constant.

Such observations guided us to use the Korteweg–de Vries (KdV) or Boussinesq type of equations in the model because of their dispersive character. On the other hand, the KdV equation cannot be used for this kind of system because of its uni-directional nature that do not agree with our visual observations. Therefore, a solution that allows us to calculate two solitons propagating in the opposite directions was retained for this work. Thus, instead of using only one equation which is a combination of conservation of mass and momentum, as is the case of Korteweg–de Vries equation, we use a set of mass and momentum equations as proposed by Boussinesq.

Peregrine (1966) has numerically studied the KdV equation as well as the mass and momentum consevation equations for a uni-directional propagation of a soliton. He found that straightforward finite difference approximations were stable for the KdV equation and unstable for the separate form of the conservation equations. Thus, he proposed a numerical scheme for the conservation of mass and momentum equations. Therefore, this numerical scheme has been used for solving the present model. The continuity equation is initially used to calculate the amplitude for an advanced time step. Then, this amplitude is used to solve the momentum equation which yields the averaged horizontal velocity. Substituting this horizontal velocity into the continuity equation, the corrected amplitude is finally obtained.

It must be pointed out that, the initial conditions for the present model are obtained from the image frames collected during the wave propagation experiments. After processing the images with an edge detector, the profile of a probable incident wave is saved and then prepared as an input file for the soliton program. The boundary conditions are obtained from the second forward and backward

difference approximations as have been discussed in Chapter 7.

To the best of author's knowledge, there is no such a study in the open literature, for slug flows in a test section containing both vertical and horizontal legs with obstructions. For this reason, the predictions of the model have been compared with the only available data, the data obtained in the course of this study, using the experimental set up as described in Chapter 3. These results include the slug frequency and the slug propagation velocity. The predicted slug frequency is obtained from the period-frequency relation, and the period is considered as the time delay between the formation of a slug precursor wave and the formation of a slug itself. As has been discussed in Chapter 7, this period consists of three lag times; first one is the propagation time of the incident wave up to the obstruction, the second lag time is the propagation time of the reflected wave up to the location where this wave is feedbacked to the program as an initial condition for the second execution of the program with two solitons, and the third one is the propagation time of two solitons up to the location where they can interfere with each other. These calculations are based on the assumption that a sequential periodicity exists, i.e., whenever an incident wave propagates to the orifice and is reflected from the orifice, it leads to an interference of the two solitons resulting in the formation of slugs, but this is obviously not realistic. Moreover, we should expect to see a time delay between the formation of a slug and its precursor wave and this time delay should be added to the calculated period which will decrease the slug frequency. As has been discussed in Chapter 7, this time delay was not taken into account; this fact may explain the differences observed between the model predictions and the experimental data. Moreover, it must be emphasized that the time period was obtained from slugs generated by precursor waves that correspond to experiments carried out without orifices. It must be expected a difference if the precursor waves are obtained with orifices.

The slug propagation velocity has been calculated based on the mass conservation equation. The comparison between the model predictions and the data shows that the model is able to predict the experimental trends. In particular, the predictions

confirm the experimental observation that the slug propagation velocity depends on neither the position nor the size of the obstruction.

The predictions of the model are, in general, close to the experimental results. However, there are some other aspects that should be included if a more elaborated approach to the slug formation would be carried out. Some of these aspects are recommanded for future studies:

1. It must be noted that the proposed model does not include dissipation terms. It could be interesting to add an appropriate dissipation term to the Boussinesq equation. The viscosity may affect the frequency since this term may cause the solitons to slow down, by changing their amplitude.

2. An experimental study should be performed to establish a physical relation between the frequency of the pulsating column in the vertical leg and the formation of high amplitude waves in the horizontal leg. This study may help to determine the time delay between slug precursor waves and introduce it into the model. It is expected that this information will help in calculating a more realistic slug frequency.

3. An experimental work should be carried out to validate the dispersion relation of surface waves in counter-current two phase flows. This study may help to justify the equations used to model the dispersive water waves.

BIBLIOGRAPHY

ANDRESUSSI, P., BENDIKSEN, K. H. and NYDAL, O. J., [1993]; "Void distribution in slug flow." Int. J. Multiphase Flow, Vol. 19, pp. 817-828.

ARDRON, K. H. and BANERJEE, S., [1986]; "Flooding in an elbow between a vertical and horizontal or near horizontal pipe, Part II : Theory." Int. J. Multiphase flow, Vol. 12, pp. 543-558.

BAKER, D., [1954]; "Simultaneous Flow of oil and gas." Oil and Gas J., Vol. 53, pp. 183-195.

BANKOFF, S. G. and LEE, S. C., [1986]; "A critical review of the flooding literature." in : Multiphase Science and Technology, Vol. 2, Chap. 2 (*Edts.*:Hewitt, G. F., Delhaye, J. M. and Zuber, N.). Hemisphere, New York.

BARNEA, D., BEN YOSEPH, N. and TAITEL, Y., [1986]; "Flooding in inclined pipes - Effect of entrance section." The Canadian Journal of Chemical Engineering, Vol. 64, pp. 177-184.

BÉDARD, S., [1997]; "Effet de la position d'une obstruction par rapport à un coude dans un écoulement diphasique contre-courant." Thése de maitrise en génie mécanique, École Polytechnique, Université de Montréal.

BHARATAN, D., WALLIS, G. B. and RICHTER, H. J., [1978]; "Air-water countercurrent annular flow in vertical tubes." EPRI Report, No. NP-786.

BHARATAN, D., WALLIS, G. B. and RICHTER, H. J., [1979]; "Air-water countercurrent annular flow in vertical tubes." EPRI Report, No. NP-1165.

BHARATAN, D. and WALLIS, G. B., [1983]; "Air-water counter-current annular flow." Int. J. Multiphase Flow, Vol. 9, pp. 349-366.

BOUSSINESQ, J., [1871]; "Theorié de l'intumescence liquid appelée onde solitaire ou de translation, se propageant dans un canal rectangulaire." Comptes Rendus

Acad. Sci. (Paris), Vol.72, pp. 755-759.

CELATA, G. P., CUMO, N., FARELLO, G. E. and SETARO, T., [1989]; "The influence of flow obstructions on the flooding phenomena in vertical channels."Int. J. Multiphase Flow, Vol. 15, pp. 227-239.

CHU, K. J., [1968]; "An analysis of slug frequency in two phase horizontal slug flow." M.S. Thesis, Univ. of Houston.

CHUNG, M. H., LEE, B. R., KIM Y. S. and NAM, H. Y., [1995]; "A criterion for the onset of slugging in horizontal stratified air-water counter-current flow." Procedings of the 7^{th} International Meeting on Nuclear Reactor Thermal-Hydraulics, NURETH-7.

CLIFT, R., PRITCHARD, C. L. and NEDDERMAN, R. M., [1966]; "The effect of viscosity on flooding conditions in wetted wall columns." Chem. Eng. Sci., Vol. 21, pp. 87-95.

CROWLEY, C. J., WALLIS, G. B. and BARRY, J. J., [1992]; "Validation of a one-dimensional wave model for the stratified-to-slug flow regime transition, with consequences for wave growth and slug frequency." Int. J. Multiphase Flow, Vol. 18, pp. 249-271.

DUKLER, A. E. and HUBBARD, M. G., [1975]; "A model for gas liquid slug flow in horizontal and near horizontal tubes." Ind. Engng. Chem. Fundam., Vol. 14, pp. 337-347.

DUKLER, A. E. and SMITH, L., [1979]; "Two-phase interaction in counter-current flow; Studies of the flooding mechanism." NUREG/CR-0617.

DUKLER, A. E., SMITH, L. and CHOPRA, A., [1984]; "Flooding and upward film flow in tubes; I. Experimental studies." Int. J. Multiphase Flow, Vol. 10, pp. 585-597.

FAN, Z., RUDER, Z. and HANRATTY, T. J., [1993]; "Pressure profiles for slugs in horizontal pipelines." Int. J. Multiphase Flow, Vol. 19, pp. 421-437.

HAWLEY, D. L. and WALLIS, G. B., [1982]; "Experimantal study of liquid film fraction and pressure drop characteristics in vertical counter-current annular flow." EPRI NP-2280. Electric Power Res. Inst., Palo Alto California.

HEWITT, G. F. and WALLIS, G. B., [1963]; "Flooding and associated phenomena in falling film flowin a vertical tube." AERE-R4032, UKAEA, Harwell, UK.

HEWITT, G. F., [1989]; "Counter-current two-phase flow." Proc. NURETH-4 (4^{th} Int. Top Mtg. On Nuclear Reactor Thermal Hydraulics) Vol. 2.

IMURA, H., KUSUDA, H. and FUNATSU, S., [1977]; "Flooding velocity in a counter-current annular two-phase flow." Chem. Engng Sci., Vol. 32, pp. 79-87.

ISHII, M. and GROLMES, M. A., [1975]; "Inception criteria for droplet entrainment in two-phase concurrent film flow." AICHE J. Vol. 21.

JEFFREYS, H., [1925]; "On the formation of water waves by wind." Proc. Roy. Soc. Lond (A), Vol. 107, pp. 189.

JEPSON, W. P. and TAYLOR, R. E., [1993]; "Slug flow and its transitions in large diameter pipes." Int. J. Multiphase Flow Vol. 19, pp. 411-420.

JOHNSON, R. S., [1997]; "A modern introduction to the mathematical theory of water waves." Cambridge University Press.

JOHNSTON, A. J., [1985]; "Transition from stratified to slug regime in counter-current flow." Int. J. Multiphase Flow Vol. 11, pp. 31-41.

KAWAJI, M., THOMSON, L. A. and KRISHNAN, V. S., [1989]; "Analysis of counter-curent flooding data obtained in vertical-to-inclined pipes containing elbows of varying angle." CNS 15^{th} Annular Reactor Simulation symposium, Missasauga, Ont.

KAWAJI, M., LOTOCKI, P. A. and KRISHNAN, V. S., [1993]; "Counter-curent flooding in pipes containing multiple elbows and an orifice." JSME, Ser. B., Vol. 36, pp. 95-110.

KORDYBAN, E. S. and RANOV, T., [1970]; "Mechanism of slug formation in horizontal two-phase flow." J. Basic Eng., Vol. 92, pp. 857-864.

KORDYBAN, E. S., [1977]; "Some characteristics of high waves in closed channels approaching Kelvin-Helmholtz Instability." Trans. ASME, Journal of Fluids Engineering, Vol. 99, pp. 339-346.

KORDYBAN, E. S., [1985]; "Some details of developing slugs in horizontal two-phase flow." AIChE Journal, Vol. 31, pp. 802-806.

KROWLEWSKI, S. SM., [1980]; "Flooding in a simulated nuclear reactor hot leg." Bachelor's Project, MIT.

LACY, C. E. and DUKLER, A. E., [1994]; "Flooding in vertical tubes-I; Experimental studies of the entry region." Int. J. Multiphase Flow, Vol. 20, pp. 219-233.

LAMB, H., [1945]; "Hydrodynamics." Dover Pub. Co., New York, Art. 231 and 232.

LEE, S. C. and BANKOFF, S. G., [1983]; "Stability of steam-water countercurrent flow in an inclined channel: Flooding." Journal of Heat Transfer (ASME), Vol. 105, pp. 713-718.

MCQUILLAN, K. W. and WHALLEY, P. B., [1985]; "A comparison between flooding correlations and experimental flooding data for gas liquid flow in vertical circular tubes." Chem. Eng. Sci., Vol. 40, pp. 1425-1440.

MEYER, B. and GIOT, M., [1987]; "Experiments and modeling of flooding phenomena." Nuclear Engineering and Design, Vol. 99, pp. 75-84.

MISHIMA, K. and ISHII, M., [1980]; "Theoretical prediction of onset of horizontal slug flow." J. Fluids Eng., Vol. 102, pp. 441-445.

MONZA, A. A., PARAS, S. V. and KARABELAS, A. J., [2002]; "The influence of small tube diameter on falling film and flooding phenomena." Int. J. Multiphase Flow, Vol. 28, pp. 1311-1331.

NICHOLSON, M. K., AZIZ, K. and GREGORY, G. A., [1978]; "Intermittent two phase flow in horizontal pipes: Predictive models." The Canadian Journal of Chemical Engineering, Vol. 56, pp. 653-663.

ONDER, N., [1998]; "Counter-current slug flow in a vertical to horizontal tube simulating header feeder system having obstructions in CANDU reactors." MS Thesis, Istanbul Technical University.

PEREGRINE, D. H., [1966]; "Calculations of the development of an undular bore." J. Fluid Mech., Vol. 25, pp. 321-330.

PRATT, W. K., [1991]; "Digital Image Processing." Wiley-Interscience Publication, New-York.

PUSHKINA, O. L. and SOROKIN, U. L., [1969]; "Breakdown of liquid film Motion in vertical tubes." Heat Transfer, Soviet Research, Vol. 1, pp. 56-64.

RICHTER, H. J., [1981]; "Flooding in tubes and annuli." Int. J. Multiphase Flow, Vol. 7, pp. 647-658.

RUDER, Z., HANRATTY, P.J. and HANRATTY, T. J., [1989]; "Necessary conditions for the existence of stable slugs." Int. J. Multiphase Flow 15, pp. 209-226.

SCHICHT, H. H., [1969]; "Flow patterns for adiabatic two-phase flow of water and air within a horizontal tube." Verfahrenstecknik, Vol. 3, pp. 153-172.

SIDDIQUI, H., BANERJEE, S. and ARDRON, K. H., [1986]; "Flooding in an elbow between a vertical and a horizontal or near horizontal pipe - Part I: Experiments." Int. J. Multiphase Flow, Vol. 12, pp. 531-541.

SUZUKI, S. and UEDA, T., [1977]; "Behaviour of liquid films and flooding in counter-current two-phase flow- Part I Flow in circular tubes." Int. J. Multiphase Flow, Vol. 3, pp. 517-532.

TAITEL, Y. and DUKLER, A. E., [1976]; "A model for predicting flow regime transitions in horizontal and near horizontal gas-liquid flow." AIChE Journal, Vol.

22, pp. 47-55.

TAITEL, Y. and DUKLER, A. E., [1977]; "A model for slug frequency during gas-liquid flow in horizontal and near horizontal pipes." Int. J. Multiphase Flow, Vol. 3, pp. 585-596.

TRONCONI, E., [1990]; "Prediction of slug frequency in horizontal two phase slug flow." AIChE Journal, Vol. 36, pp. 701-709.

TYE, P. [1998]; "Counter-current flow and flooding in vertical and horizontal tubes with and without obstructions." Ph.D. Thesis, École Polytechnique de Montréal.

VERMEULEN, L. R. and RYAN, J. T., [1971]; "Two phase slug flow in horizontal and inclined tubes." The Canadian Journal of Chemical Engineering, Vol. 49, pp. 195-201.

VIJAYAN, M., JAYANTI S. and BALAKRISHNAN, A. R., [2002]; "Experimental study of air-water counter-current annular flow under post-flooding conditions." Int. J. Multiphase Flow, Vol. 28, pp. 51-67.

WALLIS, G. B., [1969]; "One dimensional two phase flow." McGraw-Hill Book Company, New-York.

WALLIS, G. B. and DOBSON, J. E., [1973]; "The onset of slugging in horizontal stratified air-water flow." Int. J. Multiphase Flow, Vol. 1, pp. 173-193.

WALLIS, G. B. and KUO, J. T., [1976]; "The behaviour of gas and liquid interfaces in vertical tubes." Int. J. Multiphase Flow, Vol. 2, pp. 521-536.

WAN, P. T. and KRISHNAN, V. S., [1986]; "Air-water flooding in a 90° elbow with a slightly inclined lower leg." 7^{th} Annual Conference of the Canadian Nuclear Society, Toronto.

WAN, P. T., [1986]; "Counter-current steam-water flow in an upright 90° elbow." 8^{th} Int. Heat Transfer Conference, San Francisco.

WHITHAM, G. B., [1974]; "Linear and Nonlinear Waves.", Wiley-Interscience

Publication, New-York.

WILLIAM, C. E. and MARK, A. H. [1985]; "Physics of Waves.", Dover Publication, New-York.

WU, T. Y. [1998]; "Non-linear waves and solitons in water", Physica D., Vol. 123, pp. 48-63.

YONG CHOI, K. and CHEON NO, H., [1995]; "Experimental study of flooding in nearly horizontal pipes." Int. J. Multiphase Flow, Vol. 21, pp. 419-436.

ZABARAS, G. J. [1985]; "Studies of vertical annular gas-liquid flows." Ph.D. Thesis, University of Houston.

ZABARAS, G. J. and DUKLER, A. E., [1988]; "Counter-current gas-liquid annular flow, including the flooding state." AIChE Journal, Vol. 34, pp. 389-396.

ZABUSKY, N. J. and KRUSKAL, M. D., [1965]; "Interaction of solitons in a collisionless plasma and the recurrence of initial states." Phys. Rev. Lett., Vol. 15, pp. 240-243.

ZAPKE, A. and KRÖGER, D. G., [2000]; "Counter-current gas-liquid flow in inclined and vertical ducts - I: Flow patterns, pressure drop characteristics and flooding" Int. J. Multiphase Flow, Vol. 26, pp. 1439-1455.

APPENDIX A

THE ONSET OF FLOODING AND SLUGGING

The onset of flooding and the onset of slugging are presented in this appendix in the form of a table. The tables are arranged according to the orifice β ratio and the position of the orifice with respect to the elbow. The data obtained for experiments carried out without obstruction are also presented. The onset of flooding data are obtained from the Master's thesis of Bédard (1997).

The first column of the tables, presents the superficial liquid velocity (m/s) whereas the second and the third columns correspond to the superficial gas velocities necessary to initiate flooding and slugging conditions, respectively.

Table A.1 The onset of flooding and slugging for $\beta = 0.66$, Position 1.

$Q_{l,inlet}$ (m^3/h)	$Q_{g,inlet\_flood}$ (m^3/h)	$Q_{g,inlet\_slug}$ (m^3/h)	$j_{l,inlet}$ (m/s)	$j_{g,inlet\_flood}$ (m/s)	$j_{g,inlet\_slug}$ (m/s)
0.8	10.77	10.48	0.0702	0.9447	0.9194
1.1	5.50	6.31	0.0964	0.4824	0.5533
1.5	1.91	1.90	0.1316	0.1675	0.1665
1.8	0.53	2.53	0.1578	0.0465	0.2216
2.1	0.13	2.11	0.1842	0.0114	0.1847

Table A.2 The onset of flooding and slugging for $\beta = 0.72$, Position 1.

$Q_{l,inlet}$ (m^3/h)	$Q_{g,inlet\_flood}$ (m^3/h)	$Q_{g,inlet\_slug}$ (m^3/h)	$j_{l,inlet}$ (m/s)	$j_{g,inlet\_flood}$ (m/s)	$j_{g,inlet\_slug}$ (m/s)
0.4	27.27	25.93	0.0351	2.3919	2.2740
0.5	23.11	22.83	0.0439	2.0270	2.0027
0.8	15.80	15.60	0.0702	1.3859	1.3689
1.1	8.45	10.13	0.0964	0.7412	0.8200
1.5	5.08	5.20	0.1316	0.4456	0.4159
1.8	1.91	1.83	0.1578	0.1675	0.1478
2.1	0.60	0.35	0.1842	0.0529	0.0287

Table A.3 The onset of flooding and slugging for $\beta = 0.77$, Position 1.

$Q_{l,inlet}$ (m^3/h)	$Q_{g,inlet\_flood}$ (m^3/h)	$Q_{g,inlet\_slug}$ (m^3/h)	$j_{l,inlet}$ (m/s)	$j_{g,inlet\_flood}$ (m/s)	$j_{g,inlet\_slug}$ (m/s)
0.8	19.99	19.72	0.0702	1.2025	1.7296
1.1	13.71	13.52	0.0964	0.6859	1.1861
1.5	7.82	8.13	0.1316	0.4640	0.7133
1.8	5.29	4.16	0.1578	0.1859	0.3655
2.1	2.12	2.61	0.1842	0.0930	0.2284

Table A.4 The onset of flooding and slugging for $\beta = 0.83$, Position 1.

$Q_{l,inlet}$ (m^3/h)	$Q_{g,inlet\_flood}$ (m^3/h)	$Q_{g,inlet\_slug}$ (m^3/h)	$j_{l,inlet}$ (m/s)	$j_{g,inlet\_flood}$ (m/s)	$j_{g,inlet\_slug}$ (m/s)
1.1	15.80	12.63	0.0964	1.3859	1.4842
1.5	10.97	8.22	0.1316	0.9622	1.1074
1.8	7.82	8.13	0.1578	0.6859	0.7214
2.1	4.87	5.27	0.1842	0.4272	0.4628
2.5	1.27	1.27	0.2193	0.1114	0.1116

Table A.5 The onset of flooding and slugging for $\beta = 0.66$, Position 2.

$Q_{l,inlet}$ (m^3/h)	$Q_{g,inlet\_flood}$ (m^3/h)	$Q_{g,inlet\_slug}$ (m^3/h)	$j_{l,inlet}$ (m/s)	$j_{g,inlet\_flood}$ (m/s)	$j_{g,inlet\_slug}$ (m/s)
0.5	16.85	16.74	0.0439	1.4780	1.4687
0.8	10.56	10.49	0.0702	0.9262	0.9207
1.1	5.92	6.30	0.0964	0.5193	0.5529
1.5	2.12	2.11	0.1316	0.1859	0.1847
1.8	0.66	2.52	0.1578	0.0579	0.2215
2.1	0.11	2.11	0.1842	0.0096	0.2768

Table A.6 The onset of flooding and slugging for $\beta = 0.72$, Position 2.

$Q_{l,inlet}$ (m^3/h)	$Q_{g,inlet\_flood}$ (m^3/h)	$Q_{g,inlet\_slug}$ (m^3/h)	$j_{l,inlet}$ (m/s)	$j_{g,inlet\_flood}$ (m/s)	$j_{g,inlet\_slug}$ (m/s)
0.8	15.80	16.92	0.0702	1.3859	1.4842
1.1	9.39	10.53	0.0964	0.8236	0.9242
1.5	5.29	5.21	0.1316	0.4640	0.4576
1.8	2.33	2.12	0.1578	0.2044	0.1855
2.1	0.66	3.39	0.1842	0.0579	0.2751

Table A.7 The onset of flooding and slugging for $\beta = 0.77$, Position 2.

$Q_{l,inlet}$ (m^3/h)	$Q_{g,inlet\_flood}$ (m^3/h)	$Q_{g,inlet\_slug}$ (m^3/h)	$j_{l,inlet}$ (m/s)	$j_{g,inlet\_flood}$ (m/s)	$j_{g,inlet\_slug}$ (m/s)
0.8	18.94	16.96	0.0702	1.3859	1.4842
1.1	13.70	12.47	0.0964	0.8236	0.9242
1.5	8.03	10.21	0.1316	0.4640	0.4576
1.8	5.71	6.82	0.1578	0.2044	0.1855
2.1	2.76	3.42	0.1842	0.0579	0.2751

Table A.8 The onset of flooding and slugging for $\beta = 0.83$, Position 2.

$Q_{l,inlet}$ (m^3/h)	$Q_{g,inlet\_flood}$ (m^3/h)	$Q_{g,inlet\_slug}$ (m^3/h)	$j_{l,inlet}$ (m/s)	$j_{g,inlet\_flood}$ (m/s)	$j_{g,inlet\_slug}$ (m/s)
1.1	15.80	15.53	0.0964	0.8236	0.9242
1.5	10.56	11.67	0.1316	0.4640	0.4576
1.8	7.40	8.78	0.1578	0.2044	0.1855
2.1	4.24	6.84	0.1842	0.0579	0.2751
2.5	1.38	2.95	0.2193	0.0579	0.2751

Table A.9 The onset of flooding and slugging for $\beta = 1.00$.

$Q_{l,inlet}$ (m^3/h)	$Q_{g,inlet\_flood}$ (m^3/h)	$Q_{g,inlet\_slug}$ (m^3/h)	$j_{l,inlet}$ (m/s)	$j_{g,inlet\_flood}$ (m/s)	$j_{g,inlet\_slug}$ (m/s)
1.2	15.14	21.91	0.1053	1.3280	1.9221
1.4	12.99	19.94	0.1228	1.1394	1.7493
1.6	10.61	14.99	0.1403	0.9306	1.3149
1.7	9.08	13.01	0.1491	0.7964	1.1109
1.8	8.68	12.01	0.1579	0.7613	1.0530
2.0	6.49	9.03	0.1754	0.5693	0.7916
2.2	4.99	7.04	0.1930	0.4377	0.6170
2.4	2.60	5.04	0.2105	0.2281	0.4422

APPENDIX B

THE SLUG FREQUENCY

This appendix presents the slug frequency data in a table form. The tables are arranged according to the orifice β ratio and the position of the orifice with respect tio the elbow. The data for experiments carried out without obstruction are also presented.

The first and the second columns of the tables, present the volumetric flow rates of liquid and gas (m^3/h), respectively. The third and the fourth columns correspond to the superficial velocities of liquid and gas (m/s), respectively. The last column corresponds to the slug frequency in Hz.

Table B.1 Slug frequency for $\beta = 0.66$, Position 1.

$Q_{l,inlet}$ (m^3/h)	$Q_{g,inlet}$ (m^3/h)	$j_{l,inlet}$ (m/s)	$j_{g,inlet}$ (m/s)	**Frequency** (Hz)
0.8	4.2081	0.0702	0.3691	0.2880
0.8	6.3036	0.0702	0.5529	0.2770
0.8	8.3979	0.0702	0.7366	0.2760
0.8	10.4820	0.0702	0.9194	0.2700
0.8	12.5684	0.0702	1.1024	0.2580
0.8	14.6525	0.0702	1.2852	0.2430
0.8	16.7320	0.0702	1.4676	0.2020
0.8	18.8092	0.0702	1.6498	0.1990
1.1	4.2081	0.0960	0.3691	0.2800
1.1	6.3081	0.0960	0.5533	0.2790
1.1	8.3979	0.0960	0.7366	0.2900
1.1	10.4888	0.0960	0.9200	0.2400
1.1	12.5775	0.0960	1.1032	0.2400
1.1	14.6627	0.0960	1.2861	0.2200
1.1	16.7445	0.0960	1.4687	0.2150
1.1	18.8241	0.0960	1.6511	0.2100
1.5	1.8983	0.1316	0.1665	0.2950
1.5	3.9983	0.1316	0.3507	0.2900
1.5	6.0972	0.1316	0.5348	0.2800
1.5	8.1881	0.1316	0.7182	0.2850
1.5	10.2791	0.1316	0.9016	0.2640
1.5	12.3586	0.1316	1.0840	0.2420
1.5	14.4427	0.1316	1.2668	0.2100
1.5	16.5199	0.1316	1.4430	0.1960
1.5	18.6006	0.1316	1.6315	0.1800
1.8	2.5264	0.1579	0.2216	0.2850
1.8	4.6288	0.1579	0.4060	0.2830
1.8	6.7231	0.1579	0.5897	0.2800
1.8	8.8175	0.1579	0.7734	0.3050
1.8	10.9084	0.1579	0.9568	0.2640
1.8	12.9970	0.1579	1.1400	0.2210

Table B.1 Slug frequency for $\beta = 0.66$, Position 1.

$Q_{l,inlet}$ (m^3/h)	$Q_{g,inlet}$ (m^3/h)	$j_{l,inlet}$ (m/s)	$j_{g,inlet}$ (m/s)	**Frequency** (Hz)
2.1	2.1057	0.1842	0.1847	0.3400
2.1	4.2047	0.1842	0.3688	0.2950
2.1	6.3024	0.1842	0.5528	0.3080

Table B.2 Slug frequency for $\beta = 0.72$, Position 1.

$Q_{l,inlet}$ (m^3/h)	$Q_{g,inlet}$ (m^3/h)	$j_{l,inlet}$ (m/s)	$j_{g,inlet}$ (m/s)	**Frequency** (Hz)
0.4	11.4773	0.0350	1.0067	0.2830
0.4	13.5534	0.0350	1.1888	0.2120
0.4	15.6272	0.0350	1.3707	0.2170
0.4	17.6976	0.0350	1.5523	0.2150
0.4	19.7646	0.0350	1.7336	0.2000
0.4	21.8111	0.0350	1.9131	0.1490
0.4	23.8701	0.0350	2.0937	0.1575
0.4	25.9257	0.0350	2.2740	0.1343
0.4	27.9790	0.0350	2.4541	0.1312
0.5	10.4261	0.0440	0.9145	0.2660
0.5	12.5022	0.0440	1.0966	0.1660
0.5	14.5738	0.0440	1.2783	0.2170
0.5	16.6431	0.0440	1.4598	0.2300
0.5	18.7100	0.0440	1.6411	0.2000
0.5	20.7725	0.0440	1.8220	0.1680
0.5	22.8326	0.0440	2.0027	0.1510
0.5	24.8893	0.0440	2.1831	0.1425
0.5	26.9427	0.0440	2.3632	0.1312
0.5	28.9925	0.0440	2.5430	0.1282
0.8	11.4682	0.0702	1.0059	0.2180
0.8	13.5432	0.0702	1.1879	0.2050
0.8	15.6067	0.0702	1.3689	0.2000
0.8	17.6703	0.0702	1.5499	0.2000
0.8	19.7339	0.0702	1.7309	0.1575
0.8	21.7940	0.0702	1.9116	0.1510

Table B.2 Slug frequency for $\beta = 0.72$, Position 1.

$Q_{l,inlet}$ (m^3/h)	$Q_{g,inlet}$ (m^3/h)	$j_{l,inlet}$ (m/s)	$j_{g,inlet}$ (m/s)	**Frequency** (Hz)
1.1	3.1535	0.0960	0.2766	0.3017
1.1	5.2433	0.0960	0.4599	0.2500
1.1	7.2715	0.0960	0.6378	0.2655
1.1	9.3488	0.0960	0.8200	0.2575
1.1	11.4682	0.0960	1.0059	0.2430
1.1	13.5432	0.0960	1.1879	0.2000
1.1	15.6067	0.0960	1.3689	0.2310
1.1	17.6703	0.0960	1.5499	0.1800
1.1	19.7339	0.0960	1.7309	0.2050
1.5	2.7225	0.1316	0.2388	0.2425
1.5	4.8100	0.1316	0.4219	0.2830
1.5	6.8406	0.1316	0.6000	0.2716
1.5	8.9805	0.1316	0.7877	0.2289
1.5	11.0509	0.1316	0.9693	0.2310
1.5	13.1270	0.1316	1.1514	0.2255
1.5	15.1872	0.1316	1.3321	0.2000
1.5	17.2542	0.1316	1.5134	0.2050
1.5	19.3177	0.1316	1.6944	0.1575
1.8	3.7954	0.1579	0.3329	0.3000
1.8	5.8954	0.1579	0.5171	0.2800
1.8	7.9955	0.1579	0.7013	0.3050
1.8	10.0921	0.1579	0.8852	0.2580
1.8	12.1853	0.1579	1.0688	0.1950
1.8	14.2762	0.1579	1.2522	0.2020
1.8	16.3637	0.1579	1.4353	0.2170
1.8	18.4478	0.1579	1.6181	0.2180

Table B.2 Slug frequency for $\beta = 0.72$, Position 1.

$Q_{l,inlet}$ (m^3/h)	$Q_{g,inlet}$ (m^3/h)	$j_{l,inlet}$ (m/s)	$j_{g,inlet}$ (m/s)	**Frequency** (Hz)
2.1	3.3929	0.1842	0.2976	0.2197
2.1	4.5307	0.1842	0.3974	0.2900
2.1	6.6331	0.1842	0.5818	0.3000
2.1	8.7513	0.1842	0.7676	0.2990
2.1	10.8275	0.1842	0.9497	0.1900
2.1	12.9207	0.1842	1.1333	0.2200
2.1	15.0105	0.1842	1.3166	0.2000

Table B.3 Slug frequency for $\beta = 0.77$, Position 1.

$Q_{l,inlet}$ (m^3/h)	$Q_{g,inlet}$ (m^3/h)	$j_{l,inlet}$ (m/s)	$j_{g,inlet}$ (m/s)	**Frequency** (Hz)
0.8	7.3080	0.0702	0.6410	0.2319
0.8	9.3830	0.0702	0.8230	0.2255
0.8	11.4602	0.0702	1.0052	0.2510
0.8	13.5329	0.0702	1.1870	0.2260
0.8	15.6033	0.0702	1.3686	0.2170
0.8	17.6703	0.0702	1.5499	0.1660
0.8	19.7190	0.0702	1.7296	0.1255
0.8	21.7769	0.0702	1.9101	0.1800
0.8	23.8325	0.0702	2.0904	0.1425
1.1	11.4682	0.0960	1.0059	0.2170
1.1	13.5226	0.0960	1.1861	0.1950
1.1	15.5919	0.0960	1.3676	0.1340
1.1	17.6566	0.0960	1.5487	0.1500
1.1	19.7190	0.0960	1.7296	0.1536
1.5	8.1323	0.1316	0.7133	0.2471
1.5	10.2095	0.1316	0.8955	0.2170
1.5	12.2845	0.1316	1.0775	0.1880
1.5	14.3549	0.1316	1.2591	0.2300
1.5	16.4230	0.1316	1.4405	0.2000
1.5	18.4877	0.1316	1.6216	0.1975
1.9	2.0886	0.1666	0.1832	0.1587
1.9	4.1670	0.1666	0.3655	0.2319
1.9	7.7424	0.1666	0.6791	0.2686
1.9	9.8185	0.1666	0.8612	0.2340
1.9	11.8752	0.1666	1.0416	0.2050
1.9	13.9376	0.1666	1.2225	0.2500

Table B.3 Slug frequency for $\beta = 0.77$, Position 1.

$Q_{l,inlet}$ (m^3/h)	$Q_{g,inlet}$ (m^3/h)	$j_{l,inlet}$ (m/s)	$j_{g,inlet}$ (m/s)	**Frequency** (Hz)
2.1	1.2210	0.1842	0.1071	0.1800
2.1	2.6040	0.1842	0.2284	0.3500
2.1	4.6846	0.1842	0.4109	0.2500
2.1	6.7562	0.1842	0.5926	0.2563
2.1	8.8289	0.1842	0.7744	0.1831
2.1	10.8970	0.1842	0.9558	0.1648
2.1	12.9526	0.1842	1.1361	0.1830
2.1	16.2212	0.1842	1.4228	0.1739
2.3	0.8391	0.2017	0.0736	0.1434
2.3	2.0932	0.2017	0.1836	0.1526
2.3	3.1387	0.2017	0.2753	0.2045
2.3	5.2205	0.2017	0.4579	0.2502
2.3	7.3034	0.2017	0.6406	0.2869
2.3	9.3830	0.2017	0.8230	0.2289
2.3	11.4602	0.2017	1.0052	0.1831
2.3	13.5329	0.2017	1.1870	0.1983

Table B.4 Slug frequency for $\beta = 0.83$, Position 1.

$Q_{l,inlet}$ (m^3/h)	$Q_{g,inlet}$ (m^3/h)	$j_{l,inlet}$ (m/s)	$j_{g,inlet}$ (m/s)	**Frequency** (Hz)
1.1	16.9212	0.0960	1.4842	0.1495
1.1	19.0224	0.0960	1.6685	0.1404
1.5	4.2263	0.1316	0.3707	0.1965
1.5	6.3309	0.1316	0.5553	0.2050
1.5	8.4344	0.1316	0.7398	0.2680
1.5	10.5356	0.1316	0.9241	0.2000
1.5	12.6242	0.1316	1.1073	0.1580
1.5	14.7174	0.1316	1.2909	0.1575
1.5	16.8072	0.1316	1.4742	0.1340
1.8	4.0188	0.1579	0.3525	0.2000
1.8	6.1246	0.1579	0.5372	0.1905
1.8	8.2246	0.1579	0.7214	0.1830
1.8	10.3178	0.1579	0.9050	0.1745
1.8	12.4145	0.1579	1.0889	0.1650
2.1	3.1717	0.1842	0.2782	0.2080
2.1	5.2763	0.1842	0.4628	0.2170
2.1	7.3810	0.1842	0.6474	0.2593
2.1	9.4833	0.1842	0.8318	0.2575
2.1	11.5719	0.1842	1.0150	0.1650
2.1	13.6663	0.1842	1.1987	0.1575
2.5	1.2723	0.2192	0.1116	0.1404
2.5	3.3815	0.2192	0.2966	0.2255
2.5	5.4873	0.2192	0.4813	0.2300
2.5	7.5919	0.2192	0.6659	0.2500
2.5	9.6931	0.2192	0.8502	0.1500
2.5	11.7920	0.2192	1.0343	0.2000
2.5	13.8875	0.2192	1.2181	0.1700

Table B.5 Slug frequency for $\beta = 0.66$, Position 2.

$Q_{l,inlet}$ (m^3/h)	$Q_{g,inlet}$ (m^3/h)	$j_{l,inlet}$ (m/s)	$j_{g,inlet}$ (m/s)	**Frequency** (Hz)
0.5	6.3081	0.0440	0.5533	0.1344
0.5	8.4036	0.0440	0.7371	0.1343
0.5	10.4968	0.0440	0.9207	0.1220
0.5	12.5878	0.0440	1.1041	0.1160
0.5	14.6741	0.0440	1.2871	0.1038
0.5	16.7445	0.0440	1.4687	0.0915
0.5	18.8241	0.0440	1.6511	0.0915
0.5	20.9002	0.0440	1.8332	0.0793
0.8	4.2081	0.0702	0.3691	0.0824
0.8	6.3081	0.0702	0.5533	0.1404
0.8	8.3979	0.0702	0.7366	0.2868
0.8	10.4968	0.0702	0.9207	0.1160
0.8	12.5775	0.0702	1.1032	0.1190
0.8	14.6627	0.0702	1.2861	0.1038
0.8	16.7445	0.0702	1.4687	0.0885
0.8	18.8241	0.0702	1.6511	0.0854
1.1	2.0989	0.0960	0.1841	0.0946
1.1	4.2081	0.0960	0.3691	0.0213
1.1	6.3036	0.0960	0.5529	0.2228
1.1	8.3979	0.0960	0.7366	0.2471
1.1	10.4888	0.0960	0.9200	0.1251
1.1	12.5775	0.0960	1.1032	0.1251
1.1	14.6525	0.0960	1.2852	0.1038
1.1	16.7320	0.0960	1.4676	0.0946

Table B.5 Slug frequency for $\beta = 0.66$, Position 2.

$Q_{l,inlet}$ (m^3/h)	$Q_{g,inlet}$ (m^3/h)	$j_{l,inlet}$ (m/s)	$j_{g,inlet}$ (m/s)	**Frequency** (Hz)
1.5	2.1057	0.1316	0.1847	0.0122
1.5	4.2081	0.1316	0.3691	0.1495
1.5	6.3036	0.1316	0.5529	0.0701
1.5	8.3979	0.1316	0.7366	0.2594
1.5	10.4820	0.1316	0.9194	0.1220
1.5	12.5684	0.1316	1.1024	0.1160
1.5	14.6525	0.1316	1.2852	0.1007
1.5	16.7320	0.1316	1.4676	0.0946
1.8	2.5253	0.1579	0.2215	0.0213
1.8	4.6254	0.1579	0.4057	0.0335
1.8	6.7231	0.1579	0.5897	0.2777
1.8	8.8175	0.1579	0.7734	0.2564
1.8	10.9084	0.1579	0.9568	0.1038
1.8	12.9868	0.1579	1.1391	0.1038
1.8	15.0709	0.1579	1.3219	0.1038
2.1	2.1092	0.1842	0.1850	0.0275
2.1	3.1558	0.1842	0.2768	0.0213
2.1	4.2081	0.1842	0.3691	0.1648
2.1	5.2570	0.1842	0.4611	0.2563
2.1	6.3024	0.1842	0.5528	0.2899
2.1	7.3479	0.1842	0.6445	0.2746

Table B.6 Slug frequency for $\beta = 0.72$, Position 2.

$Q_{l,inlet}$ (m^3/h)	$Q_{g,inlet}$ (m^3/h)	$j_{l,inlet}$ (m/s)	$j_{g,inlet}$ (m/s)	**Frequency** (Hz)
0.8	6.3731	0.0702	0.5590	0.1255
0.8	8.4914	0.0702	0.7448	0.1281
0.8	10.6074	0.0702	0.9304	0.1160
0.8	12.7097	0.0702	1.1148	0.1190
0.8	14.8166	0.0702	1.2996	0.1800
0.8	16.9212	0.0702	1.4842	0.1922
0.8	19.0224	0.0702	1.6685	0.0824
0.8	21.1202	0.0702	1.8525	0.0701
1.1	4.2275	0.0960	0.3708	0.1068
1.1	6.3309	0.0960	0.5553	0.0824
1.1	8.4355	0.0960	0.7399	0.2685
1.1	10.5367	0.0960	0.9242	0.1098
1.1	12.6254	0.0960	1.1074	0.2411
1.1	14.7186	0.0960	1.2910	0.1098
1.1	16.8084	0.0960	1.4743	0.0030
1.1	18.8947	0.0960	1.6573	0.0824
1.5	5.2171	0.1316	0.4576	0.1425
1.5	7.2977	0.1316	0.6401	0.1373
1.5	9.3761	0.1316	0.8224	0.1340
1.5	11.4511	0.1316	1.0044	0.1340
1.5	13.5226	0.1316	1.1861	0.1000
1.5	15.5919	0.1316	1.3676	0.1300
1.5	17.6566	0.1316	1.5487	0.0790

Table B.6 Slug frequency for $\beta = 0.72$, Position 2.

$Q_{l,inlet}$ (m^3/h)	$Q_{g,inlet}$ (m^3/h)	$j_{l,inlet}$ (m/s)	$j_{g,inlet}$ (m/s)	**Frequency** (Hz)
1.8	2.1149	0.1579	0.1855	0.2899
1.8	4.2240	0.1579	0.3705	0.1160
1.8	6.3264	0.1579	0.5549	0.1745
1.8	8.4287	0.1579	0.7393	0.2746
1.8	10.5276	0.1579	0.9235	0.1160
1.8	12.6254	0.1579	1.1074	0.1340
1.8	14.7186	0.1579	1.2910	0.1068
1.8	16.8084	0.1579	1.4743	0.1007
1.8	18.8947	0.1579	1.6573	0.0600
2.1	3.1375	0.1842	0.2752	0.1500
2.1	5.2171	0.1842	0.4576	0.1650
2.1	7.2122	0.1842	0.6327	0.1434

Table B.7 Slug frequency for $\beta = 0.77$, Position 2.

$Q_{l,inlet}$ (m^3/h)	$Q_{g,inlet}$ (m^3/h)	$j_{l,inlet}$ (m/s)	$j_{g,inlet}$ (m/s)	**Frequency** (Hz)
0.8	9.4400	0.0702	0.8280	0.1129
0.8	11.5297	0.0702	1.0113	0.1050
0.8	13.6059	0.0702	1.1934	0.1000
0.8	15.6865	0.0702	1.3759	0.1100
1.1	5.2524	0.0960	0.4607	0.1129
1.1	7.3479	0.0960	0.6445	0.1170
1.1	9.4400	0.0960	0.8280	0.1500
1.1	11.5297	0.0960	1.0113	0.1000
1.1	13.6024	0.0960	1.1931	0.1000
1.1	15.6865	0.0960	1.3759	0.0950
1.1	17.7649	0.0960	1.5582	0.1038
1.5	3.1603	0.1316	0.2772	0.1234
1.5	5.2604	0.1316	0.4614	0.1170
1.5	7.3536	0.1316	0.6450	0.1340
1.5	9.4400	0.1316	0.8280	0.1420
1.5	11.5297	0.1316	1.0113	0.0867
1.5	13.6059	0.1316	1.1934	0.1000
1.8	3.1581	0.1579	0.1855	0.0061
1.8	5.2558	0.1579	0.3705	0.1129
1.8	7.3502	0.1579	0.5549	0.1312
1.8	9.4400	0.1579	0.7393	0.1098
1.8	11.5297	0.1579	0.9234	0.1038
1.8	13.6161	0.1579	1.1074	0.0915
1.8	14.7186	0.1579	1.2910	0.0488
1.8	16.8084	0.1579	1.4743	0.0183
1.8	18.8446	0.1579	1.6573	0.0213

Table B.7 Slug frequency for $\beta = 0.77$, Position 2.

$Q_{l,inlet}$ (m^3/h)	$Q_{g,inlet}$ (m^3/h)	$j_{l,inlet}$ (m/s)	$j_{g,inlet}$ (m/s)	**Frequency** (Hz)
2.1	3.1558	0.1842	0.2768	0.1490
2.1	5.2524	0.1842	0.4607	0.1000
2.1	7.3479	0.1842	0.6445	0.1000
2.1	9.4400	0.1842	0.8280	0.1080
2.1	11.5297	0.1842	1.0113	0.0950
2.1	13.6161	0.1842	1.1943	0.0600
2.1	15.6979	0.1842	1.3769	0.1000
2.1	17.7786	0.1842	1.5594	0.0915
2.5	7.2521	0.2192	0.6361	0.0950
2.5	9.3237	0.2192	0.8178	0.1000

Table B.8 Slug frequency for $\beta = 0.83$, Position 2.

$Q_{l,inlet}$ (m^3/h)	$Q_{g,inlet}$ (m^3/h)	$j_{l,inlet}$ (m/s)	$j_{g,inlet}$ (m/s)	**Frequency** (Hz)
1.1	9.3089	0.0960	0.8165	0.3723
1.1	11.1604	0.0960	0.9789	0.2655
1.1	16.6305	0.0960	1.4587	0.2533
1.1	17.4297	0.0960	1.5288	0.1464
1.5	3.7486	0.1316	0.3288	0.1282
1.5	5.6013	0.1316	0.4913	0.1617
1.5	7.4539	0.1316	0.6538	0.1495
1.5	9.2826	0.1316	0.8142	0.1770
1.5	11.1296	0.1316	0.9762	0.0214
1.5	12.9720	0.1316	1.1378	0.0214
1.8	4.9081	0.1579	0.4305	0.0702
1.8	6.8485	0.1579	0.6007	0.1740
1.8	8.7844	0.1579	0.7705	0.0397
1.8	10.7123	0.1579	0.9396	0.0580
1.8	12.6174	0.1579	1.1067	0.1495
2.1	6.8483	0.1842	0.6007	0.0610
2.1	8.7850	0.1842	0.7705	0.0366
2.1	10.7128	0.1842	0.9396	0.0793
2.1	12.6172	0.1842	1.1067	0.1556
2.5	2.9517	0.2192	0.2589	0.1495
2.5	3.9265	0.2192	0.3444	0.0885
2.5	4.9024	0.2192	0.4300	0.0702
2.5	7.8085	0.2192	0.6844	0.0793
2.5	10.2141	0.2192	0.8959	0.0763
2.5	12.4715	0.2192	1.0939	0.0092

Table B.9 Slug frequency for $\beta = 1.00$.

$Q_{l,inlet}$ (m^3/h)	$Q_{g,inlet}$ (m^3/h)	$j_{l,inlet}$ (m/s)	$j_{g,inlet}$ (m/s)	**Frequency** (Hz)
1.2	21.9140	0.1053	1.9221	0.0153
1.2	23.9062	0.1053	2.0969	0.0183
1.3	20.9413	0.1140	1.8368	0.0244
1.3	22.8896	0.1140	2.0073	0.0457
1.3	24.8468	0.1140	2.1794	0.0153
1.4	19.9441	0.1228	1.7493	0.0183
1.4	20.9179	0.1228	1.8348	0.0183
1.4	21.8896	0.1228	1.9200	0.0213
1.4	22.8590	0.1228	2.0050	0.0244
1.4	23.8529	0.1228	2.0922	0.0183
1.4	24.8190	0.1228	2.1769	0.0427
1.5	17.9696	0.1316	1.5762	0.0610
1.5	18.9468	0.1316	1.6619	0.0183
1.5	19.9218	0.1316	1.7474	0.0153
1.5	20.8946	0.1316	1.8327	0.0183
1.5	21.8896	0.1316	1.9200	0.0183
1.5	22.8590	0.1316	2.0050	0.0244
1.6	14.9913	0.1403	1.3149	0.0153
1.6	15.9730	0.1403	1.4010	0.0153
1.6	16.9524	0.1403	1.4869	0.0183
1.6	17.9496	0.1403	1.5744	0.0183
1.6	18.9258	0.1403	1.6600	0.0244
1.6	19.9218	0.1403	1.7474	0.0671

Table B.9 Slug frequency for $\beta = 1.00$.

$Q_{l,inlet}$ (m^3/h)	$Q_{g,inlet}$ (m^3/h)	$j_{l,inlet}$ (m/s)	$j_{g,inlet}$ (m/s)	**Frequency** (Hz)
1.7	13.0069	0.1491	1.1409	0.0244
1.7	13.9919	0.1491	1.2273	0.0183
1.7	14.9747	0.1491	1.3135	0.0518
1.7	15.9730	0.1491	1.4010	0.0457
1.7	16.9524	0.1491	1.4869	0.0153
1.7	17.9297	0.1491	1.5727	0.0183
1.7	18.9258	0.1491	1.6600	0.0457
1.7	19.8996	0.1491	1.7454	0.0213
1.7	20.8946	0.1491	1.8327	0.0275
1.8	12.0064	0.1579	1.0531	0.0183
1.8	12.9925	0.1579	1.1396	0.0549
1.8	13.9764	0.1579	1.2259	0.0274
1.8	14.9747	0.1579	1.3135	0.0183
1.8	15.9552	0.1579	1.3995	0.0794
1.8	16.9336	0.1579	1.4853	0.0549
1.8	17.9297	0.1579	1.5727	0.0579
1.9	10.0275	0.1666	0.8795	0.0641
1.9	11.0181	0.1666	0.9664	0.1220
1.9	12.0064	0.1666	1.0531	0.0457
1.9	13.0069	0.1666	1.1409	0.0579
1.9	13.9919	0.1666	1.2273	0.0427
1.9	14.9747	0.1666	1.3135	0.0275
1.9	15.9730	0.1666	1.4010	0.0153
1.9	16.9524	0.1666	1.4869	0.0153
1.9	17.9297	0.1666	1.5727	0.0275

Table B.9 Slug frequency for $\beta = 1.00$.

$Q_{l,inlet}$ (m^3/h)	$Q_{g,inlet}$ (m^3/h)	$j_{l,inlet}$ (m/s)	$j_{g,inlet}$ (m/s)	**Frequency** (Hz)
2.0	9.0248	0.1754	0.7916	0.0396
2.0	10.0169	0.1754	0.8786	0.0457
2.0	11.0059	0.1754	0.9653	0.1739
2.0	12.0064	0.1754	1.0531	0.2441
2.0	12.9925	0.1754	1.1396	0.2868
2.0	13.9764	0.1754	1.2259	0.0641
2.0	14.9747	0.1754	1.3135	0.5035
2.0	15.9552	0.1754	1.3995	0.0183
2.1	8.0220	0.1842	0.7036	0.0488
2.1	9.0248	0.1842	0.7916	0.0610
2.1	10.0164	0.1842	0.8786	0.1495
2.1	11.0059	0.1842	0.9653	0.0701
2.1	12.0064	0.1842	1.0531	0.0610
2.1	13.0069	0.1842	1.1409	0.0549
2.1	13.9919	0.1842	1.2273	0.2319
2.1	14.9747	0.1842	1.3135	0.0183
2.1	15.9730	0.1842	1.4010	0.5066
2.1	16.9524	0.1842	1.4868	0.5066
2.1	17.9297	0.1842	1.5727	0.3143
2.1	18.9258	0.1842	1.6600	0.0397

Table B.9 Slug frequency for $\beta = 1.00$.

$Q_{l,inlet}$ (m^3/h)	$Q_{g,inlet}$ (m^3/h)	$j_{l,inlet}$ (m/s)	$j_{g,inlet}$ (m/s)	**Frequency** (Hz)
2.2	7.0348	0.1930	0.6170	0.1220
2.2	8.0398	0.1930	0.7052	0.1709
2.2	9.0248	0.1930	0.7916	0.0549
2.2	10.0164	0.1930	0.8786	0.0579
2.2	11.0059	0.1930	0.9653	0.6103
2.2	12.0064	0.1930	1.0531	0.1953
2.2	12.9925	0.1930	1.1396	0.0915
2.2	13.9764	0.1930	1.2259	0.1098
2.2	14.9747	0.1930	1.3135	0.1007
2.2	15.9552	0.1930	1.3995	0.5219
2.2	16.9524	0.1930	1.4869	0.4272
2.2	17.9297	0.1930	1.5727	0.5219
2.2	18.9258	0.1930	1.6600	0.7812
2.3	6.0432	0.2017	0.5301	0.0549
2.3	7.0426	0.2017	0.6177	0.0732
2.3	8.0398	0.2017	0.7052	0.1251
2.3	9.0348	0.2017	0.7925	0.1038
2.3	10.0275	0.2017	0.8795	0.2197
2.3	11.0181	0.2017	0.9664	0.0519
2.3	12.0064	0.2017	1.0531	0.0579
2.3	13.0069	0.2017	1.1409	0.0549
2.3	13.9919	0.2017	1.2273	0.0549
2.3	14.9747	0.2017	1.3135	0.3479
2.3	15.9730	0.2017	1.4010	0.1770
2.3	16.9713	0.2017	1.4886	0.6042

Table B.9 Slug frequency for $\beta = 1.00$.

$Q_{l,inlet}$ (m^3/h)	$Q_{g,inlet}$ (m^3/h)	$j_{l,inlet}$ (m/s)	$j_{g,inlet}$ (m/s)	**Frequency** (Hz)
2.4	5.0415	0.2105	0.4422	0.0549
2.4	6.0432	0.2105	0.5301	0.1465
2.4	7.0426	0.2105	0.6177	0.3906
2.4	8.0398	0.2105	0.7052	0.0824
2.4	9.0348	0.2105	0.7925	0.1678
2.4	10.0275	0.2105	0.8795	0.0579
2.4	11.0181	0.2105	0.9664	0.0488
2.4	12.0064	0.2105	1.0531	0.0549
2.4	13.0069	0.2105	1.1409	0.0458
2.4	13.9919	0.2105	1.2273	0.5890
2.4	14.9747	0.2105	1.3135	0.0396
2.4	15.9730	0.2105	1.4010	0.0488
2.5	4.0377	0.2192	0.3542	0.0610
2.5	5.0415	0.2192	0.4422	0.0702
2.5	6.0432	0.2192	0.5301	0.1007
2.5	7.0426	0.2192	0.6177	0.0671
2.5	8.0398	0.2192	0.7052	0.0549
2.5	9.0348	0.2192	0.7925	0.0549
2.5	10.0275	0.2192	0.8795	0.1983
2.5	11.0181	0.2192	0.9664	0.1617
2.5	12.0064	0.2192	1.0531	0.0885
2.5	13.0069	0.2192	1.1409	0.0824

APPENDIX C

THE SLUG AVERAGE VOID FRACTION

The average void fraction obtained from the third electrode is presented in this appendix in the form of a table. The tables are arranged according to the orifice β ratio and the position of the orifice with respect tio the elbow. The data for experiments carried out without obstruction are also presented.

The first and the second columns of the tables, present the volumetric flow rates of liquid and gas (m^3/h), respectively. The third and the fourth columns correspond to the superficial velocities of liquid and gas (m/s), respectively. The last column corresponds to the average void fraction.

Table C.1 Slug average void fraction for $\beta = 0.66$, Position 1.

$Q_{l,inlet}$ (m^3/h)	$Q_{g,inlet}$ (m^3/h)	$j_{l,inlet}$ (m/s)	$j_{g,inlet}$ (m/s)	**Void Fraction** $(-)$
0.8	4.2081	0.0702	0.3691	0.7078
0.8	6.3036	0.0702	0.5529	0.7045
0.8	8.3979	0.0702	0.7366	0.6829
0.8	10.4820	0.0702	0.9194	0.6894
0.8	12.5684	0.0702	1.1024	0.6865
0.8	14.6525	0.0702	1.2852	0.6763
0.8	16.7320	0.0702	1.4676	0.6786
0.8	18.8092	0.0702	1.6498	0.6649
1.1	4.2081	0.0960	0.3691	0.7108
1.1	6.3081	0.0960	0.5533	0.7010
1.1	8.3979	0.0960	0.7366	0.6872
1.1	10.4888	0.0960	0.9200	0.6784
1.1	12.5775	0.0960	1.1032	0.6838
1.1	14.6627	0.0960	1.2861	0.6794
1.1	16.7445	0.0960	1.4687	0.6667
1.1	18.8241	0.0960	1.6511	0.6716
1.5	1.8983	0.1316	0.1665	0.6392
1.5	3.9983	0.1316	0.3507	0.7011
1.5	6.0972	0.1316	0.5348	0.7005
1.5	8.1881	0.1316	0.7182	0.6807
1.5	10.2791	0.1316	0.9016	0.6717
1.5	12.3586	0.1316	1.0840	0.6815
1.5	14.4427	0.1316	1.2668	0.6774
1.5	16.5199	0.1316	1.4430	0.6654
1.5	18.6006	0.1316	1.6315	0.6671

Table C.1 Slug average void fraction for $\beta = 0.66$, Position 1.

$Q_{l,inlet}$ (m^3/h)	$Q_{g,inlet}$ (m^3/h)	$j_{l,inlet}$ (m/s)	$j_{g,inlet}$ (m/s)	**Void Fraction** $(-)$
1.8	2.5264	0.1579	0.2216	0.6888
1.8	4.6288	0.1579	0.4060	0.6851
1.8	6.7231	0.1579	0.5897	0.6925
1.8	8.8175	0.1579	0.7734	0.6815
1.8	10.9084	0.1579	0.9568	0.6828
1.8	12.9970	0.1579	1.1400	0.6883
2.1	2.1057	0.1842	0.1847	0.6730
2.1	4.2047	0.1842	0.3688	0.6775
2.1	6.3024	0.1842	0.5528	0.6785

Table C.2 Slug average void fraction for $\beta = 0.72$, Position 1.

$Q_{l,inlet}$ (m^3/h)	$Q_{g,inlet}$ (m^3/h)	$j_{l,inlet}$ (m/s)	$j_{g,inlet}$ (m/s)	**Void Fraction** $(-)$
0.4	11.4773	0.0350	1.0067	0.6932
0.4	13.5534	0.0350	1.1888	0.6904
0.4	15.6272	0.0350	1.3707	0.6873
0.4	17.6976	0.0350	1.5523	0.6891
0.4	19.7646	0.0350	1.7336	0.6891
0.4	21.8111	0.0350	1.9131	0.7025
0.4	23.8701	0.0350	2.0937	0.6969
0.4	25.9257	0.0350	2.2740	0.6454
0.4	27.9790	0.0350	2.4541	0.6375
0.5	10.4261	0.0440	0.9145	0.6871
0.5	12.5022	0.0440	1.0966	0.6790
0.5	14.5738	0.0440	1.2783	0.6945
0.5	16.6431	0.0440	1.4598	0.6734
0.5	18.7100	0.0440	1.6411	0.6723
0.5	20.7725	0.0440	1.8220	0.6806
0.5	22.8326	0.0440	2.0027	0.6989
0.5	24.8893	0.0440	2.1831	0.6082
0.5	26.9427	0.0440	2.3632	0.6382
0.5	28.9925	0.0440	2.5430	0.6305
0.8	11.4682	0.0702	1.0059	0.6872
0.8	13.5432	0.0702	1.1879	0.6799
0.8	15.6067	0.0702	1.3689	0.6926
0.8	17.6703	0.0702	1.5499	0.6928
0.8	19.7339	0.0702	1.7309	0.6828
0.8	21.7940	0.0702	1.9116	0.6968

Table C.2 Slug average void fraction for $\beta = 0.72$, Position 1.

$Q_{l,inlet}$ (m^3/h)	$Q_{g,inlet}$ (m^3/h)	$j_{l,inlet}$ (m/s)	$j_{g,inlet}$ (m/s)	**Void Fraction** $(-)$
1.1	3.1535	0.0960	0.2766	0.7057
1.1	5.2433	0.0960	0.4599	0.6964
1.1	7.2715	0.0960	0.6378	0.6757
1.1	9.3488	0.0960	0.8200	0.5071
1.1	11.4682	0.0960	1.0059	0.5142
1.1	13.5432	0.0960	1.1879	0.6746
1.1	15.6067	0.0960	1.3689	0.6828
1.1	17.6703	0.0960	1.5499	0.6647
1.1	19.7339	0.0960	1.7309	0.6827
1.5	2.7225	0.1316	0.2388	0.6735
1.5	4.8100	0.1316	0.4219	0.6852
1.5	6.8406	0.1316	0.6000	0.6755
1.5	8.9805	0.1316	0.7877	0.6833
1.5	11.0509	0.1316	0.9693	0.6978
1.5	13.1270	0.1316	1.1514	0.6961
1.5	15.1872	0.1316	1.3321	0.6525
1.5	17.2542	0.1316	1.5134	0.6617
1.5	19.3177	0.1316	1.6944	0.6599
1.8	3.7954	0.1579	0.3329	0.6527
1.8	5.8954	0.1579	0.5171	0.6772
1.8	7.9955	0.1579	0.7013	0.6885
1.8	10.0921	0.1579	0.8852	0.6756
1.8	12.1853	0.1579	1.0688	0.7030
1.8	14.2762	0.1579	1.2522	0.6708
1.8	16.3637	0.1579	1.4353	0.6569
1.8	18.4478	0.1579	1.6181	0.6864

Table C.2 Slug average void fraction for $\beta = 0.72$, Position 1.

$Q_{l,inlet}$ (m^3/h)	$Q_{g,inlet}$ (m^3/h)	$j_{l,inlet}$ (m/s)	$j_{g,inlet}$ (m/s)	**Void Fraction** $(-)$
2.1	0.3272	0.1842	0.0287	0.5974
2.1	3.3929	0.1842	0.2976	0.6548
2.1	4.5307	0.1842	0.3974	0.6770
2.1	6.6331	0.1842	0.5818	0.6769
2.1	8.7513	0.1842	0.7676	0.6702
2.1	10.8275	0.1842	0.9497	0.6814
2.1	12.9207	0.1842	1.1333	0.7038
2.1	15.0105	0.1842	1.3166	0.6704

Table C.3 Slug average void fraction for $\beta = 0.77$, Position 1.

$Q_{l,inlet}$ (m^3/h)	$Q_{g,inlet}$ (m^3/h)	$j_{l,inlet}$ (m/s)	$j_{g,inlet}$ (m/s)	**Void Fraction** $(-)$
0.8	5.2205	0.0702	0.4579	0.6534
0.8	7.3080	0.0702	0.6410	0.7936
0.8	9.3830	0.0702	0.8230	0.7683
0.8	11.4602	0.0702	1.0052	0.7241
0.8	13.5329	0.0702	1.1870	0.7423
0.8	15.6033	0.0702	1.3686	0.7407
0.8	17.6703	0.0702	1.5499	0.7431
0.8	19.7190	0.0702	1.7296	0.7303
0.8	21.7769	0.0702	1.9101	0.6737
0.8	23.8325	0.0702	2.0904	0.6509
1.1	7.3091	0.0960	0.6411	0.7305
1.1	9.3909	0.0960	0.8237	0.7173
1.1	11.4682	0.0960	1.0059	0.7532
1.1	13.5226	0.0960	1.1861	0.7551
1.1	15.5919	0.0960	1.3676	0.6983
1.1	17.6566	0.0960	1.5487	0.7043
1.1	19.7190	0.0960	1.7296	0.6359
1.5	6.0562	0.1316	0.5312	0.6994
1.5	8.1323	0.1316	0.7133	0.6899
1.5	10.2095	0.1316	0.8955	0.7656
1.5	12.2845	0.1316	1.0775	0.7515
1.5	14.3549	0.1316	1.2591	0.7289
1.5	16.4230	0.1316	1.4405	0.6754
1.5	18.4877	0.1316	1.6216	0.6816
1.9	2.0886	0.1666	0.1832	0.6717
1.9	4.1670	0.1666	0.3655	0.7360
1.9	7.7424	0.1666	0.6791	0.7190
1.9	9.8185	0.1666	0.8612	0.7275
1.9	11.8752	0.1666	1.0416	0.7513
1.9	13.9376	0.1666	1.2225	0.7549

Table C.3 Slug average void fraction for $\beta = 0.77$, Position 1.

$Q_{l,inlet}$ (m^3/h)	$Q_{g,inlet}$ (m^3/h)	$j_{l,inlet}$ (m/s)	$j_{g,inlet}$ (m/s)	**Void Fraction** $(-)$
2.1	1.2210	0.1842	0.1071	0.6656
2.1	2.6040	0.1842	0.2284	0.6756
2.1	4.6846	0.1842	0.4109	0.7094
2.1	6.7562	0.1842	0.5926	0.7193
2.1	8.8289	0.1842	0.7744	0.7197
2.1	10.8970	0.1842	0.9558	0.7540
2.1	12.9526	0.1842	1.1361	0.7563
2.1	16.2212	0.1842	1.4228	0.7223
2.3	0.8391	0.2017	0.0736	0.6986
2.3	2.0932	0.2017	0.1836	0.7089
2.3	3.1387	0.2017	0.2753	0.7470
2.3	5.2205	0.2017	0.4579	0.7470
2.3	7.3034	0.2017	0.6406	0.7321
2.3	9.3830	0.2017	0.8230	0.7196
2.3	11.4602	0.2017	1.0052	0.7601
2.3	13.5329	0.2017	1.1870	0.7495

Table C.4 Slug average void fraction for $\beta = 0.83$, Position 1.

$Q_{l,inlet}$ (m^3/h)	$Q_{g,inlet}$ (m^3/h)	$j_{l,inlet}$ (m/s)	$j_{g,inlet}$ (m/s)	**Void Fraction** $(-)$
1.1	16.9212	0.0960	1.4842	0.7182
1.1	19.0224	0.0960	1.6685	0.6914
1.5	4.2263	0.1316	0.3707	0.6436
1.5	6.3309	0.1316	0.5553	0.7046
1.5	8.4344	0.1316	0.7398	0.6319
1.5	10.5356	0.1316	0.9241	0.6679
1.5	12.6242	0.1316	1.1073	0.7008
1.5	14.7174	0.1316	1.2909	0.6943
1.5	16.8072	0.1316	1.4742	0.7388
1.8	4.0188	0.1579	0.3525	0.6178
1.8	6.1246	0.1579	0.5372	0.6893
1.8	8.2246	0.1579	0.7214	0.6814
1.8	10.3178	0.1579	0.9050	0.6697
1.8	12.4145	0.1579	1.0889	0.7095
2.1	3.1717	0.1842	0.2782	0.5615
2.1	5.2763	0.1842	0.4628	0.6123
2.1	7.3810	0.1842	0.6474	0.6869
2.1	9.4833	0.1842	0.8318	0.6950
2.1	11.5719	0.1842	1.0150	0.7687
2.1	13.6663	0.1842	1.1987	0.7396
2.5	1.2723	0.2192	0.1116	0.5220
2.5	3.3815	0.2192	0.2966	0.5929
2.5	5.4873	0.2192	0.4813	0.6197
2.5	7.5919	0.2192	0.6659	0.7029
2.5	9.6931	0.2192	0.8502	0.6878
2.5	11.7920	0.2192	1.0343	0.7477
2.5	13.8875	0.2192	1.2181	0.6916

Table C.5 Slug average void fraction for $\beta = 0.66$, Position 2.

$Q_{l,inlet}$ (m^3/h)	$Q_{g,inlet}$ (m^3/h)	$j_{l,inlet}$ (m/s)	$j_{g,inlet}$ (m/s)	**Void Fraction** $(-)$
0.5	6.3081	0.0440	0.5533	0.6973
0.5	8.4036	0.0440	0.7371	0.7096
0.5	10.4968	0.0440	0.9207	0.7046
0.5	12.5878	0.0440	1.1041	0.7055
0.5	14.6741	0.0440	1.2871	0.7159
0.5	16.7445	0.0440	1.4687	0.7135
0.5	18.8241	0.0440	1.6511	0.7265
0.5	20.9002	0.0440	1.8332	0.7321
0.8	4.2081	0.0702	0.3691	0.6841
0.8	6.3081	0.0702	0.5533	0.6815
0.8	8.3979	0.0702	0.7366	0.7077
0.8	10.4968	0.0702	0.9207	0.7078
0.8	12.5775	0.0702	1.1032	0.7115
0.8	14.6627	0.0702	1.2861	0.7102
0.8	16.7445	0.0702	1.4687	0.7165
0.8	18.8241	0.0702	1.6511	0.7296
1.1	2.0989	0.0960	0.1841	0.6245
1.1	4.2081	0.0960	0.3691	0.6553
1.1	6.3036	0.0960	0.5529	0.6861
1.1	8.3979	0.0960	0.7366	0.7110
1.1	10.4888	0.0960	0.9200	0.7097
1.1	12.5775	0.0960	1.1032	0.7135
1.1	14.6525	0.0960	1.2852	0.7153
1.1	16.7320	0.0960	1.4676	0.7228

Table C.5 Slug average void fraction for $\beta = 0.66$, Position 2.

$Q_{l,inlet}$ (m^3/h)	$Q_{g,inlet}$ (m^3/h)	$j_{l,inlet}$ (m/s)	$j_{g,inlet}$ (m/s)	**Void Fraction** $(-)$
1.5	2.1057	0.1316	0.1847	0.6178
1.5	4.2081	0.1316	0.3691	0.6695
1.5	6.3036	0.1316	0.5529	0.6926
1.5	8.3979	0.1316	0.7366	0.7056
1.5	10.4820	0.1316	0.9194	0.7032
1.5	12.5684	0.1316	1.1024	0.7141
1.5	14.6525	0.1316	1.2852	0.7182
1.5	16.7320	0.1316	1.4676	0.7241
1.8	2.5253	0.1579	0.2215	0.6409
1.8	4.6254	0.1579	0.4057	0.6613
1.8	6.7231	0.1579	0.5897	0.6765
1.8	8.8175	0.1579	0.7734	0.7115
1.8	10.9084	0.1579	0.9568	0.5331
1.8	12.9868	0.1579	1.1391	0.7109
1.8	15.0709	0.1579	1.3219	0.5551
2.1	2.1092	0.1842	0.1850	0.6266
2.1	3.1558	0.1842	0.2768	0.6531
2.1	4.2081	0.1842	0.3691	0.6358
2.1	5.2570	0.1842	0.4611	0.6517
2.1	6.3024	0.1842	0.5528	0.6820
2.1	7.3479	0.1842	0.6445	0.6954

Table C.6 Slug average void fraction for $\beta = 0.72$, Position 2.

$Q_{l,inlet}$ (m^3/h)	$Q_{g,inlet}$ (m^3/h)	$j_{l,inlet}$ (m/s)	$j_{g,inlet}$ (m/s)	**Void Fraction** $(-)$
0.8	6.3731	0.0702	0.5590	0.7367
0.8	8.4914	0.0702	0.7448	0.7739
0.8	10.6074	0.0702	0.9304	0.8056
0.8	12.7097	0.0702	1.1148	0.7947
0.8	14.8166	0.0702	1.2996	0.7595
0.8	16.9212	0.0702	1.4842	0.7947
0.8	19.0224	0.0702	1.6685	0.7916
0.8	21.1202	0.0702	1.8525	0.8060
1.1	4.2275	0.0960	0.3708	0.7376
1.1	6.3309	0.0960	0.5553	0.6832
1.1	8.4355	0.0960	0.7399	0.7803
1.1	10.5367	0.0960	0.9242	0.7766
1.1	12.6254	0.0960	1.1074	0.8004
1.1	14.7186	0.0960	1.2910	0.7973
1.1	16.8084	0.0960	1.4743	0.7540
1.1	18.8947	0.0960	1.6573	0.7835
1.5	5.2171	0.1316	0.4576	0.6729
1.5	7.2977	0.1316	0.6401	0.7844
1.5	9.3761	0.1316	0.8224	0.7828
1.5	11.4511	0.1316	1.0044	0.8053
1.5	13.5226	0.1316	1.1861	0.7831
1.5	15.5919	0.1316	1.3676	0.7948
1.5	17.6566	0.1316	1.5487	0.7609

Table C.6 Slug average void fraction for $\beta = 0.72$, Position 2.

$Q_{l,inlet}$ (m^3/h)	$Q_{g,inlet}$ (m^3/h)	$j_{l,inlet}$ (m/s)	$j_{g,inlet}$ (m/s)	**Void Fraction** $(-)$
1.8	2.1149	0.1579	0.1855	0.6626
1.8	4.2240	0.1579	0.3705	0.6638
1.8	6.3264	0.1579	0.5549	0.7045
1.8	8.4287	0.1579	0.7393	0.7641
1.8	10.5276	0.1579	0.9235	0.7971
1.8	12.6254	0.1579	1.1074	0.8169
1.8	14.7186	0.1579	1.2910	0.7944
1.8	16.8084	0.1579	1.4743	0.7783
1.8	18.8947	0.1579	1.6573	0.7612
2.1	3.1375	0.1842	0.2752	0.7079
2.1	5.2171	0.1842	0.4576	0.7081
2.1	7.2122	0.1842	0.6327	0.7726

Table C.7 Slug average void fraction for $\beta = 0.77$, Position 2.

$Q_{l,inlet}$ (m^3/h)	$Q_{g,inlet}$ (m^3/h)	$j_{l,inlet}$ (m/s)	$j_{g,inlet}$ (m/s)	**Void Fraction** $(-)$
0.8	9.4400	0.0702	0.8280	0.8083
0.8	11.5297	0.0702	1.0113	0.7907
0.8	13.6059	0.0702	1.1934	0.7839
0.8	15.6865	0.0702	1.3759	0.7739
1.1	5.2524	0.0960	0.4607	0.7857
1.1	7.3479	0.0960	0.6445	0.7804
1.1	9.4400	0.0960	0.8280	0.8021
1.1	11.5297	0.0960	1.0113	0.7655
1.1	13.6024	0.0960	1.1931	0.7374
1.1	15.6865	0.0960	1.3759	0.7061
1.1	17.7649	0.0960	1.5582	0.8137
1.5	3.1603	0.1316	0.2772	0.7713
1.5	5.2604	0.1316	0.4614	0.7546
1.5	7.3536	0.1316	0.6450	0.8074
1.5	9.4400	0.1316	0.8280	0.8043
1.5	11.5297	0.1316	1.0113	0.7846
1.5	13.6059	0.1316	1.1934	0.8098
1.8	3.1581	0.1579	0.1855	0.7250
1.8	5.2558	0.1579	0.3705	0.7066
1.8	7.3502	0.1579	0.5549	0.7739
1.8	9.4400	0.1579	0.7393	0.8227
1.8	11.5297	0.1579	0.9234	0.7722
1.8	13.6161	0.1579	1.1074	0.7762
1.8	14.7186	0.1579	1.2910	0.6311
1.8	16.8084	0.1579	1.4743	0.7842
1.8	18.8446	0.1579	1.6573	0.7040

Table C.7 Slug average void fraction for $\beta = 0.77$, Position 2.

$Q_{l,inlet}$ (m^3/h)	$Q_{g,inlet}$ (m^3/h)	$j_{l,inlet}$ (m/s)	$j_{g,inlet}$ (m/s)	**Void Fraction** $(-)$
2.1	0.9451	0.1842	0.0829	0.6166
2.1	3.1558	0.1842	0.2768	0.7201
2.1	5.2524	0.1842	0.4607	0.6962
2.1	7.3479	0.1842	0.6445	0.7605
2.1	9.4400	0.1842	0.8280	0.8009
2.1	11.5297	0.1842	1.0113	0.8144
2.1	13.6161	0.1842	1.1943	0.8028
2.1	15.6979	0.1842	1.3769	0.7930
2.1	17.7786	0.1842	1.5594	0.7442
2.5	7.2521	0.2192	0.6361	0.7714
2.5	9.3237	0.2192	0.8178	0.7930

Table C.8 Slug average void fraction for $\beta = 0.83$, Position 2.

$Q_{l,inlet}$ (m^3/h)	$Q_{g,inlet}$ (m^3/h)	$j_{l,inlet}$ (m/s)	$j_{g,inlet}$ (m/s)	**Void Fraction** $(-)$
1.1	9.3089	0.0960	0.8165	0.6727
1.1	11.1604	0.0960	0.9789	0.7303
1.1	16.6305	0.0960	1.4587	0.6136
1.1	17.4297	0.0960	1.5288	0.6658
1.5	3.7486	0.1316	0.3288	0.6664
1.5	5.6013	0.1316	0.4913	0.7266
1.5	7.4539	0.1316	0.6538	0.7380
1.5	9.2826	0.1316	0.8142	0.6721
1.5	11.1296	0.1316	0.9762	0.7252
1.5	12.9720	0.1316	1.1378	0.7673
1.8	4.9081	0.1579	0.4305	0.6788
1.8	6.8485	0.1579	0.6007	0.7053
1.8	8.7844	0.1579	0.7705	0.7081
1.8	10.7123	0.1579	0.9396	0.6580
1.8	12.6174	0.1579	1.1067	0.6749
2.1	6.8483	0.1842	0.6007	0.6636
2.1	8.7850	0.1842	0.7705	0.7060
2.1	10.7128	0.1842	0.9396	0.6994
2.1	12.6172	0.1842	1.1067	0.7144
2.5	2.9517	0.2192	0.2589	0.5118
2.5	3.9265	0.2192	0.3444	0.6026
2.5	4.9024	0.2192	0.4300	0.5946
2.5	7.8085	0.2192	0.6844	0.6484
2.5	10.2141	0.2192	0.8959	0.7526
2.5	12.4715	0.2192	1.0939	0.7270

Table C.9 Slug average void fraction for $\beta = 1.00$.

$Q_{l,inlet}$ (m^3/h)	$Q_{g,inlet}$ (m^3/h)	$j_{l,inlet}$ (m/s)	$j_{g,inlet}$ (m/s)	**Void Fraction** $(-)$
1.2	21.9140	0.1053	1.9221	0.8538
1.2	23.9062	0.1053	2.0969	0.8687
1.3	20.9413	0.1140	1.8368	0.9189
1.3	22.8896	0.1140	2.0073	0.9242
1.3	24.8468	0.1140	2.1794	0.8755
1.4	19.9441	0.1228	1.7493	0.7854
1.4	20.9179	0.1228	1.8348	0.8647
1.4	21.8896	0.1228	1.9200	0.7240
1.4	22.8590	0.1228	2.0050	0.9293
1.4	23.8529	0.1228	2.0922	0.8647
1.4	24.8190	0.1228	2.1769	0.8983
1.5	17.9696	0.1316	1.5762	0.9360
1.5	18.9468	0.1316	1.6619	0.9279
1.5	19.9218	0.1316	1.7474	0.9232
1.5	20.8946	0.1316	1.8327	0.9088
1.5	21.8896	0.1316	1.9200	0.8707
1.5	22.8590	0.1316	2.0050	0.8556
1.6	14.9913	0.1403	1.3149	0.7475
1.6	15.9730	0.1403	1.4010	0.8122
1.6	16.9524	0.1403	1.4869	0.7133
1.6	17.9496	0.1403	1.5744	0.9148
1.6	18.9258	0.1403	1.6600	0.7053
1.6	19.9218	0.1403	1.7474	0.7946

Table C.9 Slug average void fraction for $\beta = 1.00$.

$Q_{l,inlet}$ (m^3/h)	$Q_{g,inlet}$ (m^3/h)	$j_{l,inlet}$ (m/s)	$j_{g,inlet}$ (m/s)	**Void Fraction** $(-)$
1.7	13.0069	0.1491	1.1409	0.6100
1.7	13.9919	0.1491	1.2273	0.7810
1.7	14.9747	0.1491	1.3135	0.9157
1.7	15.9730	0.1491	1.4010	0.9114
1.7	16.9524	0.1491	1.4869	0.8143
1.7	17.9297	0.1491	1.5727	0.8777
1.7	18.9258	0.1491	1.6600	0.8909
1.7	19.8996	0.1491	1.7454	0.8922
1.7	20.8946	0.1491	1.8327	0.7251
1.8	12.0064	0.1579	1.0531	0.8374
1.8	12.9925	0.1579	1.1396	0.9077
1.8	13.9764	0.1579	1.2259	0.9116
1.8	14.9747	0.1579	1.3135	0.7671
1.8	15.9552	0.1579	1.3995	0.9193
1.8	16.9336	0.1579	1.4853	0.9371
1.8	17.9297	0.1579	1.5727	0.9358
1.9	10.0275	0.1666	0.8795	0.9186
1.9	11.0181	0.1666	0.9664	0.9130
1.9	12.0064	0.1666	1.0531	0.8922
1.9	13.0069	0.1666	1.1409	0.6884
1.9	13.9919	0.1666	1.2273	0.9113
1.9	14.9747	0.1666	1.3135	0.6874
1.9	15.9730	0.1666	1.4010	0.6694
1.9	16.9524	0.1666	1.4869	0.6812
1.9	17.9297	0.1666	1.5727	0.6355

Table C.9 Slug average void fraction for $\beta = 1.00$.

$Q_{l,inlet}$ (m^3/h)	$Q_{g,inlet}$ (m^3/h)	$j_{l,inlet}$ (m/s)	$j_{g,inlet}$ (m/s)	**Void Fraction** $(-)$
2.0	9.0248	0.1754	0.7916	0.6871
2.0	10.0169	0.1754	0.8786	0.6939
2.0	11.0059	0.1754	0.9653	0.6192
2.0	12.0064	0.1754	1.0531	0.6466
2.0	12.9925	0.1754	1.1396	0.6166
2.0	13.9764	0.1754	1.2259	0.7731
2.0	14.9747	0.1754	1.3135	0.7652
2.0	15.9552	0.1754	1.3995	0.7179
2.1	8.0220	0.1842	0.7036	0.7186
2.1	9.0248	0.1842	0.7916	0.7451
2.1	10.0164	0.1842	0.8786	0.7743
2.1	11.0059	0.1842	0.9653	0.5751
2.1	12.0064	0.1842	1.0531	0.6285
2.1	13.0069	0.1842	1.1409	0.7349
2.1	13.9919	0.1842	1.2273	0.7783
2.1	14.9747	0.1842	1.3135	0.7634
2.1	15.9730	0.1842	1.4010	0.7645
2.1	16.9524	0.1842	1.4868	0.8320
2.1	17.9297	0.1842	1.5727	0.7530
2.1	18.9258	0.1842	1.6600	0.7313

Table C.9 Slug average void fraction for $\beta = 1.00$.

$Q_{l,inlet}$ (m^3/h)	$Q_{g,inlet}$ (m^3/h)	$j_{l,inlet}$ (m/s)	$j_{g,inlet}$ (m/s)	**Void Fraction** $(-)$
2.2	7.0348	0.1930	0.6170	0.8199
2.2	8.0398	0.1930	0.7052	0.8361
2.2	9.0248	0.1930	0.7916	0.7969
2.2	10.0164	0.1930	0.8786	0.8507
2.2	11.0059	0.1930	0.9653	0.7999
2.2	12.0064	0.1930	1.0531	0.7750
2.2	12.9925	0.1930	1.1396	0.8228
2.2	13.9764	0.1930	1.2259	0.8784
2.2	14.9747	0.1930	1.3135	0.8711
2.2	15.9552	0.1930	1.3995	0.8488
2.2	16.9524	0.1930	1.4869	0.8478
2.2	17.9297	0.1930	1.5727	0.7591
2.2	18.9258	0.1930	1.6600	0.8145
2.3	6.0432	0.2017	0.5301	0.6253
2.3	7.0426	0.2017	0.6177	0.5309
2.3	8.0398	0.2017	0.7052	0.4585
2.3	9.0348	0.2017	0.7925	0.5169
2.3	10.0275	0.2017	0.8795	0.7164
2.3	11.0181	0.2017	0.9664	0.5775
2.3	12.0064	0.2017	1.0531	0.5991
2.3	13.0069	0.2017	1.1409	0.6283
2.3	13.9919	0.2017	1.2273	0.6023
2.3	14.9747	0.2017	1.3135	0.6583
2.3	15.9730	0.2017	1.4010	0.6377
2.3	16.9713	0.2017	1.4886	0.6682

Table C.9 Slug average void fraction for $\beta = 1.00$.

$Q_{l,inlet}$ (m^3/h)	$Q_{g,inlet}$ (m^3/h)	$j_{l,inlet}$ (m/s)	$j_{g,inlet}$ (m/s)	**Void Fraction** $(-)$
2.4	5.0415	0.2105	0.4422	0.5009
2.4	6.0432	0.2105	0.5301	0.5746
2.4	7.0426	0.2105	0.6177	0.6776
2.4	8.0398	0.2105	0.7052	0.6031
2.4	9.0348	0.2105	0.7925	0.4502
2.4	10.0275	0.2105	0.8795	0.6020
2.4	11.0181	0.2105	0.9664	0.5899
2.4	12.0064	0.2105	1.0531	0.5855
2.4	13.0069	0.2105	1.1409	0.6356
2.4	13.9919	0.2105	1.2273	0.6923
2.4	14.9747	0.2105	1.3135	0.6447
2.4	15.9730	0.2105	1.4010	0.6496
2.5	4.0377	0.2192	0.3542	0.4602
2.5	5.0415	0.2192	0.4422	0.5999
2.5	6.0432	0.2192	0.5301	0.6141
2.5	7.0426	0.2192	0.6177	0.6171
2.5	8.0398	0.2192	0.7052	0.6765
2.5	9.0348	0.2192	0.7925	0.6642
2.5	10.0275	0.2192	0.8795	0.6905
2.5	11.0181	0.2192	0.9664	0.6137
2.5	12.0064	0.2192	1.0531	0.6125
2.5	13.0069	0.2192	1.1409	0.6063

APPENDIX D

THE SLUG PROPAGATION VELOCITY

The slug propagation velocity is presented in this appendix in the form of a table. The tables are arranged according to the orifice β ratio and the position of the orifice with respect tio the elbow. The data for experiments carried out without obstruction are also presented.

The first and the second columns of the tables, present the volumetric flow rates of liquid and gas (m^3/h), respectively. The third and the fourth columns correspond to the superficial velocities of liquid and gas (m/s), respectively. The last column corresponds to the slug propagation velocity.

Table D.1 Slug propagation velocity for $\beta = 0.66$, Position 1.

$Q_{l,inlet}$ (m^3/h)	$Q_{g,inlet}$ (m^3/h)	$j_{l,inlet}$ (m/s)	$j_{g,inlet}$ (m/s)	**Velocity** (m/s)
0.8	4.2081	0.0702	0.3691	0.7142
0.8	6.3036	0.0702	0.5529	0.6940
0.8	8.3979	0.0702	0.7366	0.7329
0.8	10.4820	0.0702	0.9194	0.7813
0.8	12.5684	0.0702	1.1024	0.6756
0.8	14.6525	0.0702	1.2852	0.6410
0.8	16.7320	0.0702	1.4676	0.6100
0.8	18.8092	0.0702	1.6498	0.5000
1.1	4.2081	0.0960	0.3691	0.6940
1.1	6.3081	0.0960	0.5533	0.7352
1.1	8.3979	0.0960	0.7366	0.7812
1.1	10.4888	0.0960	0.9200	0.7352
1.1	12.5775	0.0960	1.1032	0.7142
1.1	14.6627	0.0960	1.2861	0.6097
1.1	16.7445	0.0960	1.4687	0.7142
1.1	18.8241	0.0960	1.6511	0.5681
1.5	1.8983	0.1316	0.1665	0.7352
1.5	3.9983	0.1316	0.3507	0.7142
1.5	6.0972	0.1316	0.5348	0.7813
1.5	8.1881	0.1316	0.7182	0.8928
1.5	10.2791	0.1316	0.9016	0.6578
1.5	12.3586	0.1316	1.0840	0.6410
1.5	14.4427	0.1316	1.2668	0.6097
1.5	16.5199	0.1316	1.4430	0.6097
1.5	18.6006	0.1316	1.6315	0.6097

Table D.1 Slug propagation velocity for $\beta = 0.66$, Position 1.

$Q_{l,inlet}$ (m^3/h)	$Q_{g,inlet}$ (m^3/h)	$j_{l,inlet}$ (m/s)	$j_{g,inlet}$ (m/s)	**Velocity** (m/s)
1.8	2.5264	0.1579	0.2216	0.6756
1.8	4.6288	0.1579	0.4060	0.6940
1.8	6.7231	0.1579	0.5897	0.7813
1.8	8.8175	0.1579	0.7734	0.7813
1.8	10.9084	0.1579	0.9568	0.6250
1.8	12.9970	0.1579	1.1400	0.6410
2.1	2.1057	0.1842	0.1847	0.6940
2.1	4.2047	0.1842	0.3688	0.7142
2.1	6.3024	0.1842	0.5528	0.7813

Table D.2 Slug propagation velocity for $\beta = 0.72$, Position 1.

$Q_{l,inlet}$ (m^3/h)	$Q_{g,inlet}$ (m^3/h)	$j_{l,inlet}$ (m/s)	$j_{g,inlet}$ (m/s)	**Velocity** (m/s)
0.4	11.4773	0.0350	1.0067	0.6140
0.4	13.5534	0.0350	1.1888	0.5932
0.4	15.6272	0.0350	1.3707	0.5932
0.4	17.6976	0.0350	1.5523	0.5556
0.4	19.7646	0.0350	1.7336	0.5147
0.4	21.8111	0.0350	1.9131	0.5224
0.4	23.8701	0.0350	2.0937	0.5224
0.4	25.9257	0.0350	2.2740	0.4605
0.4	27.9790	0.0350	2.4541	0.4605
0.5	10.4261	0.0440	0.9145	0.6604
0.5	12.5022	0.0440	1.0966	0.6250
0.5	14.5738	0.0440	1.2783	0.5932
0.5	16.6431	0.0440	1.4598	0.5833
0.5	18.7100	0.0440	1.6411	0.5738
0.5	20.7725	0.0440	1.8220	0.5303
0.5	22.8326	0.0440	2.0027	0.5224
0.5	24.8893	0.0440	2.1831	0.4795
0.5	26.9427	0.0440	2.3632	0.4605
0.5	28.9925	0.0440	2.5430	0.4375
0.8	11.4682	0.0702	1.0059	0.6481
0.8	13.5432	0.0702	1.1879	0.6250
0.8	15.6067	0.0702	1.3689	0.5738
0.8	17.6703	0.0702	1.5499	0.5303
0.8	19.7339	0.0702	1.7309	0.5147
0.8	21.7940	0.0702	1.9116	0.4930

Table D.2 Slug propagation velocity for $\beta = 0.72$, Position 1.

$Q_{l,inlet}$ (m^3/h)	$Q_{g,inlet}$ (m^3/h)	$j_{l,inlet}$ (m/s)	$j_{g,inlet}$ (m/s)	**Velocity** (m/s)
1.1	3.1535	0.0960	0.2766	0.7292
1.1	5.2433	0.0960	0.4599	0.7292
1.1	9.3488	0.0960	0.8200	0.6604
1.1	11.4682	0.0960	1.0059	0.6481
1.1	13.5432	0.0960	1.1879	0.6481
1.1	15.6067	0.0960	1.3689	0.6140
1.1	17.6703	0.0960	1.5499	0.5385
1.1	19.7339	0.0960	1.7309	0.5224
1.5	2.7225	0.1316	0.2388	0.7292
1.5	4.8100	0.1316	0.4219	0.7292
1.5	8.9805	0.1316	0.7877	0.7292
1.5	11.0509	0.1316	0.9693	0.6731
1.5	13.1270	0.1316	1.1514	0.6481
1.5	15.1872	0.1316	1.3321	0.6364
1.5	17.2542	0.1316	1.5134	0.5833
1.5	19.3177	0.1316	1.6944	0.5303
1.8	1.6851	0.1579	0.1478	0.7955
1.8	3.7954	0.1579	0.3329	0.7292
1.8	5.8954	0.1579	0.5171	0.7955
1.8	7.9955	0.1579	0.7013	0.8750
1.8	10.0921	0.1579	0.8852	0.6731
1.8	12.1853	0.1579	1.0688	0.6604
1.8	14.2762	0.1579	1.2522	0.6140
1.8	16.3637	0.1579	1.4353	0.5469
1.8	18.4478	0.1579	1.6181	0.5556

Table D.2 Slug propagation velocity for $\beta = 0.72$, Position 1.

$Q_{l,inlet}$ (m^3/h)	$Q_{g,inlet}$ (m^3/h)	$j_{l,inlet}$ (m/s)	$j_{g,inlet}$ (m/s)	**Velocity** (m/s)
2.1	3.3929	0.1842	0.2976	0.7609
2.1	4.5307	0.1842	0.3974	0.7292
2.1	6.6331	0.1842	0.5818	0.8750
2.1	10.8275	0.1842	0.9497	0.6604
2.1	12.9207	0.1842	1.1333	0.6731
2.1	15.0105	0.1842	1.3166	0.6604

Table D.3 Slug propagation velocity for $\beta = 0.77$, Position 1.

$Q_{l,inlet}$ (m^3/h)	$Q_{g,inlet}$ (m^3/h)	$j_{l,inlet}$ (m/s)	$j_{g,inlet}$ (m/s)	**Velocity** (m/s)
0.8	5.2205	0.0702	0.4579	0.5147
0.8	7.3080	0.0702	0.6410	0.4861
0.8	9.3830	0.0702	0.8230	0.5469
0.8	11.4602	0.0702	1.0052	0.7292
0.8	13.5329	0.0702	1.1870	0.6140
0.8	15.6033	0.0702	1.3686	0.6482
0.8	17.6703	0.0702	1.5499	0.6250
0.8	19.7190	0.0702	1.7296	0.5303
0.8	21.7769	0.0702	1.9101	0.5395
0.8	23.8325	0.0702	2.0904	0.5147
1.1	7.3091	0.0960	0.6411	0.6482
1.1	9.3909	0.0960	0.8237	0.6364
1.1	11.4682	0.0960	1.0059	0.6863
1.1	13.5226	0.0960	1.1861	0.6604
1.1	15.5919	0.0960	1.3676	0.6035
1.1	17.6566	0.0960	1.5487	0.5738
1.1	19.7190	0.0960	1.7296	0.5384
1.5	6.0562	0.1316	0.5312	0.7140
1.5	8.1323	0.1316	0.7133	0.7000
1.5	10.2095	0.1316	0.8955	0.6862
1.5	12.2845	0.1316	1.0775	0.7000
1.5	14.3549	0.1316	1.2591	0.6363
1.5	16.4230	0.1316	1.4405	0.6140
1.5	18.4877	0.1316	1.6216	0.5645
1.9	2.0886	0.1666	0.1832	0.8537
1.9	4.1670	0.1666	0.3655	0.8537
1.9	9.8185	0.1666	0.8612	0.6731
1.9	11.8752	0.1666	1.0416	0.6863
1.9	13.9376	0.1666	1.2225	0.6604

Table D.3 Slug propagation velocity for $\beta = 0.77$, Position 1.

$Q_{l,inlet}$ (m^3/h)	$Q_{g,inlet}$ (m^3/h)	$j_{l,inlet}$ (m/s)	$j_{g,inlet}$ (m/s)	**Velocity** (m/s)
2.1	1.2210	0.1842	0.1071	0.7292
2.1	2.6040	0.1842	0.2284	0.7447
2.1	4.6846	0.1842	0.4109	0.7450
2.1	6.7562	0.1842	0.5926	0.7292
2.1	8.8289	0.1842	0.7744	0.7292
2.1	10.8970	0.1842	0.9558	0.6731
2.1	12.9526	0.1842	1.1361	0.6731
2.1	16.2212	0.1842	1.4228	0.6250
2.3	0.8391	0.2017	0.0736	0.7954
2.3	2.0932	0.2017	0.1836	0.7954
2.3	3.1387	0.2017	0.2753	0.7292
2.3	5.2205	0.2017	0.4579	0.7954
2.3	9.3830	0.2017	0.8230	0.6731
2.3	11.4602	0.2017	1.0052	0.6731
2.3	13.5329	0.2017	1.1870	0.6250

Table D.4 Slug propagation velocity for $\beta = 0.83$ Position 1.

$Q_{l,inlet}$ (m^3/h)	$Q_{g,inlet}$ (m^3/h)	$j_{l,inlet}$ (m/s)	$j_{g,inlet}$ (m/s)	**Velocity** (m/s)
1.1	16.9212	0.0960	1.4842	0.8750
1.1	19.0224	0.0960	1.6685	0.7955
1.5	4.2263	0.1316	0.3707	0.7955
1.5	6.3309	0.1316	0.5553	0.7955
1.5	8.4344	0.1316	0.7398	0.7292
1.5	10.5356	0.1316	0.9241	0.7447
1.5	12.6242	0.1316	1.1073	0.7000
1.5	14.7174	0.1316	1.2909	0.6863
1.5	16.8072	0.1316	1.4742	0.6481
1.8	4.0188	0.1579	0.3525	0.7954
1.8	6.1246	0.1579	0.5372	0.8750
1.8	8.2246	0.1579	0.7214	0.7292
1.8	10.3178	0.1579	0.9050	0.6731
1.8	12.4145	0.1579	1.0889	0.6731
2.1	3.1717	0.1842	0.2782	0.7955
2.1	9.4833	0.1842	0.8318	0.7447
2.1	11.5719	0.1842	1.0150	0.7143
2.1	13.6663	0.1842	1.1987	0.6731
2.5	1.2723	0.2192	0.1116	0.8537
2.5	3.3815	0.2192	0.2966	0.7955
2.5	7.5919	0.2192	0.6659	0.7955
2.5	9.6931	0.2192	0.8502	0.7292
2.5	11.7920	0.2192	1.0343	0.7292
2.5	13.8875	0.2192	1.2181	0.6863

Table D.5 Slug propagation velocity for $\beta = 0.66$, Position 2.

$Q_{l,inlet}$ (m^3/h)	$Q_{g,inlet}$ (m^3/h)	$j_{l,inlet}$ (m/s)	$j_{g,inlet}$ (m/s)	**Velocity** (m/s)
0.5	8.4036	0.0440	0.7371	0.7352
0.5	14.6741	0.0440	1.2871	0.6579
0.5	16.7445	0.0440	1.4687	0.5952
0.5	18.8241	0.0440	1.6511	0.5556
0.5	20.9002	0.0440	1.8332	0.5100
0.8	6.3081	0.0702	0.5533	0.6756
0.8	8.3979	0.0702	0.7366	0.6940
0.8	10.4968	0.0702	0.9207	0.6579
0.8	14.6627	0.0702	1.2861	0.5952
0.8	16.7445	0.0702	1.4687	0.6579
0.8	18.8241	0.0702	1.6511	0.5814
1.1	4.2081	0.0960	0.3691	0.7142
1.1	6.3036	0.0960	0.5529	0.6940
1.1	8.3979	0.0960	0.7366	0.6410
1.1	12.5775	0.0960	1.1032	0.6756
1.1	14.6525	0.0960	1.2852	0.6090
1.1	16.7320	0.0960	1.4676	0.6250
1.5	4.2081	0.1316	0.3691	0.7142
1.5	6.3036	0.1316	0.5529	0.6579
1.5	8.3979	0.1316	0.7366	0.6756
1.5	12.5684	0.1316	1.1024	0.7142
1.5	14.6525	0.1316	1.2852	0.6410
1.5	16.7320	0.1316	1.4676	0.6250

Table D.5 Slug propagation velocity for $\beta = 0.66$, Position 2.

$Q_{l,inlet}$ (m^3/h)	$Q_{g,inlet}$ (m^3/h)	$j_{l,inlet}$ (m/s)	$j_{g,inlet}$ (m/s)	**Velocity** (m/s)
2.1	4.2081	0.1842	0.3691	0.7813
2.1	5.2570	0.1842	0.4611	0.6940
2.1	6.3024	0.1842	0.5528	0.7352
2.1	7.3479	0.1842	0.6445	0.7142

Table D.6 Slug propagation velocity for $\beta = 0.72$, Position 2.

$Q_{l,inlet}$ (m^3/h)	$Q_{g,inlet}$ (m^3/h)	$j_{l,inlet}$ (m/s)	$j_{g,inlet}$ (m/s)	**Velocity** (m/s)
0.8	6.3731	0.0702	0.5590	0.6731
0.8	14.8166	0.0702	1.2996	0.6731
0.8	16.9212	0.0702	1.4842	0.6140
0.8	19.0224	0.0702	1.6685	0.5833
0.8	21.1202	0.0702	1.8525	0.5556
1.1	14.7186	0.0960	1.2910	0.7292
1.1	16.8084	0.0960	1.4743	0.6250
1.1	18.8947	0.0960	1.6573	0.7292
1.5	5.2171	0.1316	0.4576	0.7000
1.5	9.3761	0.1316	0.8224	0.6731
1.5	11.4511	0.1316	1.0044	0.7000
1.5	13.5226	0.1316	1.1861	0.6481
1.5	15.5919	0.1316	1.3676	0.5932
1.5	17.6566	0.1316	1.5487	0.5385
1.8	4.2240	0.1579	0.3705	0.7778
1.8	6.3264	0.1579	0.5549	0.7292
1.8	8.4287	0.1579	0.7393	0.7292
1.8	10.5276	0.1579	0.9235	0.6731
1.8	12.6254	0.1579	1.1074	0.6731
1.8	16.8084	0.1579	1.4743	0.6481
1.8	18.8947	0.1579	1.6573	0.6034
2.1	3.1375	0.1842	0.2752	0.7778
2.1	5.2171	0.1842	0.4576	0.7292
2.1	7.2122	0.1842	0.6327	0.6863

Table D.7 Slug propagation velocity for $\beta = 0.77$, Position 2.

$Q_{l,inlet}$ (m^3/h)	$Q_{g,inlet}$ (m^3/h)	$j_{l,inlet}$ (m/s)	$j_{g,inlet}$ (m/s)	**Velocity** (m/s)
0.8	11.5297	0.0702	1.0113	0.7447
0.8	13.6059	0.0702	1.1934	0.6604
0.8	15.6865	0.0702	1.3759	0.6035
1.1	9.4400	0.0960	0.8280	0.7447
1.1	11.5297	0.0960	1.0113	0.6731
1.1	13.6024	0.0960	1.1931	0.6604
1.1	15.6865	0.0960	1.3759	0.6364
1.1	17.7649	0.0960	1.5582	0.6035
1.5	3.1603	0.1316	0.2772	0.7609
1.5	5.2604	0.1316	0.4614	0.7609
1.5	7.3536	0.1316	0.6450	0.7143
1.5	9.4400	0.1316	0.8280	0.6863
1.5	11.5297	0.1316	1.0113	0.7143
1.5	13.6059	0.1316	1.1934	0.7000
1.8	11.5297	0.1579	0.9234	0.7292
1.8	13.6161	0.1579	1.1074	0.7292
1.8	14.7186	0.1579	1.2910	0.6731
1.8	16.8084	0.1579	1.4743	0.7292
1.8	18.8446	0.1579	1.6573	0.6731
2.1	3.1558	0.1842	0.2768	0.7778
2.1	5.2524	0.1842	0.4607	0.7609
2.1	7.3479	0.1842	0.6445	0.7292
2.1	9.4400	0.1842	0.8280	0.7292
2.1	11.5297	0.1842	1.0113	0.7000
2.1	13.6161	0.1842	1.1943	0.6482
2.1	15.6979	0.1842	1.3769	0.7000
2.1	17.7786	0.1842	1.5594	0.6250
2.5	7.2521	0.2192	0.6361	0.7000
2.5	9.3237	0.2192	0.8178	0.8140

Table D.8 Slug propagation velocity for $\beta = 0.83$, Position 2.

$Q_{l,inlet}$ (m^3/h)	$Q_{g,inlet}$ (m^3/h)	$j_{l,inlet}$ (m/s)	$j_{g,inlet}$ (m/s)	**Velocity** (m/s)
1.1	9.3089	0.0960	0.8165	0.6969
1.1	11.1604	0.0960	0.9789	0.6559
1.1	16.6305	0.0960	1.4587	0.5868
1.1	17.4297	0.0960	1.5288	0.5868
1.5	3.7486	0.1316	0.3288	0.8577
1.5	5.6013	0.1316	0.4913	0.7433
1.5	7.4539	0.1316	0.6538	0.6969
1.5	9.2826	0.1316	0.8142	0.6559
1.5	11.1296	0.1316	0.9762	0.61944
1.5	12.9720	0.1316	1.1378	0.5868
1.8	4.9081	0.1579	0.4305	0.7433
1.8	6.8485	0.1579	0.6007	0.7433
1.8	8.7844	0.1579	0.7705	0.6969
1.8	10.7123	0.1579	0.9396	0.6559
1.8	12.6174	0.1579	1.1067	0.6194
2.1	6.8483	0.1842	0.6007	0.7433
2.1	8.7850	0.1842	0.7705	0.6969
2.1	10.7128	0.1842	0.9396	0.6559
2.1	12.6172	0.1842	1.1067	0.1556
2.5	2.9517	0.2192	0.2589	0.7433
2.5	4.9024	0.2192	0.4300	0.7433
2.5	7.8085	0.2192	0.6844	0.7964

Table D.9 Slug propagation velocity, for $\beta = 1.00$.

$Q_{l,inlet}$ (m^3/h)	$Q_{g,inlet}$ (m^3/h)	$j_{l,inlet}$ (m/s)	$j_{g,inlet}$ (m/s)	**Velocity** (m/s)
1.2	21.9140	0.1053	1.9221	0.8538
1.2	23.9062	0.1053	2.0969	0.8687
1.3	20.9413	0.1140	1.8368	0.9189
1.3	22.8896	0.1140	2.0073	0.9242
1.3	24.8468	0.1140	2.1794	0.8755
1.4	19.9441	0.1228	1.7493	0.7854
1.4	20.9179	0.1228	1.8348	0.8647
1.4	21.8896	0.1228	1.9200	0.7240
1.4	22.8590	0.1228	2.0050	0.9293
1.4	23.8529	0.1228	2.0922	0.8647
1.4	24.8190	0.1228	2.1769	0.8983
1.5	17.9696	0.1316	1.5762	0.9360
1.5	18.9468	0.1316	1.6619	0.9279
1.5	19.9218	0.1316	1.7474	0.9232
1.5	20.8946	0.1316	1.8327	0.9088
1.5	21.8896	0.1316	1.9200	0.8707
1.5	22.8590	0.1316	2.0050	0.8556
1.6	14.9913	0.1403	1.3149	0.7475
1.6	15.9730	0.1403	1.4010	0.8122
1.6	16.9524	0.1403	1.4869	0.7133
1.6	17.9496	0.1403	1.5744	0.9148
1.6	18.9258	0.1403	1.6600	0.7053
1.6	19.9218	0.1403	1.7474	0.7946

Table D.9 Slug propagation velocity, for $\beta = 1.00$.

$Q_{l,inlet}$ (m^3/h)	$Q_{g,inlet}$ (m^3/h)	$j_{l,inlet}$ (m/s)	$j_{g,inlet}$ (m/s)	**Velocity** (m/s)
1.7	13.0069	0.1491	1.1409	0.6100
1.7	13.9919	0.1491	1.2273	0.7810
1.7	14.9747	0.1491	1.3135	0.9157
1.7	15.9730	0.1491	1.4010	0.9114
1.7	16.9524	0.1491	1.4869	0.8143
1.7	17.9297	0.1491	1.5727	0.8777
1.7	18.9258	0.1491	1.6600	0.8909
1.7	19.8996	0.1491	1.7454	0.8922
1.7	20.8946	0.1491	1.8327	0.7251
1.8	12.0064	0.1579	1.0531	0.8374
1.8	12.9925	0.1579	1.1396	0.9077
1.8	13.9764	0.1579	1.2259	0.9116
1.8	14.9747	0.1579	1.3135	0.7671
1.8	15.9552	0.1579	1.3995	0.9193
1.8	16.9336	0.1579	1.4853	0.9371
1.8	17.9297	0.1579	1.5727	0.9358
1.9	10.0275	0.1666	0.8795	0.9186
1.9	11.0181	0.1666	0.9664	0.9130
1.9	12.0064	0.1666	1.0531	0.8922
1.9	13.0069	0.1666	1.1409	0.6884
1.9	13.9919	0.1666	1.2273	0.9113
1.9	14.9747	0.1666	1.3135	0.6874
1.9	15.9730	0.1666	1.4010	0.6694
1.9	16.9524	0.1666	1.4869	0.6812
1.9	17.9297	0.1666	1.5727	0.6355

Table D.9 Slug propagation velocity, for $\beta = 1.00$.

$Q_{l,inlet}$ (m^3/h)	$Q_{g,inlet}$ (m^3/h)	$j_{l,inlet}$ (m/s)	$j_{g,inlet}$ (m/s)	**Velocity** (m/s)
2.0	9.0248	0.1754	0.7916	0.6871
2.0	10.0169	0.1754	0.8786	0.6939
2.0	11.0059	0.1754	0.9653	0.6192
2.0	12.0064	0.1754	1.0531	0.6466
2.0	12.9925	0.1754	1.1396	0.6166
2.0	13.9764	0.1754	1.2259	0.7731
2.0	14.9747	0.1754	1.3135	0.7652
2.0	15.9552	0.1754	1.3995	0.7179
2.1	8.0220	0.1842	0.7036	0.7743
2.1	11.0059	0.1842	0.9653	0.5751
2.1	12.0064	0.1842	1.0531	0.6285
2.1	13.0069	0.1842	1.1409	0.7349
2.1	13.9919	0.1842	1.2273	0.7783
2.1	14.9747	0.1842	1.3135	0.7634
2.1	15.9730	0.1842	1.4010	0.7645
2.1	16.9524	0.1842	1.4868	0.8320
2.1	17.9297	0.1842	1.5727	0.7530
2.1	18.9258	0.1842	1.6600	0.7313
2.2	7.0348	0.1930	0.6170	0.8199
2.2	8.0398	0.1930	0.7052	0.8361
2.2	9.0248	0.1930	0.7916	0.7969
2.2	10.0164	0.1930	0.8786	0.8507
2.2	11.0059	0.1930	0.9653	0.7999
2.2	12.0064	0.1930	1.0531	0.7750
2.2	12.9925	0.1930	1.1396	0.8228
2.2	13.9764	0.1930	1.2259	0.8784
2.2	14.9747	0.1930	1.3135	0.8711
2.2	15.9552	0.1930	1.3995	0.8488
2.2	16.9524	0.1930	1.4869	0.8478
2.2	17.9297	0.1930	1.5727	0.7591
2.2	18.9258	0.1930	1.6600	0.8145

Table D.9 Slug propagation velocity, for $\beta = 1.00$.

$Q_{l,inlet}$ (m^3/h)	$Q_{g,inlet}$ (m^3/h)	$j_{l,inlet}$ (m/s)	$j_{g,inlet}$ (m/s)	**Velocity** (m/s)
2.3	6.0432	0.2017	0.5301	0.0570
2.3	7.0426	0.2017	0.6177	0.2450
2.3	8.0398	0.2017	0.7052	0.1059
2.3	9.0348	0.2017	0.7925	0.0970
2.3	10.0275	0.2017	0.8795	0.2197
2.3	11.0181	0.2017	0.9664	0.0590
2.3	12.0064	0.2017	1.0531	0.0490
2.3	13.0069	0.2017	1.1409	0.0490
2.3	13.9919	0.2017	1.2273	0.0490
2.3	14.9747	0.2017	1.3135	0.1370
2.3	15.9730	0.2017	1.4010	0.5200
2.3	16.9713	0.2017	1.4886	0.6250
2.4	5.0415	0.2105	0.4422	0.0490
2.4	6.0432	0.2105	0.5301	0.0508
2.4	7.0426	0.2105	0.6177	0.2083
2.4	8.0398	0.2105	0.7052	0.1580
2.4	9.0348	0.2105	0.7925	0.1580
2.4	10.0275	0.2105	0.8795	0.0570
2.4	11.0181	0.2105	0.9664	0.1290
2.4	12.0064	0.2105	1.0531	0.0690
2.4	13.0069	0.2105	1.1409	0.0540
2.4	13.9919	0.2105	1.2273	0.5890
2.4	14.9747	0.2105	1.3135	0.0496
2.4	15.9730	0.2105	1.4010	0.0650

Table D.9 Slug propagation velocity, for $\beta = 1.00$.

$Q_{l,inlet}$ (m^3/h)	$Q_{g,inlet}$ (m^3/h)	$j_{l,inlet}$ (m/s)	$j_{g,inlet}$ (m/s)	**Velocity** (m/s)
2.5	4.0377	0.2192	0.3542	0.0600
2.5	5.0415	0.2192	0.4422	0.0600
2.5	6.0432	0.2192	0.5301	0.0950
2.5	7.0426	0.2192	0.6177	0.1812
2.5	8.0398	0.2192	0.7052	0.1780
2.5	9.0348	0.2192	0.7925	0.0580
2.5	10.0275	0.2192	0.8795	0.1490
2.5	11.0181	0.2192	0.9664	0.0880
2.5	12.0064	0.2192	1.0531	0.0650
2.5	13.0069	0.2192	1.1409	0.1100

APPENDIX E

MATLAB PROGRAMS FOR THE WAVE AMPLITUDE DETECTION

The Matlab program presented here is able to read photos from existing TIFF sequential files and returns the edges of the water free surface as a function of the axial position. The main Matlab program includes two sub-programs; one of which is the Matlab macro for the edge detection (edgedetec.m), and the other one is to obtain smooth egdes (photo.m). The main Matlab program is presented first with typical input and output file names; the subprogram *photo.m* is also included in this appendix. Since *edgedetec.m* is a Matlab macro and can be found anywhere, it is not given in this appendix.

MAIN PROGRAM

```
clear all

j=1;

for d=1:9
    s=['ql11qg12000' int2str(d) '.tif'];
    img=imread(s);
    K = rgb2gray(img);
    BW=edgedetec(K,'sobel',0.04);
    [dist,y]=photo(BW);
    t=['q11' int2str(j) '.txt'];
    fid=fopen(t,'w');
    z=[dist;y];
    fprintf(fid,'
    fclose(fid);
    j=j+1;
end

for d=10:99
    s=['ql11qg1200' int2str(d) '.tif'];
    img=imread(s);
    K = rgb2gray(img);
    BW=edgedetec(K,'sobel',0.04);
    [dist,y]=photo(BW);
    t=['q11' int2str(j) '.txt'];
    fid=fopen(t,'w');
    z=[dist;y];
    fprintf(fid,'
    fclose(fid);
    j=j+1;
end
```

```
for d=100:999
    s=['ql11qg120' int2str(d) '.tif'];
    img=imread(s);
    K = rgb2gray(img);
    BW=edgedetec(K,'sobel',0.04);
    [dist,y]=photo(BW);
    t=['q11' int2str(j) '.txt'];
    fid=fopen(t,'W');
    z=[dist;y];
    fprintf(fid,'
    fclose(fid);
    j=j+1;
end

for d=1000:4952;
    s=['ql11qg12' int2str(d) '.tif'];
    img=imread(s);
    K = rgb2gray(img);
    BW=edgedetec(K, 'sobel',0.04);
    [dist,y]=photo(BW);
    t=['q11' int2str(j) '.txt'];
    fid=fopen(t,'w');
    z=[dist;y];
    fprintf(fid,'
    fclose(fid);
    j=j+1;
end
```

MATLAB SUBPROGRAM RETURNS SMOOTH EDGES

```
function [dist,amp]=photo(BW)

img=BW;
if isa(img,'unit8') | isa(img,'unit16')
   img=im2double(img);
end

asizevert=size(img,1);
asizehor=size(img,2);

imgdouble=double(img);

a1=142.31597;
a2=170.31597;
b=-0.0036039012;

for i=1:asizehor

 f1=a1+b*i;
 f2=a2+b*i;
 f3=round(f1);
 f4=round(f2);

 sum=0;
 count=0;

 for rows=f3:f4;
   if imgdouble(rows,i) == 1
     sum=sum+rows;
     count=count+1;
   end
 end

 if count == 0
   average =f4;
 else
   average=sum/count;
 end
```

```
 totaver(i)=0.0635*(f4-average)/(f4-f3);

end

pi=3.1415927;
f=0.05;
coef1=1+0.7*(2*pi*f*1)+((2*pi*f*1)^2)/4;
coef2=2*((2*pi*f*1)^2/4-1);
coef3=1-0.7*(2*pi*f*1)+((2*pi*f*1)^2)/4;
coef4=((2*pi*f*1)^2)/4;

output(1)=totaver(1);
output(2)=totaver(2);

for i=3:asizehor
 output(i)=(1/coef1)*(coef4*(totaver(i)+2*totaver(i-1)+totaver(i-2))-...
              coef2*output(i-1)-coef3*output(i-2));
end vskip -0.05cm i=17:300;
j=1:284;
dist=0.002258*(j-1);
amp=output(i);

return
```

APPENDIX F

FORTRAN PROGRAMS FOR THE SOLITON INTERACTION

A Fortran program is written to predict the interaction of two trains of soliton and to visualize the formation of slugs. Here, the main program and the subroutines are included.

MAIN PROGRAM

```
PROGRAM Solitoninteraction

IMPLICIT NONE

CHARACTER*7 position

INTEGER                          :: beta,qlinlet,p,nnew,m,nstart,nend,delinc,n1,n2,i
INTEGER, PARAMETER               :: temp=1500,nm=50

REAL                             :: delx,coef,aver1,aver2,x,d,w1,w2,w3,z14,z15, &
                                    z16,z1,z2,z3,z4,z5,z6,z111,z222,z333,z1a,z2a, &
                                    z3a,z4a,z5a,z6a,z12,z13
REAL(4),DIMENSION(temp):: hin,h,y1,y2
REAL,DIMENSION(temp)   :: et1,et2,et3
REAL,DIMENSION(nm)     :: timei

DOUBLE PRECISION,DIMENSION(temp)      :: w,et,wnew,etnew,es,z
DOUBLE PRECISION,DIMENSION(nm,temp)   :: printw,printet
DOUBLE PRECISION,DIMENSION(temp,temp) :: l,u

CALL clear1 (position,beta,qlinlet,n1,n2,nnew,hin,h,y1,y2,e1,e1a,
             e2,e2a,e3,et1,et2,et3,q1,z,q1a,q2,q2a,q2b,w,et,
             wnew,etnew,es,timei,printw,printet,l,u)

CALL clear2 (aver1,aver2,x,d,w1,w2,w3,z14,z15,z16,z1,z2,z3,z4,z5,
             z6,z111,z222,z333,z1a,z2a,z3a,z4a,z5a,z6a,z12,z13)

CALL entree(position,coef,delx,beta,qlinlet)

CALL decision (position,nnew,n1,n2,m,nstart,nend,delinc)

CALL filein(y1,y2,hin,h)

CALL initialboundary(nnew,hin,h,aver1,aver2,w,et)

CALL solution(nnew,m,nstart,nend,delinc,w,et,printw,printet,p,timei)
```

```
CLOSE(1)

CLOSE(2)

CALL writeinfile(position,beta,qlinlet,p)

CLOSE(3)

CALL fileop(delx,p,printw,printet,timei,nnew)

END
```

SUBPROGRAMS

```
SUBROUTINE clear1 (position,beta,qlinlet,n1,n2,nnew,hin,h,y1,y2,e1,e1a,
                   e2,e2a,e3,et1,et2,et3,q1,z,q1a,q2,q2a,q2b,w,et,
                   wnew,etnew,es,timei,printw,printet,l,u) IMPLICIT NONE

CHARACTER*7 position

INTEGER                    :: beta,qlinlet,nnew,n1,n2,i,j
INTEGER, PARAMETER         :: temp=1500,nm=50

REAL(4),DIMENSION(temp):: hin,h,y1,y2
REAL,DIMENSION(temp)   :: et1,et2,et3
REAL,DIMENSION(nm)     :: timei

DOUBLE PRECISION,DIMENSION(temp)        :: w,et,wnew,etnew,es,z
DOUBLE PRECISION,DIMENSION(nm,temp)     :: printw,printet
DOUBLE PRECISION,DIMENSION(temp,temp) :: l,u

position=''
beta=0
qlinlet=0
n1=0
n2=0
nnew=0

DO i=1,temp
   hin(i)=0.0
   h(i)=0.0
   y1(i)=0.0
   y2(i)=0.0
   et1(i)=0.0
   et2(i)=0.0
   et3(i)=0.0
   z(i)=0.0
   w(i)=0.0
   et(i)=0.0
   wnew(i)=0.0
   etnew(i)=0.0
```

```
    es(i)=0.0
ENDDO

DO i=1,nm
    timei(i)=0.0
ENDDO

DO i=1,nm
    DO j=1,temp
      printw(i,j)=0.0
      printet(i,j)=0.0
    ENDDO
ENDDO

DO i=1,temp
    DO j=1,temp
      l(i,j)=0.0
      u(i,j)=0.0
    ENDDO
ENDDO

END SUBROUTINE
```

```
SUBROUTINE clear2 (aver1,aver2,x,d,w1,w2,w3,z14,z15,z16,z1,z2,z3,z4,z5,
                   z6,z111,z222,z333,z1a,z2a,z3a,z4a,z5a,z6a,z12,z13)

IMPLICIT NONE

REAL :: aver1, aver2,x,d,w1,w2,w3,z14,z15,z16,z1,z2,z3,z4,z5,z6, &
        z111,z222,z333,z1a,z2a,z3a,z4a,z5a,z6a,z12,z13

aver1=0.0
aver2=0.0
x=0.0
d=0.0
w1=0.0
w2=0.0
w3=0.0
z14=0.0
z15=0.0
z16=0.0
z1=0.0
z2=0.0
z3=0.0
z4=0.0
z5=0.0
z6=0.0
z111=0.0
z222=0.0
z333=0.0
z1a=0.0
z2a=0.0
z3a=0.0
z4a=0.0
z5a=0.0
z6a=0.0
z12=0.0
z13=0.0

END SUBROUTINE
```

SUBROUTINE entree (position,coef,delx,beta,qlinlet)

```
IMPLICIT NONE

CHARACTER*7 position

INTEGER :: beta,qlinlet

REAL    :: delx, coef

WRITE(*,*) 'Please Enter the Position;(pos1,pos2,sobt)'
READ*, position
WRITE(*,*) 'Please Enter the reflection coefficient'
READ*, coef
WRITE(*,*) 'Please Enter the deltax (changes due to the photo)'
READ*, delx
WRITE(*,*) 'Please Enter the beta ratio (66;72;77;83;10)'
READ*, beta
WRITE(*,*) 'Please Enter the inlet liquid flow rate(8;11;15;18;21)'
READ*, qlinlet

END SUBROUTINE
```

```
SUBROUTINE decision (position,nnew,n1,n2,m,nstart,nend,delinc)

IMPLICIT NONE

CHARACTER*7 position

INTEGER                 :: delinc,n1,n2,m,nnew,nstart,nend
INTEGER,PARAMETER :: npho1pos1=212,npho2pos1=212,npos1=487, &
                     m1=20000,nstart1=15000,nend1=18000
INTEGER,PARAMETER :: npho1pos2=292,npho2pos2=292,npos2=972, &
                     m2=50000,nstart2=29000,nend2=33000
INTEGER,PARAMETER :: npho1sobt=292,npho2sobt=292,nsobt=1459, &
                     m3=100000,nstart3=58000,nend3=61000 )

IF (position == 'pos1'.or. position == 'pos2'.or.  &
   position == 'sobt') THEN

      SELECT CASE (position)

        CASE('pos1')
          nnew=npos1
          n1=npho1pos1
          n2=npho2pos1
          m=m1
          nstart=nstart1
          nend=nend1
          delinc=100
        CASE('pos2')
          nnew=npos2
          n1=npho1pos2
          n2=npho2pos2
          m=m2
          nstart=nstart2
          nend=nend2
          delinc=100
        CASE('sobt')
          nnew=nsobt
          n1=npho1sobt
          n2=npho2sobt
```

```
            m=m3
            nstart=nstart3
            nend=nend3
            delinc=100

        END SELECT

ENDIF

END SUBROUTINE
```

```
SUBROUTINE filein(y1,y2,hin,h,aver1,aver2,n1,n2,nnew)

IMPLICIT NONE

INTEGER                    :: i,n1,n2,nnew

REAL                       :: aver1,aver2
REAL,DIMENSION(nnew) :: y1,hin,y2,h

CHARACTER inf1*15
CHARACTER inf2*15

WRITE(*,*) 'Please Enter the Input Filename'
READ(*,3000) inf1
WRITE(*,*) 'Please Enter the Input Filename'
READ(*,3000) inf2

3000 format(a15)

OPEN(1,file=inf1)
OPEN(2,file=inf2)

DO i=1,n1
   READ(1,5) y1(i),hin(i)
ENDDO

5 FORMAT (f7.5,17x,f6.4)

aver1=hin(1)

DO i=2,n1
   aver1=AMIN1(aver1,hin(i))
ENDDO

DO i=n1+1,nnew
   hin(i)=aver1
ENDDO

DO i=1,n2
    READ(2,5) y2(i),h(i)
ENDDO

aver2=h(1)
```

```
DO i=2,n2
   aver2=AMAX1(aver2,h(i))
ENDDO

DO i=n2+1,nnew
   h(i)=aver1
ENDDO

END SUBROUTINE
```

```
SUBROUTINE initialboundary(nnew,hin,h,aver1,aver2,w,et,coef)

IMPLICIT NONE

INTEGER                          :: i,k,nnew

REAL                             :: aver1,aver2,d,w1,w2,w3,coef
REAL,DIMENSION(nnew) :: y1,hin,y2,h,et1,et2,et3
REAL,PARAMETER           :: dx=0.5

DOUBLE PRECISION,DIMENSION(nnew) :: w,et

CHARACTER inf1*15
CHARACTER inf2*15

d=1./(3.*dx*dx)

DO i=1,nnew
   et1(i)=(hin(i)-aver1)/aver1
ENDDO

k=0

DO i=nnew,1,-1
k=k+1
   et2(k)=coef*(hin(i)-aver1)/aver1
ENDDO

DO i=1,nnew
   et3(i)=(h(i)-aver2)/aver2
ENDDO

DO i=1,nnew
   w1=et1(i)-(1/4.)*et1(i)**2
   w2=-(et2(i)-(1/4.)*et2(i)**2)
   w3=-et3(i)
   w(i)=w1+w2+w3
   et(i)=et1(i)+et2(i)+et3(i)
ENDDO

END SUBROUTINE
```

```
SUBROUTINE solution(nnew,m,nstart,nend,delinc,w,et,printw,printet,p,timei)

IMPLICIT NONE

INTEGER                   :: i,j,k,p,ip,delinc,m,nnew,nstart,nend
INTEGER, PARAMETER        :: r=0,nm=50,tempo=1500

REAL                      :: aver1,aver2,d,w1,w2,w3,coef,x,d,w1,w2,w3,
                             z14,z15,z16,z1,z2,z3,z4,z5,z6,z111,z222,z333,
                             z1a,z2a,z3a,z4a,z5a,z6a,z12,z13
REAL,DIMENSION(nnew)      :: et1,et2,et3
REAL,DIMENSION(nm)        :: timei
REAL,PARAMETER            :: dx=0.5,dt=0.004,rad=0.03175,gr=9.81
                             delt=0.0000333

DOUBLE PRECISION,DIMENSION(nnew)          :: w,et,wnew,etnew,es,z
DOUBLE PRECISION, DIMENSION(nm,nnew)      :: printw,printet
DOUBLE PRECISION, DIMENSION(tempo,tempo)  :: l,u

CHARACTER inf1*15
CHARACTER inf2*15

d=1./(3.*dx*dx) ! ============
! time step increment
! ============

p=0

do j=2,m !==================================
! Calculation of the amplitude for an advanced time step (etastar)
!==================================

es(1)=(et(1)+(-0.5*(dt/dx)*w(1))*(4.*et(2)-et(3)-3.*et(1))+  &
       (-0.5*(dt/dx)*(1.+0.5*et(1)))*(4.*w(2)-w(3)-3.*w(1)))/  &
       (1.+0.25*(dt/dx)*(4.*w(2)-w(3)-3.*w(1)))

es(nnew)=(et(nnew)+(-0.5*(dt/dx)*w(nnew))*  &
          (3.*et(nnew)-4.*et(nnew-1)+et(nnew-2))+  &
          (-0.5*(dt/dx)*(1.+0.5*et(nnew))) *  &
          (3.*w(nnew)-4.*w(nnew-1)+w(nnew-2)))/  &
          (1.+0.25*(dt/dx)*(3.*w(nnew)-4.*w(nnew-1)+w(nnew-2)))

DO i=2,nnew-1
```

```
es(i)=(et(i)+(-0.5*(dt/dx)*w(i))*(et(i+1)-et(i-1))+  &
       (-0.5*(dt/dx)*(1.+0.5*et(i)))*(w(i+1)-w(i-1)))/  &
       (1.+0.25*(dt/dx)*(w(i+1)-w(i-1)))
ENDDO

! ====================
! solving a tridiagonal linear matrix
! ====================

! LU composition

l(1,1)=0.5*(1.+2./(3.*dx*dx)-0.5*(dt/dx)*w(1))
u(1,2)=0.5*(-2./(3.*dx*dx)+0.5*(dt/dx)*w(1))/l(1,1)

DO i=2,nnew-1
    l(i,i-1)=(-d-0.25*(dt/dx)*w(i))
    l(i,i)=(2.*d+1.)-l(i,i-1)*u(i-1,i)
    u(i,i+1)=(-d+0.25*(dt/dx)*w(i))/l(i,i)
ENDDO

l(nnew,nnew-1)=-d-0.25*(dt/dx)*w(nnew)
l(nnew,nnew)=d+0.5+0.25*(dt/dx)*w(nnew)-  &
                l(nnew,nnew-1)*u(nnew-1,nnew)

!=========================================
! RHS of the matrix and multiplication of the inverse of the lower part of
! the matrix (obtaining z)
!=========================================

z1=(1.-1./(3.*dx*dx)+0.75*(dt/dx)*w(1))*w(1)
z2=(2./(3.*dx*dx)-(dt/dx)*w(1))*w(2)
z3=(-1./(3.*dx*dx)+0.25*(dt/dx)*w(1))*w(3)
z4=0.75*(dt/dx)*et(1)+0.75*(dt/dx)*es(1)
z5=(dt/dx)*et(2)+(dt/dx)*es(2)
z6=0.25*(dt/dx)*et(3)+0.25*(dt/dx)*es(3)
z111=0.5*(z1+z2+z3+z4-z5+z6)
z(1)=z111/l(1,1)

DO i=2,nnew-1
    z12=(1.+2./(3.*dx*dx))*w(i)
    z13=(-1./(3.*dx*dx)+0.25*(dt/dx)*w(i))*w(i-1)
```

```
    z14=(-1./(3.*dx*dx)-0.25*(dt/dx)*w(i))*w(i+1)
    z15= 0.25*(dt/dx)*et(i-1)+0.25*(dt/dx)*es(i-1)
    z16= 0.25*(dt/dx)*et(i+1)+0.25*(dt/dx)*es(i+1)
    z222=z12+z13+z14+z15-z16
    z(i)=(z222-l(i,i-1)*z(i-1))/l(i,i)
ENDDO

z1a=(1.-1./(3.*dx*dx)-0.75*(dt/dx)*w(nnew))*w(nnew)
z2a=(2./(3.*dx*dx)+(dt/dx)*w(nnew))*w(nnew-1)
z3a=(-1./(3.*dx*dx)-0.25*(dt/dx)*w(nnew))*w(nnew-2)
z4a=0.75*(dt/dx)*et(nnew)+0.75*(dt/dx)*es(nnew)
z5a=(dt/dx)*et(nnew-1)+(dt/dx)*es(nnew-1)
z6a=0.25*(dt/dx)*et(nnew-2)+0.25*(dt/dx)*es(nnew-2)
z333=0.5*(z1a+z2a+z3a-z4a+z5a-z6a)
z(nnew)=(z333-l(nnew,nnew-1)*z(nnew-1))/l(nnew,nnew)

!=========================
! Calculation of the momentum equation
!=========================

wnew(nnew)=z(nnew)

!================================
! wnew(i) is the advance in time value of the velocity
!================================

! Back Substitution

DO i=nnew-1,1,-1
    wnew(i)=z(i)-u(i,i+1)*wnew(i+1)
ENDDO

!=========================
! Calculation of the continuity equation
!=========================

etnew(1)=et(1)+(-0.25*(dt/dx)*(w(1)+wnew(1)))*  &
       (4.*et(2)-et(3)-3.*et(1))+(-0.25*(dt/dx)*(1.+et(1)))*  &
       ((4.*w(2)-w(3)-3.*w(1))+(4.*wnew(2)-wnew(3)-3.*wnew(1)))

etnew(nnew)=et(nnew)+(-0.25*(dt/dx)*(w(nnew)+wnew(nnew)))*  &
            (3.*et(nnew)-4.*et(nnew-1)+et(nnew-2))+  &
```

```
            (-0.25*(dt/dx)*(1.+et(nnew)))*  &
            ((3.*w(nnew)-4.*w(nnew-1)+w(nnew-2))+  &
            (3.*wnew(nnew)-4.*wnew(nnew-1)+wnew(nnew-2)))

DO i=2,nnew-1
etnew(i)=et(i)+(-0.25*(dt/dx)*(w(i)+wnew(i)))*  &
        (et(i+1)-et(i-1))+(-0.25*(dt/dx)*(1.+et(i)))*  &
        ((w(i+1)-w(i-1))+(wnew(i+1)-wnew(i-1)))
ENDDO

!====================
! writing the solutions into the files
!====================

IF (j >= nstart .and. j <= nend) THEN
    IF (mod(j,delinc) == r) THEN
      p=p+1
      timei(p)=(j-1)*delt
      DO i=1,nnew
         printw(p,i)=wnew(i)
         printet(p,i)=etnew(i)
      ENDDO
   ENDIF
ENDIF

DO i=1,nnew
   w(i)=wnew(i)
   et(i)=etnew(i)
ENDDO

ENDDO

END SUBROUTINE
```

```
SUBROUTINE writeinfile(position,beta,qlinlet,p)

IMPLICIT NONE

CHARACTER*12 inf,ext
CHARACTER*7 position

INTEGER :: beta,qlinlet,p,i

OPEN(UNIT=3,FILE='filelst.txt',STATUS='unknown')

IF (position == 'pos1'.OR. position == 'pos2'.OR.  &
   position == 'sobt') THEN

    SELECT CASE (position)

      CASE('pos1')

        SELECT CASE (int(beta))
          CASE (66)
            SELECT CASE (int(qlinlet))
              CASE(8)
                inf='q1-08b66'
              CASE(11)
                inf='q11b661'
              CASE(15)
                inf='q15b661'
              CASE(18)
                inf='q18b661'
              CASE(21)
                inf='q21b661'
            END SELECT
          CASE (72)
            SELECT CASE (int(qlinlet))
              CASE(8)
                inf='q08b721'
              CASE(11)
                inf='q11b721'
              CASE(15)
                inf='q15b721'
              CASE(18)
```

```
          inf='q18b721'
        CASE(21)
          inf='q21b721'
      END SELECT
    CASE (77)
      SELECT CASE (int(qlinlet))
        CASE(8)
          inf='q08b771'
        CASE(11)
          inf='q11b771'
        CASE(15)
          inf='q15b771'
        CASE(18)
          inf='q18b771'
        CASE(21)
          inf='q21b771'
      END SELECT
    CASE (83)
      SELECT CASE (int(qlinlet))
        CASE(8)
          inf='q08b831'
        CASE(11)
          inf='q11b831'
        CASE(15)
          inf='q15b831'
        CASE(18)
          inf='q18b831'
        CASE(21)
          inf='q21b831'
      END SELECT
  END SELECT
CASE('pos2')
  SELECT CASE (int(beta))
    CASE (66)
      SELECT CASE (int(qlinlet))
        CASE(8)
          inf='q08b662'
        CASE(11)
```

```
      inf='q11b662'
    CASE(15)
      inf='q15b662'
    CASE(18)
      inf='q18b662'
    CASE(21)
      inf='q21b662'
  END SELECT
CASE (72)
  SELECT CASE (int(qlinlet))
    CASE(8)
      inf='q08b722'
    CASE(11)
      inf='q11b722'
    CASE(15)
      inf='q15b722'
    CASE (18)
      inf='q18b722'
    CASE (21)
      inf='q21b722'
  END SELECT
CASE (77)
  SELECT CASE (int(qlinlet))
    CASE (8)
      inf='q08b772'
    CASE(11)
      inf='q11b772'
    CASE (15)
      inf='q15b772'
    CASE (18)
      inf='q18b772'
    CASE(21)
    inf='q21b772'
  END SELECT
CASE (83)
  SELECT CASE (int(qlinlet))
    CASE(8)
      inf='q08b832'
```

```
                CASE(11)
                 inf='q11b832'
                CASE (15)
                 inf='q15b832'
                CASE(18)
                 inf='q18b832'
                CASE (21)
                 inf='q21b832'
               END SELECT
          END SELECT
        CASE('sobt')
          SELECT CASE (int(qlinlet))
                CASE(8)
                 inf='q08b10'
                CASE(11)
                 inf='q11b10'
                CASE(15)
                 inf='q15b10'
                CASE(18)
                 inf='q18b10'
                CASE(21)
                 inf='q21b10'
          END SELECT
    END SELECT
END IF

ext = '.txt'

DO i = 1,p
    IF (i < 10 ) THEN
    WRITE(3,21) inf,i,ext
    ELSEIF (i >= 10) THEN
    WRITE(3,22) inf,i,ext
ENDDO

21 FORMAT(a6,i1,a4)
22 FORMAT(a6,i2,a4)

END SUBROUTINE
```

```
SUBROUTINE fileop(delx,p,printw,printet,timei,nnew)

IMPLICIT NONE

INTEGER                    :: p,j,i,ip,nnew,k
INTEGER, PARAMETER :: nm=50

REAL                       :: delx,x
REAL,DIMENSION(nm)   :: timei
DOUBLE PRECISION, DIMENSION(nm,nnew)      :: printw,printet
CHARACTER*24 a,outf

OPEN(UNIT=4,FILE='filelst.txt',STATUS='old')

j=4

DO i=1,p
   j=j+1
   READ(4,*) a
   WRITE(*,*) a
   outf=a
   OPEN(UNIT=j,FILE=outf,STATUS='unknown')
ENDDO

k=4
DO ip=1,p
   x=-delx
   k=k+1
   DO i=1,nnew
      x=x+delx
      WRITE(k,10) timei(ip),x,printw(ip,i),printet(ip,i)
   ENDDO
ENDDO

10 FORMAT (2(2x,f8.5),2(2x,f10.7))

END SUBROUTINE
```

APPENDIX G

MODEL RESULTS
(INTERFERENCE OF TWO SOLITONS)

This Appendix presents the results of simulations for the interaction of two solitons. These results are presented graphicaly. Each figure set includes four figures. Each figure set is arranged according to the orifice β ratio and the position of the orifice with respect to the elbow.

The first figure in the set shows the incident wave, where the initial profile is taken from the edge detection procedure. The second figure of each setcorresponds to the incident wave at the orifice location. The third figure in each set is the initial condition used to run the program in order to obtain a backward propagating soliton. The last figure in the set shows the final interaction of the two solitons.

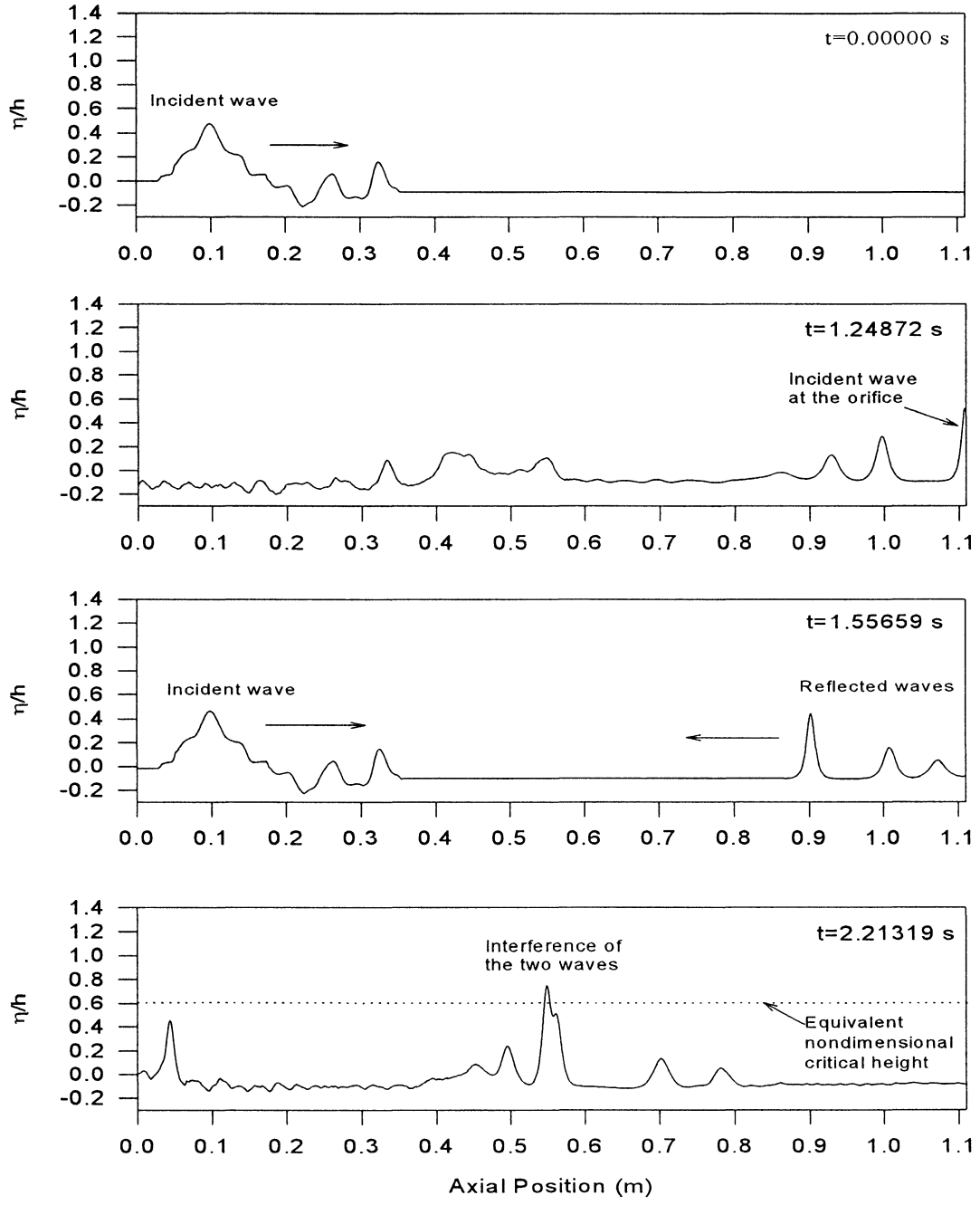

Figure G.1 The formation of slug as modeled for $\beta = 0.66$, Position 1, $Q_l = 0.8\,m^3/h$, $Q_g = 31.5\,m^3/h$

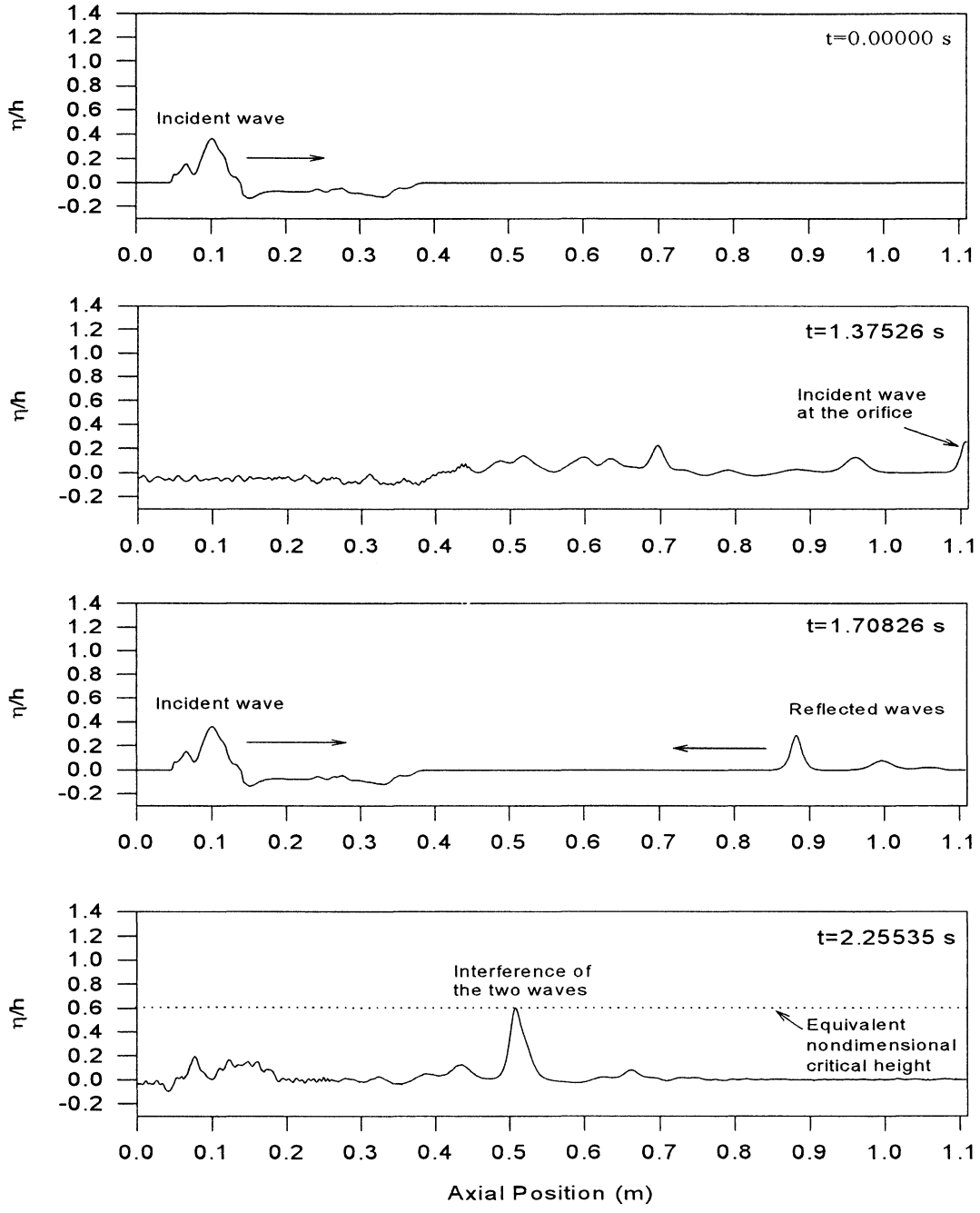

Figure G.2 The formation of slug as modeled for $\beta = 0.66$, Position 1, $Q_l = 1.1\,m^3/h$, $Q_g = 22.2\,m^3/h$

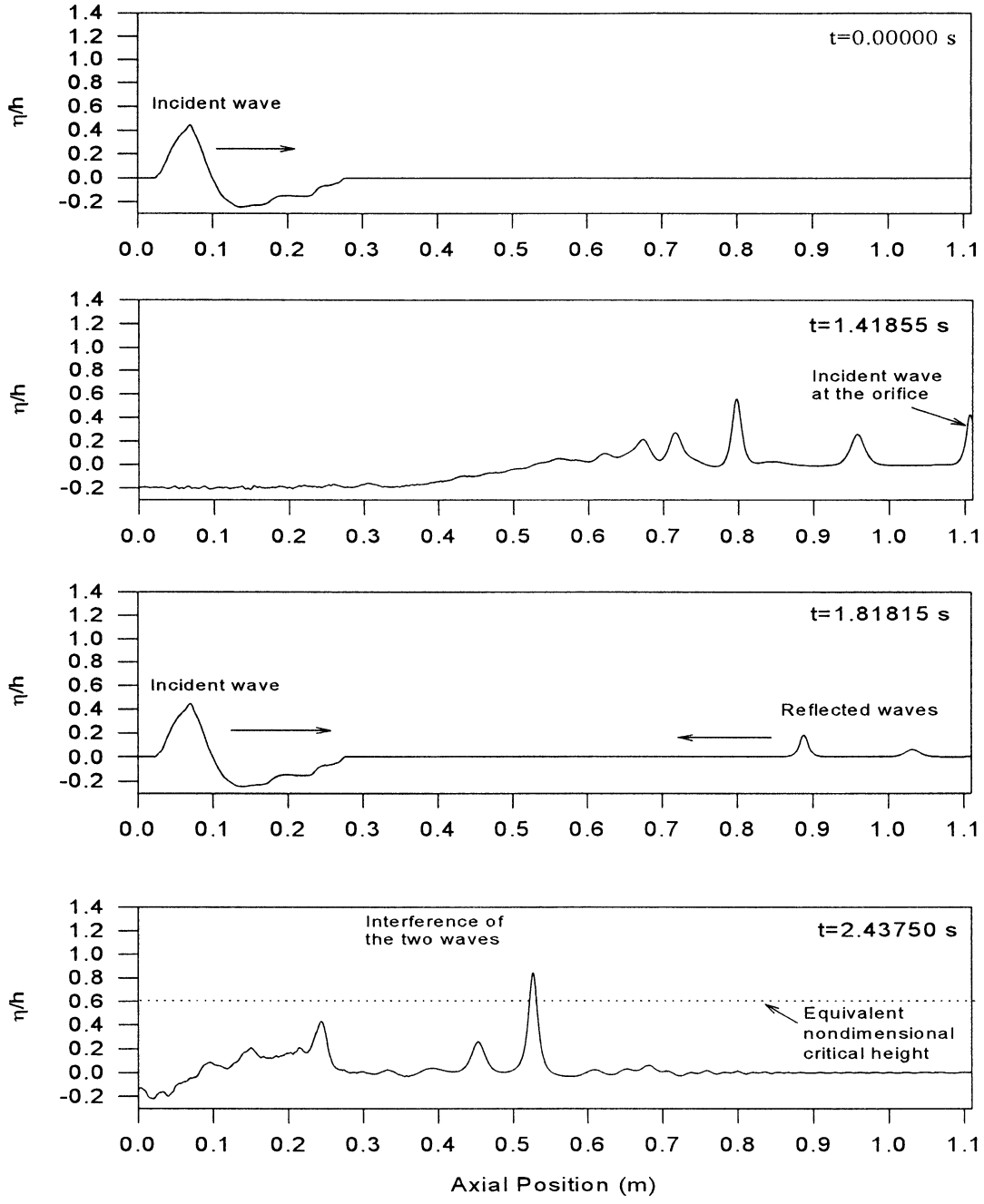

Figure G.3 The formation of slug as modeled for $\beta = 0.66$, Position 1, $Q_l = 1.5\,m^3/h$, $Q_g = 15.8\,m^3/h$

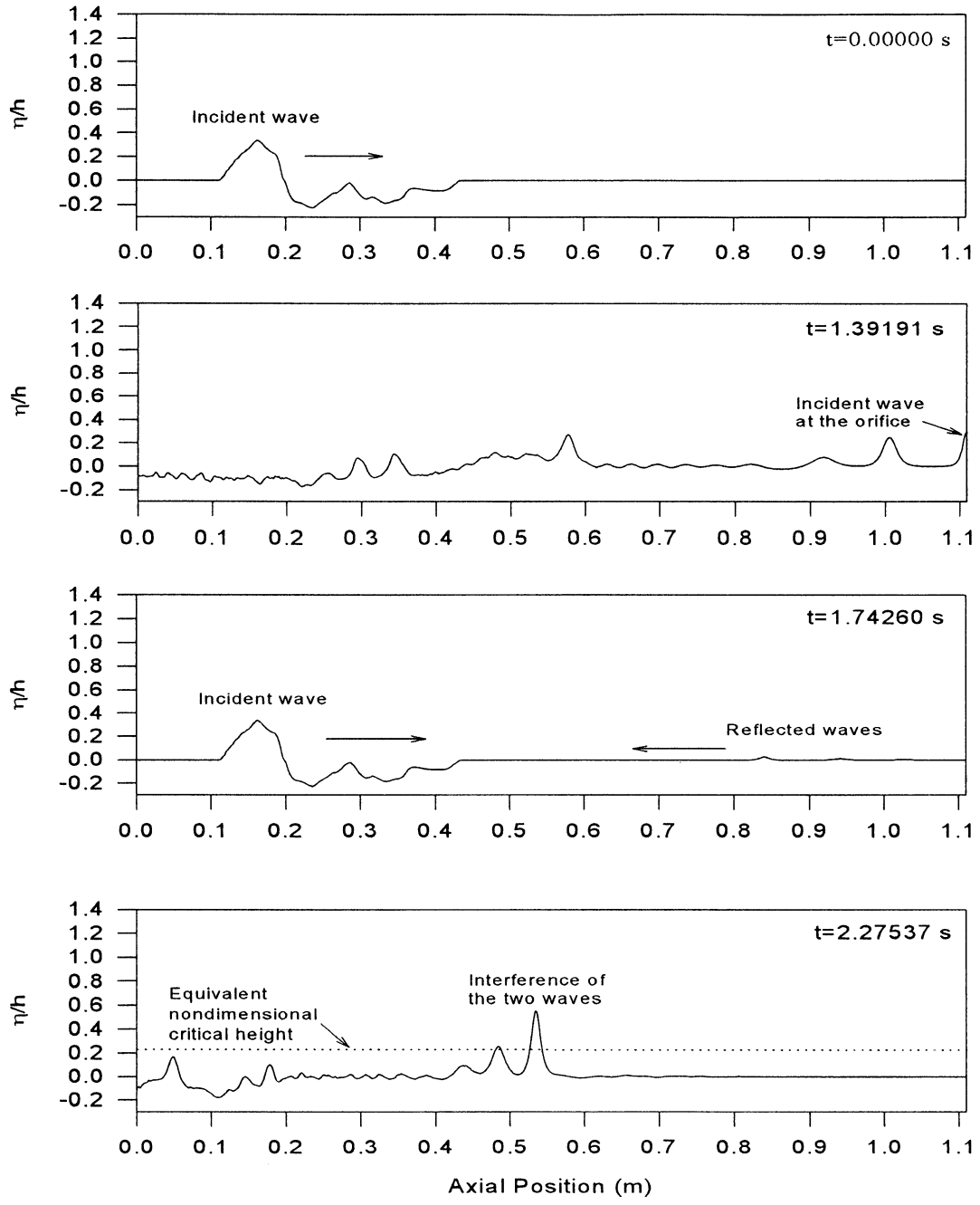

Figure G.4 The formation of slug as modeled for $\beta = 0.66$, position 1, $Q_l = 1.8m^3/h$

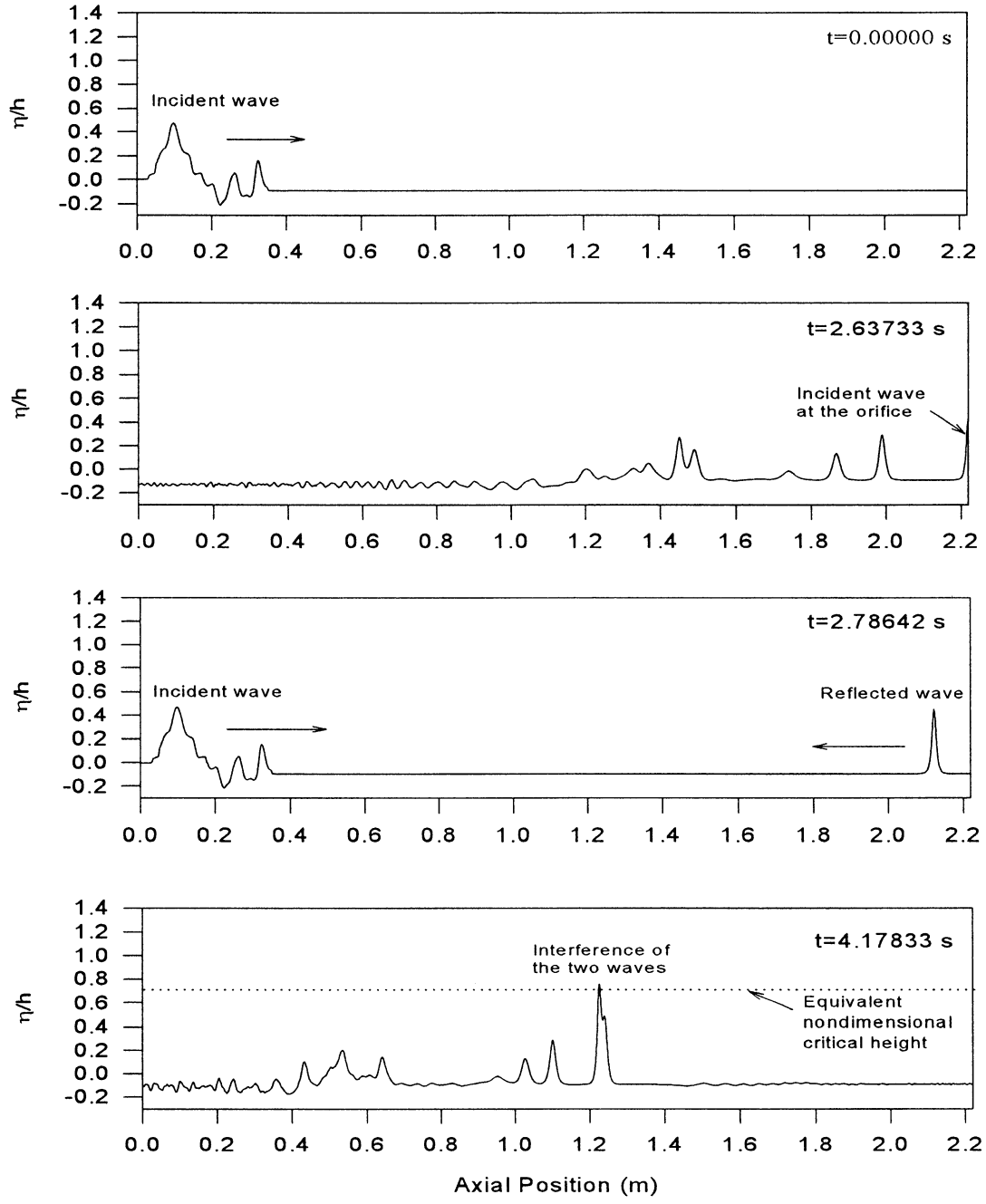

Figure G.5 The formation of slug as modeled for $\beta = 0.66$, Position 2, $Q_l = 0.8\,m^3/h$, $Q_g = 31.5\,m^3/h$

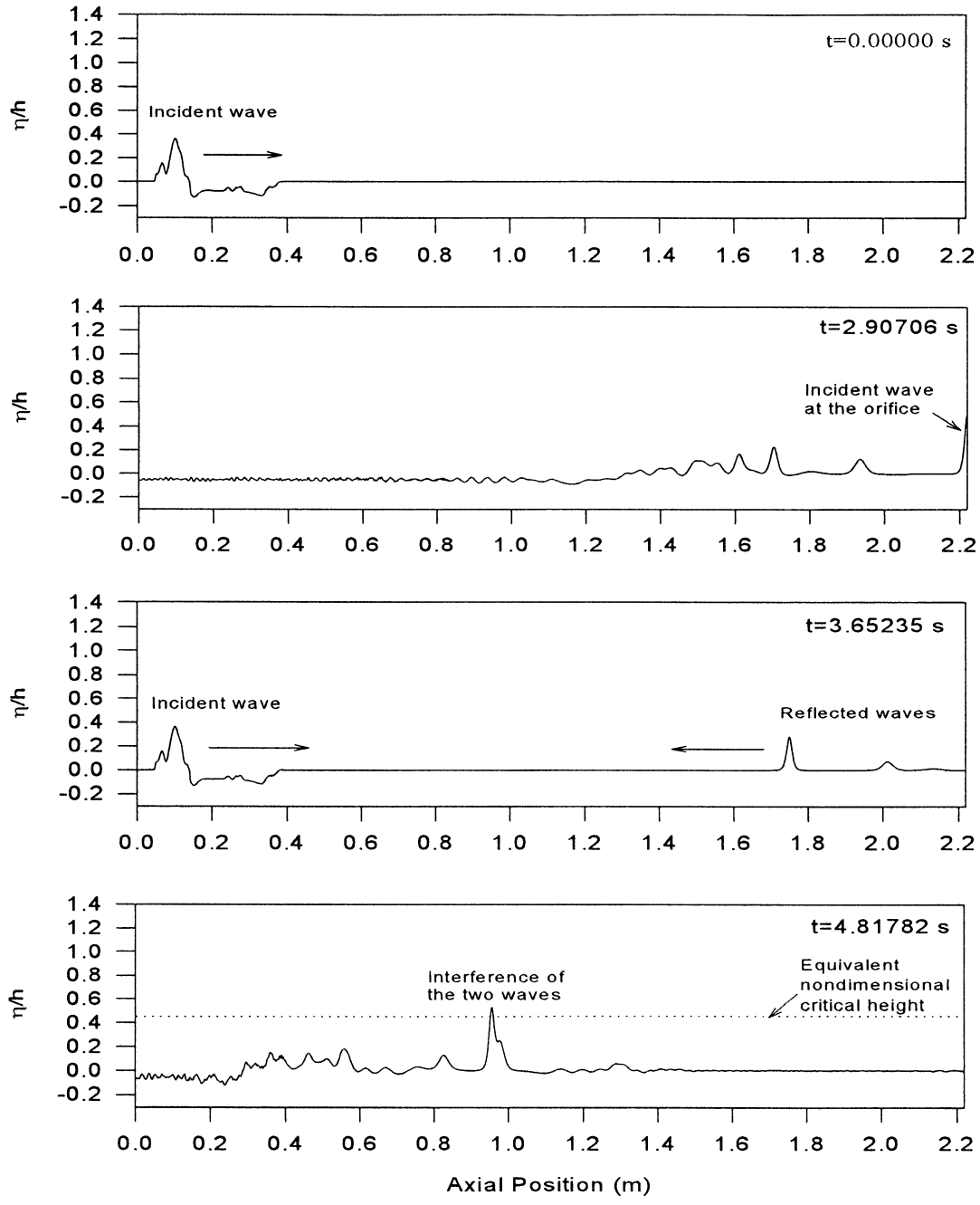

Figure G.6 The formation of slug as modeled for $\beta = 0.66$, Position 2, $Q_l = 1.1\,m^3/h$, $Q_g = 22.2\,m^3/h$

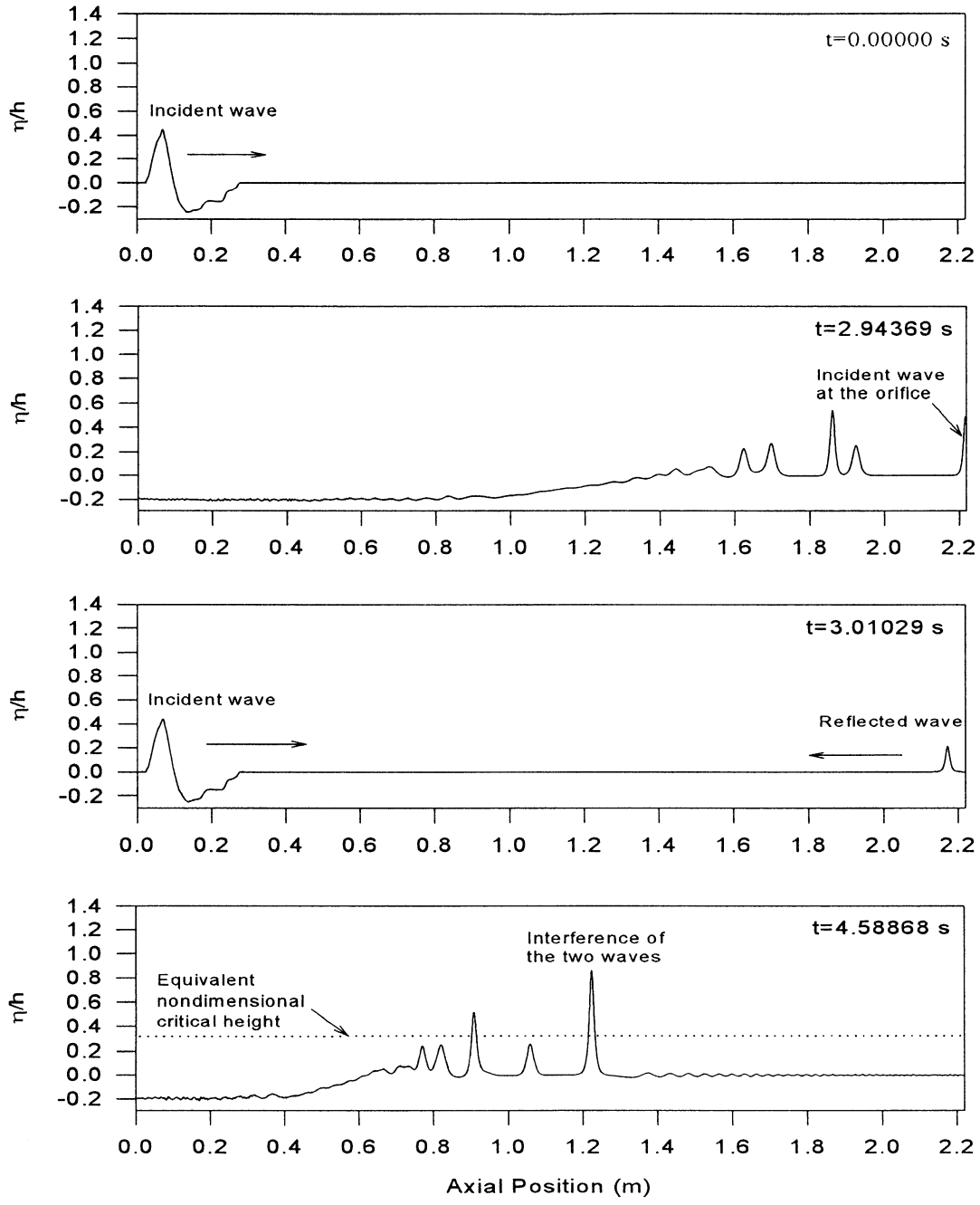

Figure G.7 The formation of slug as modeled for $\beta = 0.66$, Position 2, $Q_l = 1.5\,m^3/h$, $Q_g = 15.8\,m^3/h$

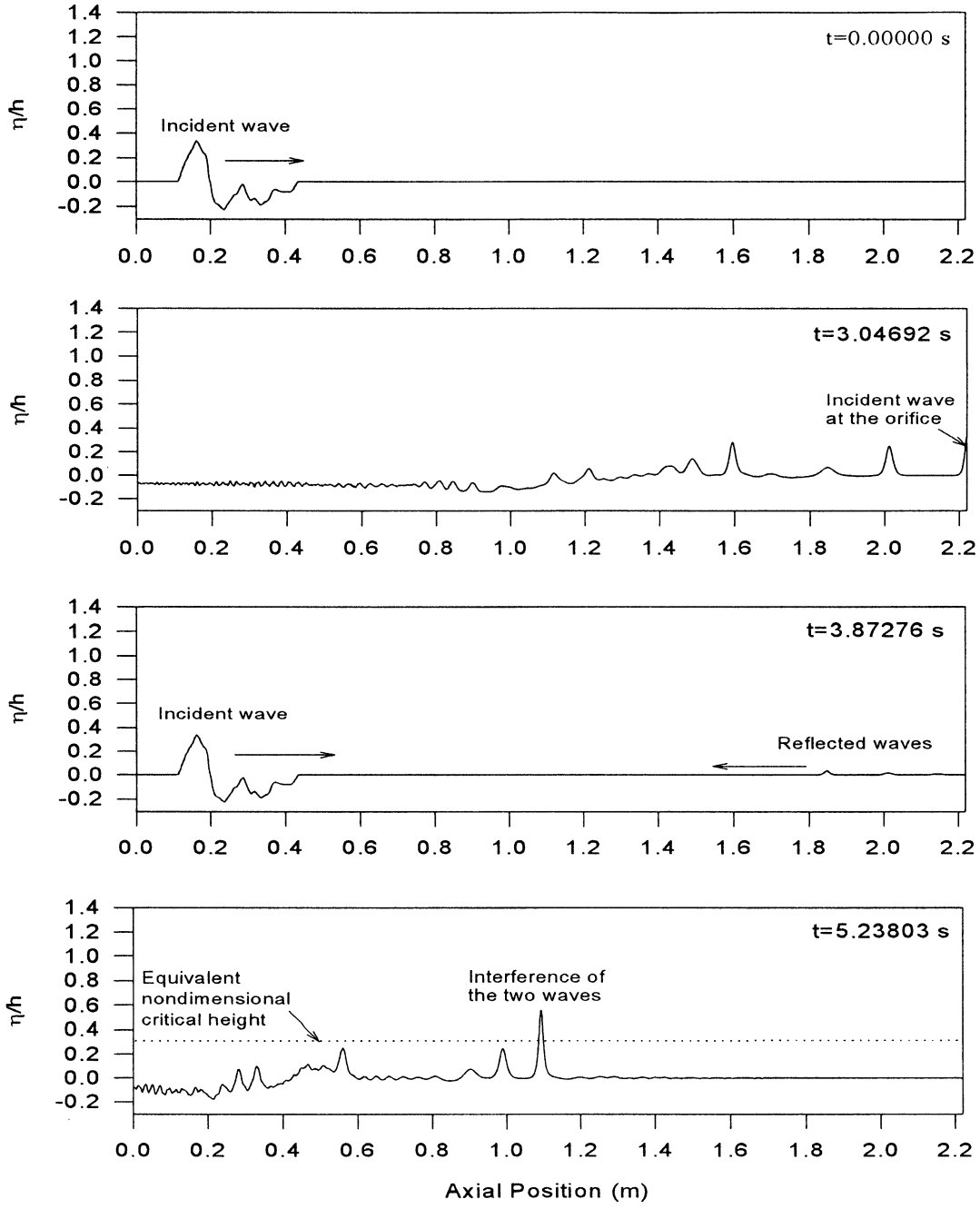

Figure G.8 The formation of slug as modeled for $\beta = 0.66$, Position 2, $Q_l = 1.8\,m^3/h$, $Q_g = 11.4\,m^3/h$

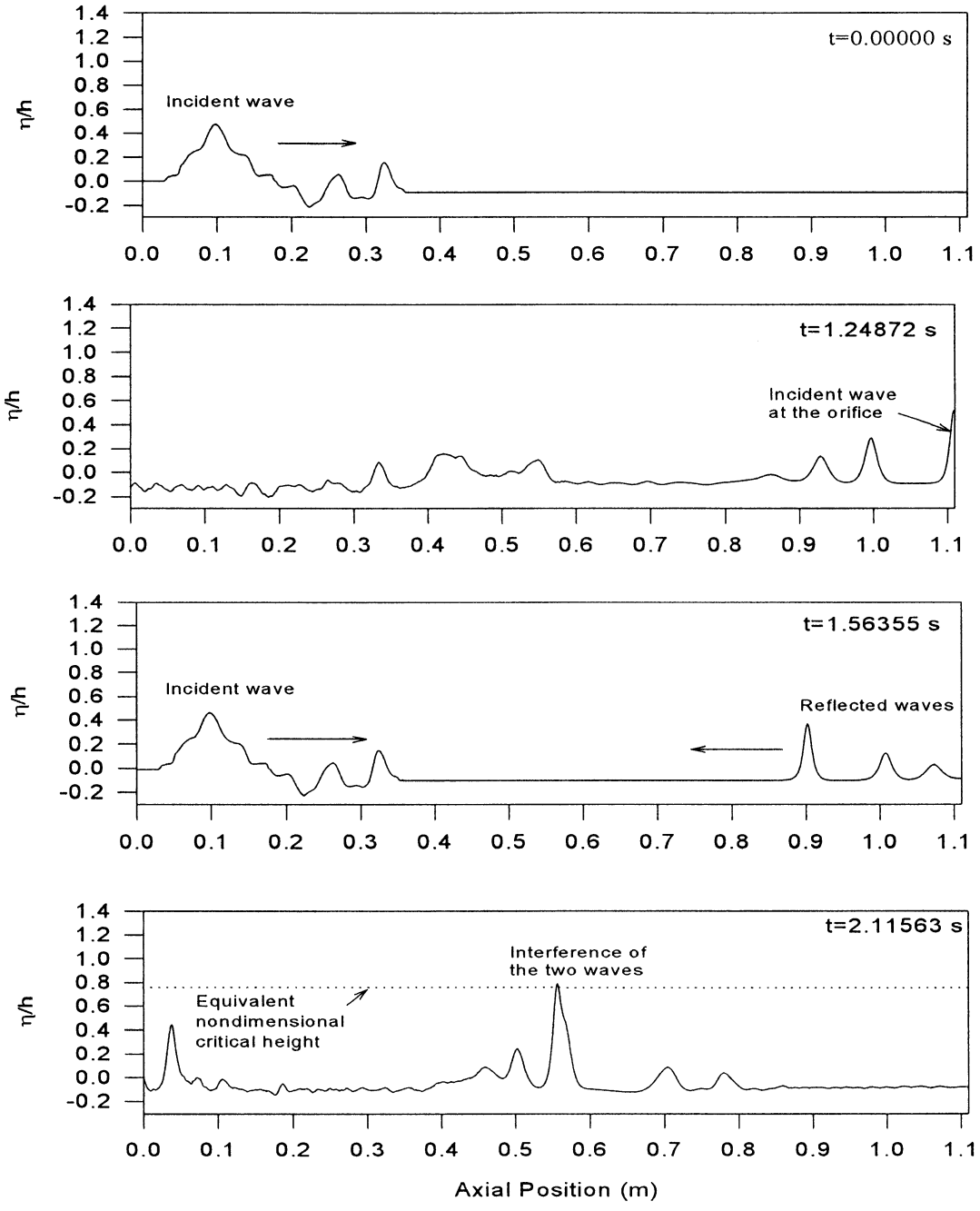

Figure G.9 The formation of slug as modeled for $\beta = 0.72$, Position 1, $Q_l = 0.8\,m^3/h$, $Q_g = 31.5\,m^3/h$

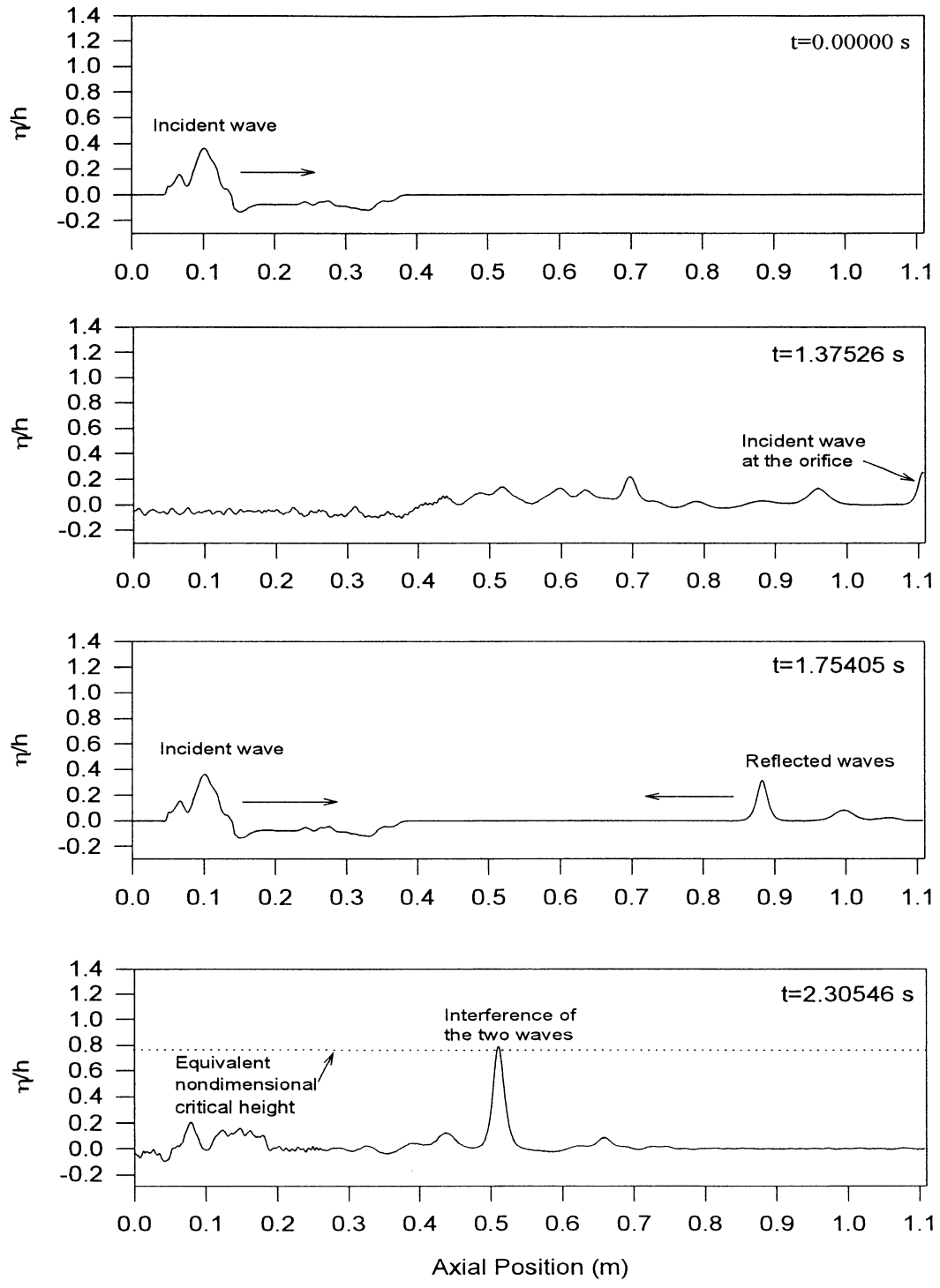

Figure G.10 The formation of slug as modeled for $\beta = 0.72$, Position 1, $Q_l = 1.1\,m^3/h$, $Q_g = 22.2\,m^3/h$

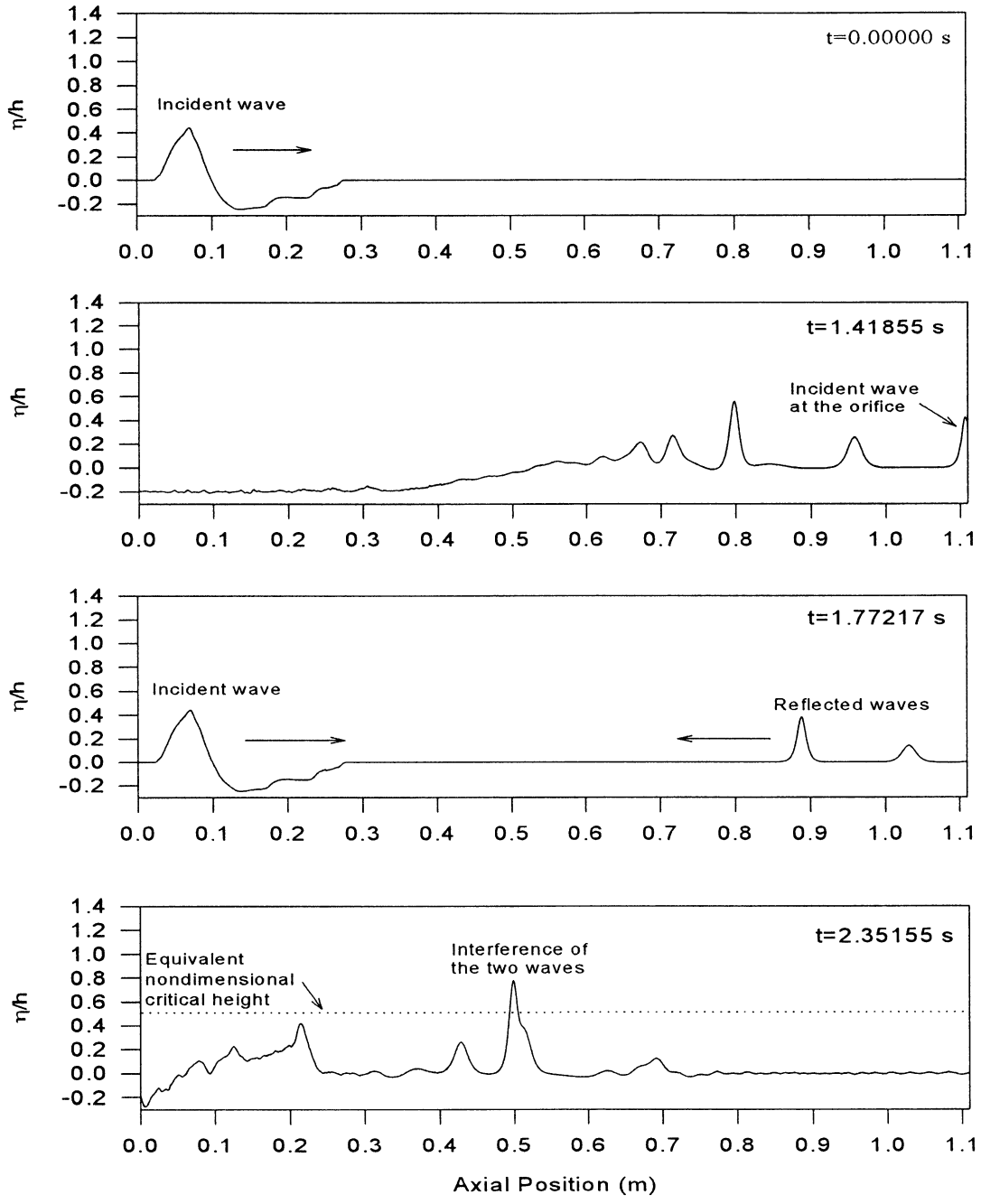

Figure G.11 The formation of slug as modeled for $\beta = 0.72$, Position 1, $Q_l = 1.5\,m^3/h$, $Q_g = 15.8\,m^3/h$

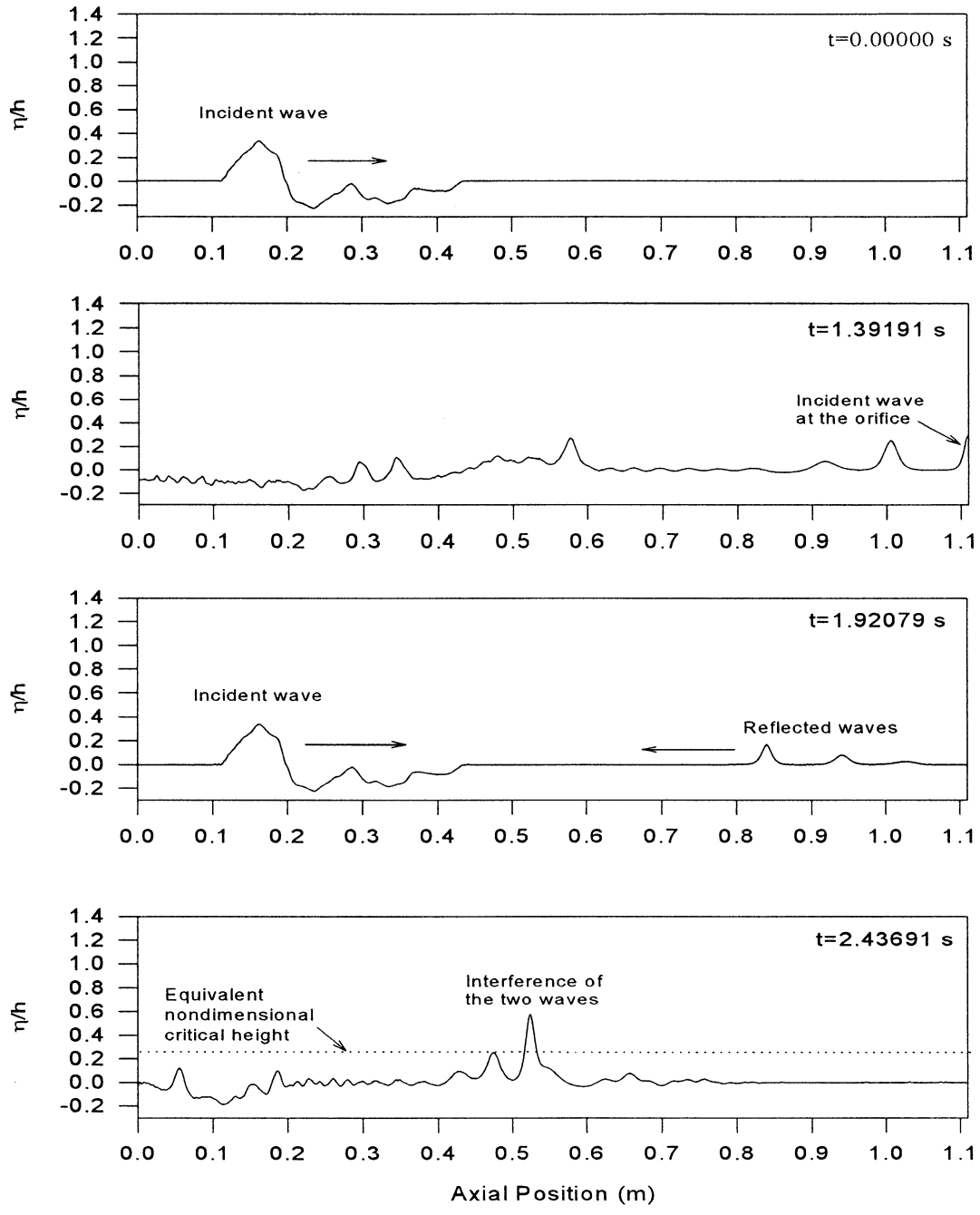

Figure G.12 The formation of slug as modeled for $\beta = 0.72$, Position 1, $Q_l = 1.8\,m^3/h$, $Q_g = 11.4\,m^3/h$

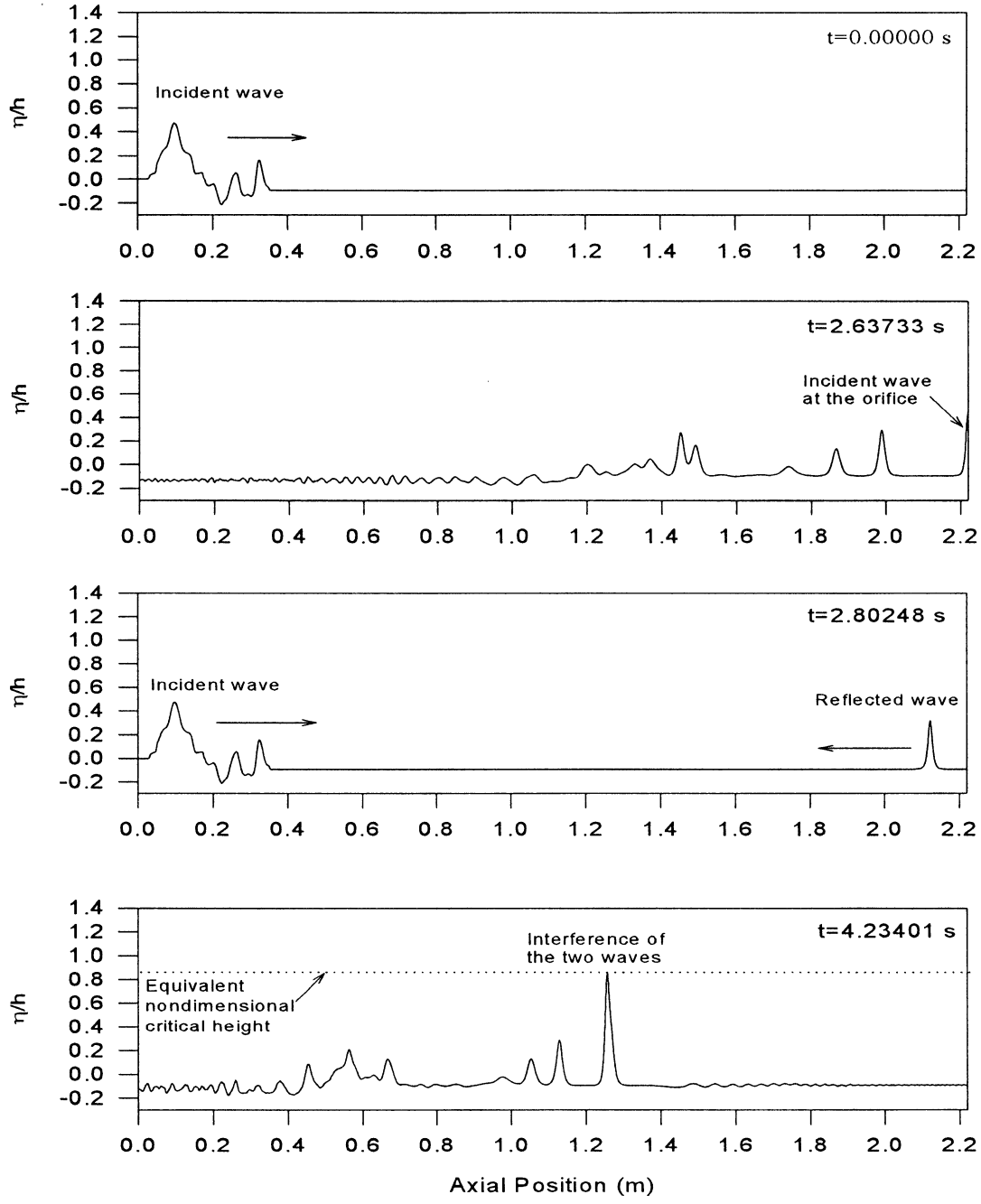

Figure G.13 The formation of slug as modeled for $\beta = 0.72$, Position 2, $Q_l = 0.8\,m^3/h$, $Q_g = 31.5\,m^3/h$

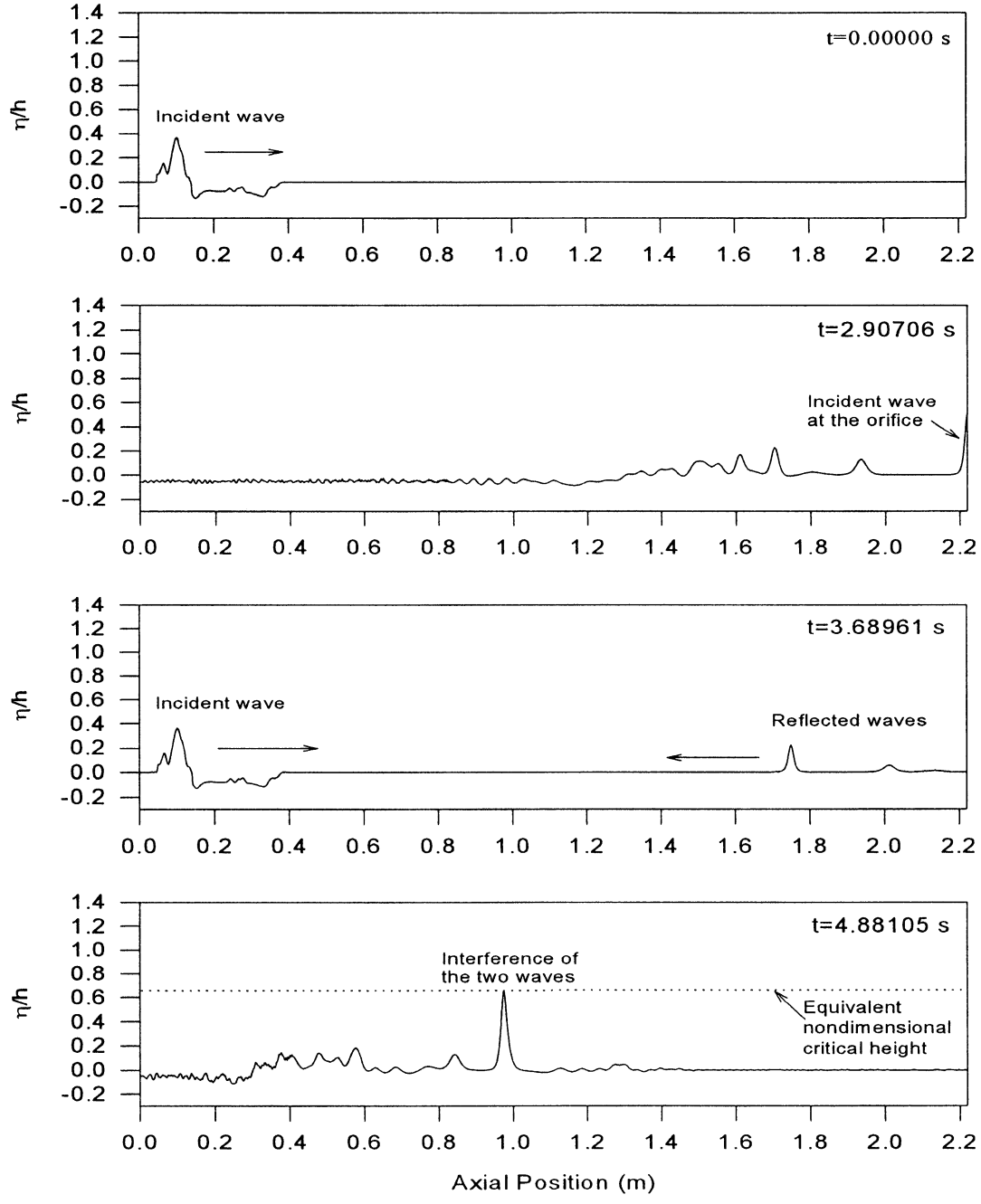

Figure G.14 The formation of slug as modeled for $\beta = 0.72$, Position 2, $Q_l = 1.1\,m^3/h$, $Q_g = 22.2\,m^3/h$

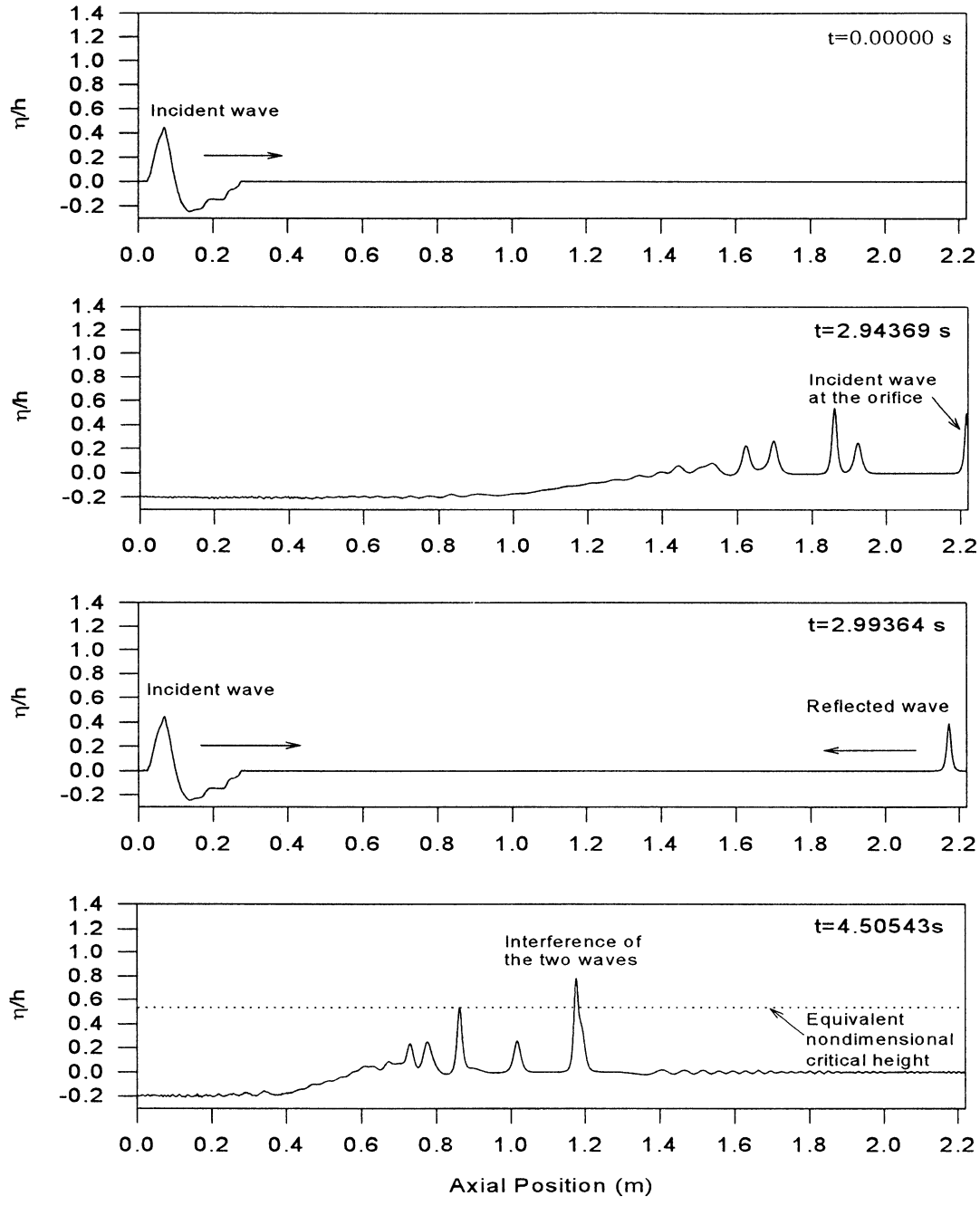

Figure G.15 The formation of slug as modeled for $\beta = 0.72$, Position 2, $Q_l = 1.5\,m^3/h$, $Q_g = 15.8\,m^3/h$

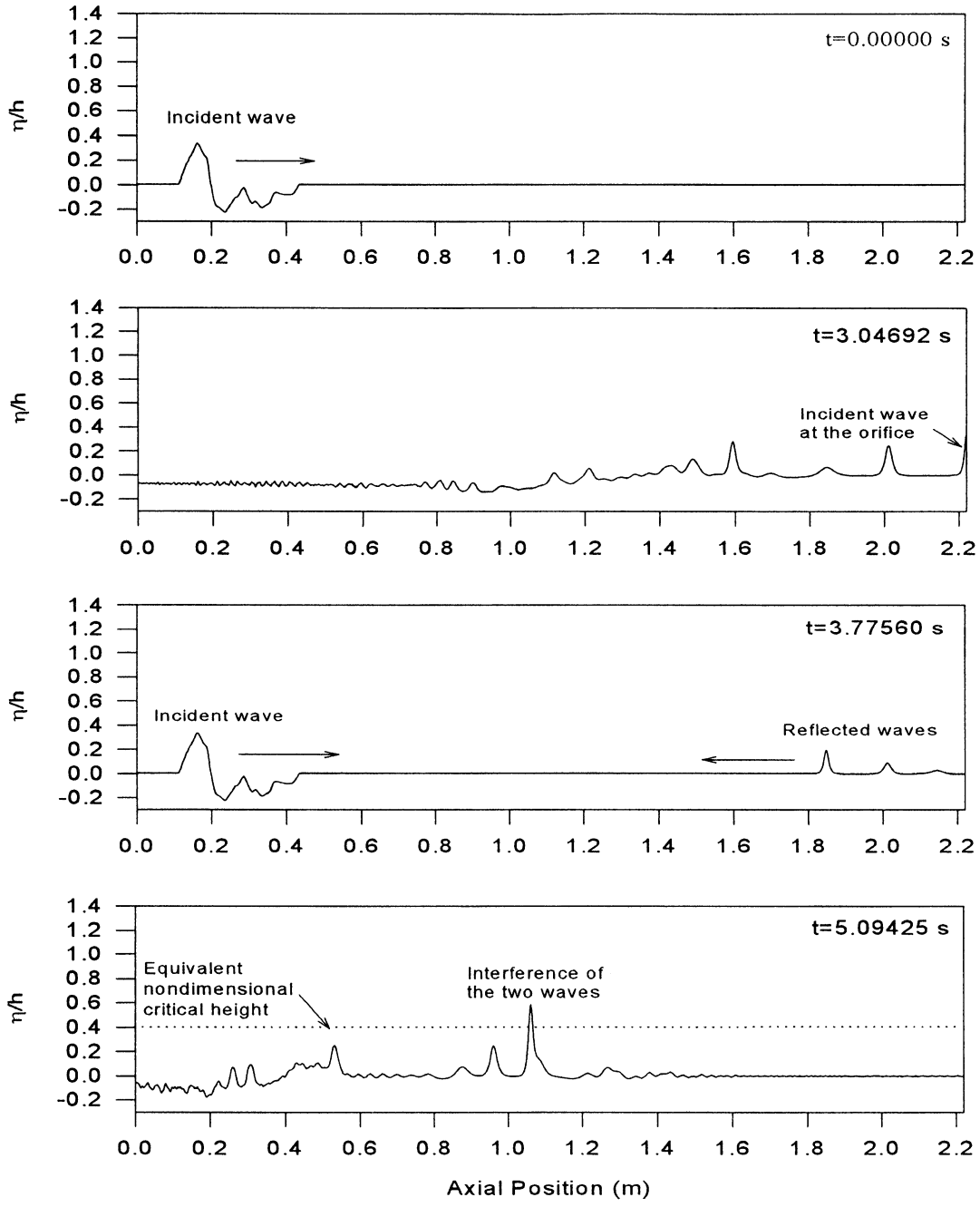

Figure G.16 The formation of slug as modeled for $\beta = 0.72$, Position 2, $Q_l = 1.8\,m^3/h$, $Q_g = 11.4\,m^3/h$

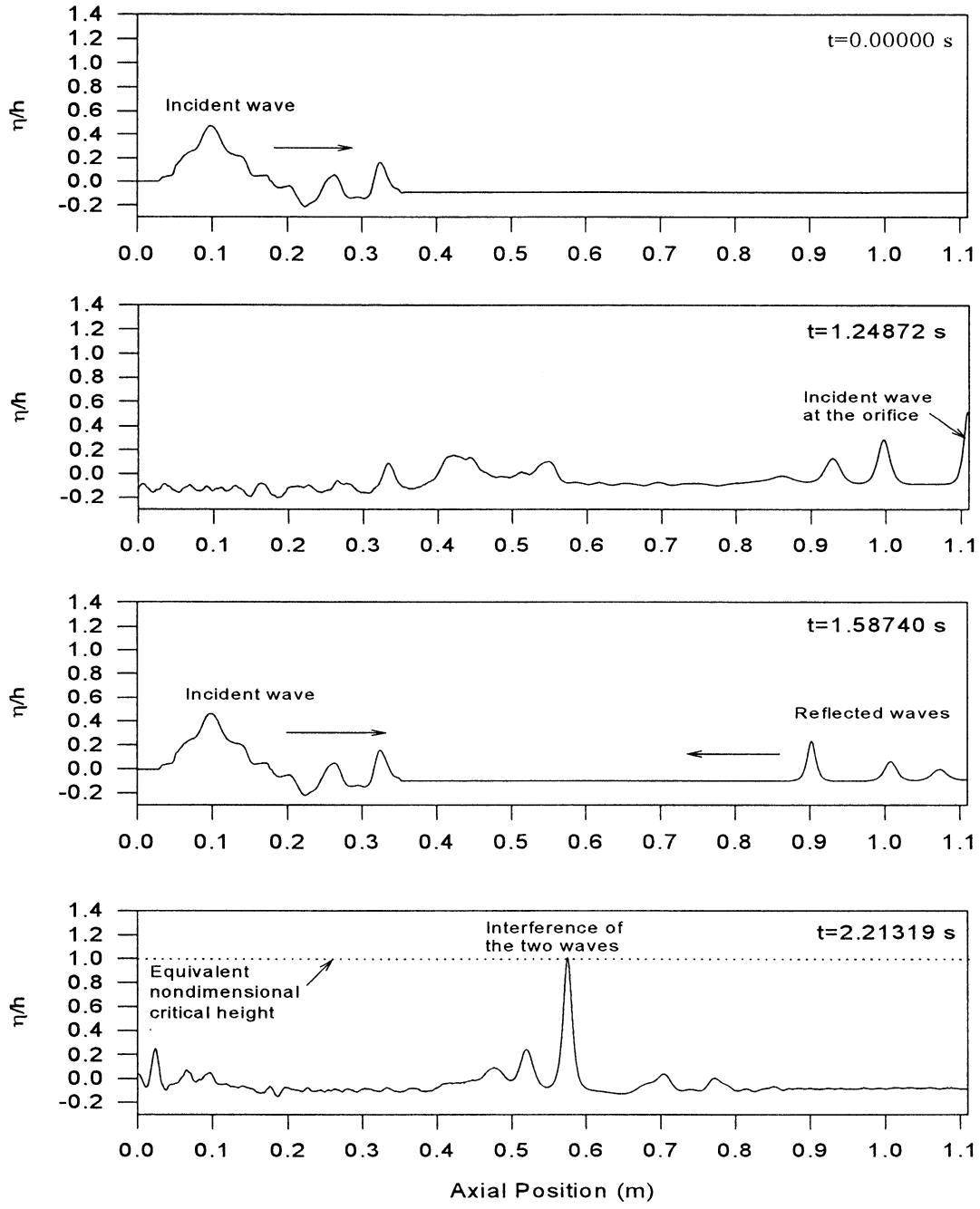

Figure G.17 The formation of slug as modeled for $\beta = 0.77$, Position 1, $Q_l = 0.8\,m^3/h$, $Q_g = 31.5\,m^3/h$

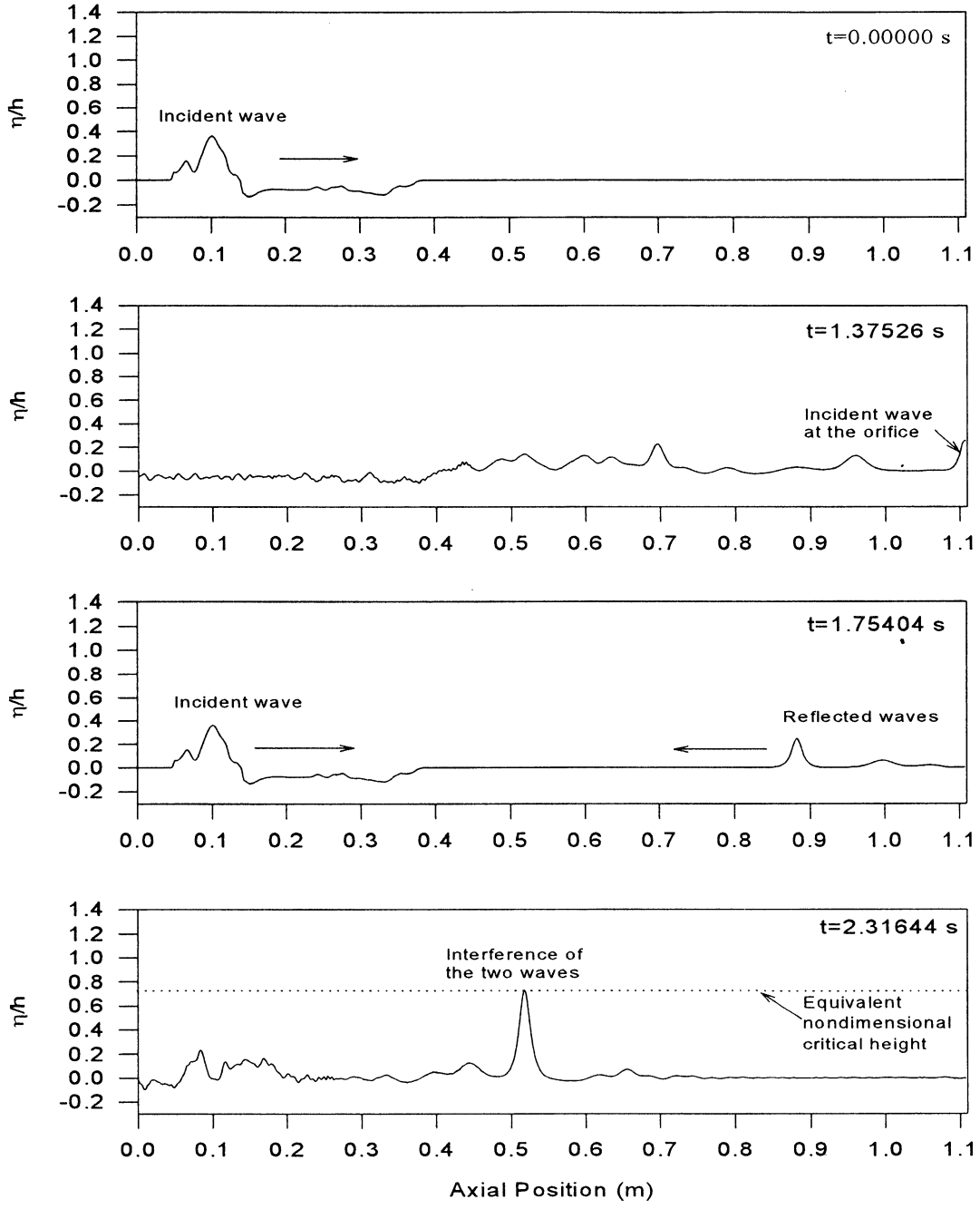

Figure G.18 The formation of slug as modeled for $\beta = 0.77$, Position 1, $Q_l = 1.1\,m^3/h$, $Q_g = 22.2\,m^3/h$

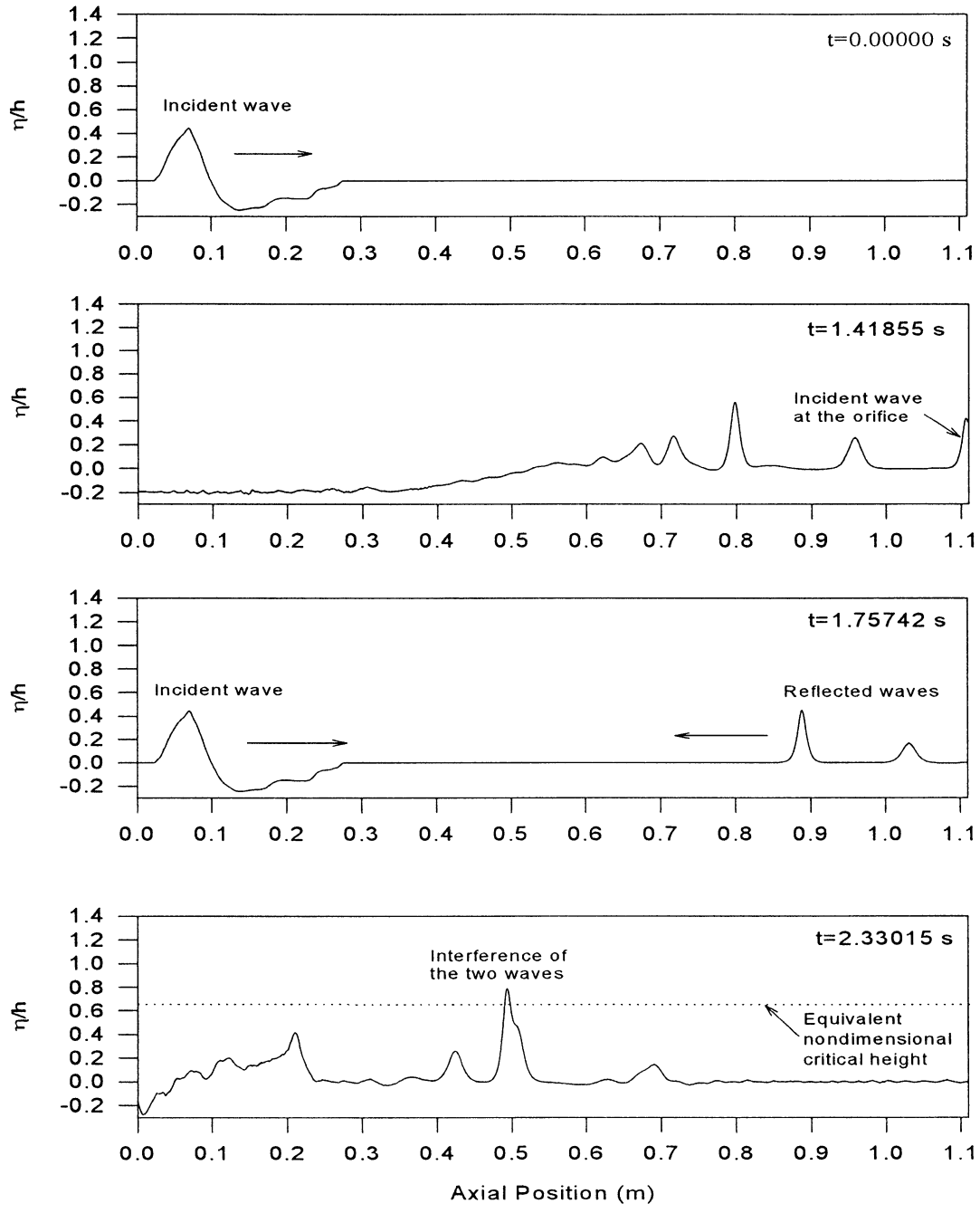

Figure G.19 The formation of slug as modeled for $\beta = 0.77$, Position 1, $Q_l = 1.5\,m^3/h$, $Q_g = 15.8\,m^3/h$

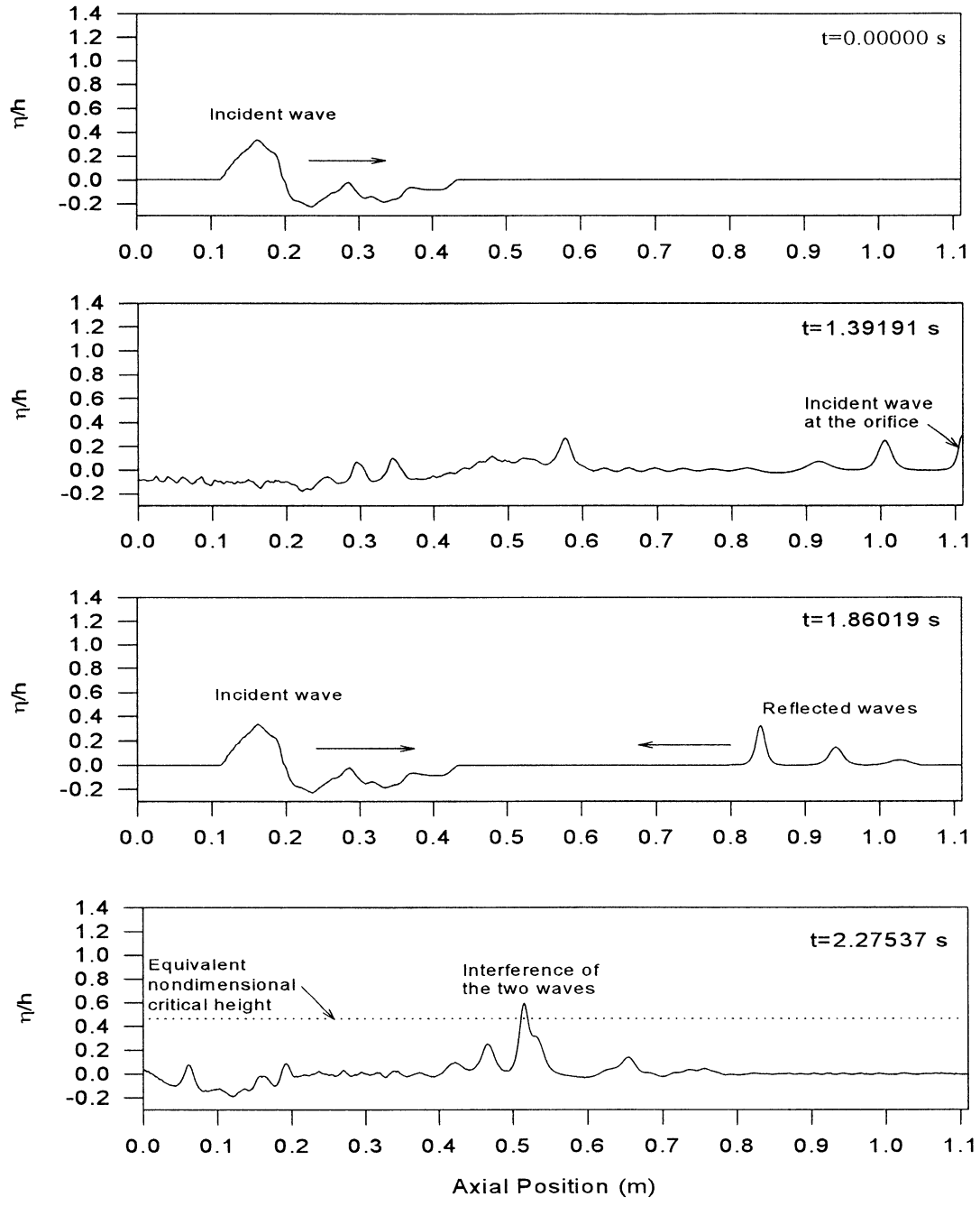

Figure G.20 The formation of slug as modeled for $\beta = 0.77$, Position 1, $Q_l = 1.8\,m^3/h$, $Q_g = 11.4\,m^3/h$

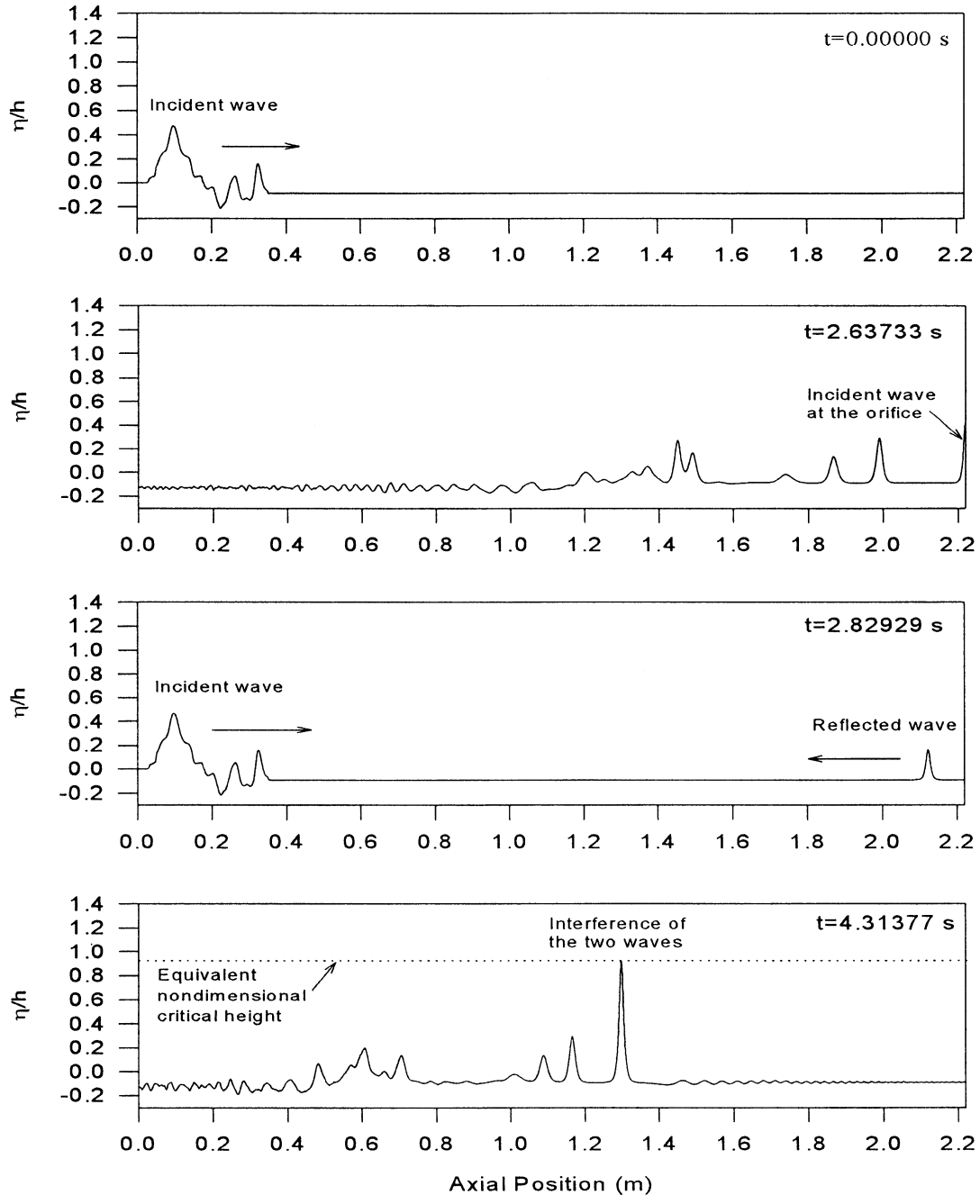

Figure G.21 The formation of slug as modeled for $\beta = 0.77$, Position 2, $Q_l = 0.8\,m^3/h$, $Q_g = 31.5\,m^3/h$

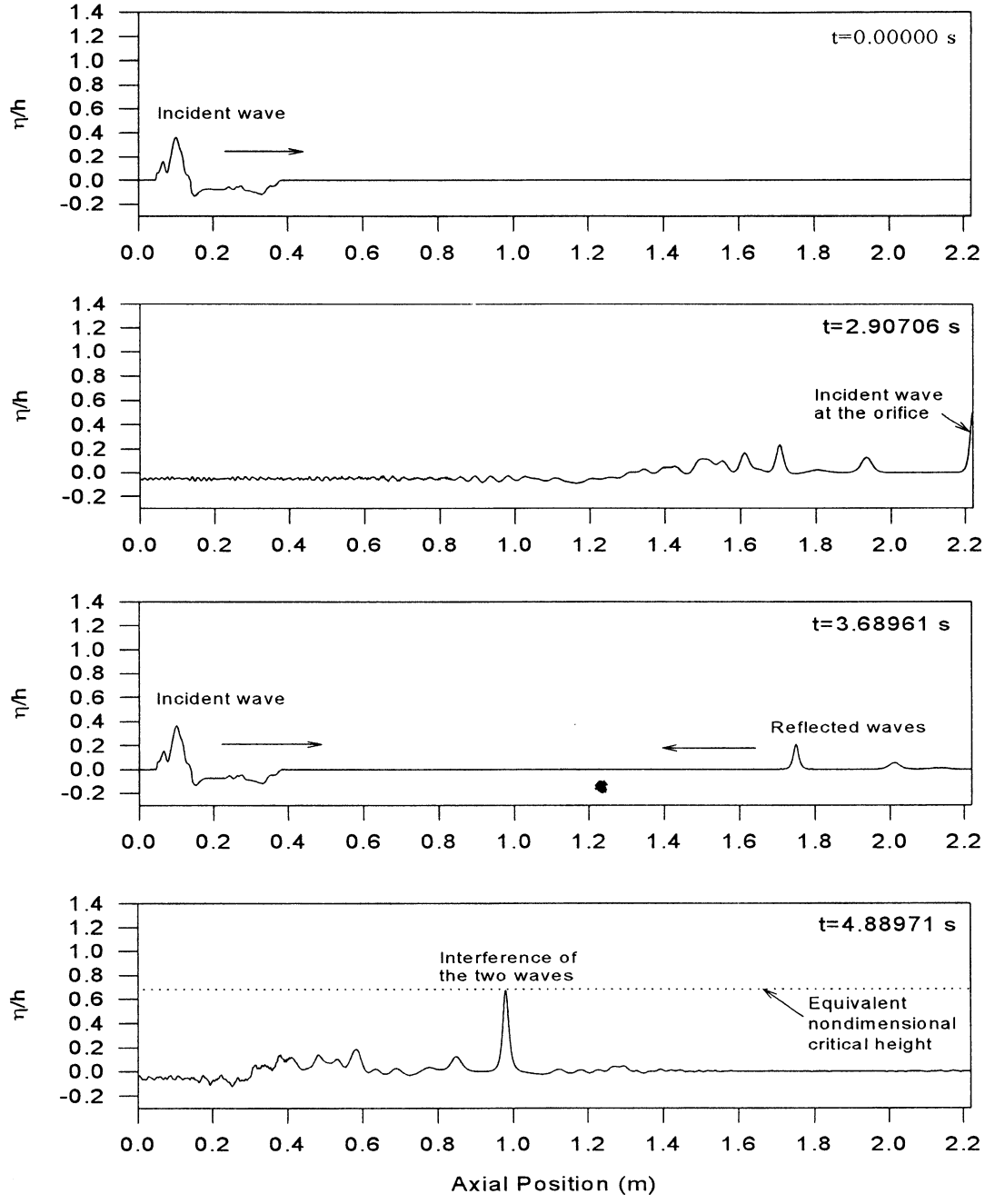

Figure G.22 The formation of slug as modeled for $\beta = 0.77$, Position 2, $Q_l = 1.1\,m^3/h$, $Q_g = 22.2\,m^3/h$

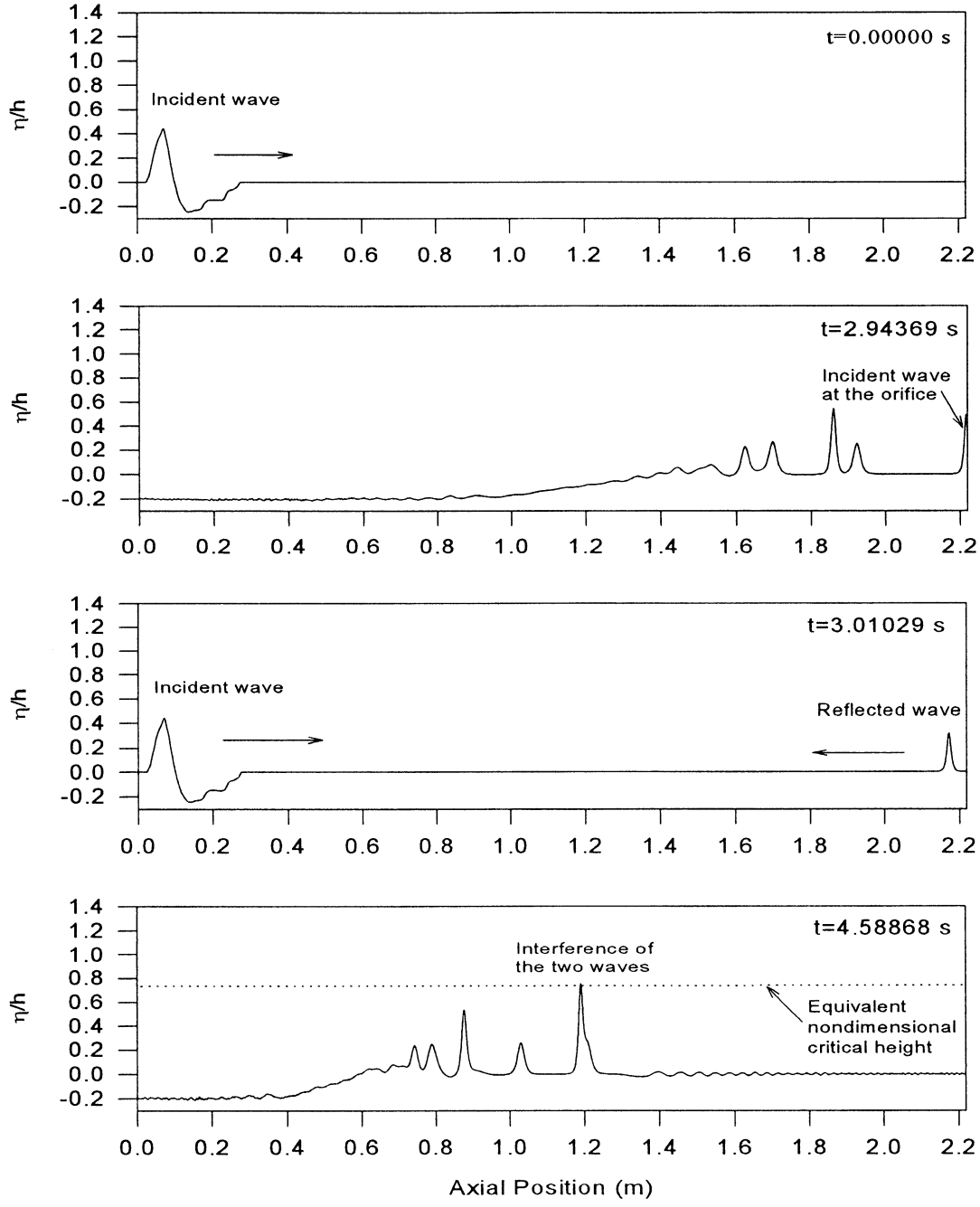

Figure G.23 The formation of slug as modeled for $\beta = 0.77$, Position 2, $Q_l = 1.5\,m^3/h$, $Q_g = 15.8\,m^3/h$

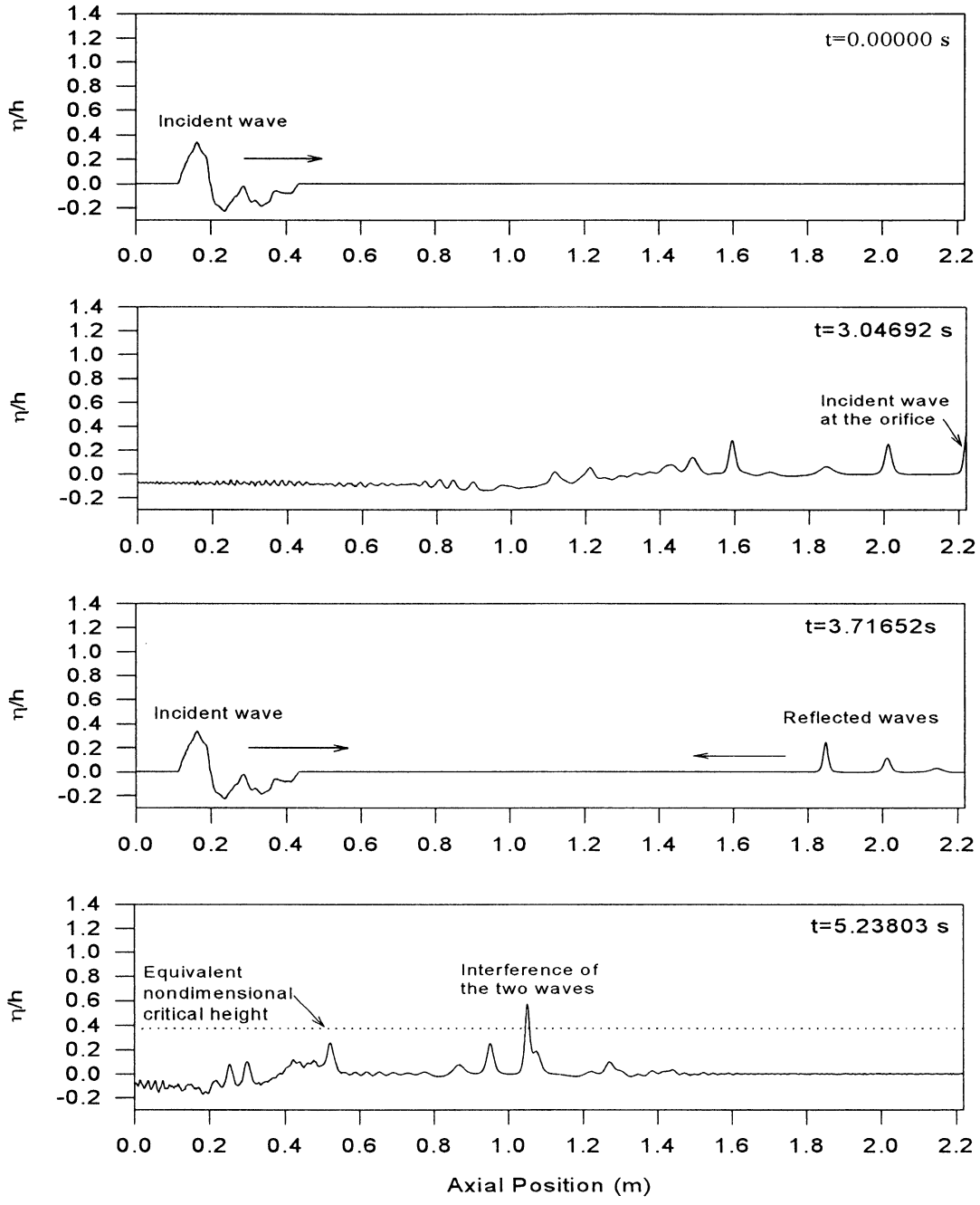

Figure G.24 The formation of slug as modeled for $\beta = 0.77$, Position 2, $Q_l = 1.8\,m^3/h$, $Q_g = 11.4\,m^3/h$

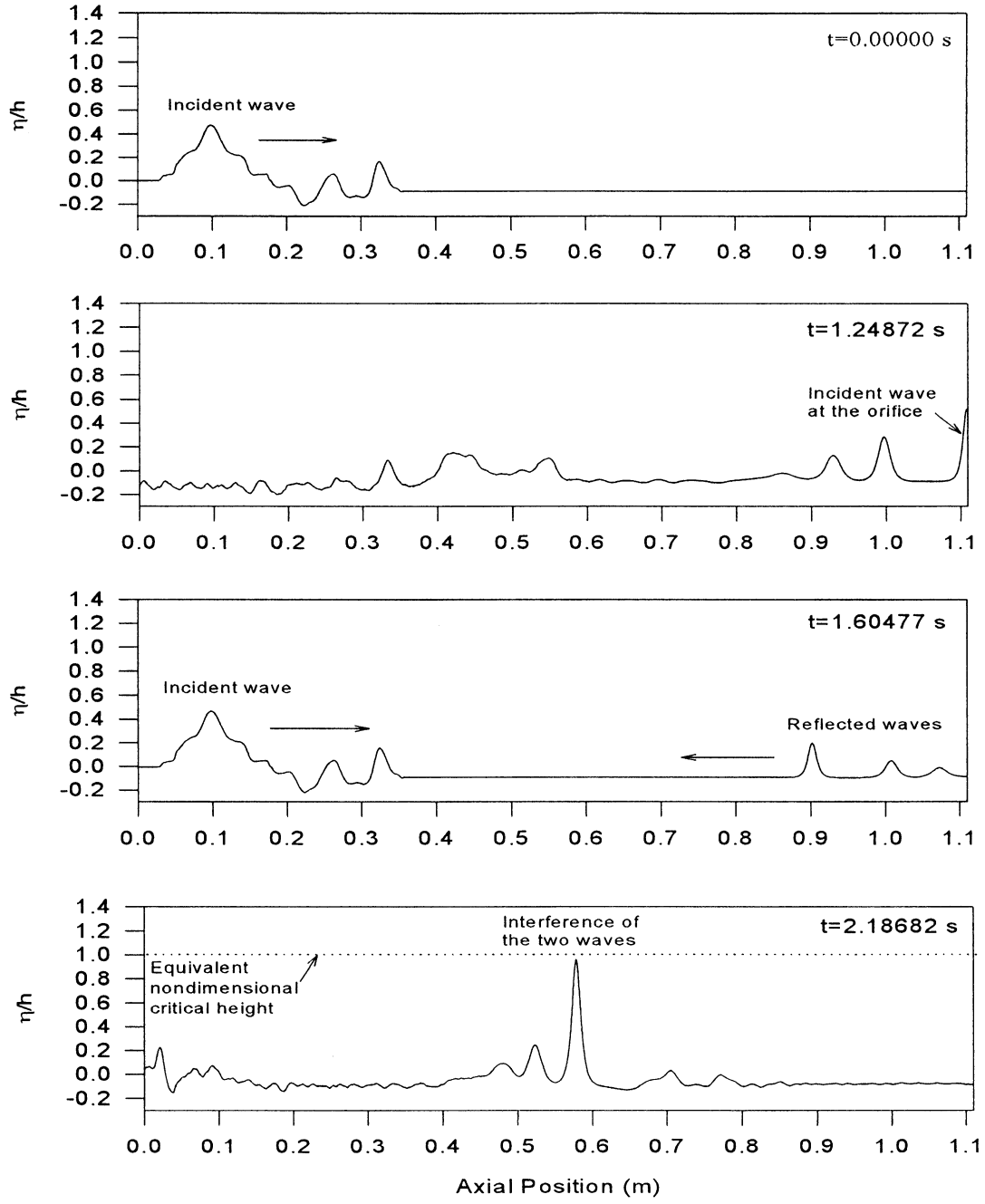

Figure G.25 The formation of slug as modeled for $\beta = 0.83$, Position 1, $Q_l = 0.8\,m^3/h$, $Q_g = 31.5\,m^3/h$

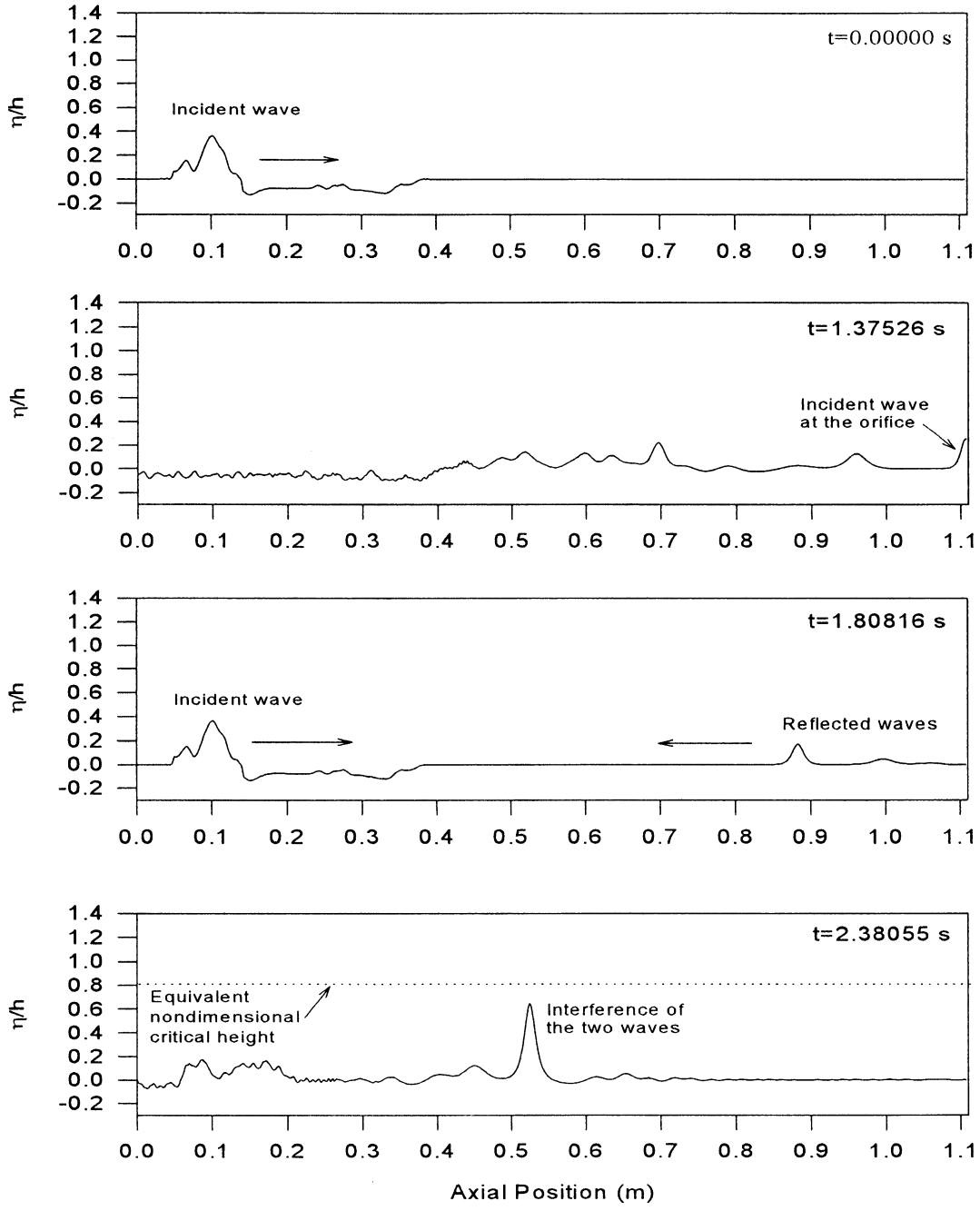

Figure G.26 The formation of slug as modeled for $\beta = 0.83$, Position 1, $Q_l = 1.1\,m^3/h$, $Q_g = 22.2\,m^3/h$

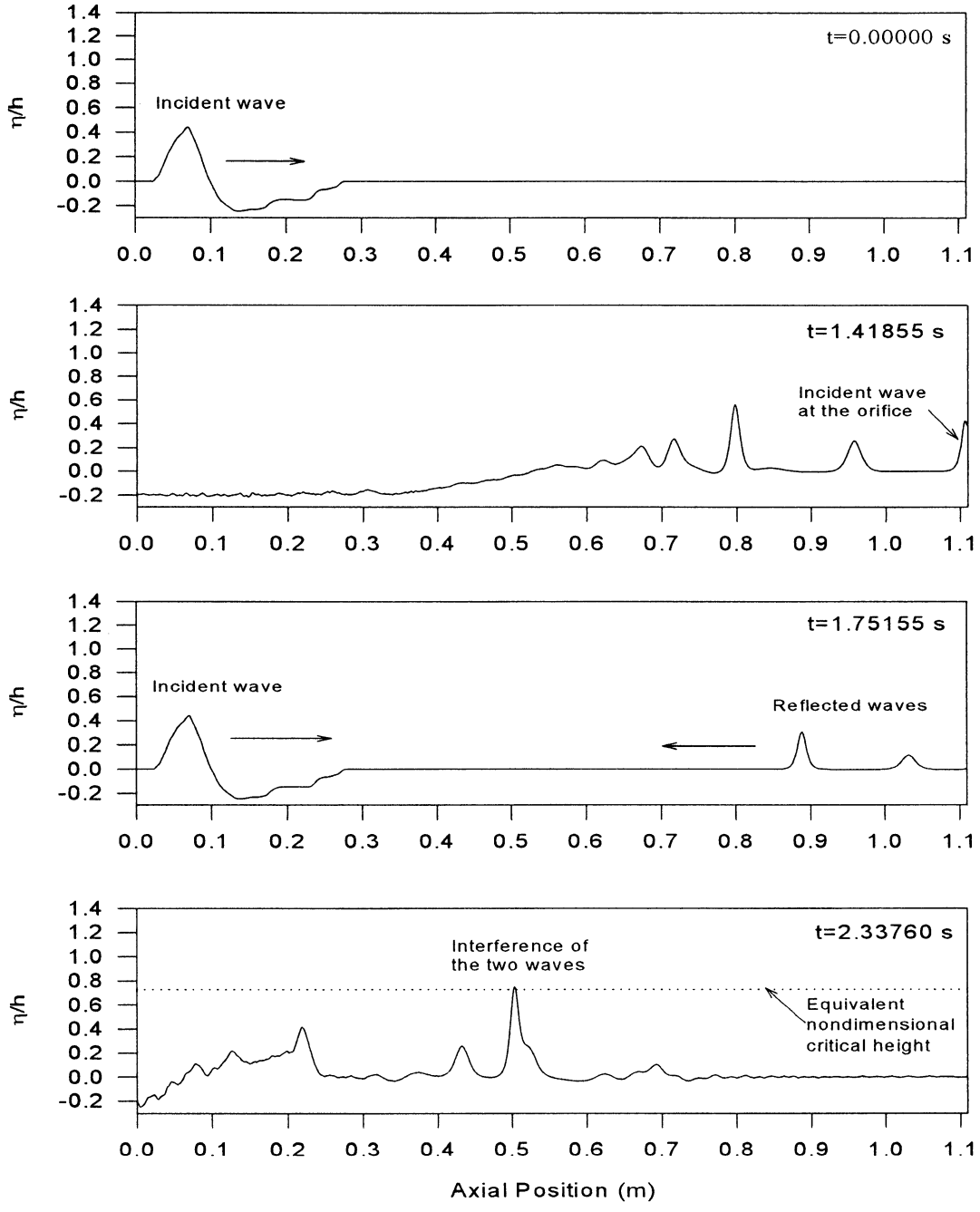

Figure G.27 The formation of slug as modeled for $\beta = 0.83$, Position 1, $Q_l = 1.5\,m^3/h$, $Q_g = 15.8\,m^3/h$

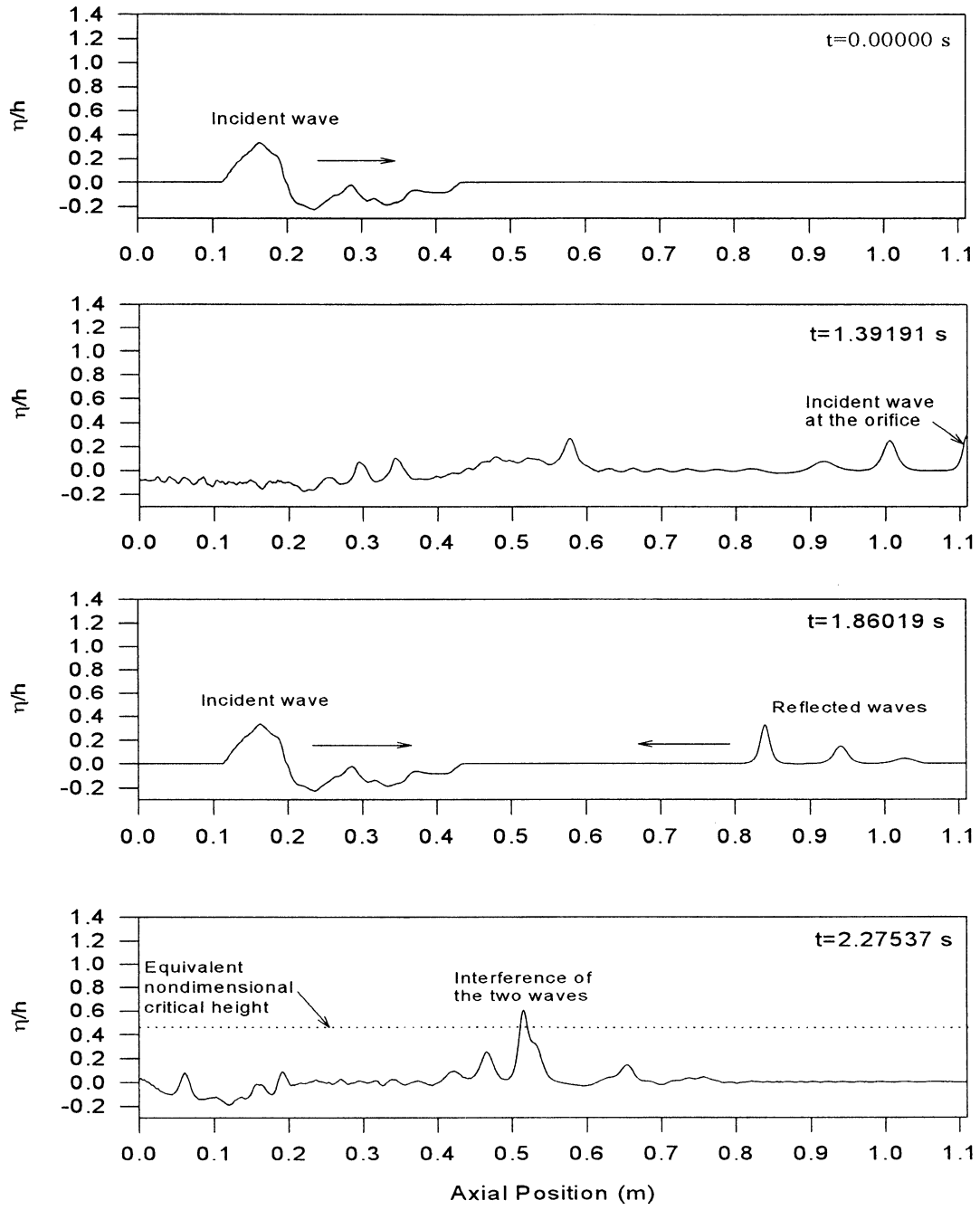

Figure G.28 The formation of slug as modeled for $\beta = 0.83$, Position 1, $Q_l = 1.8\,m^3/h$, $Q_g = 11.4\,m^3/h$

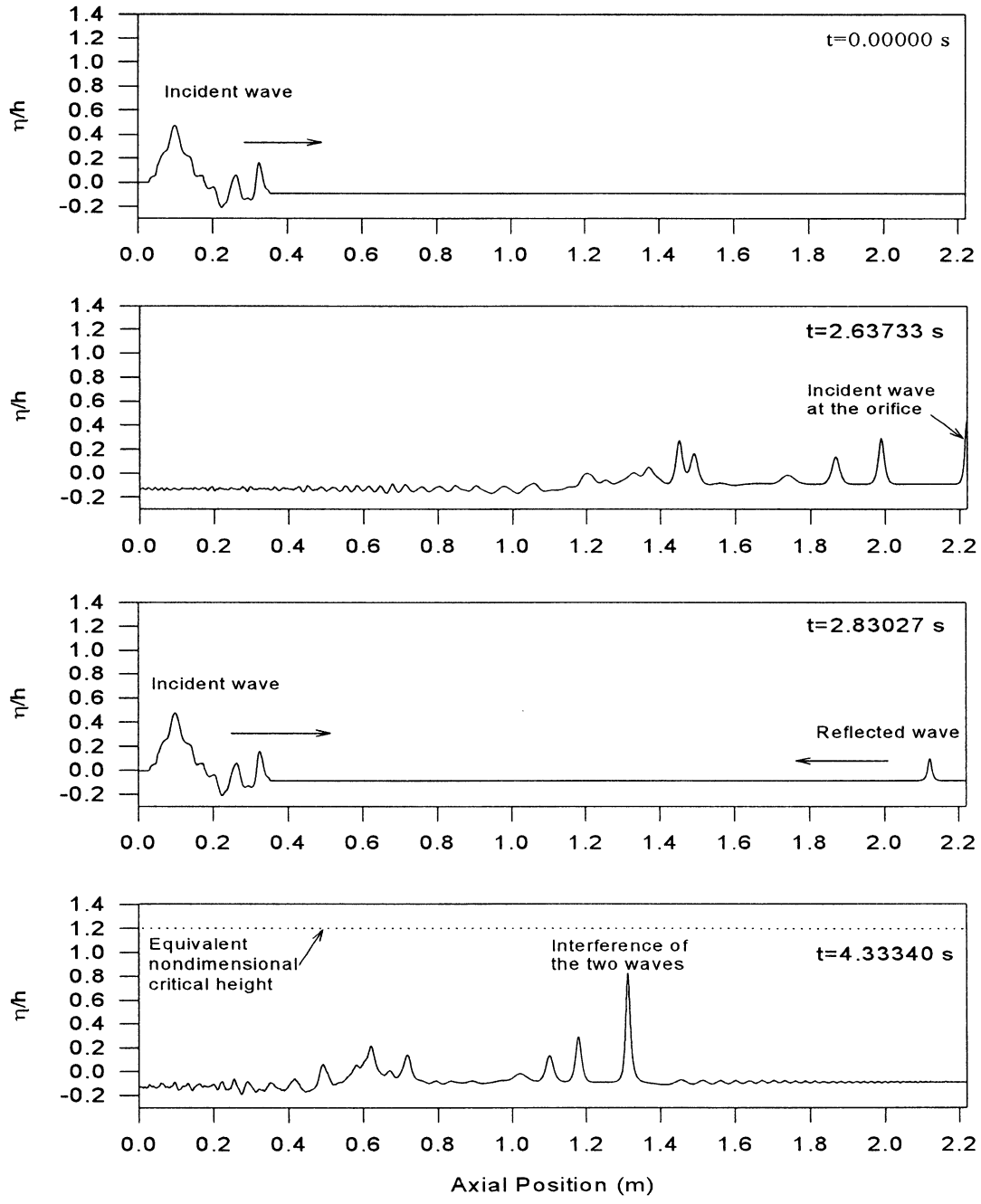

Figure G.29 The formation of slug as modeled for $\beta = 0.83$, Position 2, $Q_l = 0.8\,m^3/h$, $Q_g = 31.5\,m^3/h$

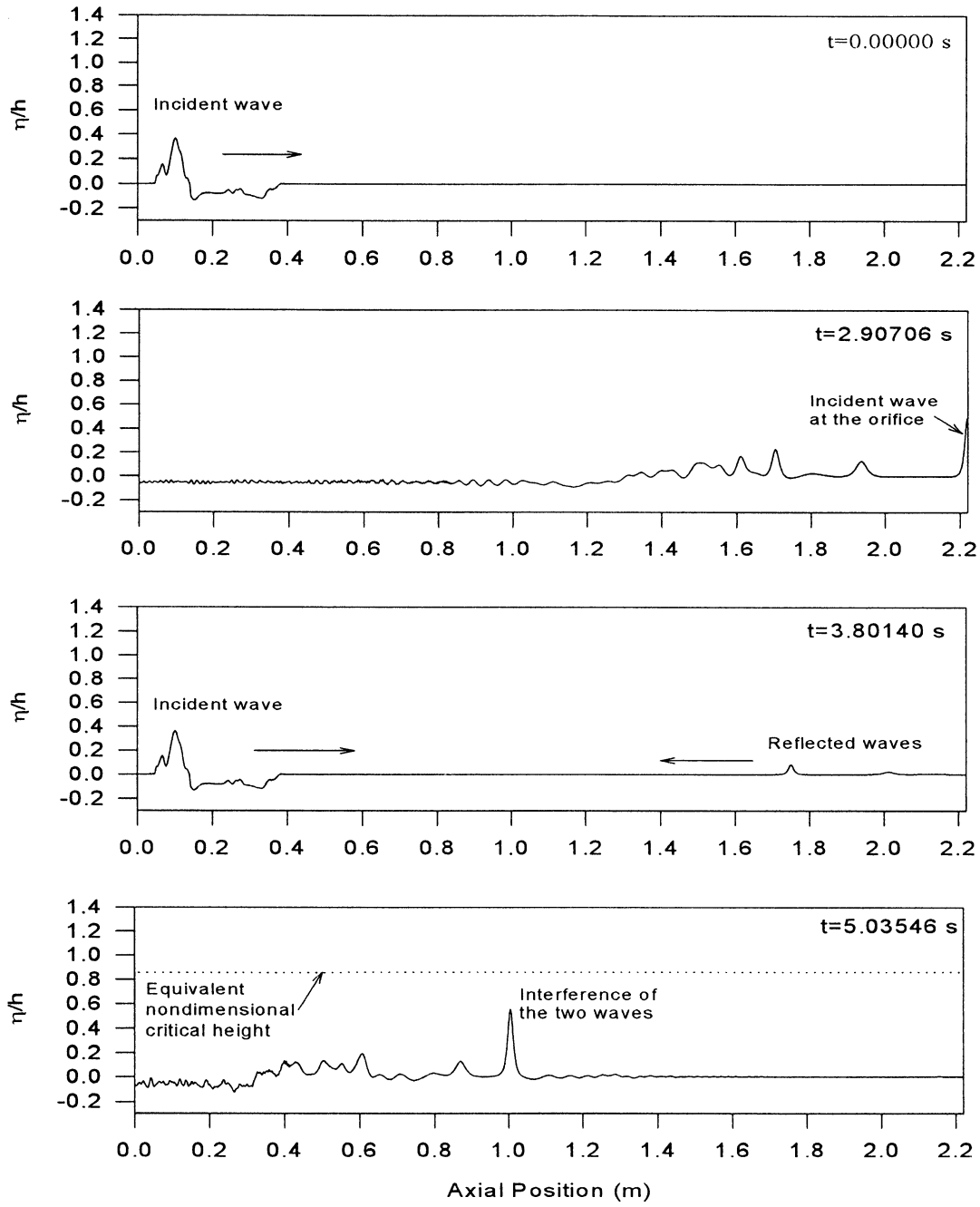

Figure G.30 The formation of slug as modeled for $\beta = 0.83$, Position 2, $Q_l = 1.1\,m^3/h$, $Q_g = 22.2\,m^3/h$

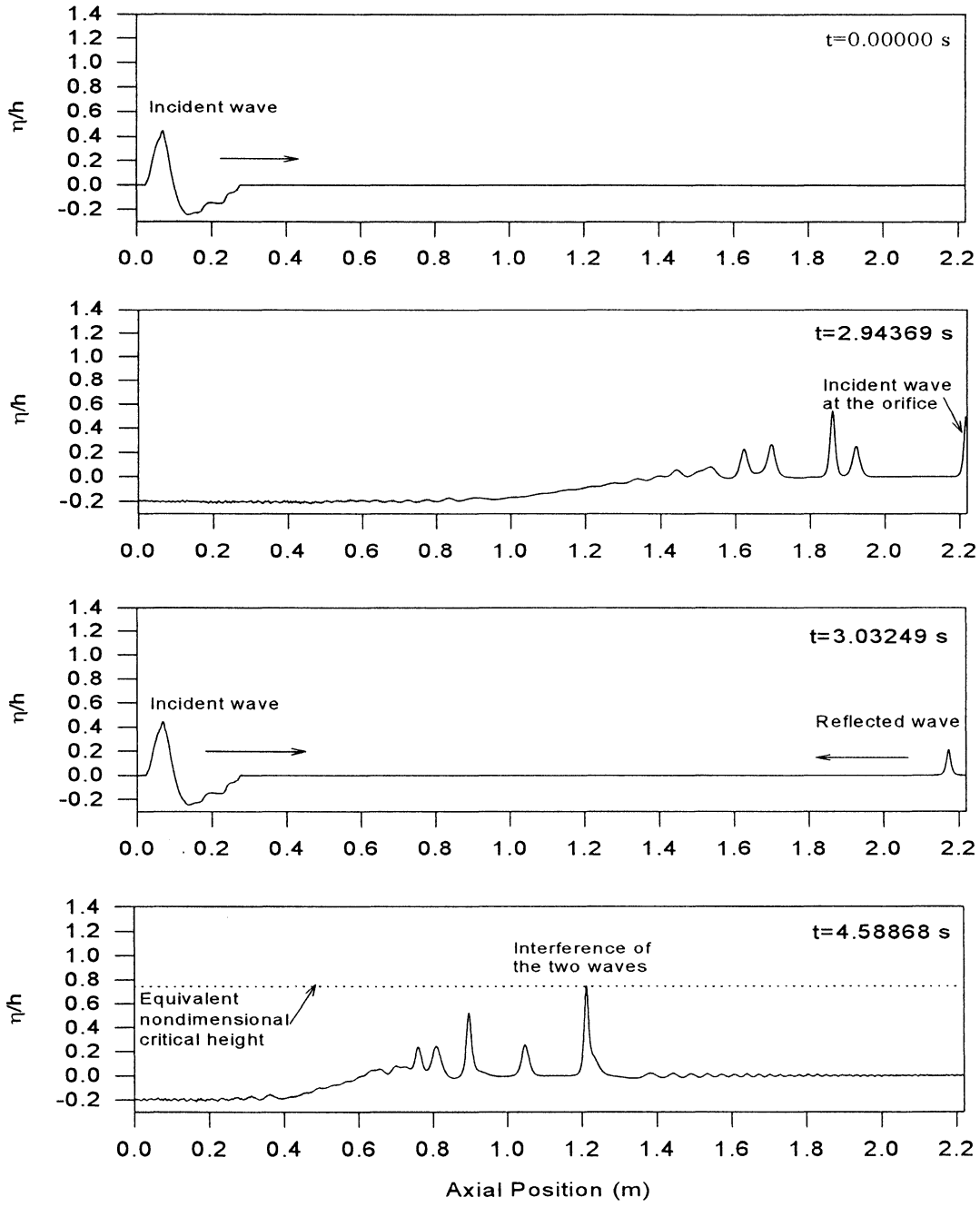

Figure G.31 The formation of slug as modeled for $\beta = 0.83$, Position 2, $Q_l = 1.5\,m^3/h$, $Q_g = 15.8\,m^3/h$

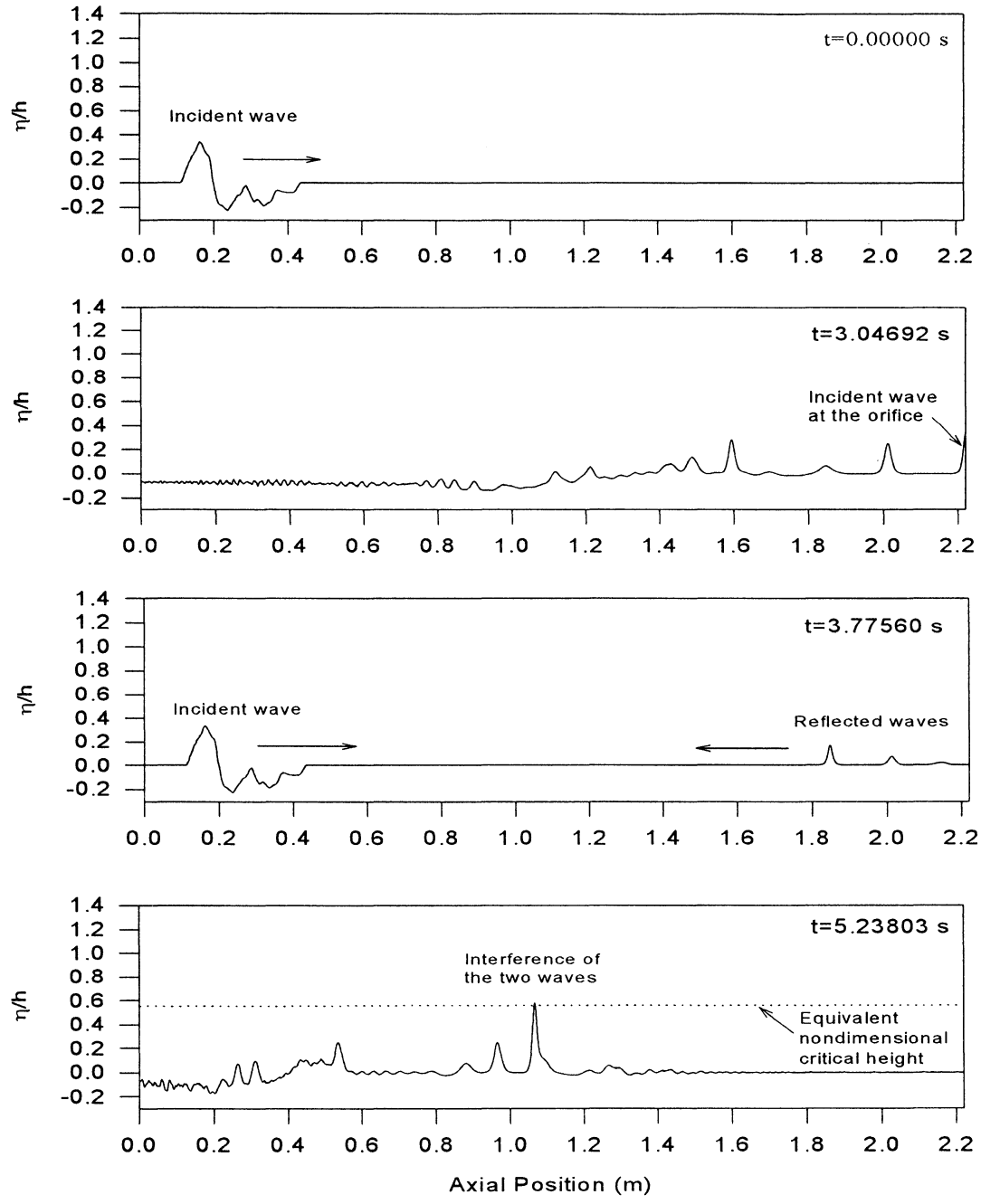

Figure G.32 The formation of slug as modeled for $\beta = 0.83$, Position 2, $Q_l = 1.8\,m^3/h$, $Q_g = 11.4\,m^3/h$

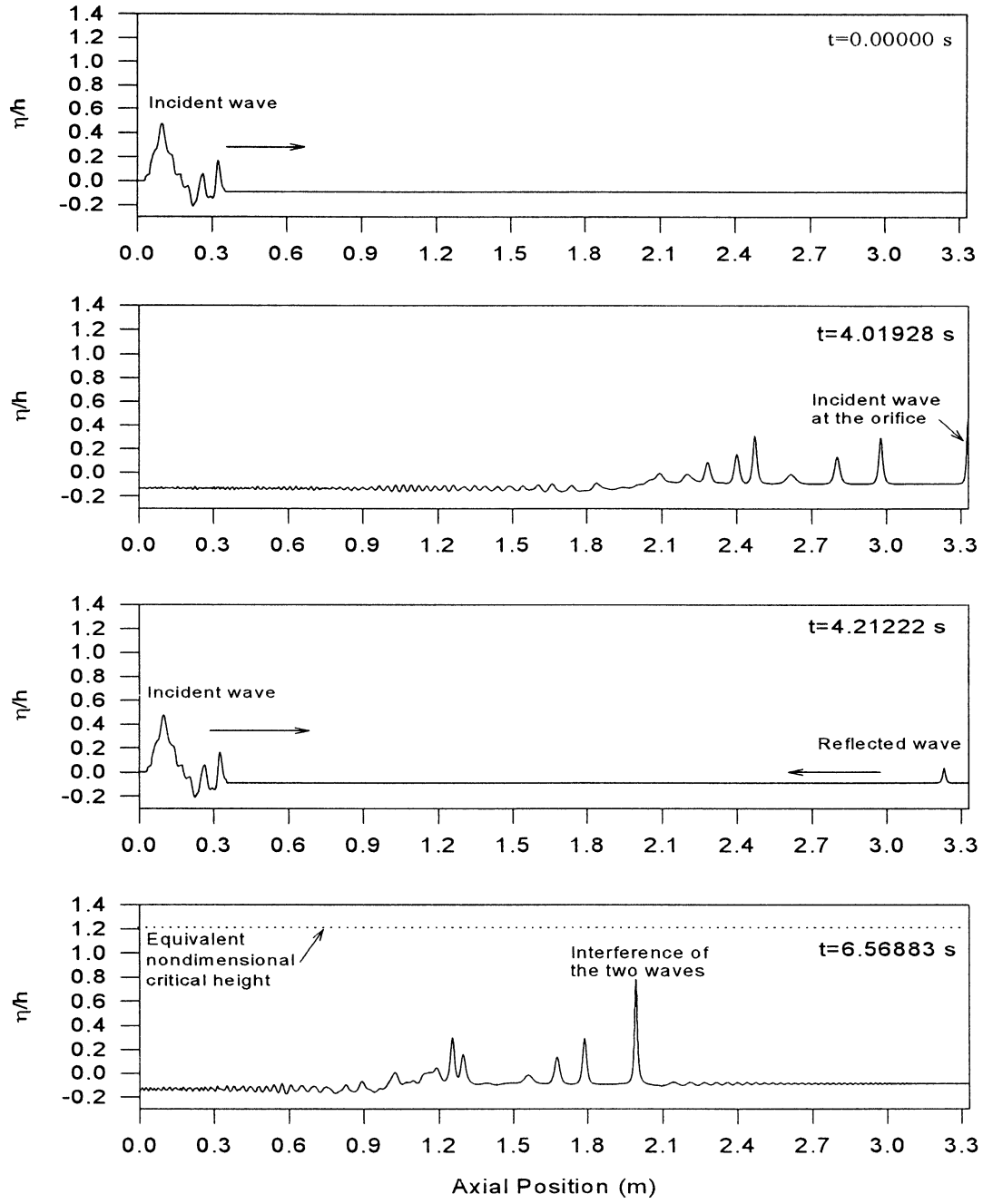

Figure G.33 The formation of slug as modeled for $\beta = 1.0$, $Q_l = 0.8\,m^3/h$, $Q_g = 31.5\,m^3/h$

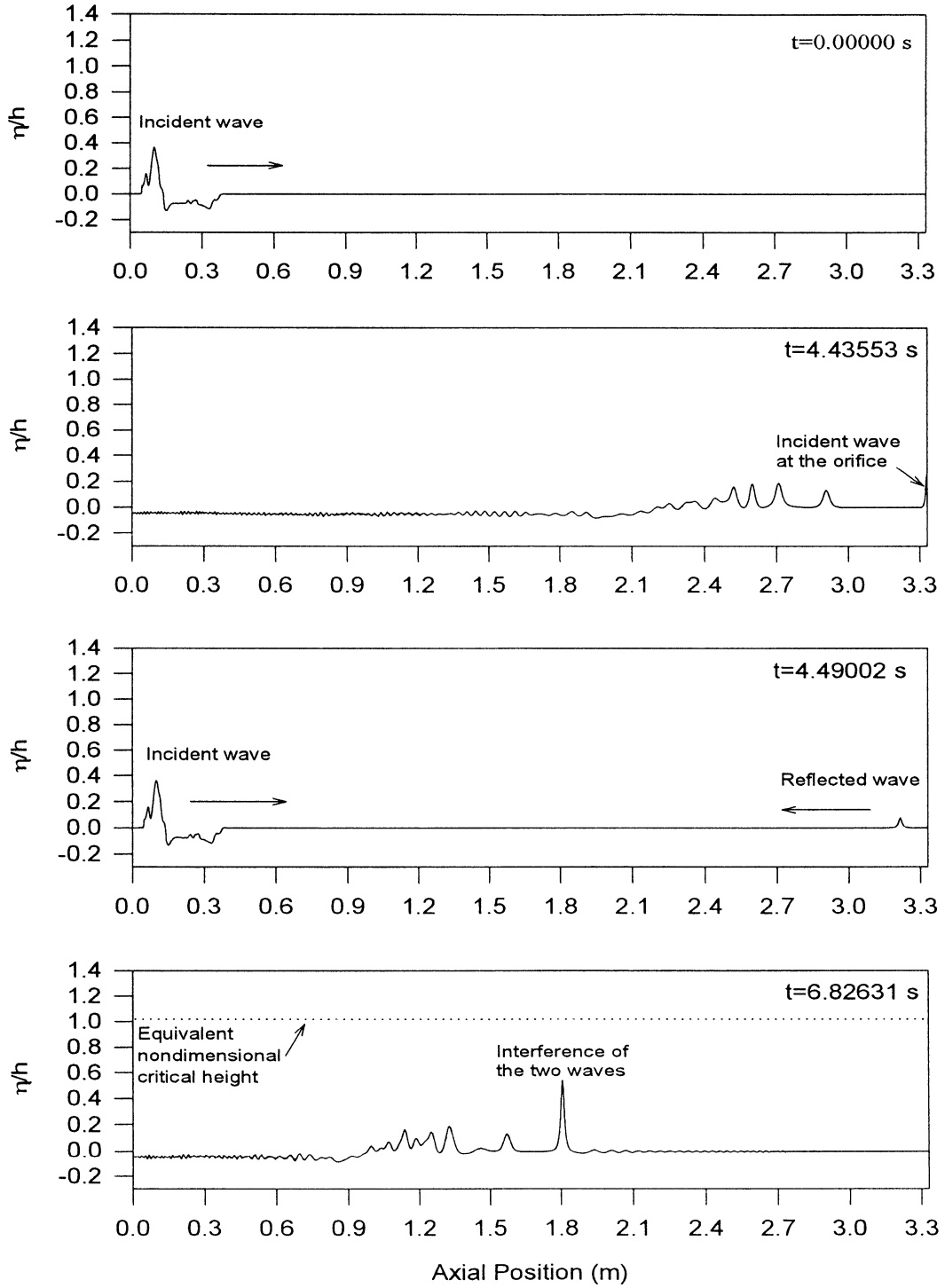

Figure G.34 The formation of slug as modeled for $\beta = 1.0$, $Q_l = 1.1\,m^3/h$, $Q_g = 22.2\,m^3/h$

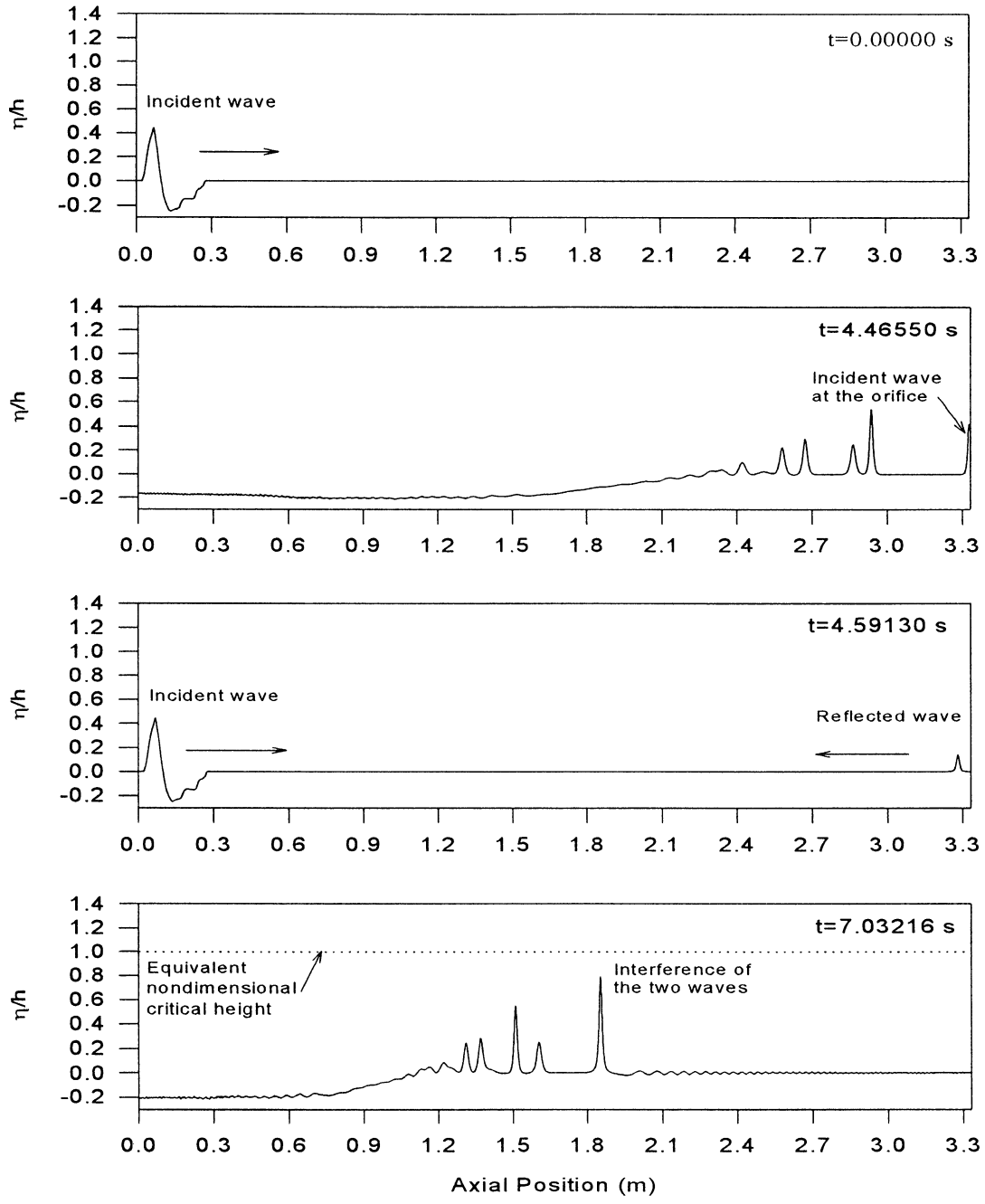

Figure G.35 The formation of slug as modeled for $\beta = 1.0$, $Q_l = 1.5\,m^3/h$, $Q_g = 15.8\,m^3/h$

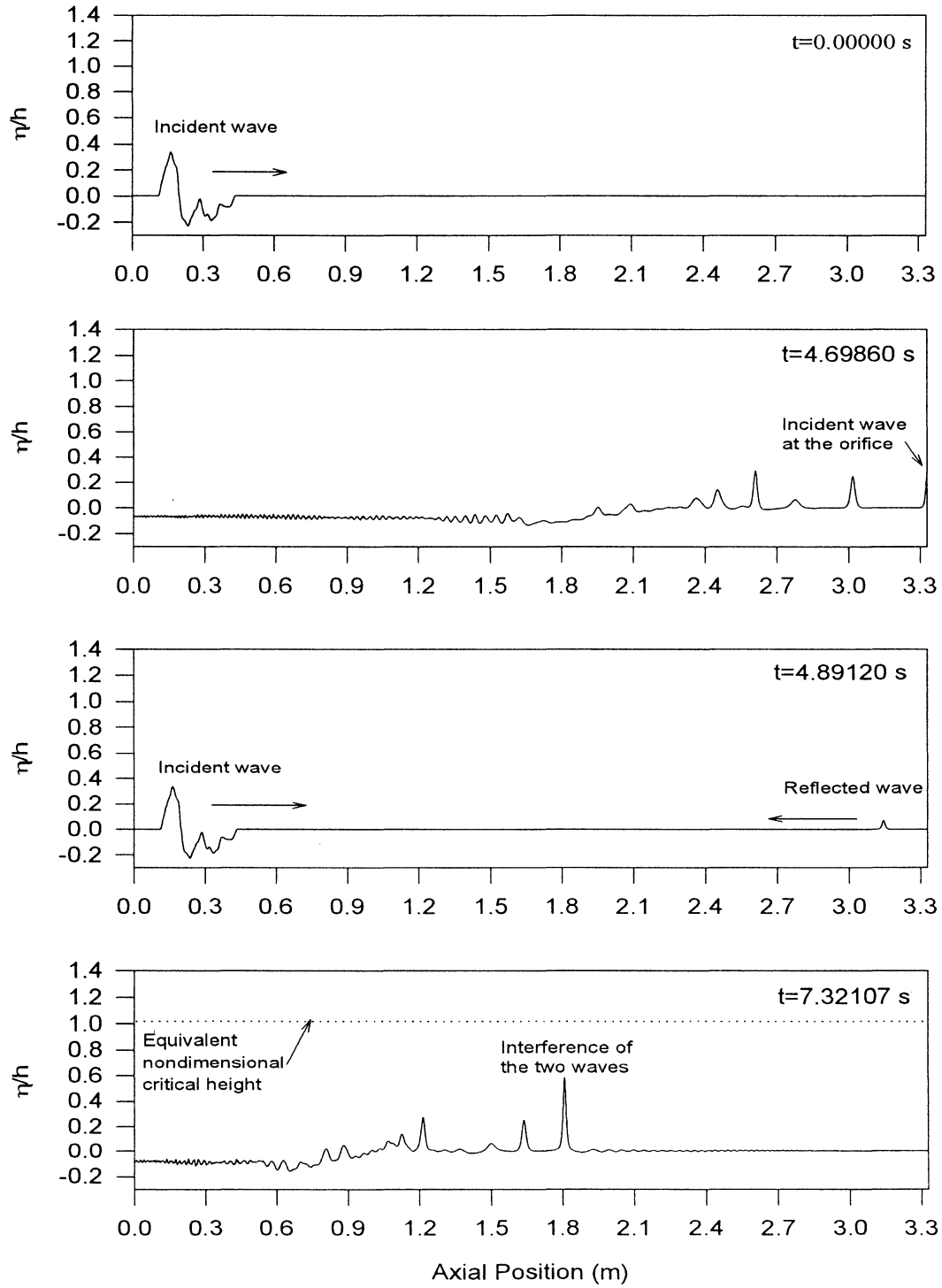

Figure G.36 The formation of slug as modeled for $\beta = 1.0, Q_l = 1.8 m^3/h$, $Q_g = 11.4\, m^3/h$